Qureshi, Muhammad Umar (2013) *Simulating the pulse wave in the human pulmonary circulation.* PhD thesis.

http://theses.gla.ac.uk/5111/

Simulating the pulse wave in the human pulmonary circulation

by

Muhammad Umar Qureshi

A thesis submitted to the
College of Science and Engineering
at the University of Glasgow
for the degree of
Doctor of Philosophy

December 2013

Abstract

This thesis deals with the development and application of an existing [169] non-linear, one–dimensional mathematical and computational model of pulse wave propagation in the human pulmonary circulation with an aim to improve our ability to predict blood pressure and flow in the pulmonary arteries and veins and enhance our understanding of haemodynamic changes occurring during health and disease. The existing model by Vaughan [169] is developed in two ways, firstly by improving the descriptions of venous geometry, values of physiological parameters, inflow and outflow boundary conditions, and then by extending the model to predict pressure drop across the pulmonary vascular beds.

The arteries and veins are treated as thin, homogeneous elastic tubes, and blood as a viscous, homogeneous and incompressible fluid. The non–linear effects of pulse wave propagation are predicted in the large arteries and veins, solving the governing equations by means of two–step Lax–Wendroff scheme. For an accurate haemodynamic prediction, the effects of downstream vasculature are incorporated through dynamic structured–tree matching conditions by linking the arterial and venous pressures and flows. For each blood vessel in the structured trees, linearised governing equations are solved analytically.

The modelling capability is enhanced by imposing four outflow conditions at the orifices of four large veins opening in the left atrium. Considering the fundamental differences between pulmonary and systemic compliance behaviour, a revised compliance parameter value is used to obtain improved predictions of the pulmonary pressure pulse. The model is applied to various hypotheses of pulmonary hypertension to analyse the haemodynamic disorders linked with the causes of the pulmonary hypertension. The prescribed flow–rate boundary condition at the system inlet limits the occurrence of any changes in the flow patterns due to the hypertension, so a new pressure boundary condition, simulating remodelling of the heart or ventricular dysfunction, is imposed to study the effects of the hypertension on the volume flow–rate. To better understand the microcirculatory characteristic in the pulmonary circulation, under normal and diseased conditions, the model is further extended to predict the mean pressure drop across the pulmonary arterioles and venules by treating the connected structure trees not only as boundary conditions but also an active fluid dynamical part of the model. A more insightful interpretation of the results is provided by separating the pulse waveforms into incident and reflected components using Wave Intensity Analysis. Finally, the model is applied to assess the effectiveness of commonly used techniques to estimate local pulse wave velocity in the pulmonary arteries.

This thesis is a step forward in understanding the performance of the pulmonary circulation and its behaviour in response to various anatomical and physiological changes in health and disease. Moreover, despite having room for further developments and validation, the model has the ability to simulate physiologically relevant pulse waveforms at a reasonable computational cost and therefore has a prospect of clinical application in the long run.

To my parents

&

Taya-Abou

Acknowledgements

I am most grateful to almighty Allah, who created me as a human being and provided me with all the favourable circumstances and abilities, which enabled me to understand and enjoy the never-ending process of human development.

Many people have supported me in many ways over the period of last four years but first and foremost, thanks to my parents for every thing they have done for me and my education over the years, despite many hardships and difficulties. I could never get to this stage in my life without their affection, prayers and firm belief in my abilities.

I am sincerely grateful to my supervisor Prof. Nicholas Hill for his guidance, encouragement, patience and kindness with which he has dealt with me from start to finish. I thank him for reading my work and correcting numerous mistakes. He has been a great mentor and a constant source of inspiration for me. I am also grateful to Prof. Mette S. Olufsen for her support, encouragement and always taking interest in my work and suggesting ideas to improve it. Without her mentoring, particularly in writing, this thesis could never be in this shape. I am also thankful for her great hospitality during my visit to N.C. State University in the summer 2013. I would especially like to mention Prof. Tasawar Hayat at Quaid-e-Azam University, Islamabad, who inspired me to study fluid mechanics at the first place and later introduced me to physiological fluid dynamics. I acknowledge with thanks his contributions in getting me to this stage.

Thanks to all the past and present colleagues of 309 for some good times and many interesting discussions through the last four years. A special thanks to one of my best office friends Dr. Xiang Liu for his wonderful company and patient responses to many non–sense question, I asked him regarding Matlab or Latex. Thanks also to Dr. Ehsan Ashraf and Dr. Moniba Shams for helping me to settle down in Glasgow, and in an entirely new working environment, during my first year.

I am grateful to all my friends for some great company and constant moral support during highs and lows of the PhD. A special thanks to all my team mates in GU student and GU staff cricket teams, friends form Stevenson badminton club, Imtiaz Ahmed, Dr. Jabbar and Dr. Amir from Glasgow and Tariq Hussain from Pakistan.

Thanks are also due to my dear brothers Asad, Usman and Abubakar for their constant support and encouragement and for looking after my parents while I spent last many years away from home to pursue my academic goals. Thanks also to other members in the family and family friends for their never ending support and encouragement.

I also acknowledge the excellent research facilities and teaching opportunities provided by the University of Glasgow.

Last but not the least, I am extremely grateful to Govt. of Pakistan, Higher Education Commission in Pakistan and my employer International Islamic University, Islamabad for the scholarship award to do PhD from Glasgow.

Statement

This thesis is submitted in accordance with the regulations for the degree of Doctor of Philosophy at the University of Glasgow.

No part of this thesis has been submitted in the past for a degree at this or at any other university.

Chapter 1, parts of Chapter 2 and Chapter 6 contain background and preliminaries. The remaining thesis is author's original work under the supervision of Prof. Nicholas Hill, unless otherwise stated explicitly with references.

Results from Chapter 3, Section 4.1, Section 4.2 and Chapter 5 have resulted in the form of a paper, which has been accepted for publication in *Biomechanics and Modelling in Mechanobiology* [138]. Results from Section 4.3 and Chapter 5 were presented in BAMC 2012 in London while the results from Chapter 6 were presented in 12th U.S. National Congress on Computational Mechanics in Raleigh, NC, USA.

Contents

List of Abbreviations

BCW: Backward compression wave

BDCW: Backward decompression wave

CTEPH: Chronic thromboembolic pulmonary hypertension

FCW: Forward compression wave

FDCW: Forward decompression wave

HLD: Hypoxic lung disease

LA: Left atrium

LPA: Left pulmonary artery

LIA: Left interlobular artery

LTA: Left trunk artery

LSV: Left superior vein

LIV: Left inferior vein

MRI: Magnetic resonance imaging

MPA: Main pulmonary artery

PH: Pulmonary hypertension

PAH: Pulmonary arterial hypertension

PVH: Pulmonary venous hypertension

PWV: Pulse wave velocity

RC: Resistor–Capacitor

RCR: Resistor–Capacitor–Resistor

RV: Right ventricle

RPA: Right pulmonary artery

RIA: Right interlobular artery

RTA: Right trunk artery

RSV: Right superior vein

RIV: Right inferior vein

RVD: Right ventricular dysfunction

WIA: Wave intensity analysis

List of Figures

List of Tables

Chapter 1

Introduction

This chapter provides a brief introduction to the subject and an overview of existing relevant work. At the end of this chapter a chapter-wise layout of the thesis is also given.

1.1 Cardiovascular circulatory systems

The cardiovascular circulation is comprised of two separate and distinct systems, the systemic and the pulmonary circulation, both connected to the heart (see Figure 1.1). The heart consists of four chambers, two ventricles and two atria, and its function is to provide the energy to move the blood through these two systems across the whole body. During a cardiac cycle the size of the heart varies due to contraction and relaxation of the heart muscles. During the contraction phase, known as systole, almost an equal volume of blood (stroke volume) is pumped through aortic and pulmonary valves into ascending aorta and main pulmonary artery (MPA). During diastole, the relaxation phase, the aortic

Figure 1.1: Diagram has been removed due to Copyright restrictions.

A depiction of cardiovascular circulatory system in the human body. The picture illustrates the arrangement of pulmonary and systemic circulations and their connection with the heart. The blue colour in the figure indicates the deoxygenated blood whereas the red colour indicates the oxygen rich blood. The right heart regulate the deoxygenated blood which is pumped in the lungs through pulmonary arteries where it gets oxygenated and transported back to the left heart through pulmonary veins. Figure taken from csuglobal.blackboard.com/bbcswebdav/courses/Recycle%20Bin/hcm305_4/hcm305_4.html# on 25/11/2013.

and pulmonary valves shut while the mitral and tricuspid valves open to fill the left and right ventricles with the blood coming from left and right atria, respectively. The systemic circulation transports oxygenated blood from the left heart to organs and muscle in the body and back to the right heart, and the pulmonary system, which serves to remove CO_2 and re-oxygenate the blood, transports blood from the right heart through the lungs and back to the left heart.

The pulse wave

Initiated by the contraction of the heart, the arterial pulse wave is a propagated pulsation or disturbance in the longitudinal direction along the arterial lumen. The propagation of the pulse involves simultaneous changes in potential (pressure) and kinetic energy (flow–rate) which propagates faster than the bulk flow velocity of the blood. The shape of the pulse, both in the systemic and pulmonary arteries, depends on the pattern of ventricular contraction, motion and properties of the blood, and the structural and material properties of the blood vessels. Thus the features of the pulse wave, such as the shape, speed and magnitude of the pressure and flow waveforms, carry vital information about the complex architecture of arterial network and its dynamic interaction with the heart. A detailed analysis of the pulse wave helps us to understand the contribution of physiologically important parameters, such as the arterial stiffness through pulse wave velocity, in understanding the overall haemodynamics in the circulation.

1.2 Modelling the circulation

The purpose of mathematical modelling is to develop a theoretical representation of the real world system that may be solved to simulate the functional behaviour of the real system. Thus a good mathematical model includes the essential features of the real world system and, more importantly, can be solved to simulate an outcome, the behaviour of which mimics with that observed in the original system. The fundamental motivation of mathematical modelling is to improve our understanding and insight into the function of the system by investigating the simulated results in detail. However, with ever improving technology and the boost in computational resources, the modeling objective has also evolved from deep understanding of a phenomenon to devise control strategies of the real world system, based on the predictions through model simulations.

Likewise the modelling of cardiovascular circulatory systems and the simulation of pulse wave propagation in the arteries is of great interest for mathematicians and physiologists alike. Computational models of blood flow significantly improve our understanding of the system and provide useful insight into the underlying mechanisms, such as the relation between blood pressure and the geometric and material properties of the blood vessels and the role of peripheral resistance in characterizing the pulse wave propagation in the main arteries. A good understanding of normal cardiovascular function also helps to improve our understanding of abnormal function. Therefore, powered by modern technology, like Magnetic Resonance Imaging (MRI), the enhanced capability to model the cardiovascular systems by incorporating the detailed *in vivo* data is playing an increasingly significant role in improving the diagnosis and treatment of the cardiovascular diseases, which remain the major cause of deaths in the developed countries.

The lungs have a unique structure, consisting of complex network of arterial and venous vessels, airways and alveoli which makes the pulmonary circulation vastly different from systemic circulation. However, most previous modelling studies (e.g. [50,52,103,116,145]) only focus on the systemic arterial system, while relatively little attention has been given to the pulmonary circulation. The physiological importance and complex anatomy not only makes modelling of pulmonary circulation a unique and interesting problem for both mathematical modellers and physiologists but it also highlights the need to model the pulmonary system as a distinct system with an aim to predict the pulmonary haemodynamic in detail. By developing a computational model specific to the pulmonary circulation, it is not only possible to predict the normal physiological behaviour of pressure and flow in the lungs but the effects of disease, like pulmonary hypertension, on the pulmonary haemodynamics may also be analysed.

1.2.1 Anatomy and physiology of the pulmonary circulation

To understand better how to approach studying the dynamics involved in predicting the propagation of pressure and flow in the pulmonary system, we first need to understand the anatomical and physiological design of the pulmonary circulation and outline similarities and differences between the systemic and pulmonary systems.

The pulmonary circulation extends from the outlet of right ventricle (RV), into main pulmonary artery (MPA), to the orifices of four pulmonary veins in the left atrium (LA). Unlike the systemic circulation there is immediate branching of the MPA towards right

Figure 1.2: Diagram has been removed due to Copyright restrictions.
A sketch of pair of human lungs, taken from Atlas of Human Anatomy by Frank H. Netter [54]. Only those vessels that are to be modelled explicitly are labelled. The picture depicts the start of pulmonary circulation from the right ventricle, its branching toward right and left lungs and return to the left atrium via four large veins.

and left lungs (right and left pulmonary arteries) which further branch rapidly and progressively until the level of the bronchi where the capillaries loop around the bronchia to facilitate maximal perfusion of oxygen and carbon dioxide with the lungs [177]. The MPA exhibits significant tapering from its proximal end to the point of bifurcation at the distal end, where it bifurcates into the left (LPA) and right pulmonary arteries (RPA) [12]. Moreover, the path length along pulmonary vascular segments are shorter than their systemic counterparts with an approximated total path length of 34 cm between pulmonary valve and the left atrium [73, 74, 148]. The two systems transport the same volume of blood, but the pulmonary system is much smaller and operates at a much lower pressure. Moreover, the pulmonary system only stores about 10% of the total blood volume (about 500 ml of blood). This is still significant, given that the lungs only comprise 1% of the total body weight [163].

A more important difference between the two systems is that, in the pulmonary circulation, the arterial and venous walls are thinner and more compliant than the systemic vessels, giving rise to a low pressure and low resistance system [105, 121]. Moreover, the pulmonary vessels do not get stiffer as they progress away from the heart [13, 121] and therefore the pulmonary capillaries are also found to be more compliant than the systemic capillaries and they also tend to dilate with a raised transmural pressure [178], however, this relationship is complex and the extent of their compliance is not clear [179]. The mean driving pressure in the pulmonary arteries is about 10 mmHg[1] compared to 91 mmHg in the systemic arteries, and, since the volume flux is equal in both systems, the resistance in the pulmonary circulation is nine times less than that of systemic circulation [63, 111] but this low resistance increases with age [90]. The low resistance in the pulmonary microcirculation also leads to the transmission of pulmonary arterial pulse pressure to the alveolar capillaries and therefore pulsatile flow in the capillaries [141] and even on the venous side

---

[1] As common for studies examining cardiovascular dynamics, all pressures are given in mmHg. The conversion to SI units is 1 mmHg = 133.3 Pa. Also 1 atm = 760 mmHg.

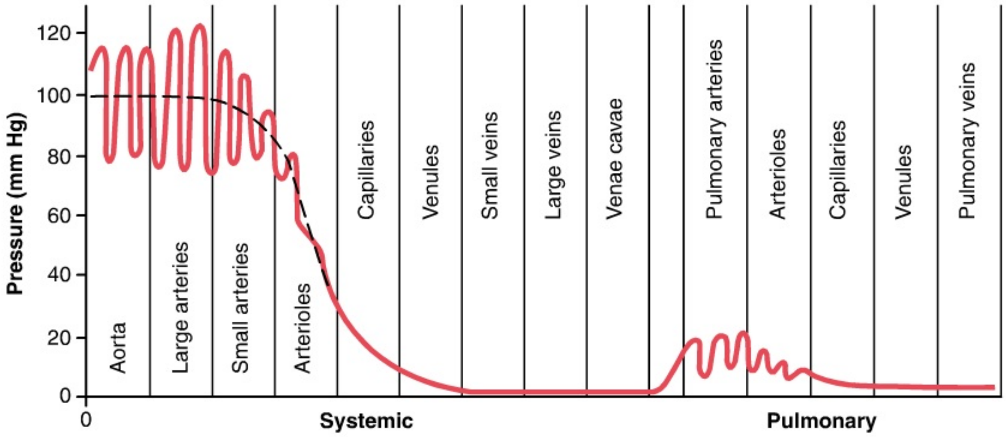

Figure 1.3: A schematic of pressure distribution across different levels of cardiovascular circulatory systems. The pressure in the pulmonary arteries is much lower than in the systemic arteries, but the pulmonary veins are pressurized unlike their systemic counterparts [63].

Figure 1.4: Diagram has been removed due to Copyright restrictions.
Anatomy of pulmonary veins. A depiction of different branching patterns of pulmonary veins anatomy found through MRI images from patients under control and with arterial fibrillation. Shaded portions indicate different parts from typical anatomy. A, typical branching pattern. B, short common left trunk. C, long common left trunk. D, right middle pulmonary vein. E, two right middle pulmonary veins. F, right middle pulmonary vein and right upper pulmonary vein (from Kato *et al.* [82]).

of pulmonary circulation is observed [18, 101].

As for the pulmonary veins, a variety of anatomic patterns may be observed in people with normal and abnormal pulmonary function (see Figure 1.4) [82]. However, the most commonly observed pattern is where four veins, left and right superior and inferior pulmonary veins, return the oxygenated blood from both lungs into the left atrium. In this thesis, as shown in Figure 1.4–A, the most common or typically healthy pulmonary venous geometry is simulated. Furthermore, the pulmonary veins serve not only as channels through which oxygenated capillary blood flow is transported into the left atrium, but they also regulate fluid filtration pressure in the upstream capillary network via active vasomotion, contributing significantly towards total pulmonary vascular resistance [56].

1.2.2 Modelling approach

The detailed modelling of structurally complex systems, like the pulmonary system, leads to mathematical complications which make it extremely difficult, if not impossible, to solve the model analytically or numerically. In such situations, by keeping in mind the application requirements and the available resources for modelling, one has to carefully decide which aspects of the systems are essential, which may be ignored, which part of the system must be modeled explicitly, and which can be approximated.

Blood flow in the arteries is a three–dimensional phenomenon and as large scale computations are becoming increasingly feasible, it is possible to simulate three dimensional pulse wave propagation in the arteries by numerically solving the governing three dimensional equations [50,61,102,107,129,170]. While this approach is useful, especially to understand the response of pressure and flow field to the local biomechanical forces occurring, e.g. due to initiation and development of atherosclerotic and aneurismal disease in the large arteries [189], in most clinical situations, e.g. during surgery, only one–dimensional pressure and flow profiles are required to monitor and infer patients' haemodynamical response. Although the information about one–dimensional pulse may be extracted from the three–dimensional models, computationally this approach is not feasible for full circulatory system particularly when one is only interested in a detailed analysis of one–dimensional pressure and flow waveforms. It has been observed that predictions through cross–sectionally averaged one–dimensional models of blood flow agree with the corresponding simulations of resulting three–dimensional models when averaged over the cross–sectional area [107,129]. Thus where detailed simulations in full scale three–dimensional circulation models remain computationally expensive, the one–dimensional models may provide accurate prediction of quantities like, cross–sectionally averaged pressure and flow along the arterial lumen, at the fraction of the cost of three–dimensional models. In this thesis we also focus on a simpler one–dimensional model to simulate the pressure and flow in the large pulmonary arteries and veins.

One–dimensional models

Linear approach: The simplest approach to study the blood flow in arteries starts by considering an invscid, incompressible fluid in an infinitely long compliant tube with uniform cross–sectional area in which the axial flow is governed by conservation of fluid volume and momentum along with a state equation that relates the undisturbed cross–

sectional area of the tube to the local transmural pressure [32]. The linearised version of governing equations is achieved by considering the small perturbations (long wavelength approximation) in the initial undisturbed state (finite pressure and zero axial velocity) of the tube and the fluid contained in it. The resulting pulse wave propagates along the tube with a constant wave velocity without changing the shape of the pulse wave while the pressure and flow waves remain in phase. If the analysis is considered in a tube of finite length, bifurcating into daughter vessels, then the changes in pressure and flow along the parent tube can be explained in terms of reflections generating from the site of impedance mismatch due to abrupt changes in the local geometry and material properties at the junction.

The phase difference between pressure and flow was discussed by J. R. Womersley for the first time in his analysis of pulsatile blood flow in the arteries [182]. He derived the system of linear partial differential equations under the assumption of axisymmetry, linear viscoealstic wall properties, and by perturbing the pressure and axial velocity about the undisturbed state to govern the fully developed pulsatile flow in an elastic vessel. The resulting system of equations can be solved analytically and the solution involves Wormesley parameter, $w = r\sqrt{\omega/\nu}$, that defines the relation between angular frequency of oscillation in pressure gradient (ω) and the kinematic fluid viscosity (ν) through the vessel radius (r). Womersley explained that at lower frequency of oscillation, ω, the viscous effects would be dominant, yielding $w \leq 1$, so the parabolic velocity profile will have enough time to develop fully during each cardiac cycle, as is the case in small blood vessels. However, in the large arteries when ω is higher, the viscous effects become weak and the shape of the velocity profile become more plug–like for large values of $w\,(\geq 10)$. In this case there is phase lag between pressure gradient and the blood velocity.

Non–linear approach: The non–linear approach for simulating the pulse wave propagation in the arteries involves solving a hyperbolic system of partial differential equation consisting cross–sectionally averaged conservation of volume and momentum and a so–called state equation that relates the vessel cross–sectional area with the transmural pressure. The one dimensional governing equations are based on the assumption that the component of blood flow velocity in the axial dimension is dominant and the changes in pressure over the cross–sectional area can be neglected for the viscous, incompressible flow in a thin walled elastic tube. The resulting non–linear system can be solved by using the method of characteristics or by using a finite–difference [113, 169] or a finite–element scheme [145] subject to suitable initial and boundary conditions.

1.2.3 Boundary conditions

Faced with increasing complexity due to rapidly increasing number of vessels and the total cross–sectional area after each generation in the vascular trees, the non–linear computations at all generations become increasingly difficult. One approach is to define a domain of interest by choosing a small subset of arteries or veins where the non–linear effects are to be simulated in detail while accounting for the remainder of the vascular tree through boundary conditions. Since the root of the arterial tree is a single vessel emanating from the heart, it is reasonable to impose a measured flow–rate or pressure profile as an inflow boundary condition. However, at points where the blood flows out of the arteries, that lie within the computational domain of interest, depending on number of generations in the tree the number of outlet points grow exponentially and it is not feasible to measure a pressure or flow–rate profile at each outlet to be imposed as outflow boundary conditions. Thus, in order to incorporate the effects of downstream haemodynamics on the pulse wave in the main arteries, an outflow boundary condition is required to be used at the terminals of main blood vessels that is not only physiological but its implementation is also feasible from the computational point of view.

This can be done by creating a simplified representation of peripheral vascular beds, which describe the general features of input impedance. One approach is by combining the effects of physiologically important parameters, such as the total peripheral resistance and compliance, in a lumped–parameter model while neglecting the spatial variations of these parameters within the model. Another relatively new approach is to prescribe a network of small blood vessels, based on the physiological description of actual vascular beds, such that the effects of spatially distributed phenomena and the aspects of wave propagation throughout the circulatory system may be taken into account. A popular example of afore mentioned lumped–parameter model is the three–element Windkessel representation of the vascular beds [9, 25, 133, 154] whereas the structured–tree representation of vascular beds is a good example of distributed downstream models. In many recent studies concerning the blood flow in the arteries [35, 36, 40, 114–116, 153, 169], the structured–tree models are further developed and preferred over the lumped–parameter models.

Windkessel model

Originally derived by the German physiologist Otto Frank in 1899 [53], the earliest resistance-capacitor (RC) or two–element Windkessel model, consisting of a resistance and a compliance element, was developed to describe the ventricular afterload in response to dynamic interaction of the heart with systemic and pulmonary arteries. Analogous to a windkessel in a fire engine (see Figure 1.5), the arterial compliance plays the role of the Windkessel[1] that helps in damping the oscillations in the blood pressure during systole and assists in maintaining the organ perfusion during diastole. However, more than often the Windkessel models are also described in analogy with electric circuits such as the one with a parallel combination of a capacitor and a resistance, i.e. the two–element Windkessel model, whereas the blood flow from the heart is considered analogous to current flowing in the circuit and the blood pressure as the time varying electric potential. The RC model interprets the entire arterial system lumped into two components: total compliance (C_T) of the larger (or proximal) arteries and the total peripheral resistance, R_T, equivalent to the combined resistance of all distal vessels in the microcirculation. The C_T is determined by the elasticity of the large arteries and obtained by calculating ratio of volume change, ΔV, to the corresponding pressure change, ΔP, i.e.

$$C_T = \frac{\Delta V}{\Delta P}.$$

The R_T is calculated as the ratio of pressure difference of mean aortic and venous pressures to the cardiac output, Q_{in}, i.e.

$$R_T = \frac{P_{\text{mean(aortic)}} - P_{\text{mean(venous)}}}{Q_{\text{in}}}.$$

To better account for the cumulative effect of vascular beds, a modified RCR or three–element Windkessel model has been implemented in many studies (e.g. Burattini *et al.* [25], Porenta *et al.* [133] and Stergiopulos *et al.* [154]) to prescribe a terminal or input impedance at the distal ends of the large terminal arteries. The RCR model consists of an additional resistance in series with a parallel combination of resistance and capacitor, and unlike the RC model, it may take into account both resistive and compliant effects of proximal vessels beyond the point of termination. The frequency–dependent input impedance $Z(0, \omega)$ of the RCR model is given by

$$Z(0, \omega) = \frac{R_T + \mathrm{i}\omega C_T R_p R_d}{1 + \mathrm{i}\omega C_T R_d},$$

---

[1] A German terminology that roughly translates to “air chamber” in English.

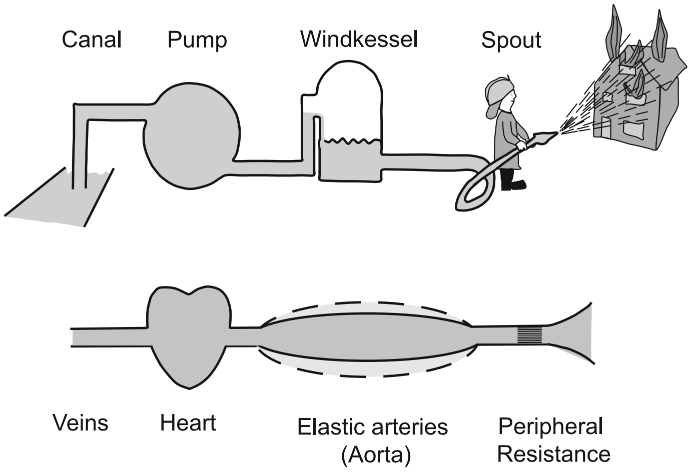

Figure 1.5: The concept of Windkessel. The large (or proximal, in case of vascular bed) arteries act as the Windkessel. The combination of compliance, together with characteristic impedance and peripheral resistance, results in a rather smooth peripheral flow. Figure 2 from Westerhof *et al.* [180].

which results in the pressure–flow relation in the time–domain [113, 154], and the outflow boundary condition takes the form

$$\frac{\partial p}{\partial t} = R_p \frac{\partial q}{\partial t} - \frac{p}{R_d C_T} + \frac{q R_T}{R_d C_T}.$$

Here R_p represents the resistance to the flow due to proximal arteries that have a total compliance C_T whereas R_d is the combined resistance of distal microvasculature. Moreover, $R_T = R_p + R_d$ is defined as the total resistance in a vascular bed. Thus for each terminal impedance three parameters C_T, R_T and R_1/R_T must be specified to implement this model as a boundary condition. A more recent development in the class of Windkessle models is the addition of a lumped inertance parameter that also takes into account the combined inertial effects of the vessels beyond the terminal artery in a four–elements RCLR model [180].

The ability of Windkessel models to adequately describe the pressure–flow relation at the entrance of the arterial system that they model, is proven [180] and the use of these models as an outflow boundary condition in a distributed models of large arteries provides fairly accurate approximation of downstream haemodynamics. Moreover, compared to fully distributed arterial models, the Windkessel representation of entire or part of the arterial system is easier to use, especially when one is only looking for ventricular–arterial or artery–arteriole coupling and is not interested in the fluid dynamical aspects of blood flow beyond explicitly simulated large arteries. Otherwise, due to spatially invariant, lumped description of physiologically meaningful parameters, the haemodynamic within these models have little physiological meanings and, for instance, the measurement of pressure distal to proximal resistance does not represent the pressure in distal vascular system. Thus the model cannot include the effects of wave propagation, blood flow distribution and local vascular changes in parts of the system it models [180], and therefore they do not make a good choice if one is interested in studying the spatially changing fluid dynamics within the vascular beds. Moreover, for a single physiological case study the parameters estimation for Windkessel requires *in vivo* pressure and flow data, which is often obtained using invasive techniques. This approach is not feasible especially when parameter estimation is required to study multiple physiological and pathological conditions. This aspect limits the use of Windkessel models to simulate only physiological waveforms, and its application for pathological conditions remains technically difficult and time consuming.

Structured–tree model

Faced with the issue of a suitable downstream boundary condition, Olufsen [113–116] developed a distributed downstream model to analytically determine the dynamic, frequency dependent, impedance of the arterial vasculature, which is viewed as an asymmetrically structured tree outside the computational domain. The method involves the use of the analytical solution of Womersley's problem in the frequency domain by defining the input impedance, $Z(0, \omega) = P(0, \omega)/Q(0, \omega)$ of a single vessel segment, based on the geometric and material properties of the vessel and the terminal (or output) impedance, $Z(L, \omega)$, and then recursively computing the input impedance of the entire vascular tree by assembling the tree using the pressure continuity and flow conservation at the bifurcations and starting from the terminal branches. The advantage of this type of boundary condition is that it allows the effects of wave propagation on the non–linear flow and pressure in the main arteries to be incorporated, compared with the lumped vascular models where the effects of entire downstream haemodynamics is predicted by a lumped–parameter model which can not include the effects of wave propagation within the model. Another advantage of this model is to be able to change the local parameter values, such as the local compliance, and the the density of the vascular beds, which enables us to study the pathological conditions. Moreover, this approach is computationally efficient too, as the input impedances only require to be computed and stored once.

Olufsen used this boundary condition to study the blood flow in the systemic [113,116] and pulmonary arteries [115] and other authors including Steele *et al.* [153] and Clipp & Steele [35, 36] also implemented this boundary condition with modified structure trees to study the blood flow in the systemic and pulmonary arteries, respectively. The most recent development in this regards came form Cousins [40] and Cousins & Gremaud [38] who adopted a different approach to obtain and solve the linearized governing flow equations for each vessel segment in the structured tree. In their work they derived the flow equations by linearizing the non–linear system of equations about a reference state and then analytically solved the wave equations by applying the Laplace transform methods in order to compute the total input impedance. However, the final simulations were found to be similar to those of Olufsen [116].

In reference to pulmonary circulation, one of the major development in this regard came from G. D. A. Vaughn [169] who extended the one–sided model of arterial structured tree to a two–sided model of connected arterial and venous structured trees with an aim of incorporating the effects of downstream vascular resistance offered by combined arterial and venous vascular beds on the blood flow in the pulmonary arteries and veins. This was an important development as the physiology of the pulmonary circulation is different to the systemic side and unlike the systemic veins the pulmonary veins are believed to regulate the upstream haemodynamics by contributing to the total peripheral vascular resistance [56, 190]. This boundary condition is also used to match the arterial pressure and outflow with the venous pressure and inflow to model the pulmonary circulation in this thesis. The details of this matching condition are provided in Chapter 2.

1.3 Related work

To the best of author's knowledge, to date only a few detailed analyses of the pulmonary haemodynamics, concerning the pulse wave propagation, can be found in the literature [35, 92, 115, 169]. All these models take a non–linear approach and incorporate the anatomical data such as the dimensions of the largest pulmonary arteries and the *in vivo* measured flow data imposed as inflow boundary condition to solve the system numerically. However, these models differ in the way they treat the downstream boundary condition, inclusion of pulmonary veins and the species under consideration.

The pulmonary circulation system consists of three longitudinal vascular segments that are arranged in a series as the arteries, the resistance vessels and the veins but many models either do not include the role of veins in flow regulation (one–sided models) [35, 115], or ignore the physical domain of vascular resistance, offered by resistance vessels in the form of vascular beds, by considering lumped–resistance models [92]. The study by Olufsen *et al.* [115] is an implementation of her structured–tree based model of systemic arteries [116] to simulate the blood flow and pressure in the human pulmonary arteries where the pulmonary specific *in vivo* anatomical data is incorporated to simulate the new geometry, and a new inflow profile is imposed at the system inlet. Moreover, in this work a new algorithm is also developed to compute the pulse pressure and the mean pressure drop across the systemic and pulmonary vascular beds. The study by Clipp & Steele [35] focuses on studying the effects of respiration and the zone dependent dynamic impedance of downstream pulmonary vasculature on the pressure and flow in sheep. The highlight of this work is the evaluation of zone specific parameters to define the size and geometry of the structured tress at different vertical levels in the lungs. Optimization algorithms and *in vivo* pressure and flow data were used to obtain these parameter values. The non–linear fluid model by Li & Cheng [92] does include the venous side of circulation but it uses a lumped parameter model to connect the arterial and venous haemodynamics. Moreover, no detailed simulations are given in this paper, nor can any follow up work can be found in the literature.

Out of the above mentioned computational models, only one model developed by G. D. Vaughan [169] includes both sides of the pulmonary circulations and the vessels of diameter $\geq 100\mu$m through connected structured trees. The connected trees represent the diverging arterial vascular beds at the microcirculation level, which is connected with a convergent venous vascular beds, after reaching a predetermined minimum radius. This model, however, includes a common venous return to the left atrium and the geometry of the pulmonary veins is considered as the mirror image of pulmonary arteries. Although Vaughan adopted this approach because of the unavailability of the subject–specific venous data for his study and that very little data about the dimensions and material properties of the pulmonary veins can be found in the literature, the resultant venous geometry was inappropriate to represent a truly physiological system. Among all the cases observed for the venous anatomy (see Figure 1.4), in no case is a single large vein is found to transport all the blood from two lungs back into the heart. Furthermore, all the above models have found to struggle with a suitable choice of compliance or stiffness parameters for the pulmonary vessels which often lead to either too low [115] or too high [169] blood pressures in the simulations. In the above studies various approaches have been adopted to pick the compliance parameter in order to simulate the pulse waveforms with observed physiological features. These approaches and the influence of compliance parameter have been discussed in detail in Chapter 3.

Other approaches concerning the computational modelling of the pulmonary circulation include image–based anatomical models of pulmonary blood flow, focusing more on blood flow heterogeneity in the lungs rather than the pulse wave propagation, by taking into account the anatomically based, zone dependent geometry of large and small blood vessels and pulmonary airways. One such example is the extensive work by K.S. Burrowes and collaborators [26–28, 162], who systemically developed a subject–specific, full–scale geometric model of human lung, based on detailed anatomical data, obtained through X-ray computed tomography imaging, for up to 25,00 vessels including large and small arteries and veins. The accompanying airways geometry and description of pulmonary capillaries are generated using empirically based algorithm [27]. The focus of analysis in most of these studies is to analyse the effects of branching structure, respiration, gravity and posture on blood flow distribution at various levels within the lung. Thus a detailed analysis of pulmonary flow, in steady state condition based on Poiseuille flow solutions in rigid tubes, is carried out within the capillary network, whilst a reduced model based on non–linear Navier–Stokes equations in compliant arteries has also been developed by Burrowes *et al* [28] to analyse the effects of important parameters on pulsatile flow and pressure within the pulmonary arteries. Although the geometric development of arterial, venous and capillary flow models in these studies is very detailed and include all the key elements of a real functioning lung, these flow models are independent of each other and haemodynamical changes in arteries, for example, does not incorporate the effects of changes in the capillary haemodynamics. The coupling technique used in this thesis may potentially be developed further to couple the anatomical flow models together to complete the flow circuit within a lung. For a more detailed overview of pulmonary blood flow models see [161].

Another aspect of the study of pulse wave propagation is the separation of measured or simulated pulse wave into incident and reflected components by using a suitable technique. Since the pulse wave observed at a given location is the composition of forward running incident and backward running reflected waves, the separation of pulse wave provides us a useful insight of underlying mechanisms involved in shaping the pulse wave and helps to interpret the result in a more rigorous manner. One such technique, routinely used for pulse wave separation, is the Wave Intensity Analysis (WIA) [117, 118]. To the best of author's knowledge only a few studies analyse this aspect of pulse wave analysis in the pulmonary circulation [47,48,69–71,150,151]. Among these studies, E. H. Hollander [69,71] carried out the first ever WIA of pulmonary arterial blood flow using the *in vivo* pressure and blood flow velocity measurements in anaesthetised open–chest dogs. Among major findings of her study is the appearance of reflected wave from the junction of the MPA and which decreases the amplitude of incident pressure wave. Among other most recent studies are by Smolich *et al.* [150, 152], Dwyer [48] and Dwyer *et al.* [47], which are also carried out by using the method of WIA and invasively measured simultaneous pressure and velocity data in the pulmonary arteries of anesthetized late–gestation fetal sheep and healthy anesthetized sheep, respectively. Dwyer *et al.* [47] also recognised the main pulmonary bifurcation as a reflector that generates pressure wave reflections which serve to reduce the amplitude of incident pressure wave, agreeing with Hollander [69]. In addition to sheep, Dwyer also reported in his thesis [48] the first ever study of arterial wave reflections by using the WIA in healthy and diseased human pulmonary vasculature. All of these investigations have been carried out by using invasively obtained *in vivo* pressure and velocity data and, to the best of author's knowledge, no such study can be found that uses the simulated pulmonary pressure and flow (or velocity) waveforms.

It is worth mentioning that the motivation and objectives of mathematical and computational modelling of the cardiovascular systems are far more diverse than studying the aspects of pulse wave propagation. In a review paper in the memory of Sir James Lighthill, T. J. Pedley [127] mentions other aspects of modelling the arterial fluid dynamics and discusses some of the developments in the study of fluid flow in complex arterial geometries. Some examples include, modelling and simulation of steady and unsteady flow in collapsable, one [128] and two–dimensional [96–98] tubes or channels and analysis and simulations of flow in tubes with, non–uniform [99] and uniform time–dependent curvature [176]. The objective of such analysis is to investigate a single physical phenomenon, such as the wall shear stress and self–excited oscillations, and study its influence on the biological properties of an isolated component of cardiovascular system, blood vessels for instance. These studies have diverse applications in variety of physiological phenomenon, e.g blood flow in coronary arteries and gas exchange in the pulmonary air ways, therefore results from theses studies can be readily reproduced for studies concerning multi–scale modelling of a particular system with an aim of analysing global aspects of related physiological phenomenon. Another aspect of cardiovascular fluid dynamics is the analysis of fluid–solid interaction by means of immersed boundary methods. Such analysis has shown to be very useful in simulating the detailed three dimensional fluid dynamics of heart valves [60]. Finally, a rather different, and computationally intensive, aspect of cardiovascular modelling is the patient–specific, image–based three–dimensional modelling of cardiovascular system, an approach classified as fully computational and non–mathematical by Pedley [127]. A most recent development in this regard is the detailed simulation of a multi–scale, three–dimensional, full–body model of human arterial network [184]. Although computationally expensive, such models are very useful in understanding the, complex multidimensional local and global haemodynamical changes due to stenosis, for example.

1.4 Motivation and objectives of this thesis

The basic motivation behind this work is to improve our understanding of pulmonary pulse wave behaviour under physiological and pathological conditions by analysing the relation between structural and functional changes in the human pulmonary vasculature. This can be achieved by simulating physiologically relevant pulse waveforms in the largest pulmonary arteries and veins through a detailed one–dimensional model of human pulmonary circulation that incorporates necessary and sufficient features of the real system. The starting point is to refine an existing, partially subject–specific, one–dimensional model of human pulmonary circulation [169]. This model includes an unrealistic venous arrangement (large veins) and uses a stiffness parameter that does not exhibit the physiological behaviour of pulmonary compliance. Consequently the pressure profiles simulated through this model exhibit higher than normal pulmonary blood pressures. To achieve our objectives we set some specific goals and follow the following line of action

- Numerically solve the revised model by assigning a new set of values to physiologically important parameters and simulate the pressure and flow profiles at different locations along the large pulmonary arteries and veins over a complete cardiac cycle for a normal physiological case.

- Apply this newly revised model to test various hypothesis of disease condition classified under the definition of pulmonary hypertension.
- Extend our analysis by developing a new algorithm to predict the mean pressure drop within the arterial and venous vascular beds.
- Improve the interpretation of our results assisted by a technique that decompose a local pulse wave into its incident and reflected wave components.
- Where possible, validate our results by comparing our observations with physiologically observed features of pulmonary pulse wave.
- Look for possibilities to exploit our model and simulations to test and improve tools for clinical purposes.

1.5 Thesis layout

This thesis is arranged into eight chapters and two appendices. This chapter (Chapter 1) gives physiological and anatomical description of cardiovascular circulatory system in general and pulmonary circulation in particular along with a brief introduction to the subject of mathematical modelling of the circulation with reference to the existing relevant work. The organization of the remaining chapters is given below.

Chapter 2 includes the description of the revised model of the pulmonary circulation and the details of preliminaries, which include: the equations governing the one–dimensional non–linear fluid dynamics in the large arteries and veins; linearised flow equations governing fluid dynamics in arterioles and venules; description of all the boundary conditions which includes inflow, outflow and bifurcation conditions whereas a detailed mathematical derivation of arterial venous matching condition is also provided. Finally a brief description of the Lax–Wendroff finite difference scheme is given at the end of the chapter. Besides the revised model description, the algorithm to execute the matching condition in Section 2.4.1 is explicitly stated for the first time while in Section 2.5.2 the inclusion of an inflow pressure condition through the numerical scheme is also the new work of author.

Chapter 3 focuses on to obtain a set of parameter values to represent the normal physiological case for this study. Most of the discussion and analysis in this chapter revolves around finding a suitable value of the compliance parameter.

Chapter 4 includes detailed simulations of the normal physiological case and apply the model to analyse the hypothesis of pulmonary hypertension for two cases (i) normal heart function (ii) with right ventricular dysfunction.

Chapter 5 extends our analysis to derive a new algorithm to predict the mean pressure drop across pulmonary vascular beds in physiology and pathology.

Chapter 6 includes some new preliminaries to describe the theory of Wave Intensity Analysis (WIA) and then apply this theory on our simulations to analyse the patterns of wave reflections in the human pulmonary arteries during health and disease.

Chapter 7 studies the effects of linear wave separation using the estimates of local pulse wave velocity and highlights the prospect of this model for clinical applications.

Chapter 8 summarises the thesis achievements and highlights the limitations of this work by suggesting some directions for future work.

Apendix A gives description of how three–dimensional system may be reduced to an axial, one–dimensional system.

Apendix B provides detailed of how bifurcation and matching conditions are incorporated through Lax–Wendroff numerical scheme.

Chapter 2

Formulations and Methods

This chapter first details the geometric description and mathematical formulation of our one–dimensional model of pulmonary circaulation followed by methods used to solve the resulting hyperbolic system of PDEs. The contents of the chapter thus include a detailed description of the geometry, equations governing the fluid structure interaction and the numerical methods used to solve the resulting problem subject to specified boundary conditions.

2.1 Model description

The pulmonary vessels are organized in a complex tree like structure in which an individual vessel can be viewed as a compliant tube that bifurcates further into pairs of daughter vessels. Most previous models of pulmonary circulation only simulate pulmonary arterial haemodynamics and completely ignore the role of pulmonary veins. Since the pulmonary veins contribute towards overall vascular resistance that regulate flow in the pulmonary arteries, studying arterial system alone is not adequate.

A complete model of the pulmonary circulation can be constructed by breaking the whole system into four regimes: large arteries, small/resistance arteries (arterioles) and veins (venules) and the large veins. The pulmonary circulation illustrated in Figure 2.1 consists of large arteries and veins organized in a tree like structure. The main pulmonary artery (MPA) emanates from the right atrium and bifurcates into two vessels, the right (RPA) and left (LPA) pulmonary arteries transporting blood to the right and left lungs. As the heart is located on the left side of the body, the RPA is significantly longer than the LPA. These two main vessels further bifurcate into the right and left interlobular arteries

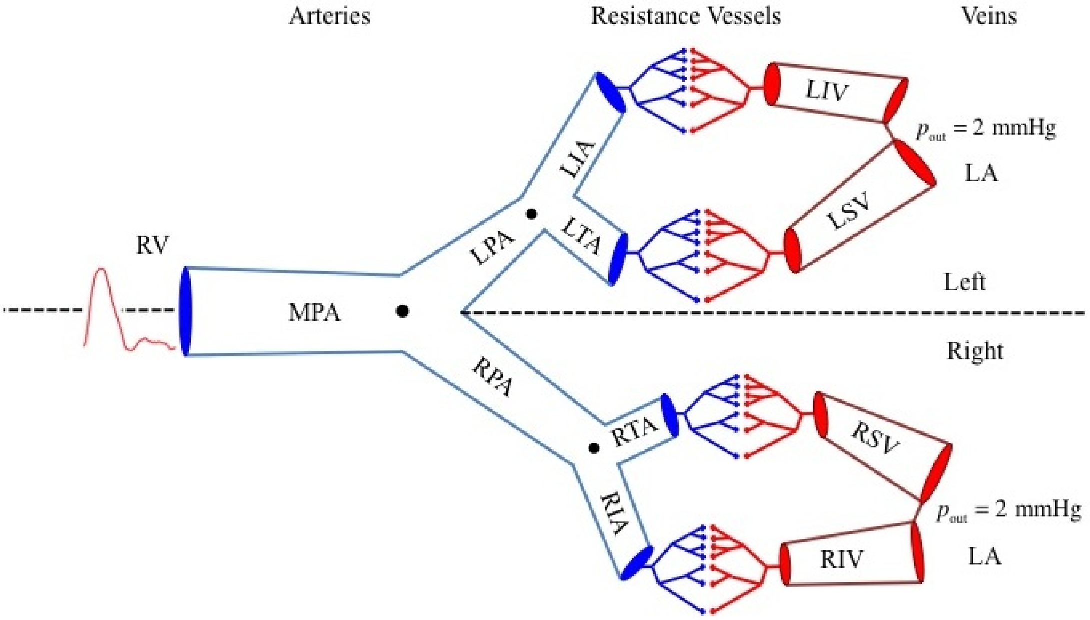

Figure 2.1: Schematic of pulmonary circulation model arranged in a sequence of larger arteries, arterioles, venules and large veins. The large pulmonary arteries and veins are specified explicitly, while the small vessels are represented by structured trees. The main pulmonary artery (MPA) is the root vessel within the pulmonary arterial tree. A flow waveform measured using MRI is specified at the inlet to this vessel. The MPA bifurcates into the right (RPA) and left (LPA) pulmonary arteries. The RPA bifurcates into the right interlobular artery (RIA) and the right trunk artery (RTA), and the LPA bifurcates into the left interlobular artery (LIA) and left trunk artery (LTA). The RIA, RTA, LIA and LTA are the **terminal** vessels of the large pulmonary arterial model, and it is to the outlet of these vessels that the structured-tree matching conditions are applied to join the arterial and venous systems. The outlet of the RIA is matched with the inlet of right inferior pulmonary vein (RIV), the RTA with the right superior vein (LSV), the LIA with the left inferior vein (LIV), and the LTA with the inlet of left superior vein (LSV). The pulmonary veins open into left atrium in pairs draining blood from left and right lungs and therefore at the outlet of each vein a constant pressure condition is applied. Continuous-pressure and flow conservation conditions are used at each bifurcating junction, marked by a '**.**' for large arteries.

(RIA and LIA) and the right and left trunk arteries (RTA and LTA). The tree of large arteries is truncated at this point (after three generations from the heart) making R/LIA and R/LTA the terminal vessels. Attached at the terminals of these arteries are structured branching trees of resistance vessels in which arteries continue to bifurcate such that the daughter vessels are scaled relative to parent vessels. After a predetermined minimum radius (r_{min}) the structured tree of smaller arteries is also truncated and joined with a topologically equivalent confluent tree of small venous vessels.

The venous vessels closely follow the branching patterns of the arteries, with the exception of four large veins, the right and left inferior (RIV and LIV) and the right and left superior (RSV and LSV) pulmonary veins, which deliver blood to the left atrium. In the large arteries and veins non-linear inertial effects cannot be neglected, whereas for the smaller vessels viscous effects play an important role [32]. Therefore the large vessels, i.e., the MPA, R/LPA, R/LIA, R/LTA, R/LIV and R/LSV, are modelled explicitly, and the small vessels, including the small arteries (veins) and arterioles (venules), are represented by structured trees. This separation is similar to other studies [115,116,153], however none of these studies considered the effects of the venous circulation. One study by Li *et al.* [92] does include both arteries and veins, but this study uses a lumped parameter model to represent the small vessels, so it is not possible to predict the effects of wave propagation and pressure drop over the complete system. Moreover, the smallest capillaries offer little flow resistance [55] and are not included.

2.1.1 Large arteries and veins

We classify large pulmonary arteries and veins together as the large vessels, which are the main region of interest for which non-linear effects on time dependent pressure and flow waves are studied. The large vessels have function of transporting blood to and from the arterioles/venules and capillaries and they constitute a small portion of the complete circulatory system. Since the pulmonary system is too extensive and complicated, computationally it is not feasible to explicitly predict the non–linear haemodynamical changes in all parts of the system.

Despite the fact that there is very little data available for geometric and material properties of human pulmonary veins and that the role of veins and their contribution towards total pulmonary vascular resistance varies significantly with species, age, conditions of the flow and vascular distention, there are sufficient evidences, which suggest that for modelling purposes pulmonary arteries and veins can be described in a similar way. Firstly the arteries and veins more or less follow the same pathway to transport blood suggesting that they have similar geometric properties. Secondly, besides the function of large vessels (transporting blood to/from small vessels), some experimental studies in animals suggest that material properties of the pulmonary arteries and venous network are similar. For instance, in a neonatal lamb lungs, it is found that when the lung was perfused in reverse, from the left atrium to the pulmonary artery to distend the veins with high transmural pressure, the fractional resistance in the veins was same as that in arteries during the forward flow [56]. Moreover, another study by Zhuang *et al.* [190] of the feline lung suggests that the pulmonary arterial and venous compliance is same for the blood vessels smaller than 2 mm in diameter. It can be inferred from these studies that the blood vessels in pulmonary arterial and venous trees share identical geometric and material properties and hence can be viewed generally as large blood vessels for modelling purpose.

Before describing how the haemodynamics is computed in the large vessels, we first describe the geometry used for generating the domain for the computational model.

Vessel geometry

As described in [115], the geometry of the large pulmonary arteries was specified from measurements from a healthy young volunteer. These data were collected using magnetic resonance imaging (MRI) at the Scottish Pulmonary Vascular Unit. Figure 2.1 shows a schematic of the measured arteries, specifically the first three generations of the pulmonary arterial tree, while vessel lengths and diameters are summarised in Table 2.1.

A comparison of proximal and distal diameters of arteries from Table 2.1 suggests that the pulmonary arteries taper along the length. Thus we model large arteries as a bifurcating tree in which individual vessels are considered to taper exponentially along the length. Thus the radius $r(x)$ at any position along the vessel is given by

$$r(x) = r_{\text{prox}}\exp(-kx),$$

where the tapering factor $k = \log(r_{\text{dist}}/r_{\text{prox}})/L$ is given by Olufsen *et al.* [116]. With this value of k the radius takes the following form

$$r(x) = r_{\text{prox}}\exp\left(\log\left(\frac{r_{\text{dist}}}{r_{\text{prox}}}\right)\frac{x}{L}\right) = r_{\text{prox}}\left(\frac{r_{\text{dist}}}{r_{\text{prox}}}\right)^{x/L}, \tag{2.1}$$

where r_{prox} and r_{dist} are the proximal and distal radii of an artery. Also at each bifurcation the distal cross–sectional area of the parent vessel is greater than the individual proximal

No.	Name	Prox. diam. (cm)	Dist. diam. (cm)	Length (cm)
1	MPA	2.72	2.60	4.50
2	RPA	1.86	1.20	5.75
3	LPA	2.20	2.16	2.50
4	RIA	1.14	1.10	1.25
5	RTA	0.92	0.92	1.00
6	LIA	2.08	1.80	2.25
7	LTA	1.16	1.16	1.00
8	RIV	1.18	1.10	1.25
9	RSV	1.02	0.92	1.50
10	LIV	1.94	1.80	2.25
11	LSV	1.28	1.16	2.00

Table 2.1: Dimensions of the large pulmonary vessels including the main pulmonary artery (MPA), the right (RPA) and left (LPA) pulmonary arteries, the right (RIA) and left (LIA) interlobular arteries, the right (RTA) and left (LTA) trunk arteries, the right (RSV) and left (LSV) superior veins, and the right (RIV) and left (LIV) inferior veins. For each vessel, the proximal and distal diameters are given together with the vessel lengths. For both arteries and veins, proximal and distal refer to vessel entry close to and away from heart. The measurement resolution for all diameters is up to 1d.p. (mm), and all vessel lengths are rounded to the nearest 2.5 mm to match the spatial resolution used in numerical computations. The RTA and LTA were too short to obtain both inlet and outlet diameters, thus these vessels were assumed not to taper and their lengths were estimated.

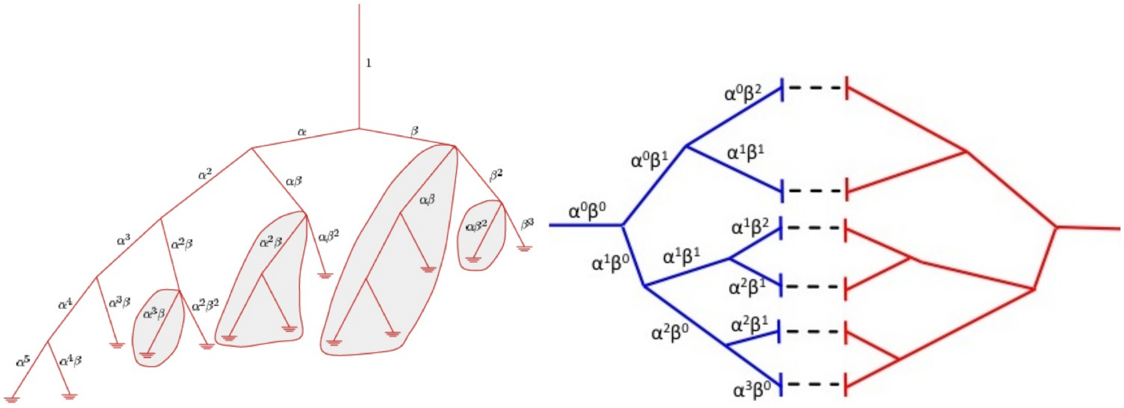

Figure 2.2: Left: Structured tree of small arterial vessels by Olufson *et al.* [114], used to provide outflow conditions to large arteries. Right: A schematic of structured trees of small arteries (blue) and veins (red), joined together to provide a matching condition to large arterial and venous trees.

cross–sectional areas of any of the daughter vessels, however, the sum of the proximal cross–sectional areas of the daughter vessels is greater than that of the distal cross–sectional area of parent vessel meaning that the total cross–sectional area increases at each junction.

Unfortunately, the MRI studies did not provide measurements for the large pulmonary veins (numbered 8–11 in Table 2.1) therefore we have obtained their dimensions from literature [83, 87]. This is done by combining the observations from these studies with the requirement that the distal diameter of each terminal large artery (i.e. each of the RIA, RTA, LIA and LTA) must be the same as the distal diameter of its matching terminal vein (the RSV, RIV, LSV and LIV, respectively) (Figure 2.1).

2.1.2 Small arteries and veins

The purpose of including arterioles and venules (small/resistance vessels) in this model is to built a resistance model that includes the effects of periphery flow dynamics outside the computational domain, by relating the arterial flow and pressure with the venous flow and pressure, through a suitable matching condition. This approach was first introduced by G. D. Vaughan [169] by prescribing separate structured tree models for the arterial and venous trees, extending Olufsen *et al.*'s (2000) [116] model for the systemic circulation, and then join these two trees. This approach completes the pulmonary system by providing a physiology based matching condition, which translates the wave propagation effects and the role of arterioles and venules on blood flow regulation. Since the small pulmonary veins are known to follow closely the course of the pulmonary arteries, the pulmonary venous

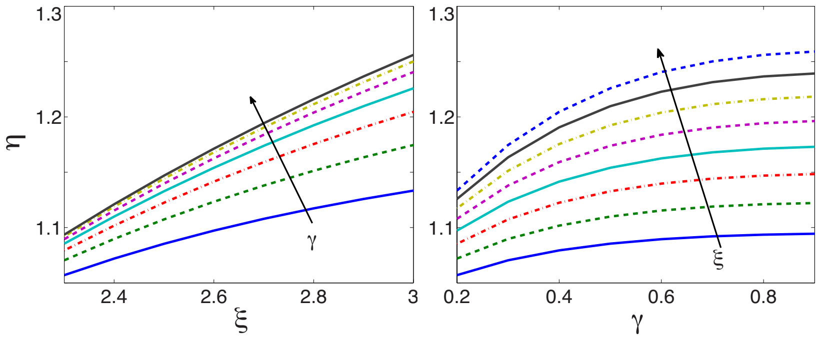

Figure 2.3: Effects of radius exponent ($\xi \in [2.3, 3]$) and asymmetry ratio ($\gamma \in [0.2, 1]$) on cross–sectional area ratio (η). η decreases by the decreasing the values of either of ξ or γ.

tree is described as a 'mirror image' of the pulmonary arterial tree depicted in Figure 2.2. The two trees are represented by the same topology, assuming a one-to-one correspondence between each vessel, but vessels are allowed to have different length-to-radius ratios and material properties (e.g. compliances), from vessels in the mirror tree. To ensure the same number of branches in arterial and venous trees, the radius of the root (i.e. largest) vessel must be the same for both arterial and venous trees. Both the arterial and venous structured trees are set up, as described by Olufsen *et al.* [114–116], assuming that at each junction the daughter vessel radius can be predicted from the parent vessels as $r_{d_1} = \alpha\, r_p$ and $r_{d_2} = \beta\, r_p$, i.e., for any vessel the radius $r = \alpha^i \beta^j r_0$, where r_0 is the radius of the root vessel. Scaling factors α and β were determined from studies suggesting that branching of smaller arteries are governed by three relations: a radius power-law, an asymmetry ratio γ and an area ratio η, given by

$$\begin{aligned} r_p^\xi &= r_{d_1}^\xi + r_{d_2}^\xi, \qquad 2.33 \le \xi \le 3, && (2.2)\\ \gamma &= r_{d_2}^2 / r_{d_1}^2, && (2.3)\\ \eta &= \frac{r_{d_1}^2 + r_{d_2}^2}{r_p^2} = \frac{1+\gamma}{(1+\gamma^{\xi/2})^{2/\xi}}, \qquad \eta > 1, && (2.4) \end{aligned}$$

where the subscript p refers to the parent vessel and subscripts $d_i, i = 1, 2$ refer to the daughter vessels. Only any two of these relations are mathematically independent. Also, in figure 2.3, it can be observed that increasing either ξ or γ leads to an increase in the area ratio η. This implies an increase in the total cross–sectional area of daughter vessels at each bifurcation, leading to more number of generations between r_0 and $r_{\min}$ and hence a denser structured tree. The value of exponent ξ in the radius relation was obtained from considerations associated with minimising work in the arterial system. A value of $\xi = 3$

is optimal for laminar flow, $\xi = 2.33$ for turbulent flow and $\xi = 2.76$ is a good choice for arterial blood flow [132, 159, 166]. Also based on earlier studies [115, 116], we choose $\eta = 1.16$, which together with $\xi = 2.76$ yield an asymmetry ratio $\gamma = 0.41$. Finally, the scaling factors α and β for these values are given by

$$\alpha = (1 + \gamma^{\xi/2})^{-1/\xi} = 0.91,$$
$$\beta = \alpha\sqrt{\gamma} = 0.58,$$

which satisfy observations that the areas $A_{d_1}, A_{d_2} < A_p$ while $A_{d_1} + A_{d_2} > A_p$.

In addition to the radius relations, the length of each vessel must be specified. For the pulmonary vessels, a length-to-radius relation was obtained by analysing data summarised by Fung [55] (based on experiments by Singhal et. al. [148]) combined with observations from studies by Huang *et al.* [75] that suggest a length-to-radius relation given by

$$l = \begin{cases} 15.75r^{1.10} & \text{for arterial radius} \geq 0.005\,\text{cm}, \\ 1.79r^{0.47} & \text{for arterial radius } \leq 0.005\,\text{cm}, \\ 14.54r & \text{for venous radius} \leq 0.2\,\text{cm}, \end{cases} \tag{2.5}$$

where the l and r (both specified in cm) denote the length and radius of the vessel, whilst throughout this thesis we will refer to coefficients of r, in each equation in (2.5), as length to radius ratio, denoted by l_{rr_i} $(i = A, V)$. Also, note that the different scaling for the arteries and veins provides asymmetry between the two structured trees.The details of how these scaling ratios are obtained may be found in [169].

A recent study by Cousins & Gremaud [38] showed that the impact on resistance from the structured trees critically depends on the value of $r_{\min}$, the minimum vessel radius at which trees are terminated. By using a one–sided structured tree with a finite number of generations, they showed that the total resistance of the structured tree converges as $r_{\min} \to 0$ if and only if $\xi > 3$ in equation (2.2). As described above that the theoretical and physiological value of $\xi \in [2.33, 3]$, and based on existing studies, we also chose $\xi = 2.76$. Therefore, for the pulmonary arterial and venous structured trees we chose $r_{\min} = 0.005\,\text{cm}$. This cutoff choice also allows us to use a single equation ($(2.5)_1$ and $(2.5)_3$) within each arterial and venous tree.

2.2 Fluid dynamics of large blood vessels

In order to derive the one–dimensional equations governing the blood pressure and flow in large blood vessels, one must use approximations that reduce a three–dimensional phenomenon to a one dimensional problem. Different approaches can be found in literature resulting in different one–dimensional systems of equations. Commonly used approaches include deriving the equations of flow directly from the theory of fluid flow for viscous, incompressible fluid in a longitudinally–tethered compliant tube without assuming any axisymmetry or shape of the cross–sectional area allowing for the no–slip conditions at the wall for an axially dominated velocity field to obtain a very general form (e.g. [77,78]). Alternatively, one may adopt the quasi–linear approach suggested by Barnard *et al.* [15], by first eliminating the radial and angular momentum equations by imposing assumptions on the velocity field ($u_r \ll u_x$) and then averaging the continuity and momentum equations by integrating them over vessel cross–sectional area.

In this thesis we follow the approach, originally based on the work from Barnard *et al.* [15] and Peskin [130] and put forward by Olufsen *et al.* [116], in which the volumetric flow–rate, blood pressure and cross–sectional area is predicted in time along one spatial dimension using two equations ensuring the conservation of volume and momentum. Among more recent studies, similar approach is also followed by R. B. Clipp [34] and W. B. Cousins [40] to study blood flow in pulmonary and systemic systems. The derivations below are from Olufsen *et al.* [116], which are also used in her more recent work on pulmonary circulation [115].

Shown in Figure 2.4 is the schematic of a large blood vessel, assumed as a compliant tube in cylindrical polar coordinate system (r, x, θ) with radius r and length L. Thus each point inside the vessel can be described by (r, x, θ) with $0 \leq r < R(x, \theta, t)$, $0 < x < L$ and $0 \leq \theta \leq 2\pi$. Here $R(x, \theta, t)$ [cm] denotes the variable radius of the tapering vessel at a fixed position along the length, L [cm] of the vessel for all t [s], implying a variable cross–sectional area $A(x, \theta, t) = \pi R^2(x, \theta, t)\,[\mathrm{cm}^2]$. Let $\mathbf{u} = [u_r(r, x, \theta, t), u_x(r, x, \theta, t), u_\theta(r, x, \theta, t)]\,[\mathrm{cm\,s^{-1}}]$ be the velocity field of the fluid within the vessel, where subscripts r, x and θ respectively represent the radial, axial and angular components of the velocity field in chosen coordinate system. Let $p(r, x, \theta, t)$ be the blood pressure [mmHg] inside the vessel and p_0 is the constant diastolic or external pressure. Moreover, at $t = 0$ we get $p(r, x, \theta, t) = p_0$ and $R(x, \theta, t) = r_0(x)$ which refers to equilibrium or unstressed state of the vessel.

Further, we consider blood to be a viscous, homogeneous and incompressible fluid with

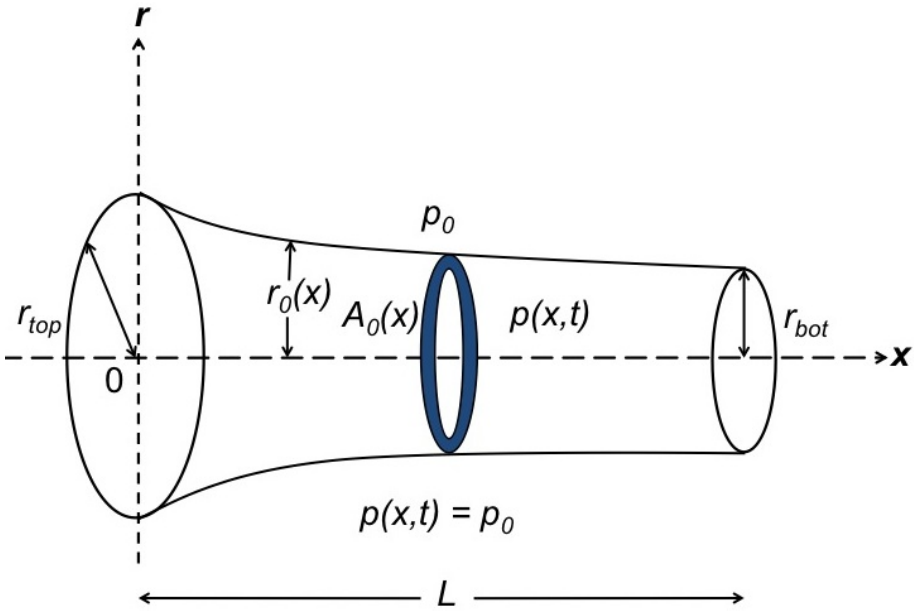

Figure 2.4: A schematic of an axisymmetric compliant vessel, with variable cross–sectional area and tapering walls, is shown in equilibrium (unstressed) state at $p = p_0$. A_0 and r_0 are the equilibrium cross–sectional area and radius whereas r_{prox} and r_{dist} denote the proximal and distal radii, respectively.

a constant viscosity $\mu = 0.49\,[\text{g}(\text{cm}\,\text{s})^{-1}]$ and density $\rho = 1.055\,[\text{g}\,\text{cm}^{-3}]$ and the flow inside the blood vessels as laminar. In order to formulate a one-dimensional model we further assume that there are no swirls in the fluid i.e. the motion in circumferential direction may be neglected implying $u_\theta(r, x, \theta, t) = 0$. Moreover, the flow in the vessel is axisymmetric i.e. the blood flow velocity and pressure are independent of the θ coordinate. Under these assumptions the conservation of mass (continuity equation) implies that the divergence of velocity field vanishes i.e.

$$\frac{\partial u_x}{\partial x} + \frac{1}{r}\frac{\partial (r u_r)}{\partial r} = 0, \tag{2.6}$$

and the radial and axial balance of momentum (Navier–Stokes equations) become

$$\rho\left(\frac{\partial u_r}{\partial t} + u_r\frac{\partial u_r}{\partial r} + u_x\frac{\partial u_r}{\partial x}\right) = -\frac{\partial p}{\partial r} + \mu\left(\frac{\partial^2 u_r}{\partial r^2} + \frac{1}{r}\frac{\partial u_r}{\partial r} - \frac{u_r}{r^2} + \frac{\partial^2 u_r}{\partial x^2}\right), \tag{2.7}$$

$$\rho\left(\frac{\partial u_x}{\partial t} + u_r\frac{\partial u_x}{\partial r} + u_x\frac{\partial u_x}{\partial x}\right) = -\frac{\partial p}{\partial x} + \mu\left(\frac{\partial^2 u_x}{\partial r^2} + \frac{1}{r}\frac{\partial u_x}{\partial r} + \frac{\partial^2 u_x}{\partial x^2}\right). \tag{2.8}$$

The left hand sides (LHS) in both equations define inertial forces through the sum of local (first terms on LHS) and advective (2nd and third terms in LHS) accelerations (or material time derivative of the velocity) in radial and axial directions. This is balanced with the sum of normal and shear stresses on the right hand side (RHS), dominated by negative pressure gradient and the viscous forces defined through shear stresses.

Due to the natural structure of the blood vessels, i.e. vessels are much longer in the axial direction than in the radial direction, we consider $R(x,t) \ll L$. Moreover, the vessel walls undergo small transverse motion and for laminar flow in a compliant vessel the maximum value of radial velocity $u_r(r,x,t)$ is the radial velocity of the vessel wall. This leads us to the assumption that $u_r(r,x,t) \ll u_x(r,x,t)$ in large blood vessels. As shown by Barnard *et al.* [15] the implication of this assumption reduces (2.7) to

$$\frac{\partial p}{\partial \tilde{r}} \approx 0, \tag{2.9}$$

which means that dependency of pressure on radial coordinate is negligible i.e. $p = p(x,t)$ only. Moreover, the last term $(\partial^2 u_x/\partial x^2)$ in (2.8) also gets eliminated in the same process, leaving us with

$$\frac{\partial u_x}{\partial t} + u_r \frac{\partial u_x}{\partial r} + u_x \frac{\partial u_x}{\partial x} = -\frac{1}{\rho}\frac{\partial p}{\partial x} + \nu \left(\frac{\partial^2 u_x}{\partial r^2} + \frac{1}{r}\frac{\partial u_x}{\partial r} \right), \tag{2.10}$$

where $\nu = \mu/\rho\,[\mathrm{cm}^2\mathrm{s}^{-1}]$ is kinematic viscosity. Detail of how (2.7) and (2.8) are reduced to (2.10) can be found in [15] and also provided in Appendix A for readers' convenience.

Further, the vessel wall is assumed to be impermeable so the fluid contained inside obeys no–slip condition at the wall i.e. the velocity of the fluid at the wall is same as the velocity of the wall. Since the vessels are also longitudinally tethered, the walls undergo transverse motion only, yielding the no–slip conditions

$$[u_x(r,x,t)]_{r=R(x,t)} = 0 \quad \text{and} \quad [u_r(r,x,t)]_{r=R(x,t)} = \frac{\partial R(x,t)}{\partial t}. \tag{2.11}$$

Carrying on to obtain a one–dimensional system, we first integrate (2.6) over cross–sectional area

$$\begin{aligned} 0 &= 2\pi \int_0^R \left(\frac{\partial u_x}{\partial x} + \frac{1}{r}\frac{\partial (r u_r)}{\partial r} \right) r dr, \\ &= 2\pi \int_0^R \frac{\partial u_x}{\partial x} r dr + 2\pi \int_0^R \frac{1}{r}\frac{\partial (r u_r)}{\partial r} r dr, \\ &= 2\pi \frac{\partial}{\partial x} \int_0^R u_x r dr - 2\pi \frac{\partial R}{\partial x}[r u_x]_R + 2\pi [r u_r]_R. \end{aligned} \tag{2.12}$$

Since $A = \pi R^2$, using the no–slip condition (2.11), the last term in (2.12) becomes

$$2\pi [r u_r]_R = 2\pi R \frac{\partial R}{\partial t} = \frac{\partial A}{\partial t}. \tag{2.13}$$

Defining volumetric flow $q(x,t)\,[\mathrm{cm}^3\mathrm{s}^{-1}]$ (volume/time) as

$$q(x,t) = 2\pi \int_0^R u_x\, r dr \tag{2.14}$$

and using (2.13) and (2.14) in (2.12), we get the one–dimensional equation of continuity

$$\frac{\partial q}{\partial x} + \frac{\partial A}{\partial t} = 0. \tag{2.15}$$

In order to obtain a one–dimensional equation ensuring balance of momentum, we now integrate (2.10) over the cross–sectional area

$$2\pi \int_0^R \left(\frac{\partial u_x}{\partial t} + u_r \frac{\partial u_x}{\partial r} + u_x \frac{\partial u_x}{\partial x} \right) r dr = -\frac{2\pi}{\rho} \int_0^R \frac{\partial p}{\partial x} r dr + 2\pi\nu \int_0^R \frac{1}{r}\frac{\partial}{\partial r}\left(r \frac{\partial u_x}{\partial r} \right) r dr. \tag{2.16}$$

Since $p \neq p(r)$, integration of RHS is straight forward, yielding

$$2\pi \int_0^R \frac{\partial u_x}{\partial t} r dr + 2\pi \int_0^R \left(u_r \frac{\partial u_x}{\partial r} + u_x \frac{\partial u_x}{\partial x} \right) r dr = -\frac{A}{\rho}\frac{\partial p}{\partial x} + 2\pi\nu \left[r \frac{\partial u_x}{\partial r} \right]_{r=R}. \tag{2.17}$$

Using the no–slip condition (2.11) and the volumetric flow defined in (2.14), the first term on the LHS of (2.17) becomes

$$2\pi \int_0^R \frac{\partial u_x}{\partial t} r dr = 2\pi \left(\frac{\partial}{\partial t} \int_0^R u_x r dr - \frac{\partial R}{\partial t} [r u_x]_R \right) = \frac{\partial q}{\partial t}. \tag{2.18}$$

Simplification of second term in (2.17) requires integration by parts and use of the no–slip condition (2.11) and the continuity equation (2.6), so

$$\begin{aligned} 2\pi \int_0^R \left(u_x \frac{\partial u_x}{\partial x} + u_r \frac{\partial u_x}{\partial r} \right) r dr =& 2\pi \int_0^R u_x \frac{\partial u_x}{\partial x} r dr + 2\pi \int_0^R u_r \frac{\partial u_x}{\partial r} r dr \\ =& 2\pi \int_0^R u_x \frac{\partial u_x}{\partial x} r dr + 2\pi \left([r u_r u_x]_R - \int_0^R u_x \frac{\partial}{\partial r}(r u_r) dr \right) \\ =& 2\pi \int_0^R u_x \frac{\partial u_x}{\partial x} r dr + 2\pi \int_0^R u_x \frac{\partial u_x}{\partial x} r dr \\ =& 2\pi \int_0^R \frac{\partial u_x^2}{\partial x} r dr. \end{aligned} \tag{2.19}$$

Substituting (2.18) and (2.19) into (2.17) gives

$$\frac{\partial q}{\partial t} + 2\pi \frac{\partial}{\partial x} \int_0^R u_x^2 r dr + \frac{A}{\rho}\frac{\partial p}{\partial x} = 2\pi\nu \left[r \frac{\partial u_x}{\partial r} \right]_R. \tag{2.20}$$

In order to evaluate the second term involving integral of u_x^2 on LHS and the frictional force term involving derivative of u_x in radial direction at the wall on the RHS of (2.20), we need to make assumptions about the velocity profile.

Studies show that the velocity profile changes from almost flat at the entry region of the aorta to a fully developed parabolic profile at the resistance arteries [111, 124, 125]. Keeping this in view, we choose an assumed Stokes–layer velocity profile, introduced by Olufson *et al.* [116] in her model of systemic circulation, given by

$$u_x(r,x,t) = \begin{cases} \bar{u}_x & \text{for} \quad r \leq R-\delta \\ \bar{u}_x(R-r)/\delta & \text{for} \quad R-\delta < r \leq R \end{cases}, \tag{2.21}$$

where $\bar{u}_x(x,t)$ is the constant axial velocity outside the Stokes–layer (or boundary layer), defined as a thin region of thickness δ such that $\delta \ll R$ along the walls, where the viscous effects are strong and transition to no–slip condition takes place. According to Lighthill [94] the thickness of Stokes–layer can be estimated from the viscous penetration depth based on the first harmonic i.e. $\delta = (\nu T/2\pi)^{1/2}$. For $\nu = 0.046$ cm^{2}s^{-1} and cardiac cycle $T = 0.7\,$s, we get $\delta = 0.07\,$cm.

It should, however, be noted that this is not the only profile that may be used to study blood flow in arteries. Many researchers (e.g. [6, 38, 103, 145]) have used a more general power–law to describe the shape of velocity profile in the vessels given by

$$u_x(r,x,t) = \frac{n+2}{n}\bar{u}_x\left[1-\left(\frac{r}{R(x,t)}\right)^n\right],$$

where the parameter n determines the shape of the profile, e.g. for $n = 2$ the velocity profile becomes fully parabolic (Poiseuille profile). A more detailed comparison of these and other velocity profiles can be found in [168].

Here we continue to the use velocity profile prescribed in (2.21). The integrals in (2.14) and (2.20) can be expanded as power series in δ as

$$q = 2\pi\int_0^R u_x r dr = A\bar{u}_x\left(1-\frac{\delta}{R}+\mathcal{O}(\delta^2)\right),$$

and

$$2\pi\int_0^R u_x^2 r dr = A\bar{u}_x^2\left(1-\frac{4}{3}\frac{\delta}{R}+\mathcal{O}(\delta^2)\right).$$

Combining these two terms yields

$$2\pi\int_0^R u_x^2 r dr = \frac{q^2}{A}\left(1+\frac{2}{3}\frac{\delta}{R}+\mathcal{O}(\delta^2)\right). \tag{2.22}$$

Using (2.21) in the frictional force term on RHS of (2.20) will provide

$$\left[r\frac{\partial u_x}{\partial r}\right]_R = -\frac{R\bar{u}_x}{\delta} = -\frac{R}{\delta}\frac{q}{A}(1+\mathcal{O}(\delta)). \tag{2.23}$$

Retaining the leading order term in (2.22) and (2.23) and inserting them in (2.20), we get the one–dimensional momentum equation

$$\frac{\partial q}{\partial t} + \frac{\partial}{\partial x}\left(\frac{q^2}{A}\right) + \frac{A}{\rho}\frac{\partial p}{\partial x} = -\frac{2\pi\nu R}{\delta}\frac{q}{A}. \tag{2.24}$$

Equation (2.15) and (2.24) involve three unknowns (A, q, p) therefore, in order to close the system, we need to relate any two of these three unknowns. This can be achieved by analysing vessel distention due to the time varying blood pressure, resulting in a relation between the vessel cross–sectional area, $A(x,t)$, and the transmural pressure, $p(x,t) - p_0$.

Let us assume that vessel wall tissue is isotropic, incompressible and homogeneous with uniform wall thickness, h, along the vessel. We also assume that vessels are thin walled ($h/r_0 \ll 1$) and longitudinally–tethered *in vivo* so they undergo transverse motion only and deformation in the axial direction is negligible i.e. $\epsilon_{xx} \approx 0$. These assumptions lead us to ignore the stresses acting in the longitudinal and radial directions and that the external stresses are acting in the circumferential direction only i.e. $\sigma_{xx}, \sigma_{rr} \ll \sigma_{\theta\theta}$ and $\epsilon_{xx}, \epsilon_{rr} \ll \epsilon_{\theta\theta}$, where σ (mmHg) and ϵ (dimensionless) denote stress and strain respectively. Under these assumptions, one may express the circumferential tensile stress by using the Laplace's law as [111]

$$\sigma_{\theta\theta} = \frac{rp}{h}. \tag{2.25}$$

A corresponding circumferential strain is defined as

$$\epsilon_{\theta\theta} = \frac{r - r_0}{r_0}, \tag{2.26}$$

where r_0 is the equilibrium or unstressed vessel radius. It should be noted that other researchers (e.g. [6,145]) have also used a slightly different geometric strain ($\epsilon_{\theta\theta} = (r - r_0)/r$) to describe pressure–area relation. The wall behaviour under these two strains is approximately same for small deformations but start to deviate significantly as deformations grow larger.

Assuming further that viscoelastic effects are small within the physiological range [160], then the vessel wall constitutive law reduces to [10]

$$\epsilon_{\theta\theta} = \sigma_{\theta\theta}\frac{1 - \upsilon_x\upsilon_\theta}{E}, \tag{2.27}$$

where $E\,(\text{mmHg})$ is the elastic (Young's) modulus and $\upsilon_x = \upsilon_\theta = 0.5$ are the Poisson ratios in the longitudinal and circumferential directions.

Finally, using (2.25) and (2.26) in (2.27) and solving for transmural pressure, one can derive a simple elastic relation between $A(x,t)$ and $p(x,t)$ as

$$p(A) \equiv p(x,t) - p_0 = \frac{4}{3}\frac{Eh}{r_0}\left(1 - \sqrt{\frac{A_0}{A}}\right). \tag{2.28}$$

Equation (2.28), also known as the tube law, was first given by Barnard *et al.* [15] and used by Olufsen [113–116], Clipp & Steele [35, 36], Vaughan [169] and Cousins [40] in recent works to predict systemic and pulmonary haemodynamics. From equation (2.28), one may write

$$A(x,t) = \frac{A_0}{(1 - 3p(A)r_0/4Eh)^2}, \tag{2.29}$$

$$\Rightarrow \quad \frac{dA}{dp} = \frac{3r_0 A_0}{2Eh(1 - 3p(A)r_0/4Eh)^3} = \frac{3r_0}{2Eh}\sqrt{\frac{A^3}{A_0}}. \tag{2.30}$$

Equations (2.29) and (2.30) tell us that if the elastic modulus E remains constant then dA/dp will increase non–linearly with an increase in p or A. This implies an increase in compliance and decrease in stiffness, which is opposite to physiological behaviour, as the arteries get stiffer with an increase in pressure, above a certain pressure. Thus corresponding to assumed Hookean properties of vessel walls, A and dA/dp will increase until at point where $p = 4Eh/3r_0$. At this pressure the vessel area will become infinite and the artery will burst. On the other hand, a negative or extremely low transmural pressure may cause the vessels to buckle [111]. This characterises the non–linear compliance of the vessel, which contradicts the assumption of linearly elastic vessel walls.

However, the blood vessels *in vivo* are tethered in all directions, which greatly inhibits the vessels' wall movement. Observations suggest [126] that within the physiological range of pressure

$$\left|\frac{A - A_0}{A_0}\right| < 0.1,$$

which means that when the pulse wave propagates along the vessel wall, *in vivo*, it may undergo only small deformations in the circumferential direction from a reference state implying, $|A - A_0| \ll A_0$. Thus as far as the blood vessels are considered thin-walled, isotropic and tethered in the longitudinal and circumferential directions, the linear elastic theory remains valid and the use of non–linear tube–law for assumed linear elastic vessels is justified within the physiological pressure range.

Finally, we use the term Eh/r_0 in equation (2.28) to describe the stiffness of the wall within a vessel and for vessels at different generations in the vascular tree. Therefore this parameter determines the system compliance and is discussed in detail in Chapter 3.

2.3 Fluid dynamics of small blood vessels

Based on Womersley's classical theory [182], we adopt Olufson's approach [113] in this thesis to study the blood flow in the small vessels. The linearized theory from Womersley is also used by Atabek and Lew [11], Atabek [10], Pedley [126] and Berger [19] to study the fluid flow in the compliant vessels. More recently Clipp & Steele [35,36] used the same model to include the description of small pulmonary arteries in their model of pulmonary circulations.

The original solutions by Womersley are obtained by analysing the motion of the fluid, motion of the vessel wall and the internal and external forces acting on the system. However, other much simpler approaches are shown to lead similar solutions. For instance, very recently Cousins & Germaud [38] have shown that a similar solution can be reached with far less calculations by linearising the averaged continuity (2.15) and momentum (2.24) equations, about $A = A_0$ and $q = 0$, rather than first linearizing and then averaging the equations, as done in Olufsen *et al.* [116]. In the following we give a brief detail of equations governing the haemodynamics in the small vessels. A detailed derivations of these equation by Womersley's theory can be found in [113].

As for the large vessels, three equations are required to determine the flow pressure and area for each small vessel in the structure trees. However, for these small vessels the viscous forces are more dominant than the inertial forces [32]. Moreover, unlike the large blood vessels we assume the small vessels to be short and non–tapering with a uniform cross–sectional area A_0 and that the flow inside small vessels is axisymmetric and have no swirl, while the effects of gravity are negligible. Under these assumptions the non–linear effects become small allowing linearization of the governing equations that yields a reduced form of axial momentum equation (2.8)

$$\frac{\partial u_x}{\partial t} + \frac{1}{\rho}\frac{\partial p}{\partial x} = \frac{\nu}{r}\frac{\partial}{\partial r}\left(r\frac{\partial u_x}{\partial r}\right). \tag{2.31}$$

Assuming that all quantities are periodic, with period T (length of a cardiac cycle), pressure and flow can be expressed in the frequency domain using complex periodic Fourier series given by

$$p(x,t) = \sum_{k=-\infty}^{\infty} P(x,\omega_k)e^{i\omega_k t}$$

$$q(x,t) = 2\pi \int_0^{r_0} u(r,x,t)r\,dr = \sum_{k=-\infty}^{\infty} Q(x,\omega_k)e^{i\omega_k t},$$

where

$$u(r,x,t) = \sum_{k=-\infty}^{\infty} U(r,x,\omega_k)e^{i\omega_k t}$$

and $\omega_k = 2\pi k/T$ is the angular frequency, with

$$P(x,\omega_k) = \frac{1}{T}\int_{-T/2}^{T/2} p(x,t)e^{-i\omega_k t}dt, \qquad Q(x,\omega_k) = \frac{1}{T}\int_{-T/2}^{T/2} q(x,t)e^{-i\omega_k t}dt,$$

and

$$U(r,x,\omega_k) = \frac{1}{T}\int_{-T/2}^{T/2} u(r,x,t)e^{-i\omega_k t}dt.$$

Thus for each value of ω_k, equation (2.31) becomes

$$i\omega U + \frac{1}{\rho}\frac{dP}{dx} = \frac{\nu}{r}\frac{\partial}{\partial r}\left(r\frac{\partial U}{\partial r}\right), \tag{2.32}$$

where for convenience we drop the suffix k. Assuming that the small vessels do not taper, equation (2.32) can be solved to give

$$U = \frac{1}{i\omega\rho}\frac{\partial P}{\partial x}\left(1 - \frac{J_0(rw_0/r_0)}{J_0(w_0)}\right),$$

where $w_0^2 = i^3 w^2$, $w^2 = r_0^2\omega/\mu$ is the Womersley number, and $J_0(x)$ is the Bessel function of the first kind and zero order.

Defining the frequency-domain volumetric flow-rate in terms of velocity,

$$Q = 2\pi\int_0^{r_0} Urdr \tag{2.33}$$

$$\Rightarrow i\omega Q = \frac{-A_0}{\rho}\frac{\partial P}{\partial x}(1 - F_J), \tag{2.34}$$

where

$$F_J = 2J_1(w_0)/w_0 J_0(w_0)$$

and $J_1(x)$ is a first-order Bessel function of the first kind.

The one-dimensional continuity equation for the small vessels is the same as for the large vessels. Using the tube law (2.28), the continuity equation (2.15) can be written as

$$C\frac{\partial p}{\partial t} + \frac{\partial q}{\partial x} = 0, \tag{2.35}$$

where C is the compliance, which can be approximated by linearizing the tube law (2.28), giving

$$C = \frac{\partial A}{\partial p} = \frac{3A_0 r_0}{2Eh}\left(1 - \frac{3pr_0}{4Eh}\right)^{-3} \approx \frac{3A_0 r_0}{2Eh} \tag{2.36}$$

as $Eh \gg pr_0$.

Using the compliance approximation in (2.35) and assuming periodicity, the continuity equation becomes

$$i\omega CP + \frac{\partial Q}{\partial x} = 0. \tag{2.37}$$

Differentiating (2.37) with respect to x and substituting the result into (2.34) gives a wave equation of the form

$$\frac{\omega^2}{c^2}Q + \frac{\partial^2 Q}{\partial x^2} = 0 \qquad \text{or} \qquad \frac{\omega^2}{c^2}P + \frac{\partial^2 P}{\partial x^2} = 0, \tag{2.38}$$

where the wave propagation velocity is given by

$$c = \sqrt{A_0(1-F_J)/\rho C}, \tag{2.39}$$

which is complex due to F_J. These equations must be solved for every vessel in the arterial and venous structured trees. Solving (2.38) and using (2.37) gives the flow and pressure in the frequency domain at any spatial position x along a vessel segment

$$Q(x,\omega) = a\cos(\omega x/c) + b\sin(\omega x/c) \tag{2.40}$$

$$P(x,\omega) = ig_\omega^{-1}\left(b\cos(\omega x/c) - a\sin(\omega x/c)\right), \tag{2.41}$$

where a and b are constants and g_ω is another complex quantity, given by

$$g_\omega = \sqrt{CA_0(1-F_J)/\rho}.$$

The zero frequency component ($\omega = 0$)

In order to obtain the solutions for Q and P corresponding to $\omega = 0$, we take $\omega = 0$ in Fourier transformed linearized x–momentum equation (2.32) to get

$$\frac{dP}{dx} = \frac{\mu}{r}\frac{\partial}{\partial r}\left(r\frac{\partial U}{\partial r}\right). \tag{2.42}$$

Since μ and dP/dx do not depend on r, integration of (2.42) with respect to r yields

$$\frac{\partial U}{\partial r} = \frac{r}{2\mu}\frac{dP}{dx} + \frac{B}{r}, \tag{2.43}$$

where B is the constant of integration, which can be evaluated by assuming that $\partial U/\partial r$ is finite at $r = 0 \Rightarrow B = 0$. Further integration of (2.43) with respect to r gives us

$$U = \frac{r^2}{4\mu}\frac{dP}{dx} + K, \tag{2.44}$$

where K is the constant of integration. Using the no-slip condition at the wall i.e. $U = 0$ at $r = r_0 \Rightarrow K = 0$, so the final velocity profile is

$$U = \frac{r^2 - r_0^2}{4\mu}\frac{dP}{dx}. \tag{2.45}$$

Using (2.45) into (2.33), we obtain

$$\begin{aligned} Q &= 2\pi \int_0^{r_0} U r dr, && (2.46) \\ &= -\frac{\pi}{8\mu}\frac{dP}{dx} r_0^4. && (2.47) \end{aligned}$$

It is to be noticed that for $\omega = 0$ we have a normal Poiseuille flow profile. Moreover, steady flow and continuity imply that $\partial q/\partial x = 0$, and the Fourier expansion of flow shows that $\partial q/\partial x = 0 \Leftrightarrow \partial Q/\partial x = 0$ so we may write

$$Q = \Upsilon, \tag{2.48}$$

where Υ is a constant. Substituting (2.48) into (2.47) and rearranging, we get

$$\frac{dP}{dx} = -\frac{8\mu\Upsilon}{\pi r_0^4}, \tag{2.49}$$

$$\Rightarrow P = -\frac{8\mu\Upsilon}{\pi r_0^4} x + \Gamma, \tag{2.50}$$

where Γ is the integration constant.

2.4 Boundary conditions

The system of equations (2.15), (2.24) and (2.28) are hyperbolic, thus to close the system for each vessel a boundary condition must be applied at each end. For the MPA, the flow is specified at the inlet (See Figure 2.1) using the MRI measured flow-rate waveform shown in Figure 2.5. This inflow profile was measured during the MRI scan to measure the dimensions of largest pulmonary arteries of a healthy male subject. The readings were taken at a proximal position in the MPA over five consecutive cardiac cycles at 45 equally spaced time points over every heart beat. This was then averaged over the five cycles and interpolated for 4096 points to match the temporal resolution of our numerical scheme.

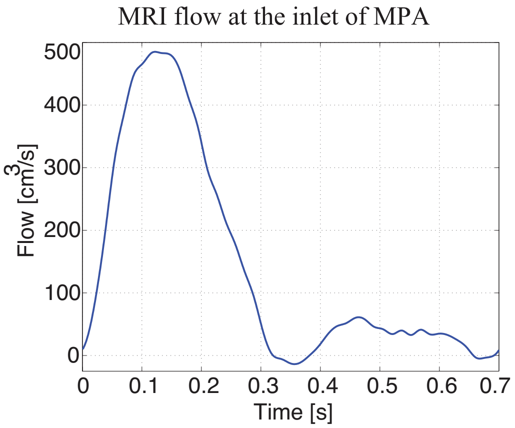

Figure 2.5: Inflow profile at the inlet of MPA. The profile is interpolated from MRI measurements sampled at 45 points per period and averaged over 5 cardiac cycles. (From Olufsen *et al.* [115]).

At each bifurcation, two conditions are required to connect outflow from the parent vessel and inflow to the daughter vessels. These are imposed by ensuring continuity of pressure and conservation of flow, i.e.

$$p_p(L,t) = \quad p_{d_1}(0,t) = p_{d_2}(0,t), \tag{2.51}$$

$$q_p(L,t) = \quad q_{d_1}(0,t) + q_{d_2}(0,t), \tag{2.52}$$

where subscript p denotes the parent vessel and subscripts $d_i, i = 1, 2$ denote the two daughter vessels.

The outflow from the large terminal arteries and the inflows to the corresponding large terminal veins are obtained by connecting arterial and venous structured trees, which is discussed in detail in the next section.

Finally, at the outflow of each large veins (at the inflow to the left atrium) we specify a constant pressure of 2 mmHg. Since this condition is to be imposed just above the left atrium, we consider this to be the left atrium filling pressure and believe that setting the pressure to a constant low value is reasonable as the blood flows relatively freely into the left atrium. Moreover fixing a constant pressure at the outlets ensures a pressure gradient throughout the system that drives the blood flow across the system.

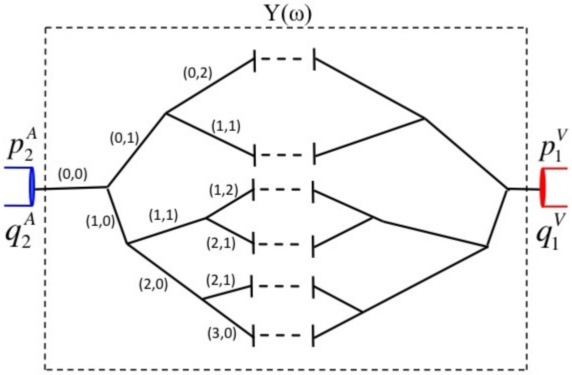

Figure 2.6: Linking an arterial tree with a venous tree. For each vessel in the arterial tree there is a mirror vessel in the venous tree which may have different compliance and length-to-radius ratio. The radii are defined as functions of root vessel radius via scaling factors α and β. Starting from terminals of structured trees, both trees are connected by joining the pairs of vessels in series and in parallel. Flows q_2^A and q_1^V, denote $q^A(L)$ (flow at distal end of large terminal arteries) and similarly $q^V(0)$ (flow at proximal end of large terminal veins), respectively, and pressures p_2^A and p_1^V, represent $p^A(L)$ and $p^V(0)$, respectively. The flows are related to the pressures by a 2×2 admittance matrix $\mathbf{Y}(\omega)$. Note that the labels of branches are the ordered pairs, which refer to generation of vessel in the tree and are powers of scaling factors α and β, i.e. the label (i, j) indicates that the radius of the vessel is $\alpha^i \beta^j r_0$.

2.4.1 Structured tree matching conditions

Originally suggested by C. S Peskin and first derived by G. D. Vaughan [169], we set up expressions determining the admittance of each structured tree using a 2×2 matrix $\mathbf{Y}$ (e.g. see [131]) relating pressure and flow at the outflow of each large terminal artery to pressure and flow at the inflow to the corresponding large terminal vein to connect the networks of arterial and venous vessels as shown in Figure 2.6. This approach is an extension of Olufsen's structured tree outflow condition for the systemic arterial [116] and pulmonary arterial circulations [115]. The advantage of such boundary conditions over lumped parameter models (e.g [6, 8, 133, 154, 156]) is that these physiology–based conditions may accurately take into account the influence of the downstream vasculature on the haemodynamics predicted in computational domain which otherwise, due to the matching complexity of the system, cannot be modelled in detail.

Moreover, unlike the structured tree outflow condition [114] in which prediction of the root impedance required a constant impedance applied at the terminal branches of the structured tree, for the structured tree matching condition no specific value of pressure

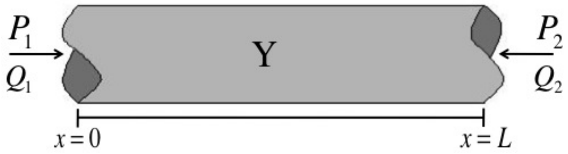

Figure 2.7: Admittance for a single vessel.

and flow relations are required at the joining points of two trees. The only condition needed to set up the admittance matrix are the junction conditions requiring continuity of pressure and conservation of volume flux. The total or root admittance is calculated by joining admittances in series and parallel as described in Algorithm 1 at the end of this section.

Admittance for a single vessel:

For every small vessel in the structured trees a 2×2 matrix $\mathbf{Y}$ can be derived using the frequency domain flow and pressure at given position x along the vessel segment. First making $P(x, w)$ and $Q(x, w)$ dimensionless by

$$\begin{aligned} P(x,\omega) &= \rho g l_c \tilde{P}(x,\omega), && (2.53)\\ Q(x,\omega) &= q_c \tilde{Q}(x,\omega), && (2.54) \end{aligned}$$

where q_c ($= 10\,\mathrm{cm}^3/\mathrm{s}$) is the characteristic flow, $g(= 981\mathrm{cm/s}^2)$ is gravitational acceleration and $l_c(= 1\,\mathrm{cm})$ is the characteristic length. Using (2.53) and (2.54) in (2.40),(2.41),(2.48) and (2.50) from Section 2.3 and removing tildes for the sake of convenience by choosing to denote $\tilde{Q}(x,\omega) \equiv Q(x,\omega)$ and $\tilde{P}(x,\omega) \equiv P(x,\omega)$, we obtain the dimensionless pressure and flow

$$\begin{aligned} Q(x,\omega) &= \frac{1}{q_c}(a\cos(\omega x/c) + b\sin(\omega x/c)), && (2.55)\\ P(x,\omega) &= \frac{i}{\rho g l_c g_\omega}(-a\sin(\omega x/c) + b\cos(\omega x/c)), && (2.56)\\ Q(x,0) &= \Upsilon/q_c, && (2.57)\\ P(x,0) &= -\frac{1}{\rho g l_c}(\frac{8\mu\Upsilon}{\pi r_0^4}x - \Gamma). && (2.58) \end{aligned}$$

One can determine the constants a and b, and eliminate Υ and Γ, by evaluating the flow and pressure at the proximal ($x = 0$) and distal ends ($x = L$) of the vessel. Thus evaluating

(2.55) and (2.56) at $x = 0$ and $x = L$, gives us

$$\begin{aligned} Q(0,\omega) &= \frac{a}{q_c}, && (2.59)\\ P(0,\omega) &= \frac{ib}{\rho g l_c g_\omega}, && (2.60)\\ Q(L,\omega) &= -\frac{1}{q_c}(a\cos(\omega L/c) + b\sin(\omega L/c)), && (2.61)\\ P(L,\omega) &= \frac{i}{\rho g l_c g_\omega}(-a\sin(\omega L/c) + b\cos(\omega L/c)). && (2.62) \end{aligned}$$

As shown in Figure 2.7, we denote the flow and pressure at proximal end by $Q(0,\omega) \equiv Q_1$ and $P(0,\omega) \equiv P_1$ and at distal end by $Q(L,\omega) \equiv Q_2$ and $P(L,\omega) \equiv P_2$. Moreover, we introduce terms $C_L \equiv \cos(\omega L/c)$ and $S_L \equiv \sin(\omega L/c)$.

Inserting (2.59) and (2.60) into (2.61) and (2.62), we get

$$\begin{aligned} Q_2 &= -Q_1 C_L + \frac{i\rho g l_c g_\omega}{q_c} P_1 S_L, && (2.63)\\ P_2 &= \frac{-iq_c}{\rho g l_c g_\omega} Q_1 S_L + P_1 C_L. && (2.64) \end{aligned}$$

Rearranging (2.63) and (2.64) and writing them in a matrix form, for $\omega \neq 0$, we obtain

$$\begin{pmatrix} Q_1 \\ Q_2 \end{pmatrix} = \frac{ig_\omega}{S_L}\frac{\rho g l_c}{q_c}\begin{pmatrix} -C_L & 1 \\ 1 & -C_L \end{pmatrix}\begin{pmatrix} P_1 \\ P_2 \end{pmatrix}. \qquad (2.65)$$

Repeating same procedure for $\omega = 0$, (2.57) and (2.58) give

$$\begin{aligned} Q_1 &= \Upsilon/q_c, && (2.66)\\ Q_2 &= -\Upsilon/q_c, && (2.67)\\ P_1 &= \Gamma, && (2.68)\\ P_2 &= \frac{1}{\rho g l_c}(\Gamma - \frac{8\mu\Upsilon}{\pi r_0^4}L). && (2.69) \end{aligned}$$

Rearranging (2.66)-(2.69), we can express flow at proximal and distal ends as functions of pressure at both ends of the vessels

$$\begin{pmatrix} Q_1 \\ Q_2 \end{pmatrix} = \frac{\rho g l_c}{q_c}\frac{\pi r_0^4}{8\mu L}\begin{pmatrix} 1 & -1 \\ -1 & 1 \end{pmatrix}\begin{pmatrix} P_1 \\ P_2 \end{pmatrix}. \qquad (2.70)$$

Matrix relations (2.65) and (2.70) are the admittance matrix relations for a single vessel and may be expressed in a more compact form as

$$\mathbf{Q} = \mathbf{Y}(\omega)\mathbf{P}, \qquad \forall\ \omega \in [0, \omega_k], \qquad (2.71)$$

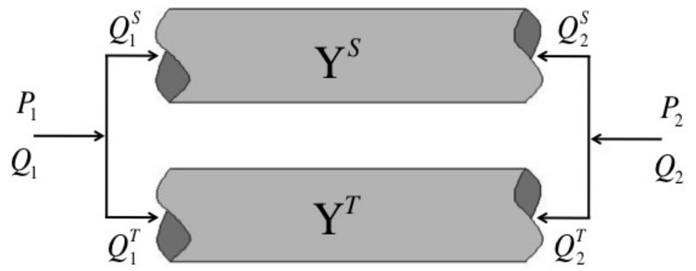

Figure 2.8: Admittance for two vessels joined in parallel.

where $\mathbf{Q} = (Q_1, Q_2)^\dagger, \mathbf{P} = (P_1, P_2)^\dagger$ and $\mathbf{Y}(\omega) = Y_{ij}$ $(i, j = 1, 2)$, so

$$\mathbf{Y} = \frac{ig_\omega}{S_L}\frac{\rho g l_c}{q_c}\begin{pmatrix} -C_L & 1 \\ 1 & -C_L \end{pmatrix} \quad \text{for } \omega \neq 0, \tag{2.72}$$

and

$$\mathbf{Y} = \frac{\rho g l_c}{q_c}\frac{\pi r_0^4}{8\mu L}\begin{pmatrix} 1 & -1 \\ -1 & 1 \end{pmatrix} \quad \text{for } \omega = 0. \tag{2.73}$$

Now given $\mathbf{Y}^S$ and $\mathbf{Y}^T$, the individual admittances of any two arbitrary vessels S and T joined in parallel or in a series, one may find a combined admittance in the form of a 2×2 matrix.

Admittance for two vessels in parallel:

Consider two vessels, S and T, in parallel connected to a common inflow and outflow, as depicted in Figure 2.8. For each vessel their exists a unique $\mathbf{Y}$ such that

$$\mathbf{Q}^S = \mathbf{Y}^S\mathbf{P}^S \quad \text{and} \quad \mathbf{Q}^T = \mathbf{Y}^T\mathbf{P}^T, \tag{2.74}$$

where $\mathbf{Q}^S = (Q_1^S, Q_2^S)^\dagger, \mathbf{Q}^T = (Q_1^T, Q_2^T)^\dagger$, $\mathbf{P^S} = (P_1^S, P_2^S)^\dagger$ and $\mathbf{P^T} = (P_1^T, P_2^T)^\dagger$. Since the pressure is continuous at a bifurcating junction, the pressure at the inlet to vessel S is the same as the pressure at the inlet to vessel T. Similarly, the pressure at the outlet of vessel S is the same as the pressure at the outlet of vessel T. Denoting the inlet and outlet pressures by P_1 and P_2, respectively, this connection can be described by $P_1^S = P_1^T = P_1$ and $P_2^S = P_2^T = P_2$. So (2.74) becomes

$$\mathbf{Q}^S = \mathbf{Y}^S\mathbf{P} \quad \text{and} \quad \mathbf{Q}^T = \mathbf{Y}^T\mathbf{P}. \tag{2.75}$$

Since the volume flux is conserved across a bifurcation, for two vessels connected in parallel, the total inflow $Q_1 = Q_1^S + Q_1^T$ and the total outflow $Q_2 = Q_2^S + Q_2^T$ means that

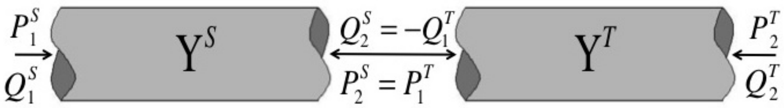

Figure 2.9: Admittance for two vessels connected in series.

the equations in (2.75) can be added to obtain

$$\mathbf{Q} = \mathbf{Y}^{\parallel}\mathbf{P}, \tag{2.76}$$

where $\mathbf{Q} = (Q_1, Q_2)^T$ and

$$\mathbf{Y}^{\parallel} = \mathbf{Y}^S + \mathbf{Y}^T \tag{2.77}$$

is the admittance of two vessels joined in parallel. Here the symbol '$\|$' indicates the combined admittance of two vessels in parallel.

Admittance for two vessels in series:

Next we consider two vessels connected in a series, as depicted in Figure 2.9. Flow and pressure at proximal and distal ends of both vessels is given by

$$\begin{aligned} Q_1^S &= Y_{11}^S P_1^S + Y_{12}^S P_2^S, && (2.78)\\ Q_2^S &= Y_{21}^S P_1^S + Y_{22}^S P_2^S, && (2.79)\\ Q_1^T &= Y_{11}^T P_1^T + Y_{12}^T P_2^T, && (2.80)\\ Q_2^T &= Y_{21}^T P_1^T + Y_{22}^T P_2^T. && (2.81) \end{aligned}$$

The system above can also be written in a compact form as

$$Q_k^i = \sum_{l=1}^{2} Y_{kl}^i P_l^i, \tag{2.82}$$

where $i = S, T$ and $k = 1, 2$ with Y_{kl} being the components of the 2×2 admittance matrix. Let $P = P_2^S = P_1^T$ along with $Q_2^S = -Q_1^T$ at the junction of two vessels in series, then the system (2.82) can be solved for P using (2.79) and (2.80) i.e.

$$Y_{21}^A P_1^S + Y_{22}^S P + Y_{11}^T P + Y_{12}^T P_2^T = 0, \tag{2.83}$$

rearranging for P, we get

$$P = -\frac{Y_{21}^S P_1^S + Y_{12}^T P_2^T}{Y_{22}^S + Y_{11}^T}. \tag{2.84}$$

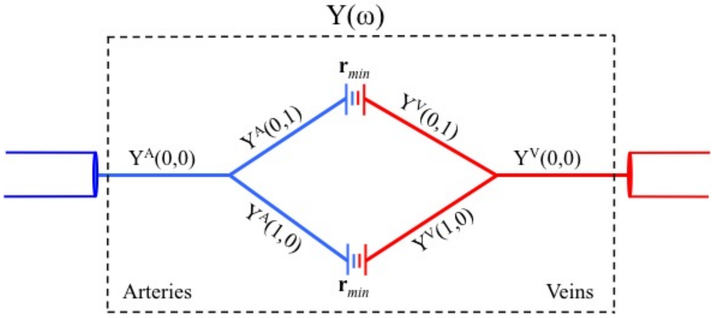

Figure 2.10: An idea of grand matrix for a simple network.

Substituting (2.84) in (2.78) and (2.81), we obtain

$$Q_1^S = \left(Y_{11}^S - \frac{Y_{21}^S Y_{12}^S}{Y_{22}^S + Y_{11}^T}\right) P_1^S - \frac{Y_{12}^S Y_{12}^T}{Y_{22}^S + Y_{11}^T} P_2^T, \tag{2.85}$$

$$Q_2^T = -\frac{Y_{21}^T Y_{21}^S}{Y_{22}^S + Y_{11}^T} P_1^S + \left(Y_{22}^T - \frac{Y_{21}^T Y_{12}^T}{Y_{22}^S + Y_{11}^S}\right) P_2^T. \tag{2.86}$$

Which can be expressed as matrix relation

$$\begin{pmatrix} Q_1^S \\ Q_2^T \end{pmatrix} = \mathbf{Y}^{\Leftrightarrow} \begin{pmatrix} P_1^S \\ P_2^T \end{pmatrix}, \tag{2.87}$$

where

$$\mathbf{Y}^{\Leftrightarrow} = \frac{1}{Y_{22}^S + Y_{11}^T} \begin{pmatrix} det(\mathbf{Y}^S) + Y_{11}^S Y_{11}^T & -Y_{12}^S Y_{12}^T \\ -Y_{21}^S Y_{21}^T & det(\mathbf{Y}^T) + Y_{22}^S Y_{22}^T \end{pmatrix} \tag{2.88}$$

is the admittance matrix for two vessels connected in series. Here the symbol '⇔' represents the admittance matrix of vessels joined in series.

Grand admittance: Linking arterial and venous trees together

To link the arterial and venous trees, the two trees should be 'mirror images' of each other in as much as that they should have the same number of bifurcations and terminal vessels, however, each tree is allowed to have different vessel properties including compliance and length-to-radius ratio. The admittance matrices (2.72) and (2.73) are computed for each individual vessel, and the total admittance of the two connected trees is found recursively by combining the admittance matrices of vessels and subtrees in series (using (2.88)) and in parallel (using (2.77)) as appropriate.

To set up the recursion algorithm, each pair of vessels (arterial and venous) are assigned an index (i, j) indicating that the radius of the vessel is $\alpha^i \beta^j r_0$; in addition each vessel is assigned a label "A" or "V" specifying if the vessel is an artery or a vein. For example, the total admittance for a small network consisting of an arterial (A) and a venous (V) tree, each having one bifurcation with branches scaled by factors α and β, is given by

$$\mathbf{Y} = \mathbf{Y}^A(0,0) \Leftrightarrow [\{\mathbf{Y}^A(1,0) \Leftrightarrow \mathbf{Y}^V(1,0)\}\|\{\mathbf{Y}^A(0,1) \Leftrightarrow \mathbf{Y}^V(0,1)\}] \Leftrightarrow \mathbf{Y}^V(0,0),$$

or equivalently

$$\mathbf{Y} = \mathbf{Y}^A(0,0) \Leftrightarrow [\{\mathbf{Y}^A(1,0)\|\mathbf{Y}^A(0,1)\} \Leftrightarrow \{\mathbf{Y}^V(1,0)\|\mathbf{Y}^V(0,1)\}] \Leftrightarrow \mathbf{Y}^V(0,0).$$

Below we describe the general algorithm valid for trees where the compliance is identical for arterial and venous vessels, while the length-to-radius ratio is larger for vessels in the venous tree.

Algorithm 1: Recursive algorithm to compute the 2×2 admittance matrix Y for a connected network of arterial and venous vessels

The root admittance matrix Y is computed recursively by calling Y = admit$(0, 0)$.

Recursive function Y(i, j) = admit(i, j)

```
• if $r(i+1,j) < r_{min}$      ($\alpha$-branch)

      *    for $k$ = A, V
               $Y^k(i+1,j)$ = eqn (2.72),    $\omega \neq 0$
               $Y^k(i+1,j)$ = eqn (2.73),    $\omega = 0$
           end

      $Y(i+1,j)$ = ser($Y^A(i+1,j)$,$Y^V(i+1,j)$)
  else
      $Y(i+1,j)$ = admit$(i+1,j)$
  end
      ____________________________

• if $r(i,j+1) < r_{min}$      ($\beta$ branch)

      *    for $k$ = A, V
               $Y^k(i,j+1)$ = eqn (2.72),    $\omega \neq 0$
               $Y^k(i,j+1)$ = eqn (2.73),    $\omega = 0$
           end

      $Y(i,j+1)$ = ser($Y^A(i,j+1)$,$Y^V(i,j+1)$)
  else
      $Y(i,j+1)$ = admit$(i,j+1)$
  end
      ____________________________

• $Y_{mid}(i,j) = Y(i+1,j) + Y(i,j+1)$

• for $k$ = A, V
      $Y^k$(i,j) = eqn (2.72),    $\omega \neq 0$
      $Y^k$(i,j) = eqn (2.73),    $\omega = 0$
```

```
end
```

- $\mathrm{Y}(i,j) = \mathrm{ser}(\mathrm{ser}(\mathrm{Y}^V(i,j),\mathrm{Y}_{mid}(i,j)),\mathrm{Y}^A(i,j))$

<u>Series function $\mathrm{Y}(i,j) = \mathrm{ser}(\mathrm{Y}^S(i,j),\mathrm{Y}^T(i,j))$</u>

For vessel (i,j) compute determinants

$$D^k = \mathrm{Y}^k_{11}\,\mathrm{Y}^k_{22} - \mathrm{Y}^k_{12}\,\mathrm{Y}^k_{21}, \quad k = S, T$$

then Y has components

$$\begin{aligned}
\mathrm{Y}_{11} &= (D^S + Y^S_{11}\,Y^T_{11})\,/\,(Y^S_{22} + Y^T_{11})\\
\mathrm{Y}_{12} &= (-Y^S_{12}\,Y^T_{12})\,/\,(Y^S_{22} + Y^T_{11})\\
\mathrm{Y}_{21} &= (-Y^S_{21}\,Y^T_{21})\,/\,(Y^S_{22} + Y^T_{11})\\
\mathrm{Y}_{22} &= (D^T + Y^S_{22}\,Y^T_{22})\,/\,(Y^S_{22} + Y^T_{11}).
\end{aligned}$$

Once a grand admittance is obtained it can be used to relate the frequency domain pressure ($P_A(L,w)$) and flow ($Q_A(L,w)$) at the end of large terminal arteries with the frequency domain pressure ($P_V(0,\omega)$) and flow ($Q_V(0,\omega)$) at the beginning of large terminal vein by the following relation

$$\begin{pmatrix} Q_A(L,\omega) \\ Q_V(0,\omega) \end{pmatrix} = \begin{pmatrix} Y_{11}(\omega) & Y_{12}(\omega) \\ Y_{21}(\omega) & Y_{22}(\omega) \end{pmatrix} \begin{pmatrix} P_A(L,\omega) \\ P_V(0,\omega) \end{pmatrix}. \tag{2.89}$$

Using the grand admittance relation obtained in (2.89), we can relate the pressures and flows at the terminals of large arteries and veins through a convolution integral in the real domain as the following:

$$q_A(L,t) = \frac{1}{T}\int_{-T/2}^{T/2} (p_A(L,t-\tau)y_{11}(\tau) + p_V(0,t-\tau)y_{12}(\tau))d\tau, \tag{2.90}$$

$$q_V(0,t) = \frac{1}{T}\int_{-T/2}^{T/2} (p_A(L,t-\tau)y_{21}(\tau) + p_V(0,t-\tau)y_{22}(\tau))d\tau. \tag{2.91}$$

The equations above can also be expressed in a more compact form as

$$q_k(t) = \sum_{l=1}^{2} \int_0^T y_{kl}(\tau)\,p_l(t-\tau)\,d\tau, \quad k = 1, 2, \tag{2.92}$$

where $q_1(t)$ and $p_1(t)$ are the volume flux and pressure at the root of the arterial tree, and $q_2(t)$ and $p_2(t)$ are the volume flux and pressure at the root of the venous tree. $y_{kl}(t)$ is the inverse Fourier transform of $Y_{kl}(\omega)$. Equation (2.92) is the matching boundary condition to be applied at the end of terminal arteries and veins.

This is a novel boundary condition that not only completes the pulmonary circulation by connecting the arteries and veins but also, as we see later, turns out to be an extremely efficient tool to predict the microcirculatory characteristics of blood flow in both arterial and venous vascular beds.

2.5 Numerical solution

The system of equations (2.15), (2.24) and (2.28) can not be solved analytically therefore we have to solve them numerically but before that it is convenient to write the governing equations((2.15),(2.24)) in dimensionless form. To do so, we define the following dimensionless variables

$$x = r_c\tilde{x} \quad t = \frac{r_c^3}{q_c}\tilde{t} \quad r = r_c\tilde{r} \quad \delta = r_c\tilde{\delta} \quad h = r_c\tilde{h}$$

$$A = r_c^2\tilde{A} \quad q = q_c\tilde{q} \quad p = \rho g r_c\tilde{p} \quad E = \rho g r_c\tilde{E}$$

Where r_c is the characteristic radius of the vessel and q_c is the characteristic flow, chosen as $r_c = 1\,\mathrm{cm}$ and $q_c = 10\,\mathrm{cm}^3/\mathrm{s}$ respectively. Also $\rho = 1.055\,\mathrm{g/cm}^3$ is the density of the blood and $g = 981\mathrm{cm/s}^2$ is the acceleration due to gravity. First, using the above quantities in (2.15), we get the dimensionless continuity equation

$$\frac{\partial\tilde{A}}{\partial\tilde{t}} + \frac{\partial\tilde{q}}{\partial\tilde{x}} = 0. \tag{2.93}$$

The dimensionless momentum equation is given by

$$\frac{\partial\tilde{q}}{\partial\tilde{t}} + \frac{\partial}{\partial\tilde{x}}\left(\frac{\tilde{q}^2}{\tilde{A}}\right) + \tilde{A}\frac{\partial\tilde{p}}{\partial\tilde{x}} = -\frac{2\pi\tilde{r}}{\tilde{\delta}\mathcal{R}e}\frac{\tilde{q}}{\tilde{A}}, \tag{2.94}$$

where $\mathcal{R}e = q_c/(\nu r_c)$ is the Reynolds number. The state equation (2.28) in the dimension–less form is given by

$$\tilde{p}(\tilde{A}) = \frac{4}{3}\frac{\tilde{E}\tilde{h}}{\tilde{r}_0}\left(1 - \sqrt{\frac{\tilde{A}_0}{\tilde{A}}}\right). \tag{2.95}$$

In equations (2.93) and (2.94) all quantities of the form $\tilde{\Phi}$ are dimensionless but from now onward, for convenience we drop tildes from the dimensionless quantities.

In order to solve the system, we adopt a two–step Lax–Wendroff method, which requires the system of equations to be written in conservation form. In order to write these equations in conservation form, we introduce a function B in the dimensionless from by

$$B(r_0(x), p(x,t)) = \int_{p_0}^{p(x,t)} [A(r_0(x), p']dp'. \tag{2.96}$$

Writing $A(x,t) = A(p(x,t); r_0(x); x, t)$ from equation (2.28), we get

$$A(x,t) = A_0 \left(1 - \frac{p(x,t)}{f(r_0)}\right)^{-2}, \tag{2.97}$$

where

$$f(r_0) = \frac{4Eh}{3r_0}.$$

Using (2.97) in (2.96), we get

$$B = f(r_0)\sqrt{A_0 A}.$$

Differentiating B with respect to x, we get

$$\begin{aligned}\frac{\partial B}{\partial x} &= \frac{\partial B}{\partial A}\frac{\partial A}{\partial p}\frac{\partial p}{\partial x} + \frac{\partial B}{\partial r_0}\frac{dr_0}{dx},\\ &= A\frac{\partial p}{\partial x} + \frac{\partial B}{\partial r_0}\frac{dr_0}{dx}.\end{aligned}$$

In view of above expressions, the momentum equation (2.94) can be written as

$$\frac{\partial q}{\partial t} + \frac{\partial}{\partial x}\left(\frac{q^2}{A} + B\right) = -\frac{2\pi r_0}{\delta \mathcal{R}e}\frac{q}{A} + \frac{\partial B}{\partial r_0}\frac{dr_0}{dx}. \tag{2.98}$$

After coupling momentum equation (2.94) with the equation of state (2.95), the last term of (2.94) is evaluated as

$$\frac{\partial B}{\partial r_0}\frac{dr_0}{dx} = \left(2\sqrt{A}\left(\sqrt{\pi}f + \sqrt{A_0}\frac{df}{dr_0}\right) - \frac{df}{dr_0}\right)\frac{dr_0}{dx}, \tag{2.99}$$

Plugging (2.99) in (2.94) and combining with continuity equation (2.93), the system can be expressed in conservation form

$$\frac{\partial}{\partial t}\mathbf{U} + \frac{\partial}{\partial x}\mathbf{W} = \mathbf{S}, \tag{2.100}$$

where $\mathbf{U}$, $\mathbf{W}$ and $\mathbf{S}$ are given by

$$\mathbf{U} = (A, q), \tag{2.101}$$

$$\mathbf{W} = (W_1, W_2) = \left(q, \frac{q^2}{A} + f\sqrt{A_0 A}\right), \tag{2.102}$$

$$\mathbf{S} = (S_1, S_2) = \left(0, -\frac{2\pi r}{\delta \mathcal{R}e}\frac{q}{A} + \left(2\sqrt{A}\left(\sqrt{\pi}f + \sqrt{A_0}\frac{df}{dr_0}\right) - \frac{df}{dr_0}\right)\frac{dr_0}{dx}\right). \tag{2.103}$$

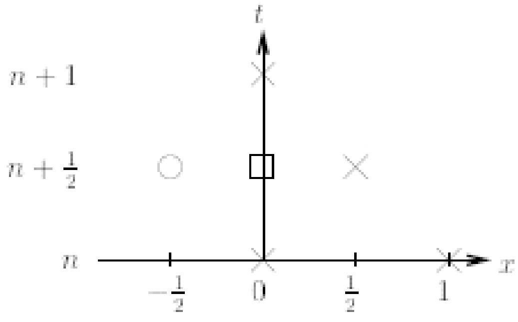

Figure 2.11: Ghost point, marked with a circle, at spatial point $x = -1/2$, i.e. *a half spatial step before the entrance of any vessel* and at time–step $n+1/2$. Points marked with a cross are known, and the point marked with a square may be found by averaging the points at adjacent time-steps.

2.5.1 Richtmeyer's two–step Lax–Wendroff scheme

Let $\mathbf{U}_m^n = \mathbf{U}(m\Delta x, n\Delta t)$ and similarly for $\mathbf{W}$ and $\mathbf{S}$. Here $m \in [0, M]$ and $n \in [0, N]$ with M and N being the maximum number of discrete points along spatial and temporal axis, respectively, of a grid in the (x, t) domain. The solution at all points in the interior (excluding boundary) is determined by first determining some intermediate values at steps $(m + 1/2, n + 1/2)$. Using a uniform grid, we can derive a four point formula, predicting the flow at time level $(n + 1)$ as follows,

$$\mathbf{U}_m^{n+1} = \mathbf{U}_m^n - \frac{\Delta t}{\Delta x}\left(\mathbf{W}_{m+1/2}^{n+1/2} - \mathbf{W}_{m-1/2}^{n+1/2}\right) + \frac{\Delta t}{2}\left(\mathbf{S}_{m+1/2}^{n+1/2} + \mathbf{S}_{m-1/2}^{n+1/2}\right) \qquad (2.104)$$

Using two intermediate points at time level $(n + 1/2)$, and using (2.102) and (2.103), it is possible to determine

$$\mathbf{\Omega}_{m+1/2}^{n+1/2} \quad \mathbf{\Omega}_{m-1/2}^{n+1/2},$$

$\mathbf{\Omega}$ being either $\mathbf{W}$ or $\mathbf{S}$, by using the definition

$$\mathbf{U}_j^{n+1/2} = \frac{\mathbf{U}_{j+1/2}^n + \mathbf{U}_{j-1/2}^n}{2} + \frac{\Delta t}{2}\left(-\frac{\mathbf{W}_{j+1/2}^n - \mathbf{W}_{j-1/2}^n}{h} + \frac{\mathbf{S}_{j+1/2}^n + \mathbf{S}_{j-1/2}^n}{2}\right). \qquad (2.105)$$

where $j = m + 1/2$ and $j = m - 1/2$.

Inflow condition

The inflow into the system is described by a periodic function, see Figure 2.5. Also, A will be determined from the boundary condition for q. In order to find A, we need to evaluate

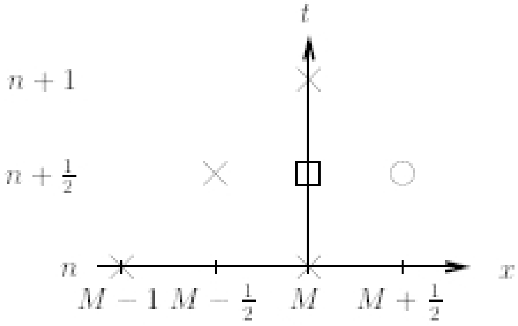

Figure 2.12: Ghost point, marked as a circle, at spatial point $x = M + 1/2$, i.e. *a half spatial step beyond the outlet of any vessel* and at time–step $n + 1/2$. Points marked with a cross are known, and the point marked with a square may be found by averaging the points at adjacent time–steps.

$q_{-1/2}^{n+1/2}$. This can be found by introducing a ghost point $q_{-1/2}^{n+1/2}$ (see Figure 2.11). Then,

$$q_0^{n+1/2} = \frac{1}{2}\left(q_{-1/2}^{n+1/2} + q_{1/2}^{n+1/2}\right) \tag{2.106}$$

$$\Leftrightarrow q_{-1/2}^{n+1/2} = 2q_0^{n+1/2} - q_{1/2}^{n+1/2} \tag{2.107}$$

and from (2.104),

$$A_0^{n+1} = A_0^n - \frac{\Delta t}{\Delta x}\left((W_1)_{1/2}^{n+1/2} - (W_1)_{-1/2}^{n+1/2}\right) + \frac{\Delta t}{2}\left((S_1)_{1/2}^{n+1/2} + (S_1)_{-1/2}^{n+1/2}\right), \tag{2.108}$$

where $(W_1)_{-1/2}^{n+1/2} = q_{-1/2}^{n+1/2}$ and $(S_1)_{-1/2}^{n+1/2} = 0$.

Outflow Condition

In contrast to the inflow to the system at the entrance of the MPA, at offices of four large veins i.e. the outflow from the system the pressure is known but the flow q is unknown. Sine the area A can be expressed in terms of pressure by using (2.97), the area A is also known at the system outflow and therefore q can be determined from the boundary condition for A. To do this, we need to evaluate $A_{M+1/2}^{n+1/2}$. This can be done by using another ghost point beyond the outlet of terminal vessels, see Figure 2.12, so that

$$A_M^{n+1/2} = \frac{1}{2}\left(A_{M-1/2}^{n+1/2} + A_{M+1/2}^{n+1/2}\right) \tag{2.109}$$

$$\Leftrightarrow A_{M+1/2}^{n+1/2} = 2A_M^{n+1/2} - A_{M-1/2}^{n+1/2}. \tag{2.110}$$

Now, (2.104) gives us

$$q_M^{n+1} = q_M^n - \frac{\Delta t}{\Delta x}\left((W_2)_{M+1/2}^{n+1/2} - (W_2)_{M-1/2}^{n+1/2}\right) + \frac{\Delta t}{2}\left((S_2)_{M+1/2}^{n+1/2} + (S_2)_{M-1/2}^{n+1/2}\right), \tag{2.111}$$

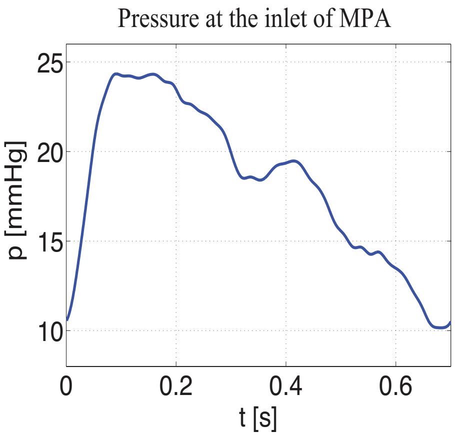

Figure 2.13: A computed pressure profile to replace an MRI measured inflow at the inlet of MPA.

where $(W_2)^{n+1/2}_{M+1/2}$ and $(S_2)^{n+1/2}_{M+1/2}$ are given by (2.102) and (2.103) respectively. Equation (2.104) also tells us that,

$$A^{n+1}_M = A^n_M - \frac{\Delta t}{\Delta x}\left((W_1)^{n+1/2}_{M+1/2} - (W_1)^{n+1/2}_{M-1/2}\right) + \frac{\Delta t}{2}\left((S_1)^{n+1/2}_{M+1/2} + (S_1)^{n+1/2}_{M-1/2}\right) \quad (2.112)$$

$$\Rightarrow q^{n+1/2}_{M+1/2} = \frac{\Delta x}{\Delta t}\left(A^n_M - A^{n+1}_M\right) + q^{n+1/2}_{M-1/2}\,, \quad (2.113)$$

since $(W_1)^n_m = q^n_m$ and $(S_1)^n_m = 0$. Equations (2.110), (2.111) and (2.113) provide us a system of three equations for in three unknowns $A^{n+1/2}_{M+1/2}$, $q^{n+1/2}_{M+1/2}$, and q^{n+1}_M.

2.5.2 Time varying pressure as an inflow condition

The work presented in this section is new and it results in simulated waveforms presented in Section 4.3. The motivation of using a new inflow pressure boundary condition is described in Section 4.3, for now we only provide details of how this new inflow pressure boundary condition can be incorporated in the numerical scheme.

Using the two–step Lax–Wendroff scheme it is possible to replace the flow–time relation with a pressure–time relation as an input boundary condition at the inlet of MPA. However, we are interested in using a physiologically relevant pressure rather than using any arbitrary data set to be seen as pressure. Since we are using a physiological inflow at the inlet of the pulmonary system, we may choose the corresponding computed pressure at the boundary and then fix it by letting the flow to be a dependent quantity at the inlet. To do this we need to modify the numerical equations at the upstream boundary by rewriting cross–sectional area $A(x,t)$ as a function of transmural pressure $p(A(x,t))$ in (2.28) and then deriving the corresponding numerical equations at $x = 0$ for the MPA.

Now the pressure p, given in Figure 2.13, is fixed instead of flow q at the inlet of large arterial tree so, again by using (2.97), the area A is known and the flow q will be determined by using this time varying p. To do this, we need to evaluate $A_{-1/2}^{n+1/2}$ by again using a ghost point explained in Figure 2.11, so that

$$A_0^{n+1/2} = \frac{1}{2}\left(A_{-1/2}^{n+1/2} + A_{1/2}^{n+1/2}\right) \tag{2.114}$$

$$\Leftrightarrow A_{-1/2}^{n+1/2} = 2A_0^{n+1/2} - A_{1/2}^{n+1/2}. \tag{2.115}$$

Now, (2.104) tells us that,

$$q_0^{n+1} = q_0^n - \frac{\Delta t}{\Delta x}\left((W_2)_{1/2}^{n+1/2} - (W_2)_{-1/2}^{n+1/2}\right) + \frac{\Delta t}{2}\left((S_2)_{1/2}^{n+1/2} + (S_2)_{-1/2}^{n+1/2}\right), \tag{2.116}$$

where $(W_2)_{1/2}^{n+1/2}$ and $(S_2)_{1/2}^{n+1/2}$ are given by (2.102) and (2.103) respectively. Also from (2.104) we have

$$A_0^{n+1} = A_0^n - \frac{\Delta t}{\Delta x}\left((W_1)_{1/2}^{n+1/2} - (W_1)_{-1/2}^{n+1/2}\right) + \frac{\Delta t}{2}\left((S_1)_{1/2}^{n+1/2} + (S_1)_{-1/2}^{n+1/2}\right)$$

$$\Rightarrow q_{1/2}^{n+1/2} = \frac{\Delta x}{\Delta t}\left(A_0^n - A_0^{n+1}\right) + q_{-1/2}^{n+1/2}, \tag{2.117}$$

since $(W_1)_m^n = q_m^n$ and $(S_1)_m^n = 0$.

Equations (2.115), (2.116) and (2.117) provide us with a system of three equations for the three unknowns $A_{1/2}^{n+1/2}$, $q_{1/2}^{n+1/2}$, and most importantly, q_0^{n+1}.

Full details of numerical implementation of bifurcation and matching conditions through two–step Lax–Wendroff scheme are separately provided in Appendix B at the end of the thesis.

2.6 Summary of the chapter

In this chapter, we have set up a one–dimensional model of human pulmonary circulation that includes both small and large arteries and veins to enable simulations of blood flow and pressure along the complete path emanating at the right ventricle and ending at the left atrium. The geometric description of the large arteries and the inflow boundary condition (flow-rate) is based on subject–specific anatomical measurements of large pulmonary arteries and the inflow data, obtained from MRI experiment, whereas the pulmonary veins were set up according to the most prevalent venous anatomy and dimensions found in the literature. Moreover, the systems of equations governing the fluid–structure interaction in the large and small blood vessels are given and a set of boundary conditions is prescribed, and explained in detail, to complete the modelling process. In particular, a detailed derivation of the structured tree matching condition is provided and an algorithm is stated for the first time to compute the admittances in the structured tree. Finally a numerical strategy is devised to solve the resulting model.

Chapter 3

Pulmonary Compliance

The aim of this chapter is to determine a set of parameter values (ξ, γ, $r_{\min}$, l_{rr_A}, l_{rr_v}, C), which represent the normal physiological case for this study. In particular, the compliance parameter, C, remains an undetermined parameter at this point in our study and therefore we discuss in detail the determination of C in this chapter. It is essential that the selected parameters values not only represent the normal case but also provide us the flexibility to change the value of a certain parameter in a plausible range around the normal value in order to simulate some disease case scenarios, such as pulmonary hypertension. The contents of this chapter thus include discussion on existing studies, approaches used in other pulmonary models and our analysis regarding the effects of compliance on our simulations, which finally leads us to specify the value of C.

3.1 Compliance of the pulmonary vessels

Compliance refers to the ability of an elastic structure to distend from its equilibrium state under pressure, thus it gives us a measure of distensibility or stiffness of that structure and can be obtained by computing the fractional change in volume per unit change in pressure. Since the blood vessels are elastic in nature, the elastic properties of vessel wall tissues determine the compliance of the entire system, which may change significantly throughout the system. From Section 2.3 (the linearised theory of pulse–wave propagation), it can easily be illustrated that the compliance, C, affects the pressure–flow relation and the change in total blood volume in response to an alteration in blood pressure. Thus any change in C influences the distribution of blood flow and the pulse–wave propagation throughout the lung and hence determines the changes in shape, speed and magnitude of the pulse–wave.

Due to the anatomical and functional differences the behaviour and the distribution of compliance in the two cardiovascular systems is significantly different. In the systemic arterial tree the compliance is mainly located in aorta (80% of total compliance in thoracic-abdominal aorta) whereas in the pulmonary circulation the compliance is distributed over the entire circulation system [21, 144]. For instance, in the pulmonary circulation the total number of peripheral vessels is 8–10 times more than those in the systemic system and that it has an exceptional ability to recruit blood vessels during periods of high flow (e.g during exercise), which makes the pulmonary circulation a highly compliant system [48]. Moreover, unlike the systemic circulation, the pulmonary circulation is known for its varying anatomy and physiology within a population, especially in the case of human beings in whom the value of pressure and vessel diameters varies over a large range among individuals. This suggests that the direct comparison between systemic and pulmonary compliance is not trivial, yet several studies [49,59,120] report pulmonary arteries about 2–10 times more compliant than the systemic arteries. These numbers depict a large variation and in the absence of subject–specific measurements of *in vivo* pressure and diameters it becomes difficult to have a consensus about what value of pulmonary compliance should be used in theoretical studies. Faced with this problem, different pulmonary models [92, 115,169] adopt different approaches to approximate the compliance parameter by defining $C = C(Eh/r_0)$ (see equation (2.36)).

3.1.1 Parameter estimation for mathematical models

In the context of modelling circulation, a good approximation of C is important to simulate physiologically relevant pulse waveforms. Therefore, one must look to use the parameter approximations which translate the underlying mechanisms of observed behaviours. For a subject–specific study, ideally one would like to have *in vivo* measurements of pressure and diameters to determine C but such measurements involve highly invasive procedures. Thus in the absence of detailed anatomical data it becomes impossible to determine the subject–specific parameters. Alternatively, one may refer to existing studies in the literature and infer the parameter value by taking into account the qualitative conclusions from these studies. A drawback of the later approach is that it may not always be possible to reproduce the physiologically observed features from a theoretical model by implementing the existing approximations without taking into account other study aspects like experi-

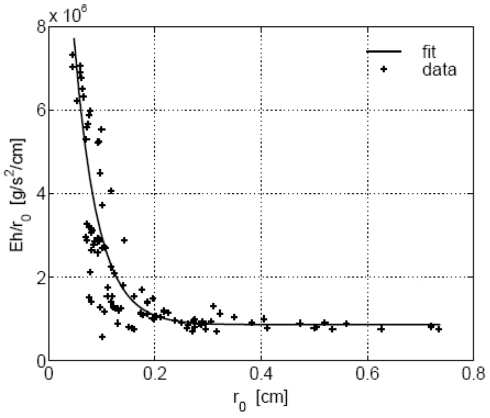

Figure 3.1: Radius dependent modulus of systemic compliance given by Olufsen [116].

mental technique, study conditions (*in vivo* or *ex vivo*) or the species under investigation. Since this study is only partially subject–specific and we do not have detailed *in vivo* data of pressures and diameters for the subject under consideration, we have no choice but to explore the literature to infer a valid compliance approximation for our model.

3.1.2 Use of a radius–dependent systemic modulus

One common approach is to use a systemic compliance modulus by scaling it up to represent the pulmonary compliance [35, 169]. Among recent studies, Clipp & Steele [35, 36] support using a larger compliance value, about three times that of systemic arterial compliance value, for their model of pulmonary arteries. They choose this particular scaling based on the observation that the simulated pulse pressure is in close agreement with average experimental pulse pressure. Whilst reasonable, this approach may lead to a neglect of any shape features of the pulse waveform that, from a clinical point of view, are as important as the magnitudes.

Both Clipp [35, 36] and Vaughan [169] estimate the compliance parameter by scaling down the radius–dependent stiffness modulus of systemic arteries, presented by Olufsen [116] (see Figure 3.1.2),

$$\frac{Eh}{r_0} = k_1 \exp(k_2 r_0) + k_3, \tag{3.1}$$

where $k_1 = 2 \times 10^7 \text{g/s}^2\text{cm}$, $k_2 = -22.53/\text{cm}$ and $k_3 = 8.65 \times 10^5 \text{g/s}^2\text{cm}$.[1] As $C = C(Eh/r_0)$, both studies used this modulus by scaling down the constant k_3 by a factor of 0.3 and 0.5 respectively.

---

[1] $1\text{mmHg} = 1333.333\,\text{g}\,\text{s}^{-2}\text{cm}^{-1}$

3.1.3 Direct measurement of pulmonary compliance

Besides the systemic compliance approach, a number of studies can be found in literature [59, 67, 88, 89, 95, 140, 185, 186], which either study pulmonary compliance or provide data, which may be used to estimate the pulmonary compliance. However, most of these studies are carried out using data obtained from *in vivo* and *ex vivo* experiments on animals and the results reflect sensitivity to the study conditions as the elastic properties of blood vessels change subject to whether they are *in vivo* or excised [167]. One of the major mechanical differences between *in vivo* and *ex vivo* conditions is that *in vivo*, the vessels are longitudinally tethered and surrounded by tissues and they transmit a continuous cardiac activity, which keeps the whole system under constant stress state. On the other hand, only some residual stress is present in the wall tissues of an excised vessel and vessels are largely in a stress–free state and tend to shrink as they are no longer tethered longitudinally or surrounded by tissues.

A few of the above mentioned studies concern human pulmonary vasculature for which the measurements are available both *in vivo* [59, 67], e.g. during open heart surgery and right heart catheterization, and *ex vivo* [185, 186], such as from postmortem lungs. In this regard, however, one of the most comprehensive sets of data was accumulated by Krenz & Dawson [89]. Collected from 26 studies of six different species including human, they used linear fit to a mixture of *in vivo* and *ex vivo* measurements of pressure and diameters on a log–log scale, to propose a very specific pulmonary compliance value of $0.02\,\mathrm{mmHg}^{-1}$.

Below we discuss in detail the methodology and findings of Krenz & Dawson [88, 89], followed by brief discussions on source studies, used by Krenz & Dawson, specifically dealing with human pulmonary circulation.

Krenz & Dawson (2002 & 2003) Some experimental studies [2, 3, 41], conducted on pulmonary vasculature of canine, suggest that despite the variations in vessel wall composition and several orders of magnitude range in vessel diameter throughout the pulmonary circulation, the distensibility of pulmonary vessels is essentially constant and independent of vessel diameter and wall composition. Based on these conclusions Krenz & Dawson published two studies [88, 89], first in a diverging arterial tree of distensible vessels with a common inlet and multiple outlet branches [88] and then in connected trees of diverging arteries and converging venous with a common outflow or inflow pressure [89], to analytically prove that any arbitrary vessel in these trees will receive the same fraction of the total inflow regardless of the total inflow or pressure at the tree inlet. In other words, if F denotes the total inflow to the tree, for each vessel n in the tree there exists a constant f_n such that $F_n/F = f_n$, where F_n represent the flow in the nth vessel. They proved this by assuming a Poiseuille flow profile for every vessel in the tree that obeys the same distensibility relation of the form $D/D_0 = f(P)$. They also assumed that every terminal vessel in the tree has the same terminal pressure and that the viscosity of the blood in an individual vessel remains constant. The analytical proof in the study leads to the conclusion that the compliance of the pulmonary arteries is diameter independent over the several order of magnitude range in vessel diameter, which is unlike the compliance behaviour of systemic arteries [116] (see Figure 3.1.2).

The simple pressure–diameter relation, specific to pulmonary vessels [2], used by Krenz & Dawson [89] is given by

$$\frac{D}{D_0} = 1 + \lambda P, \tag{3.2}$$

where $P = p - p_0$ is the transmural pressure, where, in most experimental studies, p_0 is taken as diastolic pressure [59,67,95]. Also, D_0 is the diameter at zero transmural pressure, which is normally taken as the diastolic diameter. Further, λ (denoted by α in the actual study [89]) is the linear coefficient of distensibility (or compliance) defined as the gradient of fractional change in diameter corresponding to the change in pressure

$$\lambda = \frac{(D - D_0)/D_0}{P} = \frac{D - D_0}{PD_0} \tag{3.3}$$

with the units of mmHg^{-1}.

Using this definition of λ, Krenz & Dawson [89] compiled the data for vessels of various internal diameters from 26 different studies, including five studies related to human beings [59,67,95,185,186], to show that the data is in good agreement with the fitted straight line with a gradient $\lambda = 0.02\,\text{mmHg}^{-1}$ (see Figure 3.2) and inferred that the pulmonary compliance remains constant over large range of diameters. However, a close inspection of Figure 3.2 shows that where the data for other mammalian species show good agreement with the fitted line, the human data seems to be scattering away in most cases and may not show such a good agreement with the fit for the same λ, if plotted alone.

Despite the fact that Krenz & Dawson, in both of their studies [88, 89], ignored the effects of pulsatile flow and non-Newtonian behaviour of the blood in capillaries, it seems reasonable to conclude that the pulmonary compliance is distributed more uniformly than the systemic compliance and that the pulmonary compliance modulus is diameter indepen-

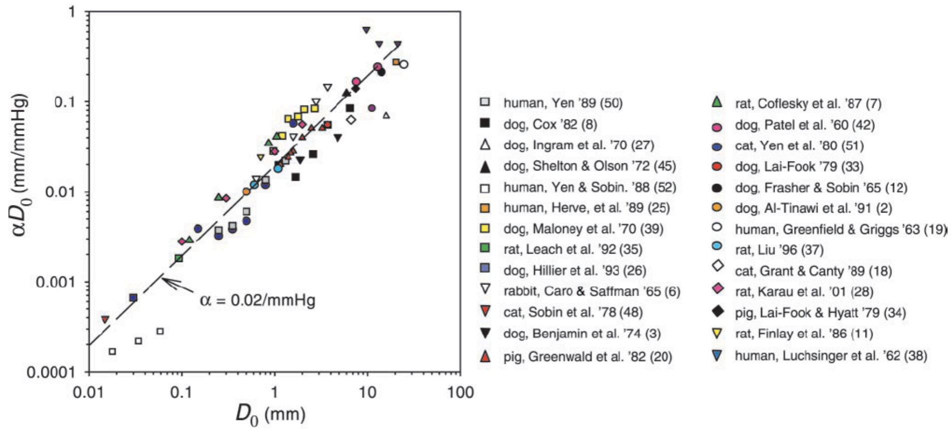

Figure 3.2: Figure (7) by Krenz & Dawson [89] showing the relationship of change in diameter per mmHg pressure rise (αD_0) to the unstressed/diastolic vessel diameter (D_0) measured in isolated pulmonary vessels (arteries, veins, capillaries) in 6 different mammalian species. It should be noted that the same value of λ can be obtained by correlating λP with P instead of λD_0 with D_0.

dent. This conclusion is further supported when we take into account the anatomical and functional differences between systemic and pulmonary circulation and reflect upon the design feature of pulmonary system that stabilises the effect, in the face of large variations in cardiac output (from rest to exercise), on the flow distribution i.e. if the distensibility is a function of vessel diameter it is unlikely that stability could be achieved.

In order to relate λ with $C = C(Eh/r_0)$ in our model, let us rewrite equation (3.2) as

$$\frac{r}{r_0} = 1 + \lambda(p - p_0), \quad \text{with} \quad \lambda = 0.02\,\text{mmHg}^{-1}, \tag{3.4}$$

Also rewriting the equation of state (2.28) gives us

$$\frac{r}{r_0} \approx 1 + \frac{3r_0}{4Eh}(p - p_0). \tag{3.5}$$

Comparing (3.5) with (3.4), we get

$$\frac{Eh}{r_0} = \frac{3}{4\lambda}. \tag{3.6}$$

For $\lambda = 0.02\,\text{mmHg}^{-1}$, we obtain

$$\frac{Eh}{r_0} = 37.5\,\text{mmHg} \approx 0.5 \times 10^5\,\text{g}\,\text{s}^{-2}\text{cm}^{-1}.$$

This value of Eh/r_0 is approximately 17 times smaller than that of k_3 in the systemic stiffness modulus (3.1), which would imply that pulmonary arteries are 17 times more compliant than the systemic arteries, significantly larger than the factor of 2–10 proposed by several *in vivo* studies [49, 59, 120]. Olufsen *et al.* [115] used this values of λ in her structured tree based model of pulmonary circulation and, albeit for a different outflow condition, it leads to a low (3–14 mmHg) and rather featureless pulmonary arterial pressure profile, whereas the typical pulmonary arterial pressure should range from 10–25 mmHg [55, 63]. Thus whereas it is reasonable to conclude a diameter–independent human pulmonary compliance, the absolute value of λ proposed by Krenz & Dawson does not fit with pulmonary circulation models. On the other hand, the value used by Vaughan [169], one half of the systemic compliance, produces a significantly higher systolic (32 mmHg) and pulse (23 mmHg) pressures.

With this in mind, we decide to choose a value of compliance parameter somewhere in the middle so that the simulations performed with our model agree better with the reported pressure range in the literature. In order to do this we first give a brief review of published studies concerning the elastic properties of human pulmonary vessels.

J. C. Greenfield & D. M. Griggs (1963) : One of the earliest studies analysing the pressure–diameter relation in the human MPA is by Greenfield & Griggs [59]. With an aim to get insight behaviour of pulmonary compliance, Greenfield & Grigges tabulated pressure (units of [cmH_2O])[2] and diameter [cm] measurements (along with heart rate, diagnosis, weight (kg) and age) of *in vivo* MPA of 11 patients during open heart surgery. Three of these patients were suffering from Pulmonary Hypertension (PH) whereas the other 8 patients had normal pulmonary function. By using these measurements they computed the pressure–strain elastic modulus, given by $E_p = \Delta P R_0 / \Delta R \, (\approx \lambda^{-1})$, to analyse the distensibility (units of [cm(cmH_2O)$^{-1}$]) of the MPA. They also published a figure (see Figure 3.3) that reveals some of the shape features of normal pulmonary pressure pulse and demonstrates the remarkable similarity between radius and pressure pulsations.

The analysis in this work draws some useful conclusions. Firstly, it was found that the normal pulmonary artery appears to be about five times as distensible as the ascending aorta. The mean change in the area of the MPA (22.9%) during the cardiac cycle was found more than twice of that in the ascending aorta (11%) obtained using the same experimental technique. It was also observed that *in vivo* area change in the MPA was less than that of excised pulmonary artery of man [104], which suggests that pulmonary

---

[2] $1\,\mathrm{cmH_2O} = 1.3556\,\mathrm{mmHg}$

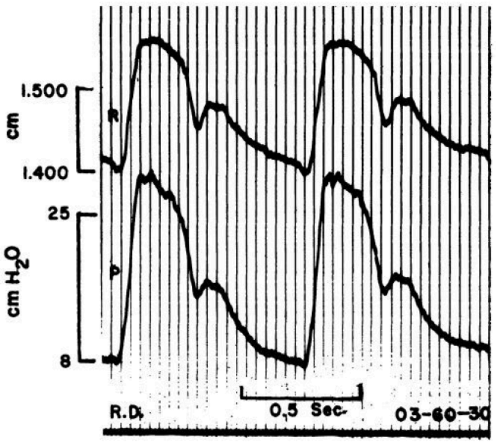

Figure 3.3: Figure (2) taken from Greenfield & Griggs [59] showing a remarkable similarity between lateral intravascular pressure and radius of MPA.

arteries are relatively stiffer *in vivo* than they are *ex vivo*. The data published in this study is also used by Krenz & Dawson to estimate the pulmonary compliance behaviuor and we have also utilised this data to estimate λ for the MPA.

Philippe Herve *et al.* (1989) : Published in 1989 by Philippe Herve and collaborators, this study was originally meant to understand the effects of Almitrine[3] on the pulmonary distensibility with a stated hypothesis that Almitrine decreases the pulmonary distensibility of large pulmonary arteries in man. Although the focus of this paper is disease related, it provides a good set of data from 9 patients, known not to suffer from any pulmonary condition, before and after using Almitrine. The diameters [mm] and pressures [mmHg] were measured *in vivo* in all patients in supine position by using cinefluroscopic and catheterization techniques. The complete data, tabulated in the paper, shows a mean distensibility (λD_0) of 0.27 for the RPA only. Used by Krenz & Dawson, we also choose to use these measurements to predict the slope of linear pressure–diameter relation for the RPA.

---

[3] A drug used to improve the ventilation–perfusion matching under a pulmonary condition.

Ref.	Vessel	P (sys.) mmHg	P_0(diast.) mmHg	D (sys.) cm	D_0 (diast.) cm
Greenfield & Griggs [59]	MPA	20.0	6.00	3.2	2.8
		21.8	4.60	3.9	3.3
		22.1	5.40	3.3	2.9
		28.0	12.3	3.4	2.9
		18.0	6.00	2.3	2.3
		19.9	12.0	2.7	2.5
		16.5	7.10	2.5	2.3
		21.0	11.3	2.5	2.3
Mean ± S.D.		20.9 ± 3.2	8.1 ± 3.2	3.0 ± 0.5	2.7 ± 0.4
P. Herve *et al.* [67]	RPA	15.0	3.00	2.3	2.0
		28.0	7.00	2.7	2.1
		27.5	10.0	3.0	2.5
		30.0	15.0	2.6	2.3
		24.0	12.0	2.7	2.4
		22.0	12.0	2.3	2.2
		20.0	9.00	2.6	2.3
		20.0	9.00	2.8	2.4
		22.0	8.00	3.1	2.5
Mean ± S.D.		23.2 ± 4.7	9.4 ± 3.4	2.7 ± 0.3	2.3 ± 0.2
Combined average	± S.D.	22.1 ± 4.2	8.8 ± 3.3	2.8 ± 0.4	2.5 ± 0.4

Table 3.1: *In vivo* measurements of systolic and diastolic pressures and corresponding diameters of the MPA and RPA from the literature. The values of pressure and diameter are presented after making the units consistent with mmHg and cm, respectively.

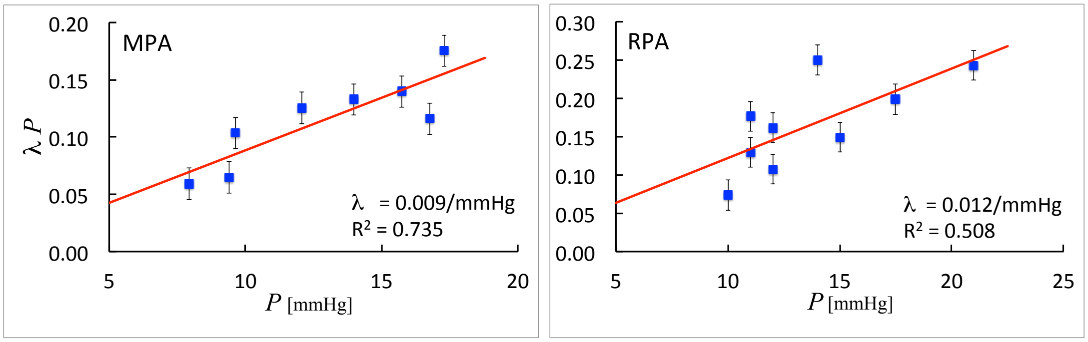

Figure 3.4: An estimation of coefficient of compliance, λ, for the MPA (from [59]) and RPA (from [67]), by using the values given in Table 3.1. A linear regression is fitted for $\lambda P \pm$ S.E. that shows a very similar value of λ for both vessels.

Estimating λ for the MPA and RPA

Table 3.1 presents the *in vivo* pressure and diameter measurements given in [59] and [67]. For the case of the MPA, we ignore the measuerments of three patients suffering with pulmonary hypertension. After making the units consistent (mmHg and cm) we compute λ for every single patient. It is observed from the table that the average pressure ranges from approximately 8–21 mmHg in the MPA and from 9.4–23 mmHg in the RPA, whereas a combined average of approximately 9–22 mmHg is observed for these vessels. A regression line is then fitted for individual groups to $\lambda P \pm$S.E vs P to estimate λ both for the MPA and RPA. As shown in Figure 3.4 that the RPA is slightly more compliant ($\lambda = 0.012\,\text{mmHg}^{-1}$) than the MPA ($\lambda = 0.009\,\text{mmHg}^{-1}$), however, R^2 is also lower in the case of RPA than that of MPA. We discuss these findings further in the next sections along with some other values of λ proposed for different diameter ranges.

R. T. Yen & S. S. Sobin (1988) and R. T. Yen *et al.* (1990) : Yen & Sobin [186] studied elasticity of non-capillary microscopic vessels of diameter $< 100\mu$m (0.01 cm) in human pulmonary vascular beds by using the measurements from three postmortem lungs of healthy young individuals. Later, Yen and coworkers [185] also analysed elastic properties of pulmonary arterial vessels, with diameters ranging from 200–1600 μm (0.02–0.16 cm), and pulmonary venous vessels with diameters in the range of 100–1200 μm (0.01–0.12 cm). The measurements for the later study were obtained from three postmortem lungs, different from the previous study [186]. In the first study, both for the arteries and the veins, they estimated λ (with units of [μm(cmH$_2$O)$^{-1}$]) by linearly correlating vessel diameter [μm] with transmural pressure ($p - p_0$) (units of [cmH$_2$O]) [186]. In the later study they estimated λ (with units of [$\mathrm{cmH_2O^{-1}}$]) as the slope of linear relationship between the fractional change in vessel diameter and the transmural pressure. To the best of our knowledge, these are the only most detailed studies available in the literature, which provides a good picture of elastic behaviour of the excised pulmonary vessels and therefore have also been used by Krenz & Dawson [89].

Data source	Vessel type	D_0 (cm)	λ ($\mathrm{mmHg^{-1}}$)	Eh/r_0 (mmHg)	Eh/r_0 $\times 10^5$ ($\mathrm{g/s^2cm}$)
Figure 3.4, (right)	MPA	2.7	0.009	83	1.11
Figure 3.4, (left)	RPA	2.3	0.012	63	0.84
[185]	Arterioles	0.16–0.10	0.009	83	1.11
		0.10–0.06	0.009	83	1.11
		0.06–0.04	0.006	125	1.67
		0.04–0.03	0.007	107	1.43
		0.03–0.02	0.008	94	1.25
[186]	non– cappillaries (arterial)	0.006	0.002	375	5.00
		0.003	0.003	250	3.33
		0.002	0.005	150	2.00
Mean			0.007	141	1.89
[185]	Venules	0.12–0.08	0.005	150	2.00
		0.08–0.04	0.006	125	1.67
		0.04–0.02	0.009	83	1.11
		0.02–0.01	0.013	58	0.77
[186]	non– cappillaries (venous)	0.006	0.003	250	3.33
		0.003	0.005	150	2.00
		0.002	0.007	107	1.43
Mean			0.007	132	1.76
Mean	(all vessels)		0.007	137.5	1.83

Table 3.2: Estimation of linear distensibility parameter adopted from literature [185, 186] and approximated by using available data (see Figure 3.4).

3.2 Choice of λ

Based on the findings and data available from the studies discussed above, we summarise the values of λ [mmHg^{-1}], after making the units consistent, in Table 3.2. Except the MPA and the RPA, all other values are taken directly from literature and they belong to *ex vivo* studies. The last two columns illustrate the stiffening of blood vessels, where values of Eh/r_0 are converted from λ by using equation (3.6). From Table 3.2, one may observe the overall trend of compliance distribution across human pulmonary arterial and venous tree.

It seems that the compliance of largest pulmonary arteries remains almost constant above a diameter of 0.06 cm, except for the RPA which is more compliant than other vessels in this range but also has a smaller R^2 value than the MPA in Figure 3.4. Below $D_0 = 0.06$ cm, the vessels get stiffer in the diameter range 0.06–0.04 cm. However, further below this point the compliance increases again and smaller arteries (arterioles) become very compliant at $D_0 = 0.02$ cm again. At the non–capillary level, the smallest vessels are observed to be stiffer than the larger arteries but at this level too the compliance keeps increasing down the tree, a similar pattern observed for vessels in diameter range 0.06–0.02 cm.

As for the venous side, unfortunately, no data was available for the four largest pulmonary veins opening into the left atrium which means that we have to estimate the compliance values for these vessels. However it can be observed from the table that the smaller veins (venules), in diameter range of 0.12–0.01 cm, are more compliant than the larger veins. Although the venous vessel at the non–capillary level are more compliant than their arterial counterparts in the similar diameter range, the general trend of compliance at this level remains same i.e. vessels are stiffer than the larger vessels but become compliant towards capillaries. Moreover, the averaged value of $\lambda = 0.007\,\text{mmHg}^{-1}$ (or $Eh/r_0 = 138$ mmHg) is same for both arterial and venous sides and it appears specific to human pulmonary vasculature. This value is less than half of that proposed by Krenz & Dawson [89] (i.e. $\lambda = 0.02\,\text{mmHg}^{-1}$) yet significantly larger than the systemic compliance, about five times.

Ideally, we should be able to simulate reasonable pressure and flow profiles by assigning the compliance values, given in Table 3.2, to the vessels belonging to corresponding diameter ranges in the model. Unfortunately, this approach does not work as the resulting pressure and flow profiles appear to be either too chaotic to be termed as physiological or the numerical solution fails to converge in some cases. This leaves us with no choice but to make some adjustments in the parameter values and perform trial simulations to obtain physiological pressure and flow waveforms.

Since the arterial and venous structured trees are joined together when $r_{\min} = 0.005\,\text{cm}$ ($\text{D}_0 = 0.01\,\text{cm}$), the observations from [186] about non–capillary arterial and venous vessels are not directly applicable in this study. Also from Table 3.2, based on a comparatively low accuracy of the linear fit for RPA, if we ignore the compliance difference of the RPA then the overall compliance of the pulmonary arteries above $\text{D}_0 = 0.06\,\text{cm}$ becomes constant. Further, based on the averaged compliance behaviour, we assume the same compliance distribution for arterial and venous sides. Finally, we stick with the radius–independent compliance value and keep λ uniform for both arteries and veins but different for large and small vessels.

Besides the compliance parameter C, the other parameters of interest are $r_{\min}$, ξ, γ, l_{rr_A} and l_{rr_V}. These parameters are chosen as described in Section 2.1.2, i.e. $\xi = 2.76$, $\gamma = 0.41$, $l_{\text{rr}_A} = 15.75\,\text{cm}$, $l_{\text{rr}_V} = 14.51\,\text{cm}$ and $r_{\min} = 0.005\,\text{cm}$. However, the simulations are also very sensitive to $r_{\min}$, so where appropriate, we vary $r_{\min}$ a bit in combination with compliance for the purpose of trial simulation. Thus keeping ξ, γ, l_{rr_A} and l_{rr_V} fixed, we select 9 different combinations of parameter values for $r_{\min}$, λ_{large} and λ_{small} and divide them in three general groups A, B, and C. The grouping is done based on how the compliance of large and small vessels is different, e.g. in group A the large vessels are more compliant than the small vessels, a generally observed phenomenon in the systemic arteries, whereas the λ for small vessels is forced to be consistent with some of the values in the literature. This is opposite in group B and C where large vessels are stiffer than the small ones but the base value of λ in Group C is smaller than Group B. All these values are presented in Table 3.3 along with C– and s–ratios in columns 6 and 9 representing the ratio of large to small compliance and stiffness, respectively.

3.2.1 Results

We run our numerical code for 9 combinations given in Table 3.3 by solving the system of equations (2.100)–(2.103) with a the two–step Lax–Wendroff scheme at a temporal resolution of 4096 per cardiac cycle. The results for pressure and flow–rate waveforms are plotted for the MPA and RSV at proximal, midpoint and distal locations over one cardiac cycle.

Group	No.	r_{min} (cm)	λ_{large} (mmHg^{-1})	λ_{small} (mmHg^{-1})	C–ratio	$(\frac{Eh}{r_0})_{\mathrm{large}}$ (mmHg)	$(\frac{Eh}{r_0})_{\mathrm{small}}$ (mmHg)	s–ratio
A	1	0.005	0.040	0.009	4.44	18.7	78	0.24
	2	0.001	0.020	0.006	3.33	37.5	123.8	0.30
	3	0.005	0.009	0.002	4.50	82.5	375	0.22
B	4	0.200	0.020	0.33	0.06	37.5	2.3	16.3
	5	0.050	0.011	0.10	0.11	67.5	7.5	9.00
	6	0.007	0.009	0.10	0.09	82.5	7.5	11.0
C	7	0.005	0.0051	0.03	0.17	146.25	26.5	5.52
	8	0.005	0.0043	0.02	0.21	176.25	37.5	4.70
	9	0.005	0.0038	0.02	0.19	195.00	37.5	5.20

Table 3.3: A selection of three groups (A, B & C), each consisting of three distinct sets of parameter values with main focus on the variability of the stiffness of both small and large vessels. λ is the distensibility parameter whereas Eh/r_0 is the stiffness parameter involved in our calculation through the tube–law. The C–ratio and the s–ratios are respectively the ratios of large vessel distensibility and stiffness to those of small vessels. After experimental simulations a single set of values (C(9)) is proposed as the normal physiological values for our model of pulmonary circulation.

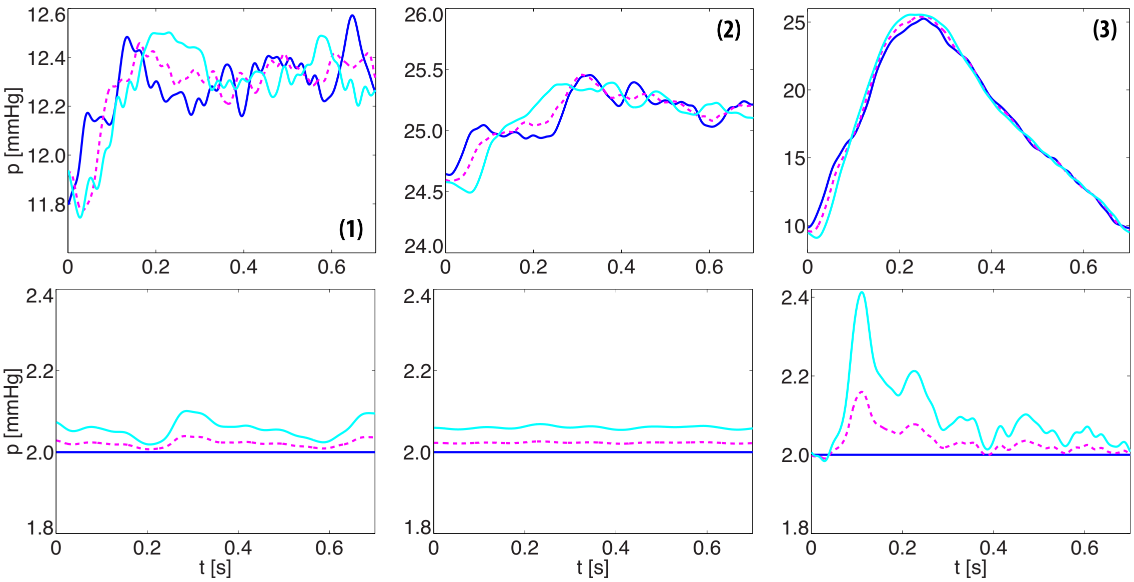

Figure 3.5: Pressure in the MPA (top) and RSV (bottom) corresponding to three sets in Group A given Table 3.3. The pressure is predicted at three different locations, at the vessel inlet (solid blue), the midpoint (dashed magenta) and at the end of both vessels (solid cyan).

Group A : Figures 3.5 and 3.6 show the pressure and flow–rate profiles corresponding to the combinations in group A. For combinations A(1) and A(2), we have kept large vessels about 3–4 times more compliant than the small ones but also keeping the large vessels more compliant than the generally observed compliance (0.04 & 0.02 vs 0.009) at the same time. As a result, both pressure and flow waveforms in the MPA are extremely chaotic and their appearances is far from being physiological. The panels corresponding to combination A(3), however, show very different behaviour. As observed from the figure, the pressure in the MPA ranges from 10–25 mmHg, agrees almost perfectly with the pressures reported in the literature [55, 63], but the pressure profiles at all locations are extremely smooth and featureless and do not share any of the shape features observed in Figure 3.3. This may be due to significantly stiffer large and small vessels and the highest C–ratio within this group. Furthermore, for A(3), the corresponding flow and pressure in the MPA and RSV, respectively, show some unusual oscillations whereas the shape of flow waveform in the RSV looks more like arterial pressure. If we only stick to the criterion of agreement of arterial pulse pressure with that of experimental studies, then the values in A(3) may be the most appropriate choice for this study.

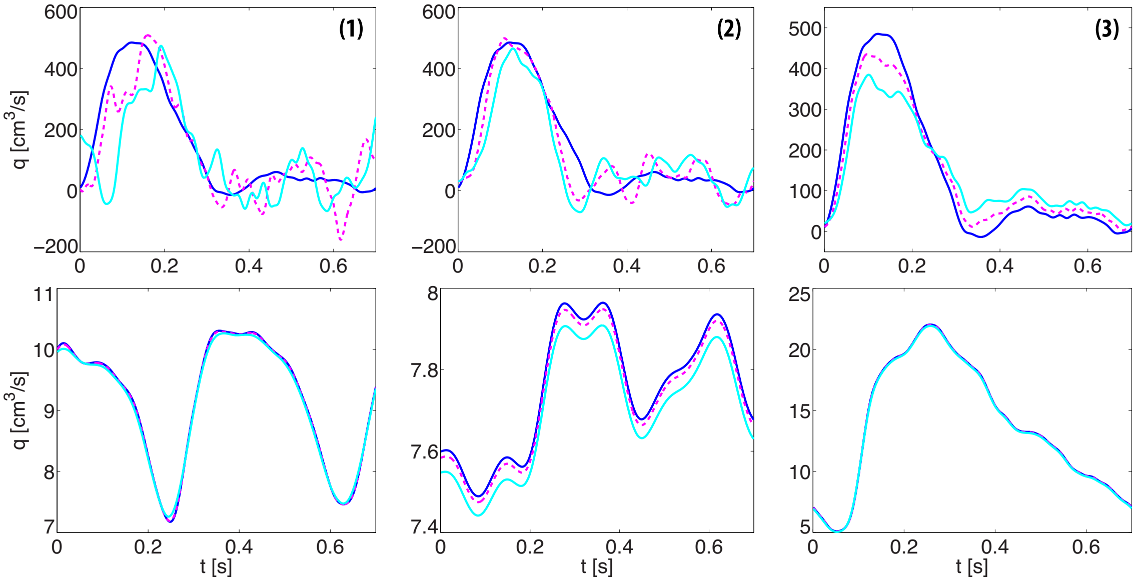

Figure 3.6: Predicted volume flow–rate in the MPA (top) and RSV (bottom) corresponding to three sets in Group A given Table 3.3. The flow is predicted along three positions, at the vessel inlet (solid blue), at the midpoint (dashed magenta) and at the end of both vessels (solid cyan).

Group B : In Figures 3.7 and 3.8 we predict the pressure and flow–rate for the combinations of values given in group B. In terms of C–ratio, for two cases, B(4) and B(6), we maintain highly compliant large vessels by keeping λ_{large} similar to those in group A, but unlike group A, we make smaller vessels extremely compliant, in fact about 16 times more compliant than the larger vessels. This is an exaggeration of the pattern when smaller vessels are more compliant than the larger ones. The purpose of doing this is to observe the other extreme and then look for something in the middle.

It can be observed from theses figures that the pressure profiles are much more consistent than those in group A but initially show a much lower pressure than expected (3–9 mmHg for B(4)). However, the pressure increases gradually as the large vessels are made stiffer. It must be noted though, for these choices of compliance values we have to compromise for the value of $r_{\min}$, as $r_{\min}$ varies the most in group B. As far as the shape is concerned, the pressure profiles look more like flow–rate profiles with an amplified second peak during diastole. Again by increasing the stiffness of large vessels the shapes change a little, but still look very different than the physiological shape of pressure waveform. Analysing the flow waveforms in Figure 3.8, we observe that, unlike group A, the deviations in the compliance parameters hardly affect arterial and venous flow and they behave

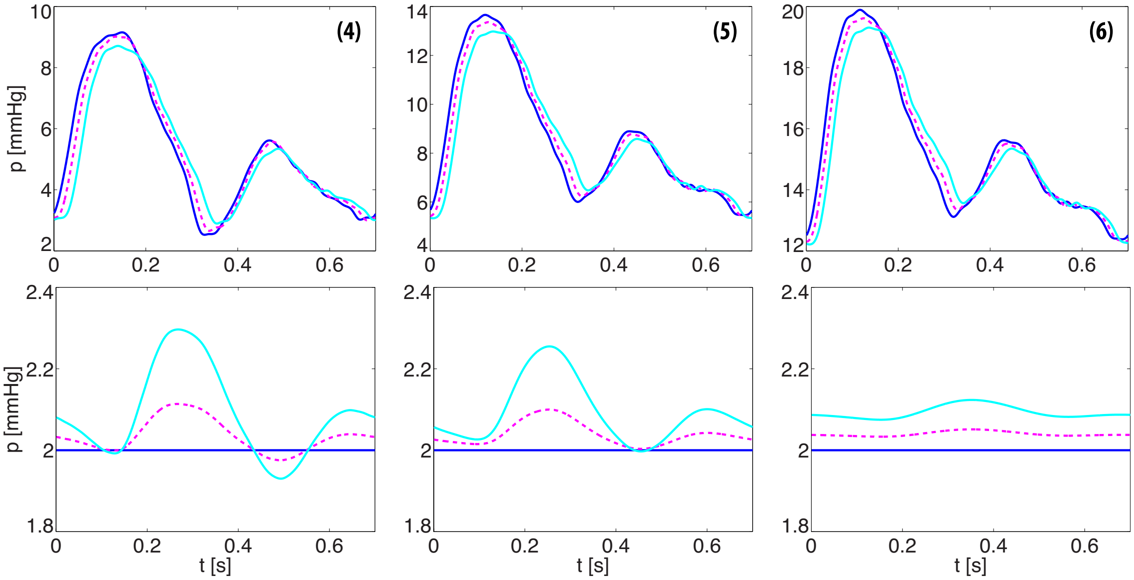

Figure 3.7: Pressure in the MPA (top) and RSV (bottom) corresponding to the sets in Group B given Table 3.3. The pressure waveforms are simulated along three different positions in both the vessels, i.e. at the proximal end (solid blue), the midpoint (dashed magenta) and the the distal end (solid cyan).

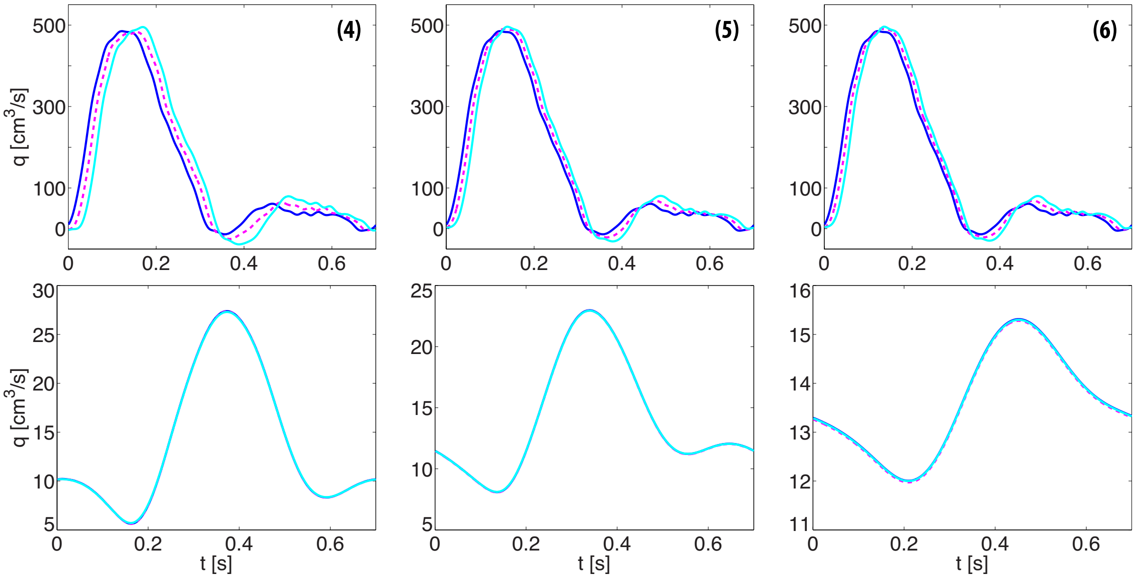

Figure 3.8: Flow rate in the MPA (top) and RSV (bottom) corresponding to three sets in Group B given Table 3.3. The flow is evaluated at three locations in both vessels, i.e at the proximal end (solid blue), the midpoint (dashed magenta) and the the distal end (solid cyan).

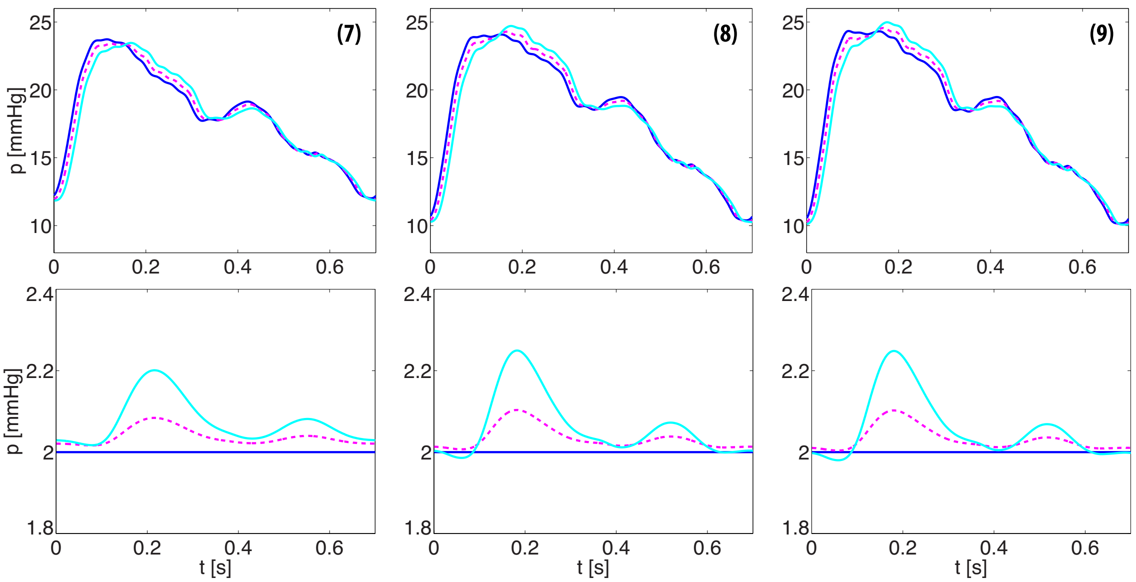

Figure 3.9: Pressure profiles corresponding to different compliance values stated in Group C of Table 3.3 for the MPA (top row) and the RSV (bottom row). The results are plotted at proximal (solid blue), midpoint (dashed magenta) and distal ends (solid cyan) of both vessels.

very consistently.

Group C : Finally we run our numerical code for combinations 7–9 in group C to simulate pressure and flow in the MPA and RSV. Taking into account the outcomes of group A and B, which suggest (a) the large vessels should be stiffer than the small vessels and (b) increasing stiffness of large vessels, while maintaining a suitable C–ratio, improves both shape and magnitudes of pressure waveforms, we make both large and small vessels stiffer by maintaing a C–ratio $= 0.2$. As seen from Figures 3.9 and 3.10, this is by far the most well behaved group that allows us to run all the simulations, for all three cases, with a fixed $r_{\min} = 0.005\,\text{cm}$. The results from C(8) and C(9) show that not only we achieve a physiologically observed pressure range of 10–25 mmHg but also the shape features are very similar to those observed in *in vivo* MPA pressure waveform [59].

As for the veins, although we do not have any physiological venous pressure waveform, the simulated pressure waveforms for RSV are also consistent for the value given in this group. The same holds for both arterial and venous flow wave forms.

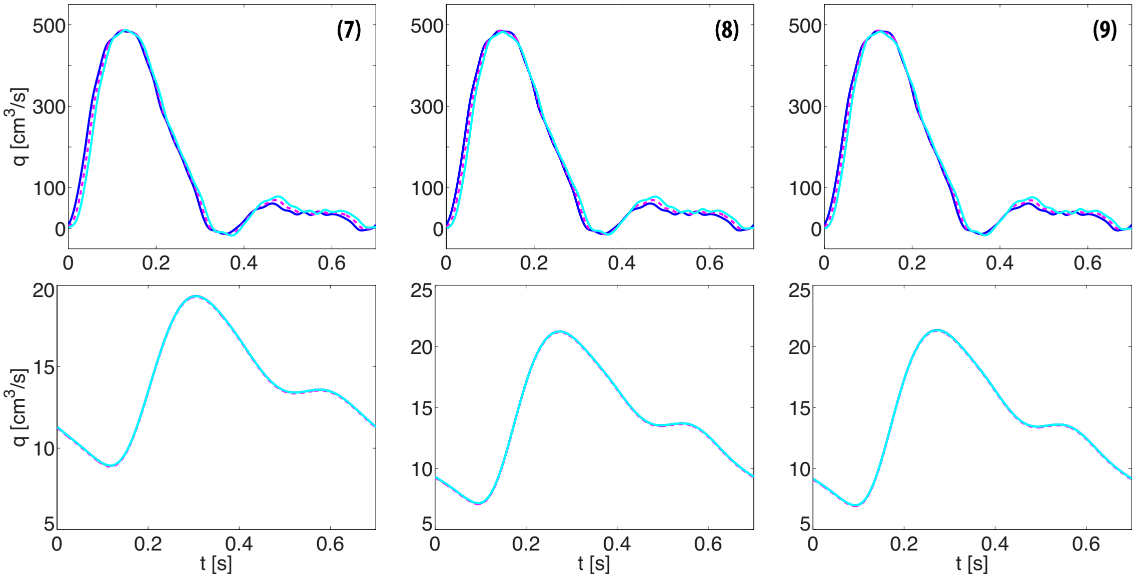

Figure 3.10: Flow–rate simulations in the MPA (top) and RSV (bottom) corresponding to three sets in Group C given Table 3.3. The flow is predicted along three positions, at the vessel inlet (solid blue), at the midpoint (dashed magenta) and at the end of both vessels (solid cyan).

3.3 Discussion

From these results, we observe that the compliance of pulmonary vessels is indeed one of the most influencing parameters in our model. We note that despite the fact that the small vessels are outside the computational domain, their compliance is a key determinant of pressure waveforms in the large vessels, which testify the role of peripheral vessels on upstream haemodynamics and highlights the need of including the effects of these vessels in a circulation model through physiology based dynamic boundary condition.

After examining all the options in Table 3.3, we conclude that for this study it is appropriate to choose the parameter combination C(8) or C(9) to represent the normal physiological case. It should be noted that these simulations are obtained for the values of $\lambda_{\text{large}} \approx 0.004$, which is significantly smaller than the observed $\lambda = 0.009\,\text{mmHg}^{-1}$ for the MPA, and $\lambda_{\text{small}} = 0.02$, the value proposed by Krenz & Dawson [89]. Moreover, the predicted pressure through this group is closest to the suggested pulmonary pressures in the literature i.e. 10–25 mmHg [55, 63], and the averaged pressure range calculated from data in Table 3.1, which is 8.8–22.1 mmHg.

Moreover, our simulations look much better when compared with the predicted pressure waveforms from other structured tree based models of human pulmonary circulation given

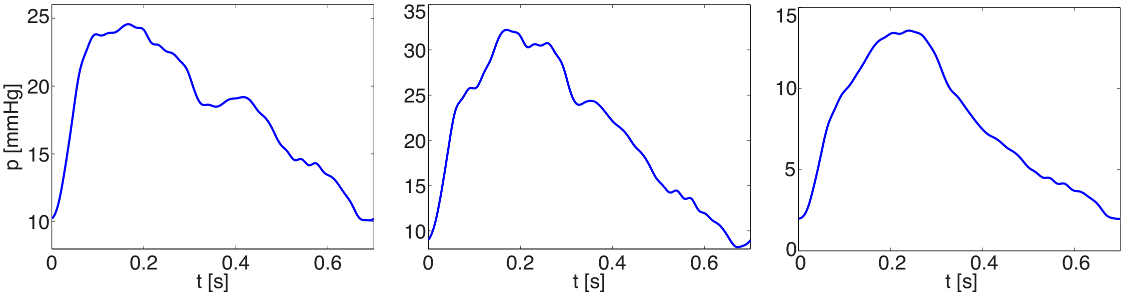

Figure 3.11: Pressure wave simulation over one cardiac cycle at the midpoint in the MPA from three different pulmonary models, all based on a structured tree related boundary condition. Left: waveform simulated through our model using C(9) in Table 3.3, Middle: by Vaughan [169] and Right: by Olufsen *et al.* [115].

by Vaughan [169] and Olufsen *et al.* [115]. As shown in Figure 3.11, Vaughan predicted 10–33 mmHg of pressure in the MPA, measuring a much higher pulse pressure of 23 mmHg. Also the predicted pressure given by Olufsen *et al.* [115] is much lower, ranging between 3–14 mmHg. As for the shape, the behaviour of our predicted pressure profile shares most features of *in vivo* measured pressure waveform presented by Greenfield & Griggs [59] (see Figure 3.12), whereas the pressure profile put forward by Vaughan shows a prominent, and clinically significant, left shoulder (or point of inflection) in the early systole. While, on the other hand, due to a high compliance value throughout the system Olufsen's wave profile is rather smooth and featureless and predicts a low blood pressure. Finally, although we partially adopted Clipp & Steele's approach [36] to determine compliance value for our model, our simulations are not exactly comparable to them as their study deals with pulmonary circulation of sheep with specific focus to study effects of respiration on the pulmonary pulse wave.

3.4 Conclusion

Based on discussion, we can conclude this chapter by selecting a set of parameter values that predict pressure waveforms, which share most features of the pulmonary pressure pulse from the literature. In this chapter, we also observe that the suggested value of $\lambda = 0.02\ \mathrm{mmHg}^{-1}$ by Krenz & Dawson [89] for the entire pulmonary system is too large for our study (about 17 times than the systemic arteries) and does not conform with the suggested relative approximations of pulmonary arterial compliance [49, 59, 120] i.e.

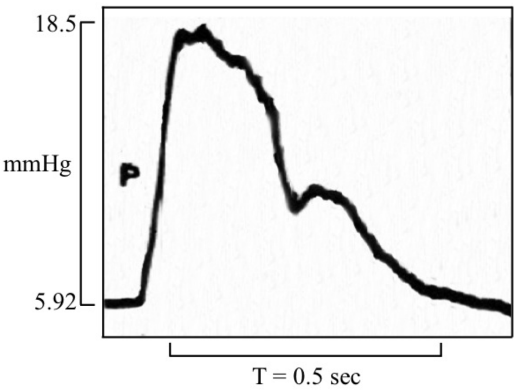

Figure 3.12: The pressure profile in the MPA, published by Greenfield & Griggs [59]. Cropped and modified for the purpose of comparison.

pulmonary arteries are 2–10 times more compliant than the systemic arterial compliance, significantly less than the factor of 17. This difference may be due to the fact that mechanical properties of blood vessels change when they are excised [167], whereas Krenz & Dawson use all sort of data that result in this value. However, most studies agree with a uniform compliance distribution at different levels of the pulmonary system suggesting a constant compliance parameters both for large and small vessels. Consequently, a constant compliance parameter is used by taking $(Eh/r_0)_{\text{large}} = 195\,\text{mmHg}$ $(2.6 \times 10^5\,\text{g}\,\text{s}^{-2}\text{cm}^{-1})$, which is approximately the same value chosen by Clipp & Steele [35, 36] after scaling k_3 in the radius dependent systemic compliance modulus and $(Eh/r_0)_{\text{small}} = 37.5\,\text{mmHg}$ $(0.5 \times 10^5\,\text{g}\,\text{s}^{-2}\text{cm}^{-1})$, the value proposed by Krenz & Dawson [89]. In the absence of published data for the elastic properties of the pulmonary veins, we use the same value for pulmonary arterial and venous vessels. Moreover, the sudden transition between two compliances is more of a model requirement than the true physiological behaviour, which limits the use of these values to this model only and may not necessarily provide good results in other structured tree based models. Nevertheless, these values give simulated pressure waveforms consistent with the physiological pressure range [59, 63, 67] and shape [59] and enable us to improve the existing results given by Vaughan [169].

Chapter 4

Simulating The Normal Pulse and Applications To Disease Conditions

In this chapter we present the results of pressure and flow waveforms for a healthy young subject, whose measured vessel diameters are given in Table 2.1, followed by results for computational models of pulmonary hypertension. While vessel geometries and inflow into the MPA were partially obtained from measurements, other quantities such as density, viscosity, and scaling ratios, were determined from literature values. The system of equations (2.100)–(2.103) is solved by a two–step Lax–Wendroff scheme at temporal resolutions of 4096 in order to predict the pressure and flow–rate waveforms in the large arteries and veins subject to the set of normal physiological parameters values concluded in Chapter 3. Finally, this new pulmonary model is applied to analyse four clinical conditions associated with pulmonary hypertension, viz. pulmonary arterial hypertension (PAH) associated with increased resistance and stiffening of pulmonary arterioles and venules, pulmonary venous hypertension (PVH) triggered by increased left atrium (LA) pressure due to a left heart condition, vascular remodelling associated with hypoxic lung disease (HLD) and chronic thromboembolic pulmonary hypertension (CTEPH) represented by increased stiffness of the large pulmonary arteries. We also analyse the effects of pulmonary hypertension combined with right ventricular dysfunction (RVD) by modifying our model to read the time varying pressure at the system inlet, instead of the MRI flow–rate, as the inflow boundary condition.

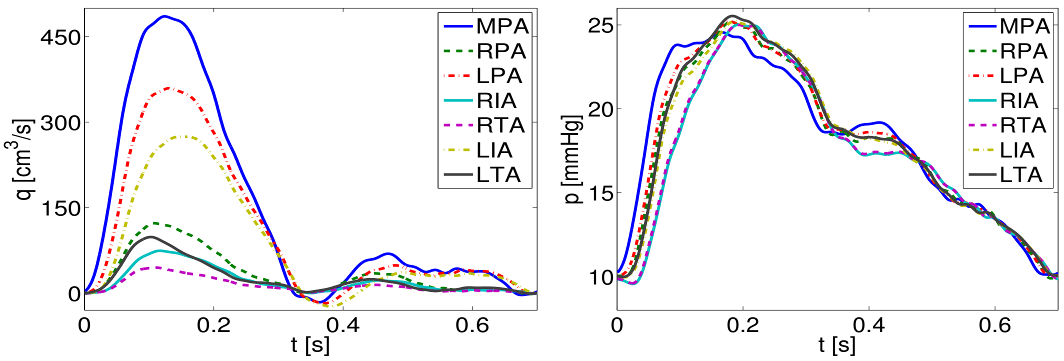

Figure 4.1: Distribution of flow (left) and the propagation of pressure wave (right) through the tree of large arteries over one cardiac cycle. The waveforms are predicted at the midpoint in each artery.

4.1 Normal case

The arterial side

Figure 4.1 shows the flow partitioning and the pressure wave propagation through the large arterial tree. The waveforms are plotted at the midpoint of each artery over one cardiac cycle. In the first panel, it is observed that the the blood volume is distributed such that the arteries with larger inlet cross–sectional area receive more volume flux than those with the smaller cross–sectional area. Moreover, the flow behaviour in all the arteries maintains the key features of imposed MRI measured inflow profile such as the maximum volume flux during systole and minimal during diastole. However, a small retrograde flow is observed at the end of systole in the MPA and the vessels bifurcating from it, i.e the RPA and LPA, which disappears in the vessels after second bifurcation in the tree (RIA, RTA, LIA, LTA). This may be due to the closure of pulmonary valve and seems not to propagate too far in the system. Also the flow during diastole in all vessels is influenced by wave reflections originating from the junctions and periphery vessels.

The second panel in Figure 4.1 depicts the simultaneously predicted pressure wave, which reveals the effects of wave propagation throughout the tree. It is observed that the foot of the pressure wave, at the beginning of systole, propagates forward in time as it arrives slightly late in the distal vessels whereas the peak pressure not only propagates forward but also increases towards the distal locations in the tree. The peaking of pressure is due to the effect of vessel's taper and positive wave reflections in the microcirculation whereas the wave propagation is an attribute associated with the normal physiology of the

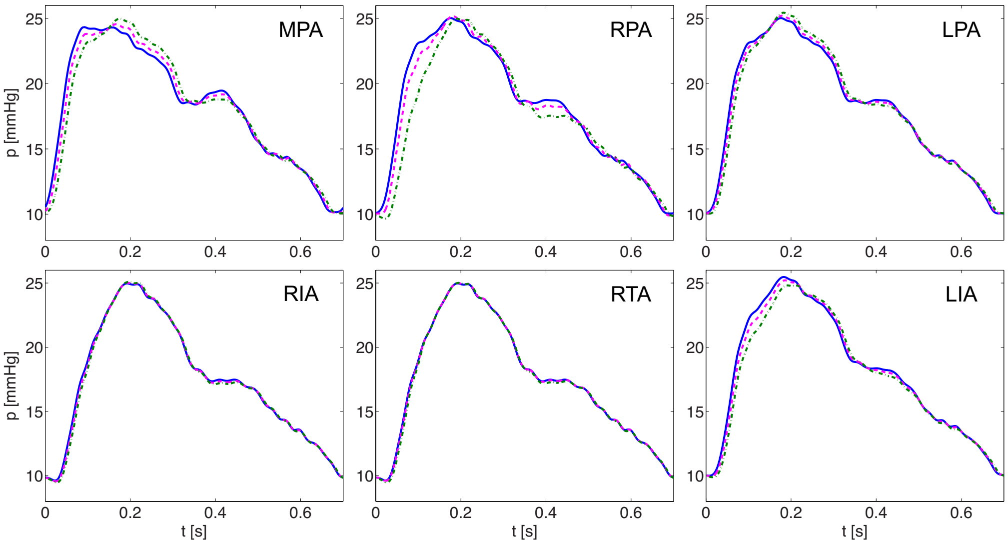

Figure 4.2: Predicted pressure at three locations along the large arteries. For each artery, pressures are evaluated at the vessel inlet (solid blue), at the midpoint (dashed magenta), and at the end (dashed-dot green).

pulse wave. In diastole, a very pronounced dicrotic notch, giving rise to a local minimum, appears in the proximal vessels but tends to fade away with distance and become more like a point of inflection in the distal arteries. The dicrotic notch corresponds to the negative flow–rate at the end of systole and thus indicate the moment the pulmonary valve closes to begin diastole.

In order to have a closer look at the behaviour of pressure and flow–rate along individual arteries, we plot these waveforms separately for the first six arteries in Table 2.1. Figures 4.2 and 4.3 show the predicted pressure and flow at three locations along the MPA, RPA, LPA, RIA, RTA and LIA. In Figure 4.2, the pressure in the large arteries range from about 10–25 mmHg. Moreover, slight differences in peak pressure and arrival time for the reflected waves can be observed between proximal and distal ends of the MPA, RPA and LIA while no significant difference can be observed in the LPA, RIA and RTA. The visible increase in pressure in the distal MPA and LPA suggests that vessel tapering plays a role despite the fact that pulmonary vessels are more compliant and shorter compared to their systemic counterparts. Moreover, in the case of the LPA, we observe limited effects of wave propagation because the LPA is short (2.5 cm). Similarly, RIA and RTA are too short for wave propagation to be effective and the transmission of pressure is almost instantaneous along these vessels.

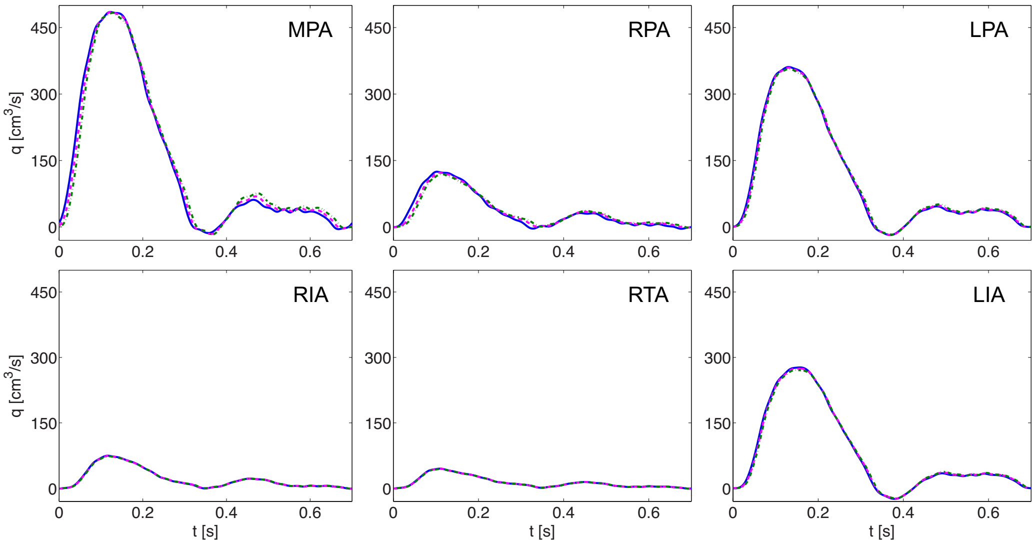

Figure 4.3: Simulated flow at three locations along the large arteries. For each artery, flow and pressure are evaluated at the vessel inlet (solid blue), at the midpoint (dashed magenta), and at the end (dashed-dot green.)

As for the flow in these arteries, very little change is observed with distance along individual vessels, but the differences in geometry between the left- and right-sided vessels lead to a greater flow in the LPA and LIA than in the RPA, RIA and RTA. For instance, a significantly greater flow enters the LPA compared to the RPA, because the diameter of the LPA in this subject is significantly larger than the RPA (1.8 vs. 2.2 cm). Moreover, for LIA, RIA and RTA, since tapering is minimal and no side branches are included within these three vessels, the flow does not vary significantly among the three locations within each vessel.

The venous side

In Figure 4.4, we predict the blood flow distribution and the pressure wave behaviour at the midpoint of four largest veins (RIV, RSV, LIV, LSV). Just like the arteries, the veins geometry plays an important role in the blood volume distribution, and the vein with the largest distal cross–sectional area (LIV with $A = 2.8\,\mathrm{cm}^2$) receives the greatest flux, $q \approx 150\mathrm{cm}^3/\mathrm{s}$. However, unlike the arteries, the flow in the veins is much smoother and the maximum flux passes through the veins during diastole, during which flow from the veins fills the left–atrium (LA). As for the pressure, the magnitude and variations in the pressure are low and the pressure in all four veins either oscillates about the constant fixed pressure or shows a biphasic profile with two maxima.

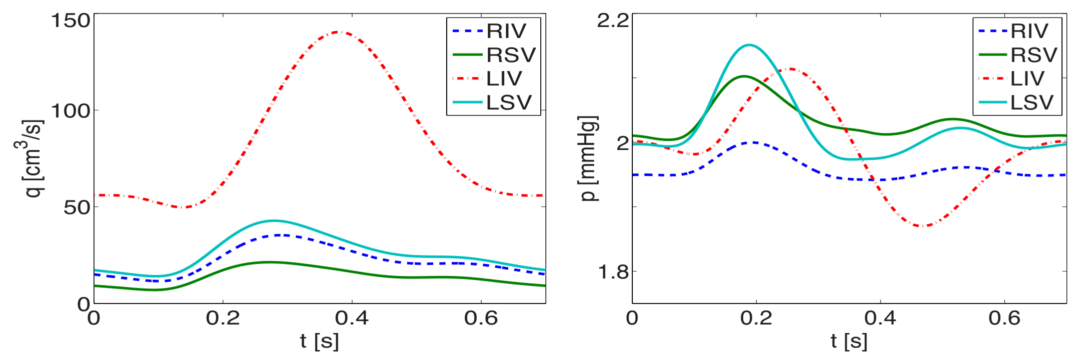

Figure 4.4: Flow partitioning (left) and the pressure wave simulations (right) in the large veins. The waveforms are predicted at the midpoint in each vein over one cardiac cycle.

A more detailed picture of pulmonary venous haemodynamics is given in Figure 4.5, which shows the pressures and flow waveforms along three positions in all four veins. The four panels in the top row show the venous pressure dynamics. Also depicted in Figure 4.4, we observe that the pressures in RIV, RSV and LSV are biphasic and the LIV pressure oscillates about 2 mmHg, the constant right atrial pressure specified in the model. In the RSV and LSV, the pressure remains above 2 mmHg, however the maximum pressure variation is only about 0.4 mmHg in the LIV and LSV. The geometry may also explain different oscillatory pressure behaviour observed in veins.

The second row in Figure 4.5 shows the venous flow–rate waveforms. It can be seen from the Figure that there is almost no change in the flow with distance along individual vessels, a behaviour similar to that observed in the arteries. Moreover, the flow through the LIV is much larger than the other veins, since the LIV is connected to the LIA, which has a large distal diameter (1.8 cm), and since the way in which we have constructed the structured-tree model for the vascular beds requires the distal diameters of pairs of large arteries and veins to be the same. Thus the flow distribution in veins is governed by the way they are connected with the corresponding arteries in left and right lungs.

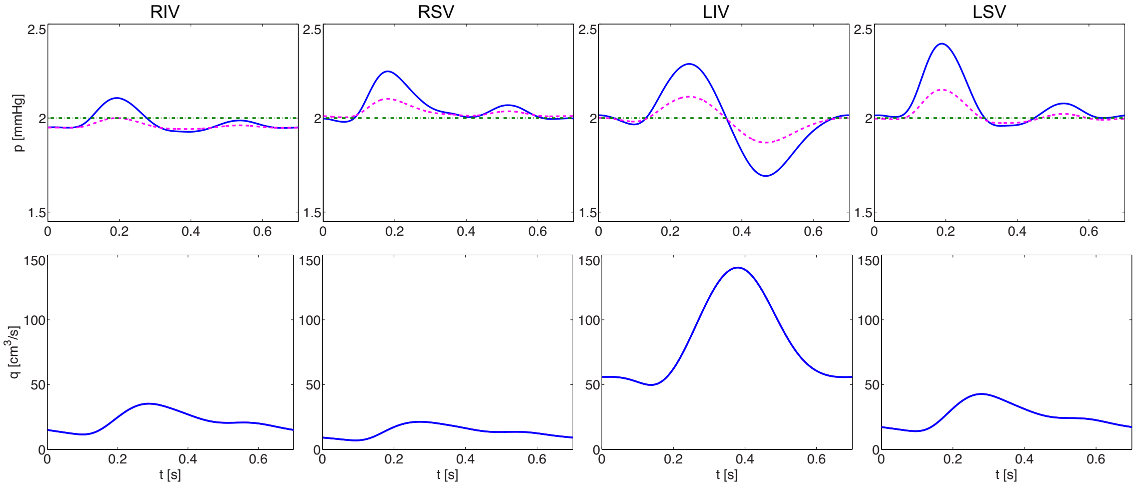

Figure 4.5: Predicted pressure (first row) and flow (second row) at three locations along the large veins. For each vein, pressure and flow are evaluated at the vessel inlet (solid blue), at the midpoint (dashed magenta), and at the end (dashed-dot green).

4.2 Pulmonary hypertension

Pulmonary hypertension is a rare condition, with less than 50 cases per million people [122]. However, its occurrence is significantly higher for at-risk patient groups including HIV patients [62,149], patients with systemic sclerosis [108], and with sickle cell disease [51,100]. Moreover, the consequences of the disease for those affected are often severe. The condition may arise as the result of multiple mechanisms, and as a result the disease is often divided into subcategories [123, 146]. In 1998, a new classification was proposed that divided pulmonary hypertension on the basis of presumed underlying etiology of the pulmonary vascular disease [142]. While a large number of specific subcategories are explained in the most recent updates [147], in this study we analyse the effect of pulmonary hypertension according to four major groups characterised by observed anatomical changes of the blood vessels. These include:

Group I : Pulmonary arterial hypertension (PAH)

Patients with pulmonary arterial hypertension have idiopathic pulmonary arterial hypertension (IPAH), formally called primary pulmonary hypertension, localized to the small pulmonary arterioles, such as connective tissue disease [72]. This group of conditions includes pathophysiology observed in patients with increased stiffness and resistance of small pulmonary vessels of diameters less than 500 μm [90, 140].

Group II : Pulmonary venous hypertension (PVH)

Often referred as secondary pulmonary hypertension, the patients in this group have elevated pulmonary pressure, most frequently as a consequence of either mitral valve disease or left ventricular (LV) diastolic dysfunction [142]. Particularly the condition occurs due to the inefficiency of the left heart to adequately pump the blood into the systemic system [146] that leads to a chronic elevation in the diastolic filling pressure of the left heart, causing a backward transmission of the pressure to the pulmonary venous system, which triggers vasoconstriction in the pulmonary arterial bed [142, 183].

Group III : Pulmonary hypertension associated with hypoxic lung disease (HLD)

Hypoxia, combined with medial hypertrophy of more proximal arteries, induces muscularization and loss of distal vessels, which is compounded by the loss of lung parenchyma in the setting of lung disease [142]. Thus this pathophysiology is associated with vascular remodelling associated with underlying respiratory disease, typically affecting vessels with a diameter less than 500 μm. In particular, it has been reported that due to the loss of lung parenchyma, patients with HLD have a reduced density of vessels within the pulmonary vascular bed (microvascular rarefaction[1]) [164].

Group IV : Chronic thromboembolic pulmonary hypertension (CTEPH)

The patients in this group have slowly progressive onset of dyspnea[2] with physical exertion and ultimately develop the signs and symptoms of right heart failure. The problem is initially located in larger vessels, which display decreased vessel diameter and increased stiffness, while there are arterial pathways that appear relatively unaffected by vascular disease [142]. However, the condition may eventually propagate and also affect small pulmonary vessels as observed for patients with PAH [33, 43]. With the involvement of distal microvessels the pathology may more closely resemble to that of PAH [142], which often indicates a worse prognosis.

---

[1] **Terminology alert**: Not to confuse the term ‘rarefaction’ with ‘rarefaction waves’ in Physics. In physiology ‘rarefaction’ refers to functional or structural modifications in the small arteries such as the reduction in microvascular density within a given volume of tissue. Throughout this thesis we use this term in physiological context.

[2] Shortness of breath, a subjective symptom of breathlessness.

4.2.1 Simulations of pulmonary hypertension

Since our model of pulmonary circulation takes into account the contribution of microvascular haemodynamics through structure trees of small vessels and explicitly includes the venous description, we may extend this model to simulate the disease conditions with pathophysiology located in the large pulmonary vessels or in the distal microcirculation i.e. the small vessels. Therefore, in this section we apply our model to test the disease hypothesis, explained above, and the results of computations simulating these four disease classes are shown and discussed below. Since the normal patterns of pressure and flow in the RIA, RTA and LIA do not appear to be significantly different than the patterns in the MPA, RPA and LPA (see Figures 4.2 and 4.3), the pressures and flows are predicted for all four conditions of pulmonary hypertension along the midpoint in the MPA, RPA and LPA only, the same is also done for all the veins i.e RSV, RIV, LSV and LIV.

Pulmonary arterial hypertension (PAH)

Pulmonary arterial hypertension can be triggered by a variety of pathologies [17], but an underlying feature of the condition is the stiffening of the smaller pulmonary arteries. In [140], it was shown that the arterial distensibility is decreased in healthy ageing and in patients with chronic hypoxia, and that reduced distensibility leads to increased stiffening of the small vessels. In this study, the reduction of distensibility is modelled by increasing the stiffness parameter Eh/r_0, which is inversely proportional to the distensibility parameter.

Figure 4.6 shows the effects of small-vessel stiffening within the arterial and venous structured trees on predicted pressures and flows in large arteries. Also the effects of PAH in veins can be observed in Figure 4.7. In the arteries the increased stiffness results in an increase in peak and pulse (the peak minus trough) pressure, and amplified oscillations of the pulmonary venous pressure and flow waveforms, with little change in the flow through the arteries. Moreover, the increased small-artery stiffness results in a delay of the peak pressure wave arrival.

Pulmonary venous hypertension (PVH)

The main causes of pulmonary venous hypertension are associated with LV dysfunction, including systolic dysfunction, diastolic dysfunction and valvular heart disease [72] leading to an elevated left atrium (LA) filling pressure [142] and ultimately causing PVH. In this

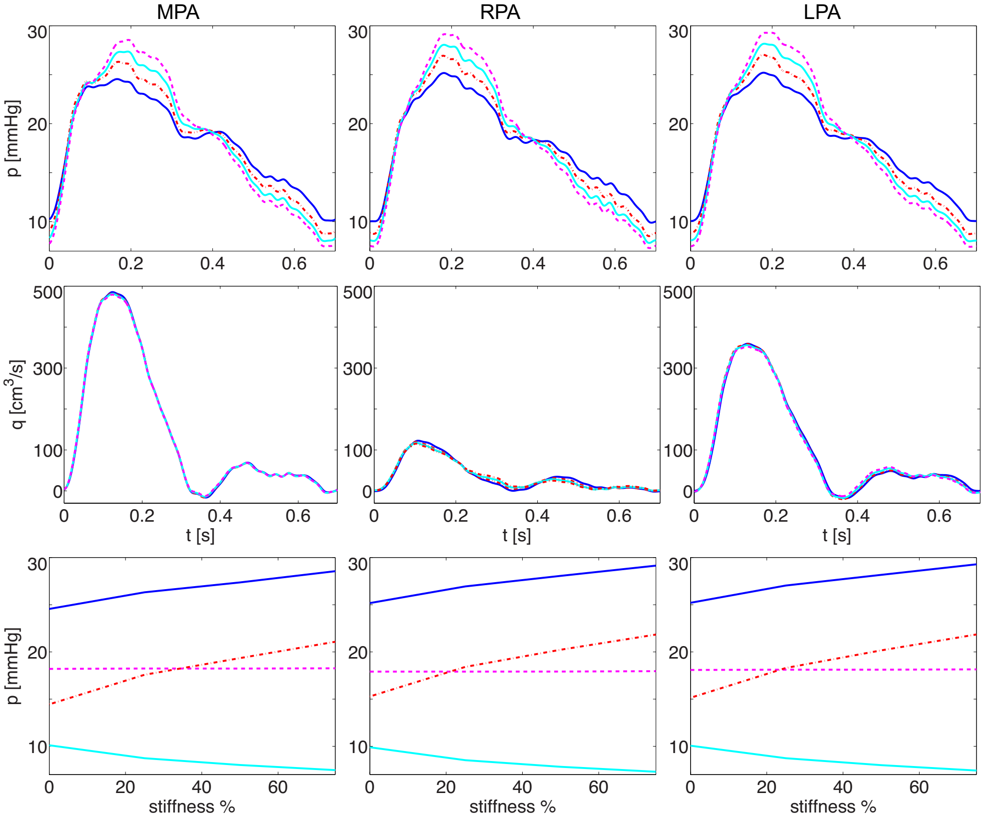

Figure 4.6: Effect of PAH (Group-I) on pressure and flow at midpoints of the MPA, RPA and LPA. The curves correspond to change in small vessel stiffness parameters as: normal stiffness (solid blue), 25% increase (dashed-dot red), 50% increase (solid cyan), 75% increase (dashed magenta). The third row gives peak (solid blue), mean (dashed magenta), pulse (dashed-dot red) and trough (solid cyan) pressures.

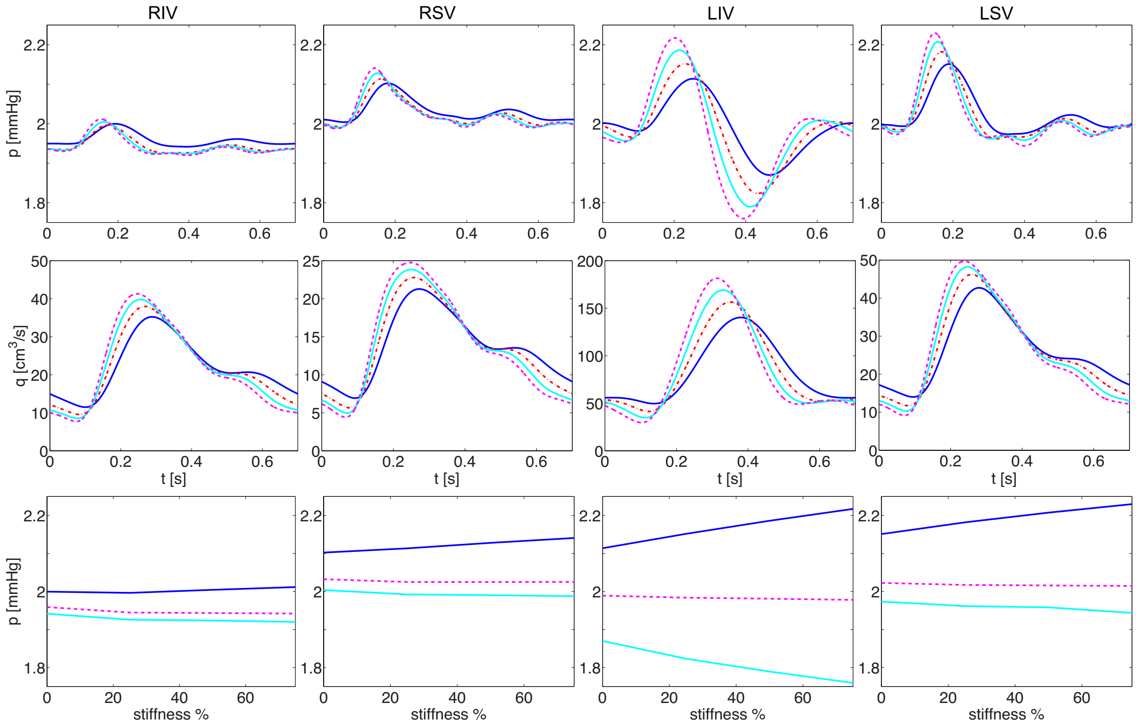

Figure 4.7: Effect of PAH (Group-I) on pressure and flow at midpoints of the RIV, RSV, LIV and LSV. The pressure and flow waveforms shown in the first two rows correspond to modulation of small vessel stiffness parameters as: normal stiffness (solid blue), 25% increase (dashed-dot red), 50% increase (solid cyan), 75% increase stiffness (dashed magenta). The third row gives peak (solid blue), mean (dashed magenta) and trough (solid cyan) pressures.

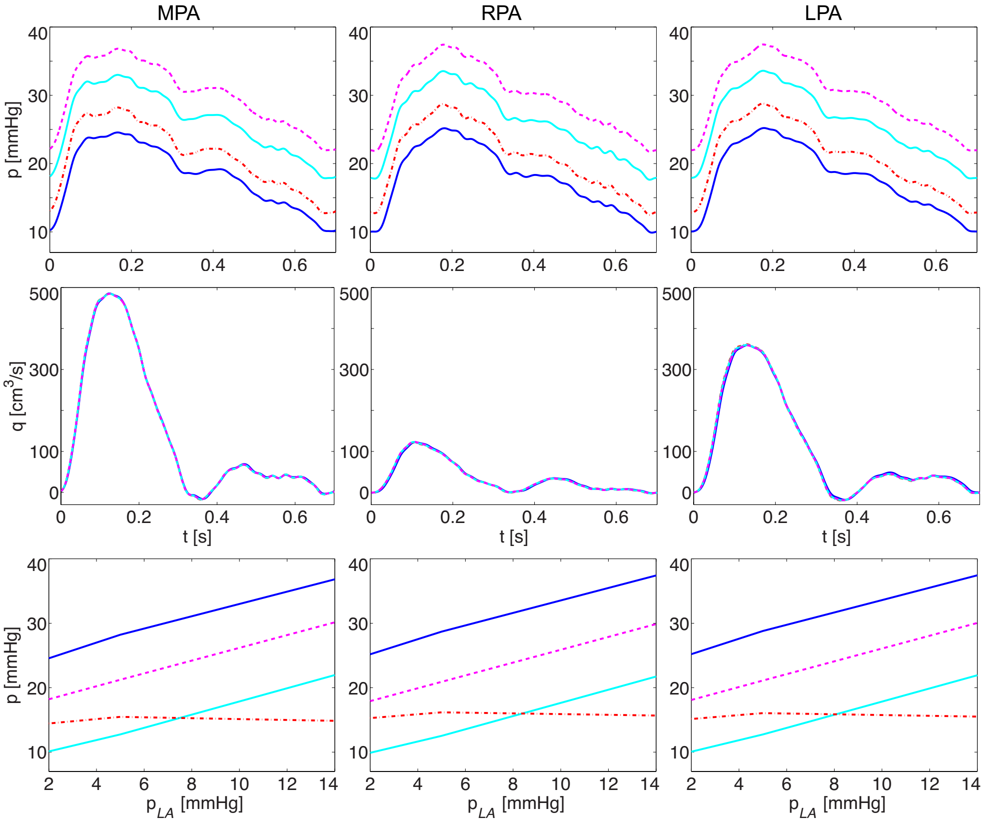

Figure 4.8: Influence of PVH (Group-II) on haemodynamics at the midpoint in each of the MPA, RPA and LPA. The first two rows show the pressure and flow waveforms which correspond to the increase in left atrium (LA) (or outflow) pressure as: 2 mmHg (solid blue) (normal case), 5 mmHg (dashed-dot red), 10 mmHg (solid cyan) and 14 mmHg (dashed magenta). The changes in peak (solid blue), mean (dashed magenta), pulse (dashed-dot red) and trough (solid cyan) pressures with elevated LA pressure are shown in third row.

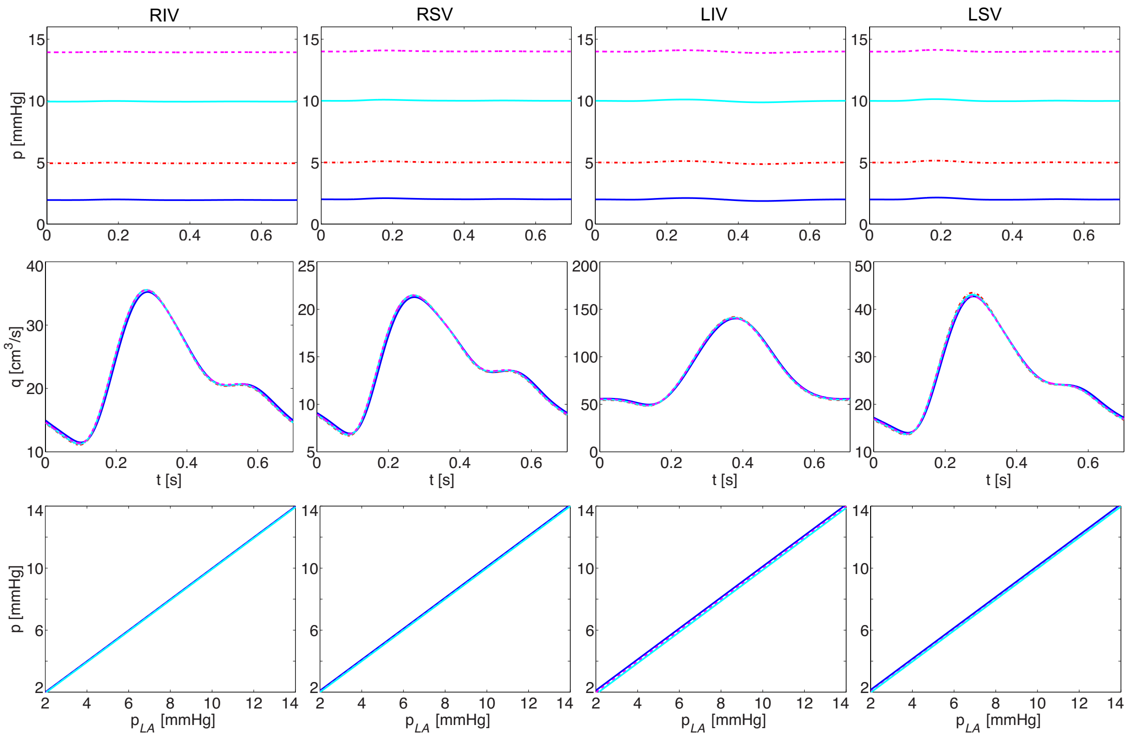

Figure 4.9: Variations in pressure and flow at midpoints of the RIV, RSV, LIV and LSV under PVH (Group-II). The first two rows depict the pressure and flow waveforms in the face of increased LA pressure as: 2 mmHg (solid blue), 5 mmHg (dashed-dot red), 10 mmHg (solid cyan), 14 mmHg (dashed magenta). The third row gives peak (solid blue), mean (dashed magenta) and trough (solid cyan) pressures.

study, we model this condition by increasing the pressure at the opening of largest veins into LA i.e. by altering the outflow boundary pressure at the venous. The corresponding simulations are shown for arteries and veins in Figures 4.8 and 4.9, respectively.

It is clear from Figures 4.8 and 4.9 that under PVH the mean, peak and trough pressures in the large vessels have a linear relationship with the LA pressure, which leaves the overall pulse pressure unaltered. Moreover, the pressure shifts upward, by the same amount as the pressure increase at the system outlet, in arteries and veins alike without having any significant effect on the pressure wave propagation or on the flow in these vessels.

Pulmonary hypertension associated with hypoxic lung disease (HLD)

Hypoxic lung disease results in hypoxic pulmonary vascoconstriction, microvascular rarefaction and vascular remodelling [164], all of which contribute to pulmonary hypertentsion

ξ	# of vessels $\times 10^5$	% change
2.40	4.6	-27
2.50	5.1	-20
2.60	5.6	-12
2.76	**6.3**	**0**
2.90	7.1	+12
3.00	7.7	+22

Table 4.1: The effects of changing radius exponent ξ on the vascular density within the vascular beds. The deviation in the total number of small vessels from normal values is presented for the arterial structured tree connected to the RIA. The minus sign indicates a reduction in density while a plus indicates an increase.

that aggravates the hypoxaemia already present. Here we focus on vascular rarefaction and its contribution to pulmonary hypertension. In [115], rarefaction within the systemic arterial vascular beds was modelled by reducing the radius exponent ξ and the asymmetry ratio γ. Decreasing these parameters results in a decrease of the area ratio η within the structured tree (see Figure 2.3). This approach is extended here to study the reduction of total cross—sectional area within both arterial and venous structured trees. For a typical structured tree the effects of changing ξ, in the neighbourhood of the normal physiological value ($\xi_{\text{normal}} = 2.76$), on the vascular density are shown in Table 4.1.

Figure 4.10 shows predicted pulse pressure and the flow waveforms in the arteries. In all three arteries, rarefied vascular beds result in significant increases in peak, trough and mean arterial pressures. Further, as the degree of rarefaction is increased, the separate peaks from the incident and reflected pressure pulses merge forming a single, more featureless, peak. Figure 4.11 illustrates the effects of rarefaction on the pulmonary veins, where the amplitude of the pressure and flow waveforms are reduced. In addition, rarefaction causes a phase shift in the venous pulse waves, with both venous pressure and flow waveforms peaking earlier.

Chronic thromboembolic pulmonary hypertension (CTEPH)

The pathophysiology associated with chronic thromboembolic pulmonary hypertension is similar to that of pulmonary arterial hypertension, except that it occurs in the large

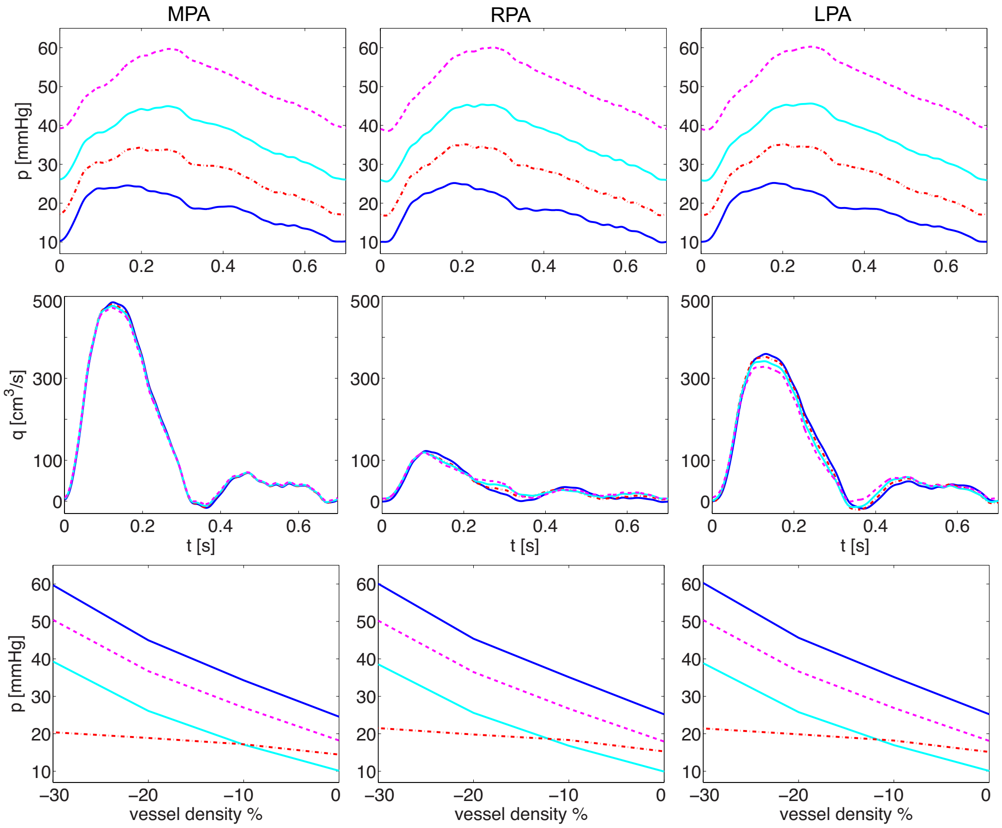

Figure 4.10: Effect of HDL associated PH (Group-III) on pressure and flow at midpoints of the MPA, RPA and LPA. The first two rows show pressure and flow waveforms where the curves correspond to the reduction in vascular beds density as: normal vascular bed density (solid blue), 10% decrease (dashed-dot red), 20% decrease (solid cyan) and 30% decrease (dashed magenta) in the density of small vessels in the vascular beds. The corresponding peak (solid blue), mean (dashed magenta), pulse (dashed-dot red) and trough (solid cyan) pressures are shown in row three.

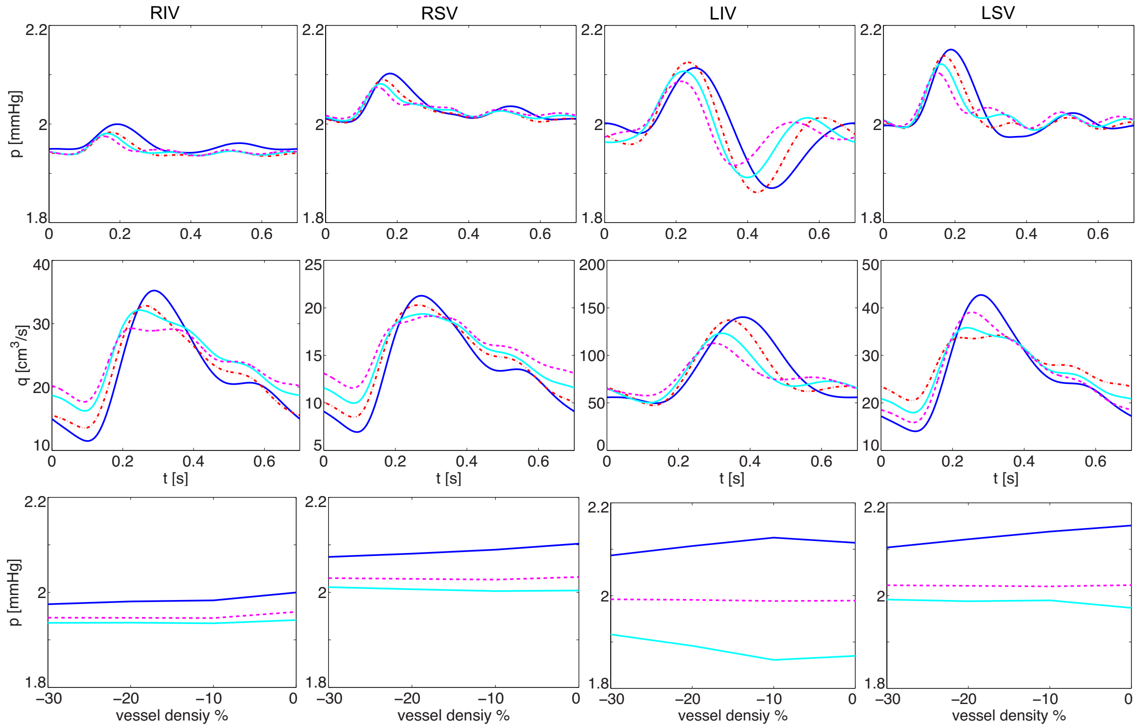

Figure 4.11: Changes in pressure and flow at midpoints of the RIV, RSV, LIV and LSV due to rarefied vascular beds (Group-III). The first and second rows show the venous pressure and flow during HLD associated hypertension as: normal vascular bed density (solid blue), 10% decrease (dashed-dot red), 20% decrease (solid cyan) and 30% decrease (dashed magenta) in the vascular bed density. The third row gives peak (solid blue), mean (dashed magenta) and trough (solid cyan) pressures.

proximal pulmonary arteries [33,43], and eventually the small vessels may get affected. In Figure 4.12 and 4.13, we simulate the effects of CTEPH on pressure and flow initially by stiffening the large vessels only. Subsequently, we also model the later involvement of small vessels by uniformly stiffening the walls of both large arteries and the small arteries and veins in the vascular beds.

The first, third and fifth rows in Figures 4.12 and 4.13 show the effects of increasing the stiffness of the large pulmonary arteries. The results show an increase in peak and pulse pressure in all three arteries, with a steeper earlier pressure peak followed by secondary pressure peak appearing shortly after the first peak in the MPA. However, this steep earlier peaking of pressure tends to fade in the RPA and LPA where the peak looks more like a right shoulder or point of inflection. The increase in pressure and appearance of a second peak agrees with observations of pressure pulses in patients with chronic thromboembolic pulmonary hypertension by [90], although the observed increase in peak pressure is much greater than our predictions. When the small and large vessels are stiffened uniformly, the results look almost identical to those obtained for PAH (see Figure 4.6), which caused a significant increase in arterial pressure and earlier peaking of the pressure pulse. However, the observed increase in the peak and pulse pressures is still significantly lower than those observed in [90] under CTEPH (p_{pulse}: 26 vs 45 mmHg and p_{peak}: 32 vs 70 mmHg, approximately). Nevertheless, due to significant increase in the pulse pressure, these results may be more closely related with those observed by [90]. As for the flows, predicted flows in the arteries hardly show any effects with increased stiffness, see Figure 4.7.

In the pulmonary veins, increased stiffness of the large arteries leads to a slight decrease in the amplitude of the pressure waveform without significantly affecting the timings of peak arrival (see Figure 4.13). Also a slight increase of flow waveform without any notable changes in the shape of the waveforms is observed in all four veins. However, just like arteries, the simultaneous increase in stiffness of large arteries and small vessels simulate results similar to that of PAH, where an earlier peaking in pressure and flow was observed with a significant increase in the venous flow.

4.2.2 Discussion of results

In order to analyse the clinical applications of our model, we extended our model to simulate four cases of pulmonary hypertension i.e PAH, PVH, HLD, and CTEPH. In PAH the dicrotic notch tends to disappear and the peak and pulse pressures increase with the

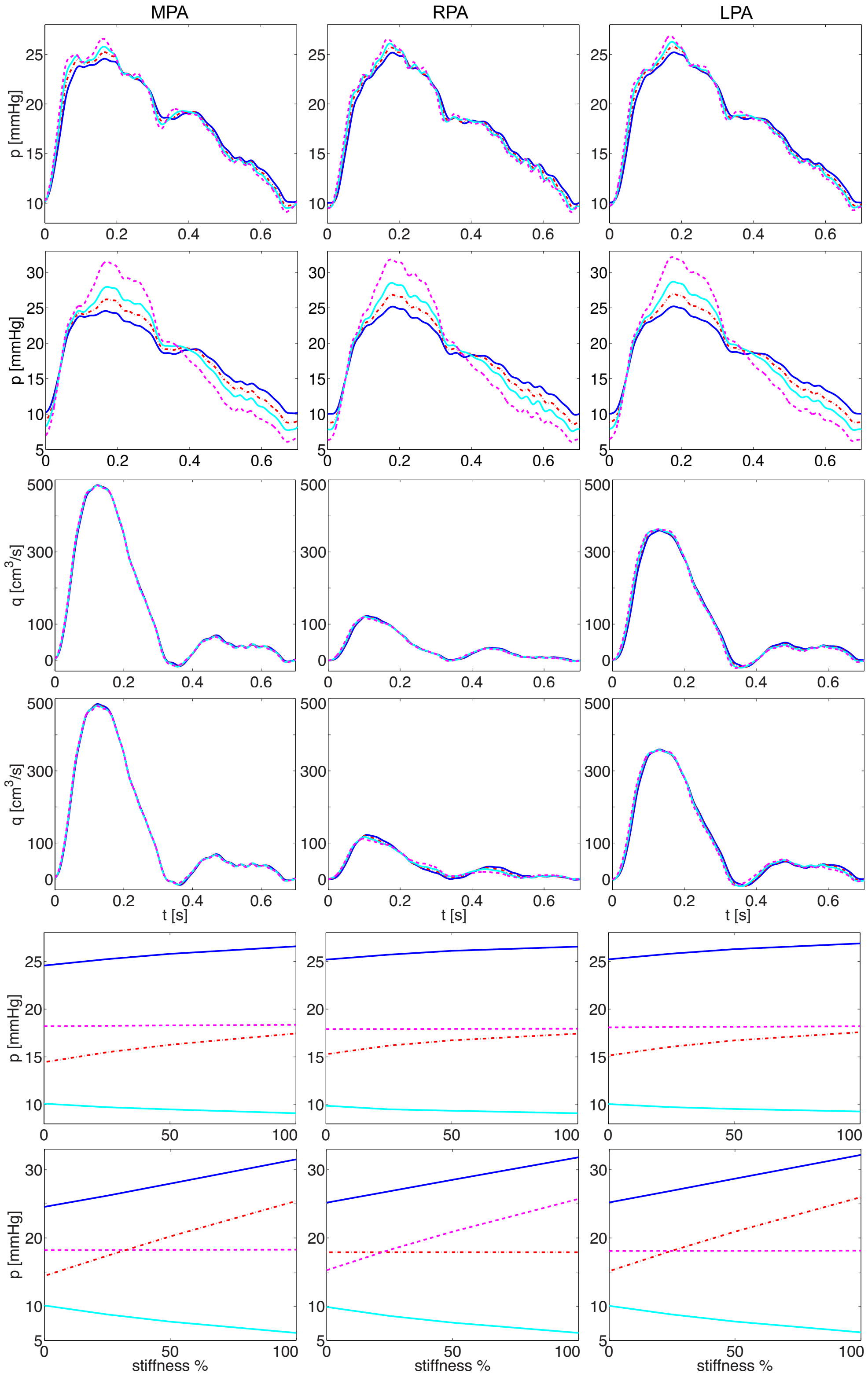

Figure 4.12: Effects of CTEPH (Group-IV) on pressure and flow at midpoints of the MPA, RPA and LPA. Initial effects of CTEPH (modulation of large arterial stiffness only) are shown in the odd rows whereas the even rows depict the effects of uniform increase in the stiffness of large arteries and small vessels. The results are simulated for the normal stiffness (solid blue), 25% increase (dashed-dot red), 50% increase (solid cyan) and 100% increase (dashed magenta) in the vascular stiffness. The corresponding peak (solid blue), mean (dashed magenta), pulse (dashed-dot red) and trough (solid cyan) pressures are shown in the last two rows.

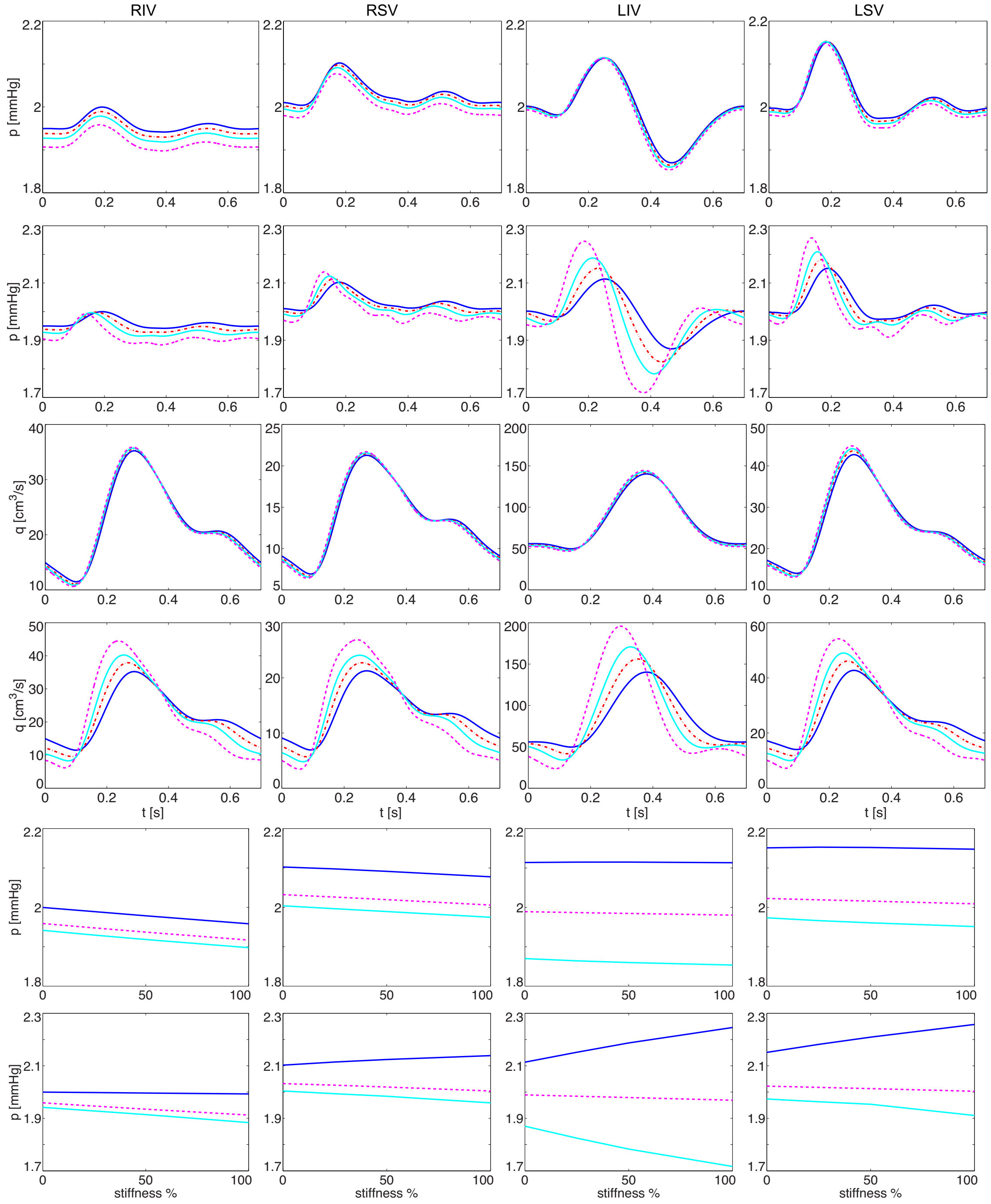

Figure 4.13: Effects of CTEPH (Group-IV) on pressure and flow at midpoints of the RIV, RSV, LIV and LSV. Initial effects of CTEPH (modulation of large arterial stiffness only) are shown in the odd rows whereas the even rows depict the effects of uniform increase in the stiffness of large arteries and small vessels. The results correspond to normal stiffness (solid blue), 25% increase (dashed-dot red), 50% increase (solid cyan) and 100% increase (dashed magenta) in the stiffness. The corresponding peak (solid blue), mean (dashed magenta) and trough (solid cyan) pressures are shown in the last two rows.

severity of the condition. These qualitative observations agree with observations by [90] who compared a control group with data from patients with idiopathic pulmonary hypertension. Similarly the increase in pressure and the appearance of a second peak under CTEPH also agrees with the observations by [90] from patients with chronic thromboembolic pulmonary hypertension, although the observed increase in peak pressure for the two conditions is much greater than our predictions. However, when we simultaneously increase both the small and large vessel stiffnesses, the observations about increase in pressure are then more in line with those of [90]. The maximum change in pressure is observed under PVH and HLD where pressure increases rapidly with increasing LA pressure and rarefaction of the vascular beds. The results for PVH show a simple shift in the normal pressure waveforms and do not affect wave propagation in any way, suggesting that although we can simulate the pressure rise in the arteries corresponding to elevated left atrium pressure, it misses a feed back mechanism that affects the wave propagation and causes the phenomena like flow reversal and pulmonary edema in PVH. For the HLD related hypertension, however, some interesting observations appear. The pulmonary circulation is normally characterised by negative or open-end type wave reflections [71] which reduce the right ventricular afterload but in the case of HLD, the observed increase in a rather featureless pressure waveform suggests that within rarefied vascular beds positive or closed-end reflections develop, amplifying the incident pressure waves and thereby increasing the right ventricular afterload. This hypothesis needs more investigation, but it does indicate that smaller vessels are the site of disease pathophysiology, an agreement with clinical observations [142], and play an important role in improving or worsening the disease condition.

Whilst pressure profiles are modulated by disease, predicted flows in the arteries show negligible variations under disease conditions, unlike the observations reported by Lankhaar *et al.* in [90], where a significant retrograde flow is observed at the end of systole. This is because no measurements of flow and vessel dimensions were available for the disease conditions and the flow profile obtained by MRI measurements from a healthy young subject is imposed even for simulations set up to predict the effect of disease. Maintaining a healthy flow at the system inlet forces the flow to be normal, especially in the proximal locations such as the MPA.

4.3 Pulmonary hypertension under right ventricular dysfunction

The right ventricle is affected by and contributes to a number of disease process, including pulmonary hypertension [173]. In the event of chronic pulmonary hypertension, the right ventricle is exposed to pressure overload, which, after the initial adaptive response, is followed by progressive contractile ventricular dysfunction due to myocardial hypertrophy[3] [46, 173]. The weak right ventricular muscles can not produce the pressure required to pump sufficient stroke volume into the pulmonary circulation, which leaves distal part of lungs short of perfusion leading to pulmonary dysfunction. Besides hypertension other diseases may also weaken the heart muscles and impair the ability of the RV to perform its normal function, for instance arrthymogenic right ventricular cardiomyopathy[4], which primarily affects muscles in the right ventricle and causes right ventricular dysfunction (RVD) [57].

Since pulmonary hypertension and heart remodelling is an interactive two-way process and the observations about flow waveforms in previous section also highlight the importance of including a heart model instead of fixing flow at the system inlet for all times. A coupled heart model with our model would enable us to invoke a feedback mechanism that can adapt in the face of increasing RV afterload due to pulmonary hypertension. Since this is beyond the scope of this thesis, we devise a simpler way to mimic the RVD in order to observe the effects on pulmonary flow dynamics through the system. To do this we replace MRI flow waveform with the computed pressure profile (see Figure 2.13 in Chapter 2) at the inlet of MPA. By doing so we ensure that only a certain pressure can propel the flow through the system in all situations including the down stream vascular remodelling. This case is just like the right ventricular dysfunction when the right ventricle can only produce a fixed pumping pressure which ultimately affects the flow distribution through the system.

---

[3] Thickening or enlargement of heart wall tissues, leading to the narrowing of ventricular space.

[4] A special case of cardiomyopathy condition, occurring due to viral infection or deposits of harmful substances in or between the heart muscle cells or degeneration of heart muscle cells in inherited diseases.

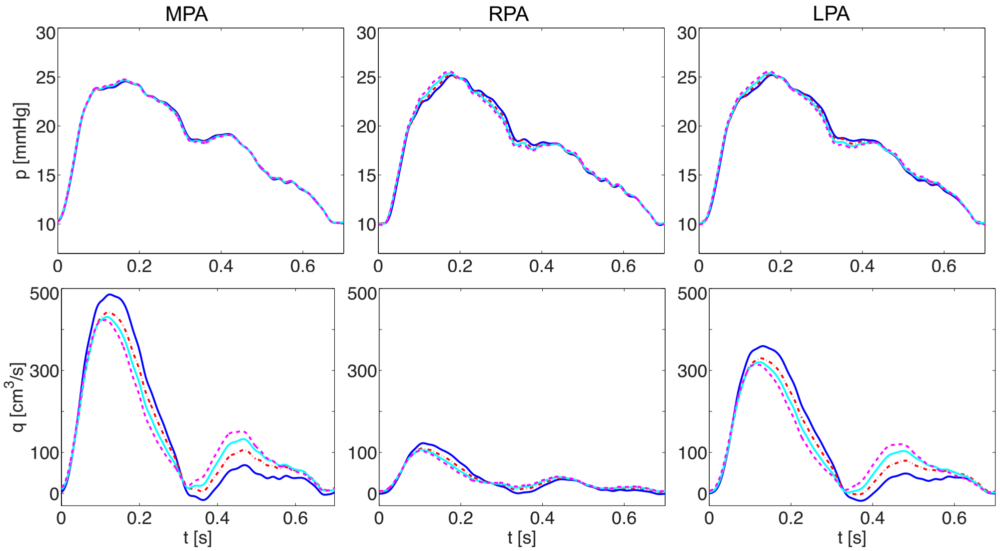

Figure 4.14: Effect of PAH (Group-I) under RVD on pressure and flow at midpoints of the large arteries. The curves correspond to change in small vessel stiffness parameters as: normal stiffness (solid blue), 25% increase (dashed-dot red), 50% increase (solid cyan), 75% increase (dashed magenta).

4.3.1 Simulations of pulmonary hypertension under RVD

In this section we present and discuss the results of computations simulating the four categories of pulmonary hypertension by modifying our model to apply the time varying pressure at the system inlet in order to mimic the condition of right ventricular dysfunction (RVD). The pressure and flow waveforms are predicted at the midpoint in the MPA, RPA, LPA and the four veins in our model.

Pulmonary arterial hypertension (PAH)

Figures 4.14 and 4.15 show the effects of PAH combined with an impaired right ventricle on pressure and flow in the large blood vessels. In the arteries, very little change in pressure is observed with the stiffened small vessels in the structured tree. Only a slight increase and earlier peaking of pressure is observed in the RPA and LPA. However, imposing pressure as an inflow condition reveals some interesting flow dynamics as the flow through the arteries during systolic phase gets significantly lower with stiffened small vessels, however, this behaviour reverses during diastole where an increasingly antegrade flow is observed with stiffened vessel. This effect was missing in the previous case without RVD.

As for the veins, a slight increase and an earlier arrival of pressure and flow peaks is

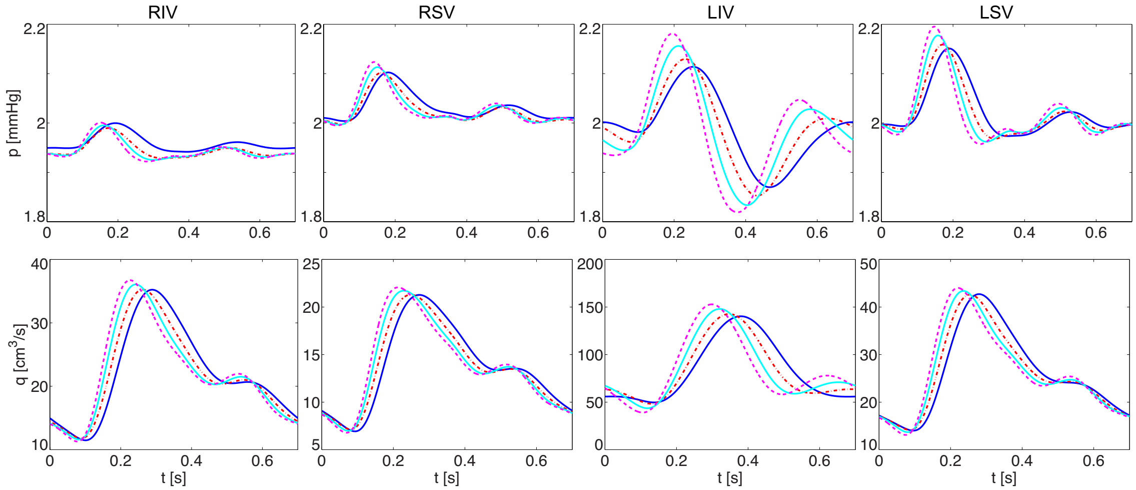

Figure 4.15: Changes in pressure and flow due to PAH (Group-I) under RVD, predicted at the midpoints of the RIV, RSV, LIV and LSV. The waveforms correspond to modulation of small vessel stiffness parameters as: normal stiffness (solid blue), 25% increase (dashed-dot red), 50% increase (solid cyan), 75% increase stiffness (dashed magenta).

observed under PAH with RVD. This behaviour is same as we observed previously without RVD, however the amount of flow through each vein is significantly lower this time.

Pulmonary venous hypertension (PVH)

In Figures 4.16 and 4.17 we show the simulations for pressure and flow under PVH in the event of RVD. Contrary to the case of imposed MRI flow-rate boundary condition, where variations in flow were non–existent, with an elevated right atrium pressure, we observe significant amount of retrograde or back flow in arteries and veins. Moreover, the flow decreases with an increasing venous pressure. As for the pressure, the elevated left atrium pressure does not affect the pressure in the large arteries but increases the venous pressure just like we observed in the case without RVD.

Pulmonary hypertension associated with hypoxic lung disease (HLD)

Figures 4.18 and 4.19 illustrate the effects of rarefied vascular beds on arterial and venous haemodynamics. In arteries we observe minimum variations in pressure in the MPA whereas a significant increase and earlier peaking of pressure, with increasingly rarefied vascular beds, is visible in RPA and LPA. In the veins, however, rarefied vascular beds cause a slight drop in pressure with an earlier peaking, an effect similar to that with the

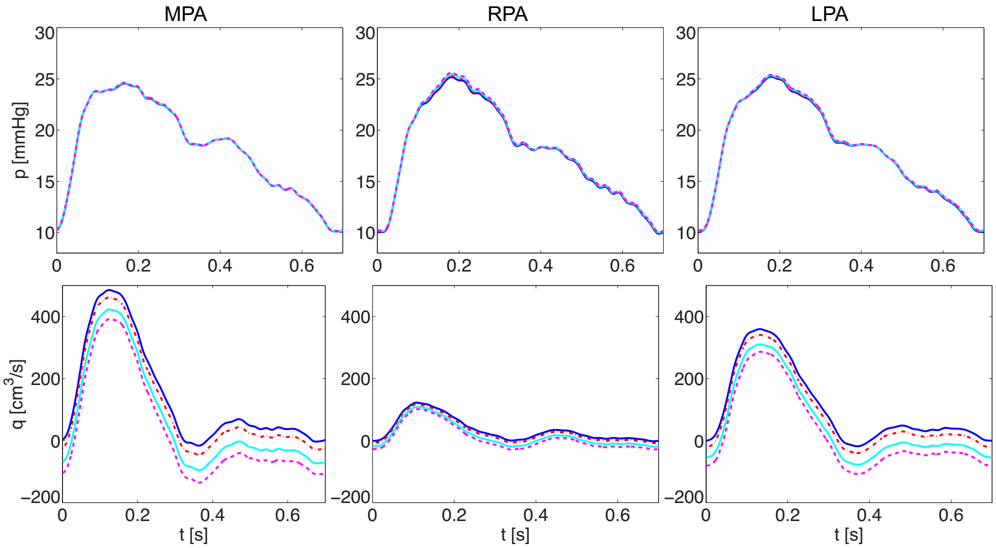

Figure 4.16: Influence of PVH (Group-II) along with RVD on haemodynamics in the MPA, RPA and LPA. The pressure and flow waveforms correspond to the increase in left atrium (LA) (or outflow) pressure as: 2 mmHg (solid blue) (normal case), 5 mmHg (dashed-dot red), 10 mmHg (solid cyan) and 14 mmHg (dashed magenta).

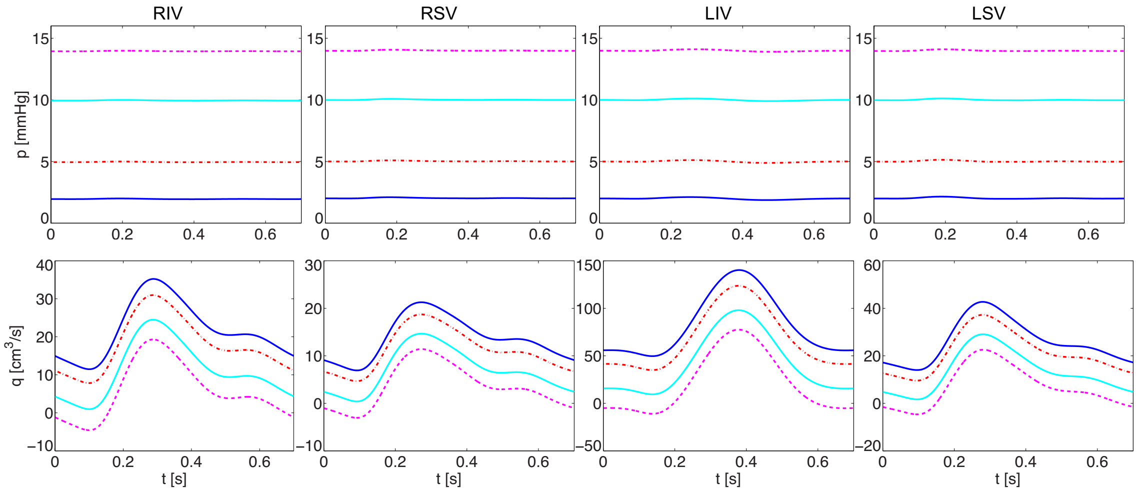

Figure 4.17: Variations in pressure and flow at midpoints of the RIV, RSV, LIV and LSV due to PVH (Group-II) and RVD. The results depict the pressure and flow waveforms in the face of increased LA pressure as: 2 mmHg (solid blue), 5 mmHg (dashed-dot red), 10 mmHg (solid cyan), 14 mmHg (dashed magenta).

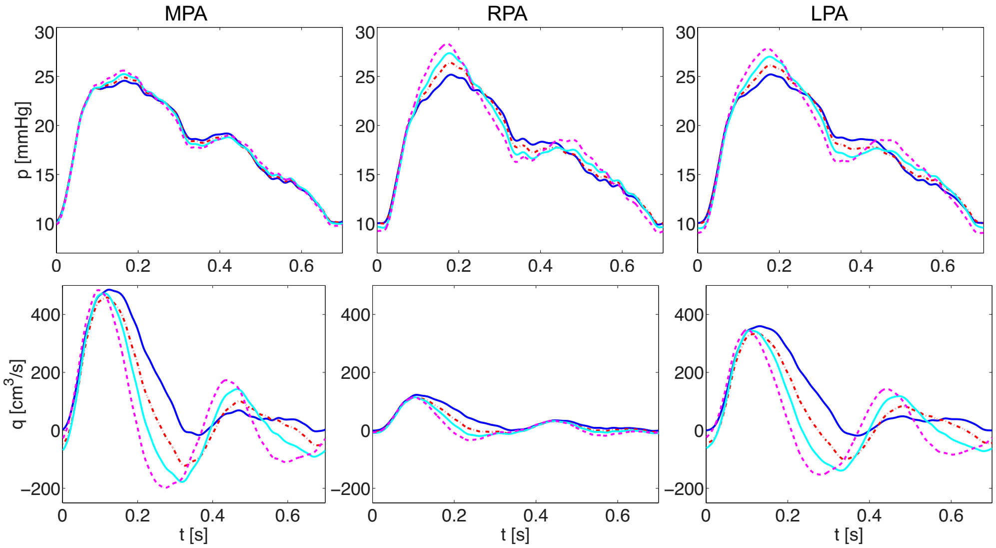

Figure 4.18: Effect of HLD associated PH (Group-III) under RVD on pressure and flow at mid-points of the MPA, RPA and LPA. The waveforms are for the reduction in vascular beds density plotted as: normal vascular bed density (solid blue), 10% decrease (dashed-dot red), 20% decrease (solid cyan) and 30% decrease (dashed magenta) in the density of small vessels in the vascular beds.

imposed MRI inflow profile.

From Figures 4.18 and 4.19 one may also observe significant effects of HLD induced hypertension on the flow-rate through arteries and veins. In arteries, increasingly rarefied vascular beds cause greater oscillations with considerable retrograde flow during systole, which is followed by significant amount of positive flow during diastole. It is also worth noting that systolic flow in arteries does reach a maximum but drops sharply in the case of HLD forming a narrower systolic flow profile and creating an overall biphasic flow waveform. As for the veins, an earlier peaking and significant drop in the flow is evident in rarefied vascular beds.

Chronic thromboembolic pulmonary hypertension (CTEPH)

The results for the effects of CTEPH under RVD on pressure and flow are shown in Figure 4.20 for arteries and in Figure 4.21 for veins. In both the figures, the initial effects are simulated by increasing the stiffness of large arteries only (first and third row), which is then extended to small vessels and results are predicted corresponding to uniform increase in stiffness of large arteries and small vessels in the connected structured trees (second and forth row). As seen from the figures, CTEPH under RVD has negligible effects on

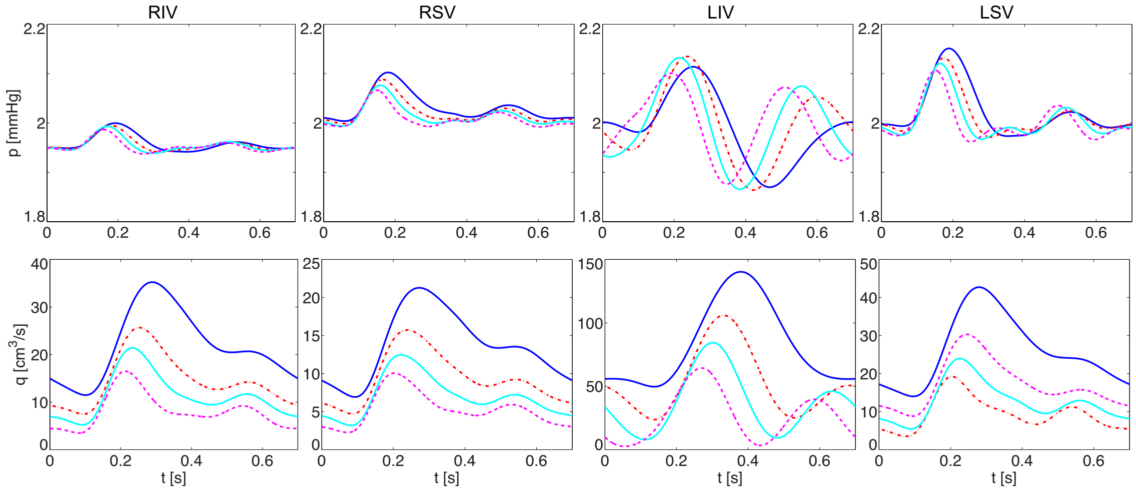

Figure 4.19: Changes in pressure and flow at the midpoints of the RIV, RSV, LIV and LSV due to rarefied vascular beds (Group-III) under RVD. The pressure and flow during HLD associated hypertension are shown as: normal vascular bed density (solid blue), 10% decrease (dashed-dot red), 20% decrease (solid cyan) and 30% decrease (dashed magenta) in the vascular bed density.

arterial pressure whereas in veins initially the pressure drops slightly but with involvement of stiffened small vessels an earlier peaking and increase in pressure is observed, an effect similar to that observed in PAH. A small decrease in arterial flow is observed with the stiffened large arteries during systole and this flow depletion exaggerates with further involvement of stiffened small vessels. Also in the veins, narrowing of flow waveforms with amplification and earlier arrival of peak is observed with progressing CTEPH.

4.3.2 Discussion of results

In order to observe the influence of pulmonary hypertension on the pulmonary flow, we simulated the condition of pulmonary hypertension, classified into four groups, under right ventricular dysfunction in which right ventricle can only produce a certain pressure that compromises its ability of maintaining adequate flow in the face of increasing afterload on pulmonary valve. This is done by replacing the MRI flow waveform with the computed pressure waveform as the inflow boundary condition.

In PAH and CTEPH, there is smaller flow during systole and an antegrade flow during diastole with stiffened arteries and small vessels but at no point we observe retrograde flow, an observation contrary to that reported in [90], whereas in IPAH and CTEPH a considerable amount of retrograde flow is observed at the beginning of diastole. However,

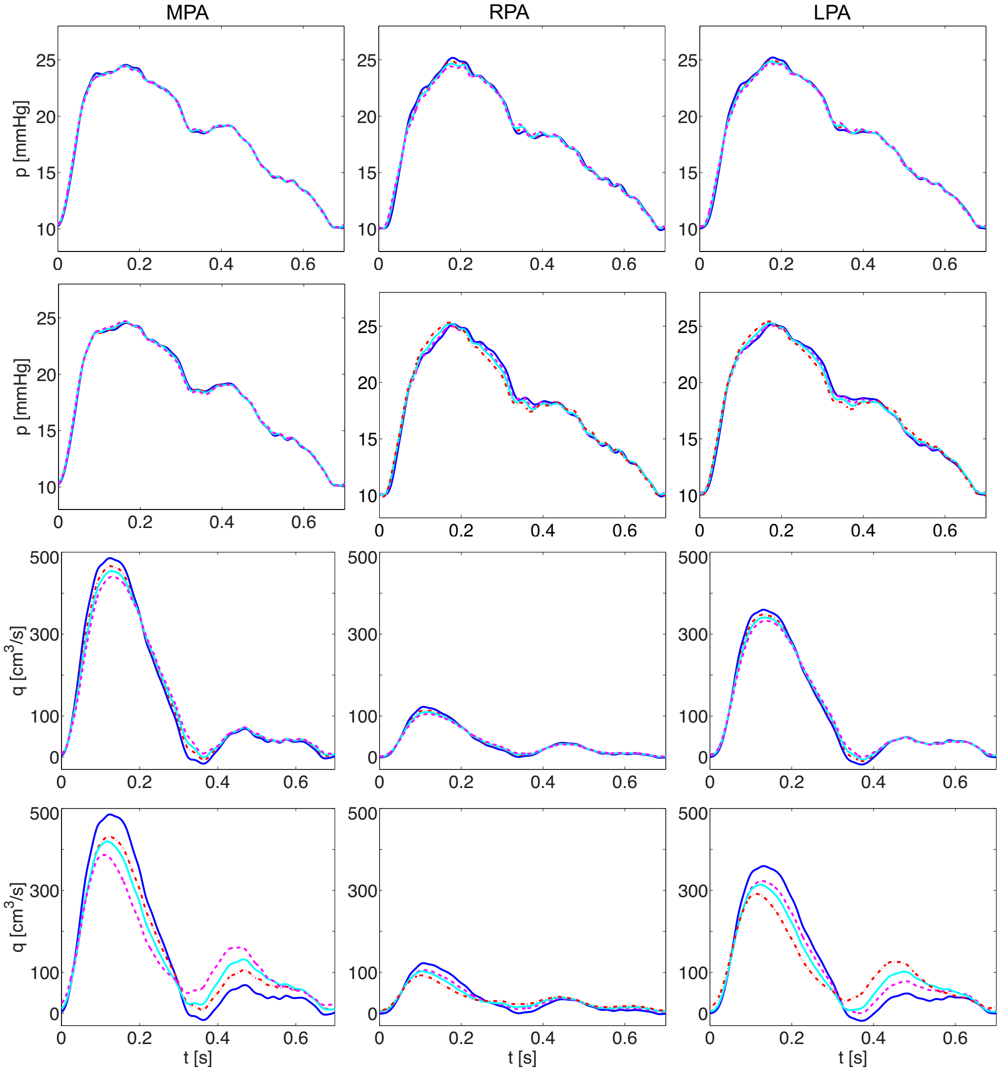

Figure 4.20: Effects of CTEPH (Group-IV) along with RVD on pressure and flow at midpoints of the MPA, RPA and LPA. Initial effects of CTEPH (modulation of large arterial stiffness only) on pressure and flow are shown in the first and third rows whereas the second and fourth rows depict the effects more developed form of CTEPH (uniform increase in the stiffness of large arteries and small vessels). The results correspond to normal stiffness (solid blue), 25% increase (dashed-dot red), 50% increase (solid cyan) and 100% increase (dashed magenta) in the stiffness.

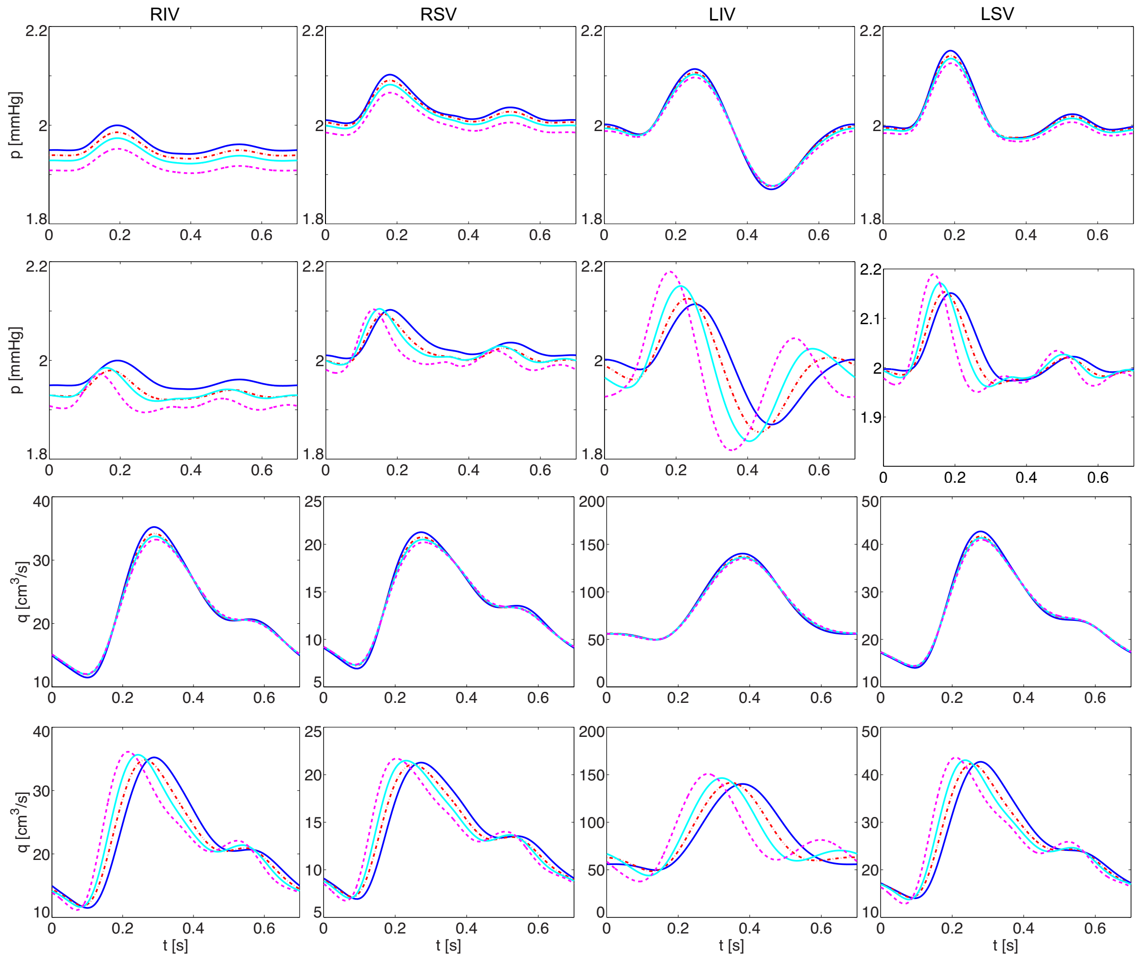

Figure 4.21: Effects of CTEPH (Group-IV) under RVD on pressure and flow at midpoints of the RIV, RSV, LIV and LSV. Initial effects of CTEPH (modulation of large arterial stiffness only) are shown in the first and third rows whereas second and fourth rows depict the effects of uniform increase in the stiffness of large arteries and small vessels on pressure and flow waveforms. The results correspond to normal stiffness (solid blue), 25% increase (dashed-dot red), 50% increase (solid cyan) and 100% increase (dashed magenta) in the stiffness.

our observation is in close agreement with a more recent study [65] where the carotid flow waveform was found to be unidirectional and bimodal with systolic and diastolic maximal peaks and this phenomenon is positively related with parameters related to aortic stiffness like impedance and pulse wave speed. Also in our results, an overall drop in venous flowrate by changing the inlet boundary condition indicates the effect of left heart dysfunction and the compromised ability of RV under hypertension. During PVH a uniform rise in venous pressure and a downward shift in the arterial and venous flows with an increase in RA pressure, lead to a retrograde flow in the arteries at the beginning and end of systole, which is an artifact of our outflow boundary condition than the true physiological behaviour. In the case of rarefied structured trees due to HLD, increasing oscillations and a very significant flow reversal with narrowing systolic profile suggest the presence of dominant wave reflections, which also contribute in increasing peak pressure in the RPA and LPA. Also the reduction in venous flow with increasingly rarefied vascular beds show that a significant volume of blood flow pooled upstream, a phenomenon that causes pulmonary edema.

4.4 Fidelity of model predictions

In this chapter the effects of pulmonary hypertension on pressure and flow in the largest pulmonary arteries and veins are studied by appropriately changing parameter values in a neighbourhood of the normal physiological values that were determined in Chapter 3. The values of the compliance (or stiffness) parameter for the large and small blood vessels, the exponent ξ in the radius relation (2.2) and the static pressure at the outlet boundaries are changed to simulate the results of hypertension. Varying the value of a particular parameter about the normal (or base) value may lead to computational challenges, and therefore in this section we discuss the confidence intervals for these parameters within which one may vary a particular parameter in order to simulate the new results presented in this chapter. Although a detailed sensitivity analysis for this model may be carried out, the reason why we did not perform this in this study is that a detailed sensitivity analysis of the one–sided systemic circulation model by Olufsen [113], which has been extended to develop this model, already exists in the literature. Since both models are governed by similar equations, which are solved using the same computational approach, the parameters involved in both models are identical and one may infer the qualitative effects of identical parameters for this model too.

For majority of the results, we changed one parameter at a time to simulate the cases of PAH, PVH, HLD and CTEPH, whereas both small and large vessel stiffnesses were increased simultaneously, by the same factor, for the developed form of CTEPH. All results are simulated subject to an inflow boundary condition, $r_{\text{min}} = 50\,\mu\text{m}, \eta = 1.16$ (yielding a value of $\gamma = 0.41$), $\mu = 0.49\,\text{g/cm s}$, $\rho = 1.055\,\text{g/cm}^3$, $T = 0.7\,\text{s}$, $l_{rr_A} = 15.75\,\text{cm}$ and $l_{rr_V} = 14.54\,\text{cm}$. Also, for the large blood vessels, we fixed r_{prox}, r_{dist} and the length of each vessel as given in Table 2.1. Thus the only parameters for which the values have been changed are ξ, outflow pressures (p_{out}), $(Eh/r_0)_{\text{large}}$ and $(Eh/r_0)_{\text{small}}$ (kept same for arterial and veinous sides).

In Chapter 3, we observed that the numerical solution converges and behaves consistently only if s–ratio> 1 (i.e. $(Eh/r_0)_{\text{large}} > (Eh/r_0)_{\text{small}}$), but we also observed that independently changing the compliance parameter is not always possible and for particular values of compliance, e.g. those given in Group B in Table 3.3, other parameters, such as r_{min}, used to be increased to obtain a realistic simulation. For the base values of $(Eh/r_0)_{\text{large}} = 195\,\text{mmHg}$ and $(Eh/r_0)_{\text{small}} = 37.5$ mmHg, (s–ratio $= 5.2$), the simulations were found to be in close agreement with physiological range of pulmonary arterial pressure [63]. Besides this s–ratio $= 4.7$, which is the smallest s–ratio (> 1) displayed in Table 3.3, also provides physiologically relevant pulse wave–forms. In the case of CTEPH, we held all the other parameters fixed, including $(Eh/r_0)_{\text{small}}$, and increased $(Eh/r_0)_{\text{large}}$ by up to 100% for each large vessel (see Figure 4.12 and 4.13). The s–ratio in this case increases maximum by a factor of 2 and remains signficantely greater than 1. So stiffening the large blood vessels does not affect the numerical stability and provides results consistent with physiological observations. Similar is the case when both large and small blood vessels are stiffened simultaneously to simulate the developed form of CTEPH. In order to simulate the PAH, only $(Eh/r_0)_{\text{small}}$ is increased to stiffen the small vessels by up to 75%, whilst keeping the large arterial compliance fixed. Doing so, however, yields an s–ratio (≈ 3), a value significantly less than the smallest s–ratio ($= 4.7$) in Group C in Table 3.3. So although the numerical solution still converges, as s–ratio$\,> 1$, simulations of PAH are improved by first increasing $(Eh/r_0)_{\text{large}}$ approximately by 23% and then increasing $(Eh/r_0)_{\text{small}}$ by up to 75%. Thus s–ratio$\,\in [3.9, 6.8]$ corresponding to new base value of $(Eh/r_0)_{\text{large}}$ and variations of 75–0% in $(Eh/r_0)_{\text{small}}$. As observed from the first row in Figure 4.12 that a 25% increase in the large arterial stiffness have minimal effect on the arterial pressure pulse, stiffening the large vessels by 23% is not very significant.

Another influential parameter in the structured tree models is r_{min}, the effects of which have been extensively studied by Olufsen [113] and Vaughan [169], and by Cousins and Gremaud [38] in reference with branching exponent ξ. The result in [38] may easily be augmented to show that if $r_{\text{min}} \to 0$ then we must have $\xi > 3$ for a convergent admittance of the connected trees. However, $\xi \in [2.3,\ 3.0]$, a variation of approximately 17% below and 9% above the normal value of $\xi (= 2.76)$, for almost all kind of flow conditions observed under physiological conditions [113]. Moreover, both Olufsen [113] and Vaughan [169] observed that by decreasing $r_{\text{min}} < 50\,\mu\text{m}$, the resistance in the structured trees increases dramatically, which leads to an increase in peak, mean and trough pressures. Thus with the current representation of the structured trees in the model, i.e. with constant viscosity μ and uniform branching exponent ξ at all levels in the tree, any value of $r_{\text{min}} < 50\,\mu\text{m}$ would yield a higher than normal pressure in the pulmonary vessels. However, increasing r_{min} up to any appropriate value in the neighbourhood of root radii, would reduce the downstream resistance, leading to low pressures in the system. Considering the strong influence of r_{min} on the tree admittance, and hence on the total periphery resistance in the connected trees, we kept $r_{\text{min}} = 50\,\mu\text{m}$ (0.005 cm) fixed for all simulations, which also allows us to vary ξ in the interval $[2.3, 3.0]$ to simulate the pulmonary hypertension associated with HLD. Since the case of HLD is characterised by the reduction in vascular density, it is sufficient to vary ξ in the interval [2.35, 2.76] to predict the effects of HLD on the pulmonary pressure pulse.

Finally, it should be mentioned that all the results of pulmonary hypertension are simulated by using the anatomical data from a healthy, young male subject by imposing a healthy flow or pressure profiles at the system inlet as inflow boundary conditions. Moreover, the effects of hypertension on cardiac cycle (T), stroke volume (q_{in}) or morphometric remodelling of the blood vessels have been ignored in this study. These limitations are subject to availability of detailed anatomical data specific to particular cases of the pulmonary hypertension, and should there be any data available to us in the future the model can be applied to quantify the uncertainty due to simulation of disease condition using the anatomical data from a healthy subject.

4.5 Conclusions

After developing a detailed mathematical and computational model of the pulmonary circulation in previous chapters, in this chapter we presented and discussed the simulation of normal pressure and flow waveform and extended our model to study four hypotheses of hypertension subject to two different inflow boundary conditions. From the study of normal case, we conclude that the pulmonary haemodynamics strongly depends on vascular dimensions and, with more complete data from a single subject, it will be possible to obtain more detailed patient-specific results. We also observed that under normal conditions vascular beds, or structured trees in this model, are the site of maximum resistance where most of the pressure drops. However, at this point in this thesis, we are not clear about the relative contribution of small arterial and venous vessels toward overall resistance. This aspect is studied in detail in the next chapter.

As for the cases of hypertension, we found that hypertension in association with HLD is the condition that influences the pulmonary haemodynamics most strongly, whereas the PAH and developed CTEPH are also found to be in line with the clinical observations. Moreover, in most cases of hypertension, except PVH, the wave reflections from distal locations seem to be an important determinant of shape and magnitude of pressure and flow waveforms. This hypothesis also requires more investigation in order to understand the underlying mechanism of elevated pressures with particular shapes. In summary, it appears that the microcirculation is also the site of pathophysiology and it could not be possible to study the diseases conditions like PAH and PH in association with HLD in the absence of physiologically based structured tree boundary condition.

Finally, where most of our results tend to agree with clinical observations, we need to incorporate important elements of circulatory system like a functioning heart model in order to be able to predict more physiological results of pulmonary hypertension. By fixing $q(t)$ and $p(t)$ as the inflow boundary condition, we actually simulate two extreme conditions linked with PH and the transition phase of two-way process of disease progression, where pulmonary hypertension causes right heart remodelling that in return influences the smooth functioning of pulmonary system, remains missing. We have briefly discussed some of the suggestions in Chapter 8 and would be keen to address these issues in future investigations. Nevertheless, the model in its present shape provides an important new tool for investigating normal condition and the hypotheses associated with pulmonary hypertension.

Chapter 5

Mean Pressure Drop Within Pulmonary Arterioles and Venules

In Chapter 4 we observed a maximum pressure drop across the vascular beds, represented by the structured trees, which model the downstream matching condition. In this chapter we extend our analysis to investigate the mean pressure drop within the pulmonary arterioles and venules by shifting our focus from treating the connected structured trees as boundary condition to use them as an active fluid dynamical part of the model. Thus in this chapter, we first derive a new algorithm to compute the mean pressure across the connected structured trees (vascular beds) and then give results to analyse the pressure drop under physiological and pathological conditions.

5.1 Introduction

In the pulmonary circulation the veins play an active role when regulating haemodynamics [56] and the pressure drop continues over both arteries and veins [190], whereas in the systemic circulation the veins are passive and the majority of the pressure drop can be found within the arteries and arterioles. Although in both the systemic and pulmonary circulations the precapillary arterioles are the major site of resistance under both normal and hypoxic conditions [16, 29, 91, 115, 134], there is still some confusion as to the relative contribution of arteries, capillaries and veins to total resistance to the flow in the lungs [29, 56]. Some results [91, 134, 190] suggest that the pre-capillary pressure drop takes place across the small vessels of diameter 10–300 μm making the vascular beds the location of maximum resistance to the blood flow and the greatest pressure drop. This is also consistent with our observations in Chapter 4, where we noticed maximum pressure drop in between the large arteries and veins i.e. the locations of structure trees.

The only study that has attempted to use computation to assess the pressure drop over both large and small vessels is by Olufsen *et al.* [115], who predicted the pressure drop across the systemic and pulmonary arterial vascular beds using a structured-tree model. To our knowledge, there is no study that includes the effects of both arterioles and venules on microcirculatory characteristics of blood flow in the pulmonary circulation. Keeping this in mind, we extend our analysis to predict the mean pressure drop within the vascular beds. The analysis is further applied to study the effects of hypertension on microcirculatory pulmonary haemodynamics.

5.2 Method

In this section we develop a new algorithm to recursively compute the mean pressure (for $\omega = 0$) as a function of radius within the connected structured trees representing arterioles and venules and linking the outflow from large arterial tree to the inflow into the veins. This is done by using the admittance matrix computed in section 2.4.1. To do so, it is necessary to first compute the pressures at the terminals of large vessels P_2^A and veins P_1^V for $\omega = 0$. These mean pressures can be extracted from the simulations in previous chapter, and assigned to the root of the structured arterial and venous trees as

$$P_1^A(0,0) = P_2^A \ , \quad P_2^V(0,0) = P_1^V,$$

where $P_k^A(0,0)$ and $P_k^V(0,0)$, (for $k = 1,2$) denote the pressures (for $\omega = 0$) at the roots $(\alpha^0\beta^0)$ of the structured trees. The corresponding flows can be found from equation (2.71) as

$$\mathbf{Q}(0,0) = \mathbf{Y}(0,0)\,\mathbf{P}(0,0), \tag{5.1}$$

where $\mathbf{Q} = (Q_1^A \ \ Q_2^V)^\dagger$ and $\mathbf{P} = (P_1^A \ \ P_2^V)^\dagger$ are pressures and flows at the proximal ends of arterial and venous vessels and $\mathbf{Y}(0,0)$ is the admittance of the connected arterial and venous tree.

For each vessel, the pressure at distal ends of arterial and venous root vessels can be computed from equation (2.64) as

$$P_2^A(0,0) = P_1^A(0,0) - \frac{8\mu L^A}{\pi r^A}(0,0)\frac{q_c}{\rho g l_c}Q_1^A(0,0),$$

$$P_1^V(0,0) = P_2^V(0,0) - \frac{8\mu L^V}{\pi r^V}(0,0)\frac{q_c}{\rho g l_c} Q_2^V(0,0).$$

The above equations may be expressed in a more compact form as

$$\begin{aligned} P_k^S(0,0) &= P_l^S(0,0) - R^S(0,0)\, Q_l^S(0,0), \\ R^S &= \frac{8\mu L^S}{\pi r^S}\frac{q_c}{\rho g l_c}, \end{aligned} \tag{5.2}$$

where $(k,l) = (2,1)$ if $S = A$ and $(k,l) = (1,2)$ if $S = V$.

Pressure drop along α and β pathways

Suppose that there is a maximum of n generations along α branches from the root vessel, i.e. vessels scaled by $\alpha^i\beta^0,\ i = 1,\ldots,n$. Then, following the similar steps as those for the root vessel, one may compute pressure and flow in any vessel segment along the α branch. So for any vessel indexed $(i,0)$ in the tree, continuity of pressure gives

$$\begin{aligned} P_1^A(i,0) &= P_2^A(i-1,0), \\ P_2^V(i,0) &= P_1^V(i-1,0), \end{aligned}$$

which can also be expressed as

$$P_l^S(i,0) = P_k^S(i-1,0), \tag{5.3}$$

where $(k,l) = (2,1)$ if $S = A$, and $(k,l) = (1,2)$ if $S = V$. Again, the flows can be computed from

$$\mathbf{Q}(i,0) = \mathbf{Y}(i,0)\,\mathbf{P}(i,0), \tag{5.4}$$

where $\mathbf{Y}(i,0)$ is the admittance matrix involving all the vessels of and between generations $\alpha^i\beta^0$. Finally, the pressure at the distal end of every vessel is given by

$$P_k^S(i,0) = P_l^S(i,0) - R^S(i,0)\, Q_l^S(i,0). \tag{5.5}$$

In a similarly way, one may compute the pressure along the β branch with m generations.

Pressure in vessels at all generations

For any other generation vessel in the connected trees, the pressure continuity in the case of α parentage implies that

$$P_l^S(i,j) = P_k^S(i-1,j) \tag{5.6}$$

and if the vessel has β parentage then

$$P_l^S(i,j) = P_k^S(i,j-1), \tag{5.7}$$

where $i = 1,\ldots,n$ and $j = 1,\ldots,m$ and k,l are defined for vessel S as $(k,l) = (2,1)$ if $S = A$ and $(k,l) = (1,2)$ if $S = V$. The flows at the respective ends are given by

$$\mathbf{Q}(i,j) = \mathbf{Y}(i,j)\,\mathbf{P}(i,j). \tag{5.8}$$

Finally, the pressures at the distal end of any vessel in the tree can be computed from

$$P_k^S(i,j) = P_l^S(i,j) - R^S(i,j)\,Q_l^S(i,j). \tag{5.9}$$

On the next page, we give the recursive algorithm for computing the mean pressures across α branches. Similar algorithm can also be derived to compute the mean pressure across β branches and across branches at all generations.

Algorithm 2: Mean pressure along α branches

```
Result: PMEAN

Input: Terminal $p_2^A(t)$ and $p_1^V(t)$

• Apply FFT (fast Fourier transform)

      $P_2^A(\omega) = \mathrm{FFT}(p_2^A(t))$
      $P_1^V(\omega) = \mathrm{FFT}(p_1^V(t))$

• if $\omega = 0$

  For each vessel $(i, j)$, $i = 0, \ldots, n$, $j = 0, \ldots, m$, compute and store admittances

      $\mathrm{comp}(i, j, :, :) = \mathbf{Y}(i, j)$

• for $i = 0 : n$

    *  if $(i = 0)$
           $P_1^A(i, 0) = P_2^A$
           $P_2^V(i, 0) = P_1^V$

       else

           $P_1^A(i, 0) = P_2^A(i-1, 0)$
           $P_2^V(i, 0) = P_1^V(i-1, 0)$

           $\mathrm{Y}(i, 0) = \mathrm{comp}(i, 0, :, :)$

        for $(S, k) = (A, 1)$ and $(V, 2)$

           $Q_k^S(i, 0) = $ eqn (5.4)

       for $(S, k) = (A, 2)$ and $(V, 1)$

           $P_k^S(i, 0) = $ eqn (5.5)

       end

• Apply IFFT (inverse fast Fourier transform)

      $(\mathrm{PMEAN})_2^A = \mathrm{IFFT}(P_2^A(0))$
      $(\mathrm{PMEAN})_1^V = \mathrm{IFFT}(P_1^V(0))$
```

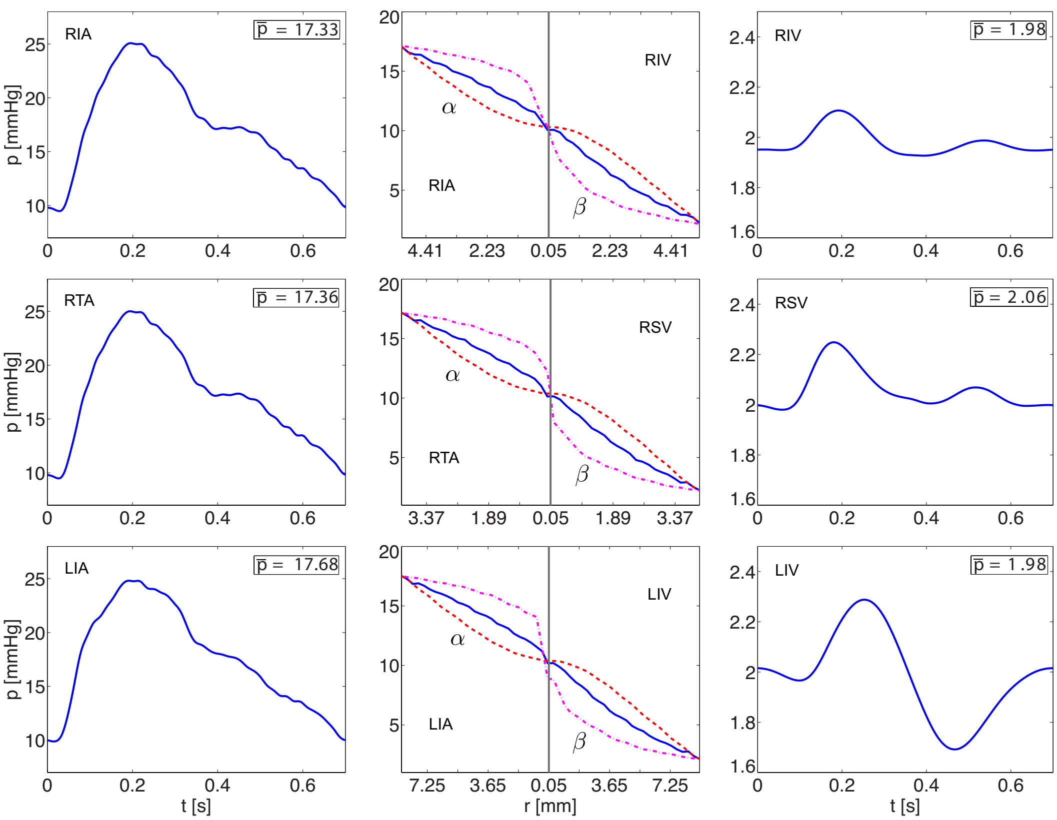

Figure 5.1: Pressure profiles in vascular beds (center). The first and third columns give pressures at the roots of the vascular bed connecting the large terminal arteries with large veins. The graphs in middle column show mean pressure changes along the α (dashed red) and β (dashed-dot magenta) pathways, together with the mean over all vessels of the same radius (solid blue). The mean (time-averaged) pressure is plotted against vessel radius on a linear-log scale.

5.3 Results

In this section we present the simulations of mean (time-averaged over one cardiac cycle) pressure within the pulmonary vascular beds (structured trees) by implementing the algorithm developed in the previous section. First we show the results for the healthy young subject followed by the simulations under three categories of pulmonary hypertension viz. PVH, PH associated with HLD and CTEPH. These classifications of pulmonary hypertensions are described in detail in Section 4.2.

Figure 5.1 shows the mean pressure drop across the arterial and venous vascular beds connecting the RIA with the RIV (first row), the RTA with the RSV (second row) and the LIA with the LIV (third row). The first and last panels in each row depict the pressures at the root of the arterial and venous trees. These pressures are imposed as

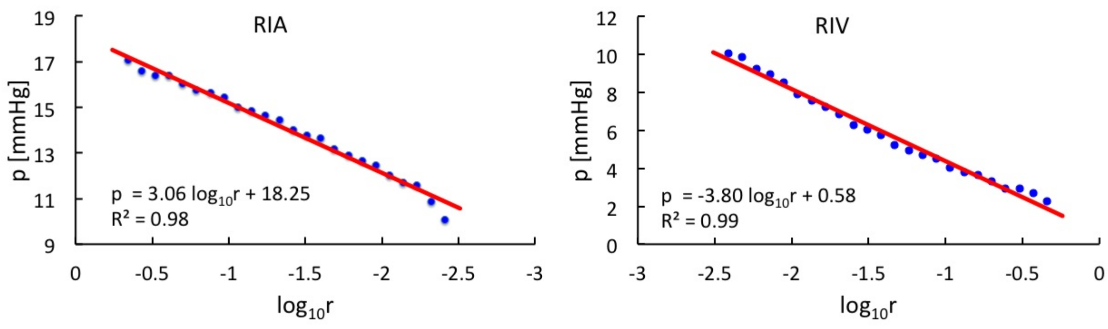

Figure 5.2: The logarithmic relationship between mean pressure and radius within the pulmonary vascular bed connecting RIA and RIV. Doted blue curve is the computed mean pressure over all vessels of the same radius and the solid red line is the liner fit.

boundary conditions and used to compute the mean pressure drop along the small vessels connecting the large terminal arteries to the large veins. The second panel in each row shows the mean pressure drop across the combined arterial and venous beds. The mean pressures are plotted along the α branch (composed of vessels scaled by $\alpha^i\beta^0, i = 1, \ldots, n$), the β branch (composed of vessels scaled by $\alpha^0\beta^j, j = 1, \ldots, m$ where $m < n$), and the average computed over all branches of the same radius. The scale used for the radius r is logarithmic ($\log_{10} r$), ranging from the largest to smallest arteries and then from the smallest to largest veins.

Along the arterial trees the pressure drops from about 17 to 10 mmHg, and along the venous trees the pressure continues to decrease from about 10 to 2 mmHg. It should be noted that the pressure drops differ significantly between the two extreme cases: on the arterial side, pressures in the β branches are greater than those in the α branches, and vice versa on the venous side. For the α branches, the greatest pressure drop occurs in the larger arteries and veins, whereas the opposite holds for the β branches. Due to the negligible difference in the input mean pressures the results are similar for all the vascular beds, therefore for the rest of the chapter we chose to display results only for one vascular bed that connects the RIA to the RIV.

Figure 5.2 illustrates the continuous pressure drop phenomenon across the arterial and venous vascular beds in the form of a log–linear relation between mean pressure and the vessel radii. The fits to p vs $\log_{10}r$ suggest that the arterial and venous mean pressures are fitted well by

$$p = \begin{cases} 3.06 \log_{10} r + 18.25 \quad \text{mmHg}, & \text{for arterioles}, \\ -3.80 \log_{10} r + 0.58 \quad \text{mmHg}, & \text{for venules}, \end{cases} \tag{5.10}$$

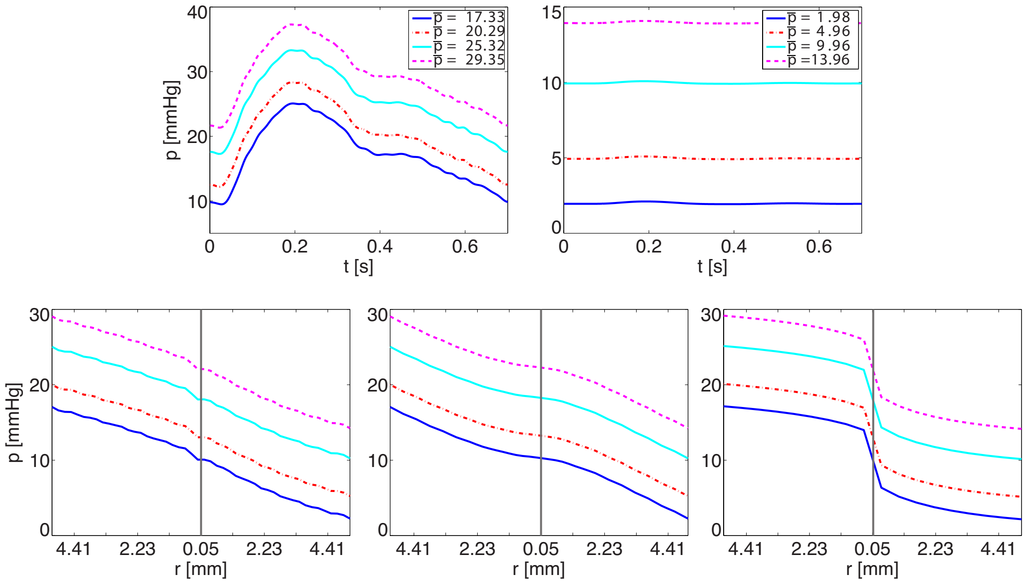

Figure 5.3: Effects of PVH on mean pressure in vessels connecting the RIA with the RIV. Mean pressure is plotted against vessel radius on a linear log scale. The curves correspond to an elevation in venous pressure as: 2 mmHg (normal case) (solid blue), 5 mmHg (dashed-dot red), 10 mmHg (solid cyan) and 14 mmHg (dashed magenta). The two panels in the first row show the pressures (and mean pressures; $\bar{p}$ in the legend) at the the roots of the RIA and RIV in the case of PVH whereas the panels in the second row correspond to the pressure averaged over all vessels of the same radius (first panel), the α branch (second panel), and the β branch (third panel).

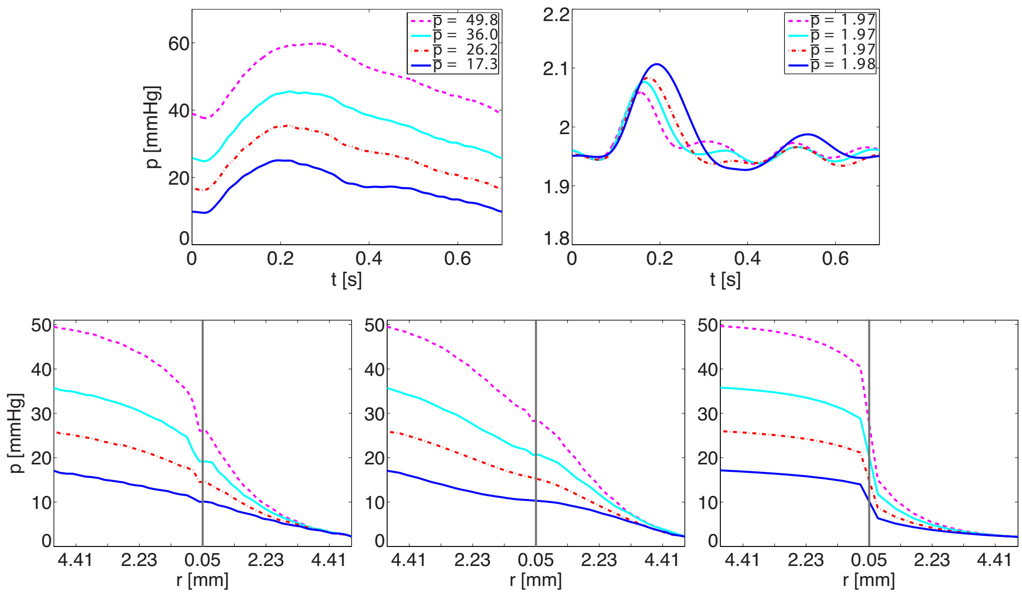

Figure 5.4: Effects of PH associated with HLD on mean pressure in vessels connecting the RIA with the RIV, plotted against $\log_{10} r$. The curves correspond to a reduction in vascular density: normal (solid blue), 10% decrease (dashed-dot red), 20% decrease (solid cyan) and 30% decrease (dashed magenta). The second row shows the pressures in: averaged over all vessels of the same radius (first panel), the α branch (second panel) and the β branch (last panel) whereas the pressures at the the roots of the RIA and RIV in the case of HLD (panels in the first row) are imposed as boundary conditions.

where $0.005 \leq r \leq 0.55\,\text{cm}$ both for arterioles and venules.

As for the pulmonary hypertension, since the pathophsiology of PAH and advanced CTEPH is similar, we chose to simulate the effects of PVH, PH associated with HLD and CTEPH on mean pressure drop across pulmonary vascular beds connecting RIA and RIV.

Figure 5.3 shows the effect of PVH on the pressure drop across the vascular bed connecting the RIA and RIV. It is observed that the pressure rise throughout the system due to PVH also increases the overall vascular bed pressure both in the small arteries and veins by the same magnitude. Similar to our previous observations about PVH, the overall behavior of pressure drop in all the vessels including α and β branches remains constant and only an upward shift in vascular bed pressure is observed in PVH.

Figure 5.4 illustrates how the small-vessel remodelling (HLD) affects the pressure drop across the vascular bed connecting the RIA and RIV. Most significantly, the increased pressure at the inlet to the vascular bed raises the overall pressure in both the small arteries and veins. In particular, the arteries in branches that decrease rapidly in radius

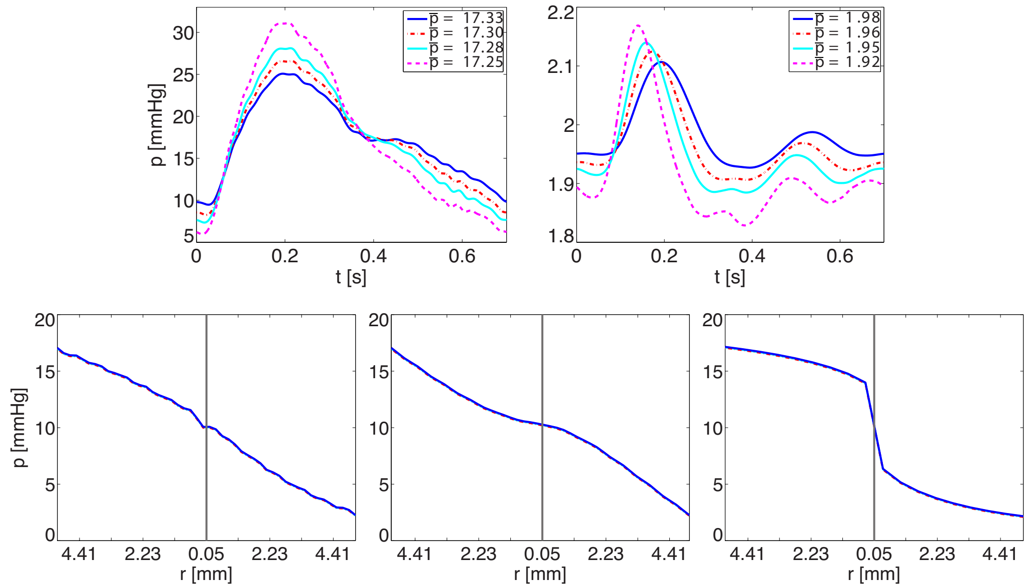

Figure 5.5: Effects of CTEPH, on mean pressure in vessels connecting the RIA with the RIV. Mean pressure is plotted against vessel radius on a linear log scale. The curves correspond to a uniform increase in vascular stiffness as: normal (solid blue), 25% increase (dashed dot red), 50% increase (solid cyan) and 100% increase (dashed magenta). The pressures at the the roots of the RIA and RIV in the case of CTEPH (first row) are imposed as boundary conditions. The three panels in second row show: the pressure averaged over all vessels of the same radius (first panel), the α branch (second panel) and the β branch (third panel).

with generation number, such as the β branch illustrated in the last panel of bottom row, experience higher pressures than average for their radius making them even more susceptible to further injury and disease.

Finally, the effects of chronic thromboembolic pulmonary hypertension (CTEPH) on pressure drop across the vascular bed connecting the RIA and RIV are depicted in Figure 5.5. Although there is a significant variation in pressure waveforms at the root of structured trees in CTEPH, the negligible difference in the corresponding mean pressures at the root (see the top row panels in Figure 5.5) barely show any effects of stiffened pulmonary vasculature on the pressure dynamics in the small arteries and veins.

5.3.1 Pressure–drop across pulmonary capillary network

The capillaries in the human body are known to have the largest vascular surface area [55] and therefore, despite having very small radii, the pressure drop (= flow × laminar flow resistance) through capillary vessels remains small, due to small flux in the periphery

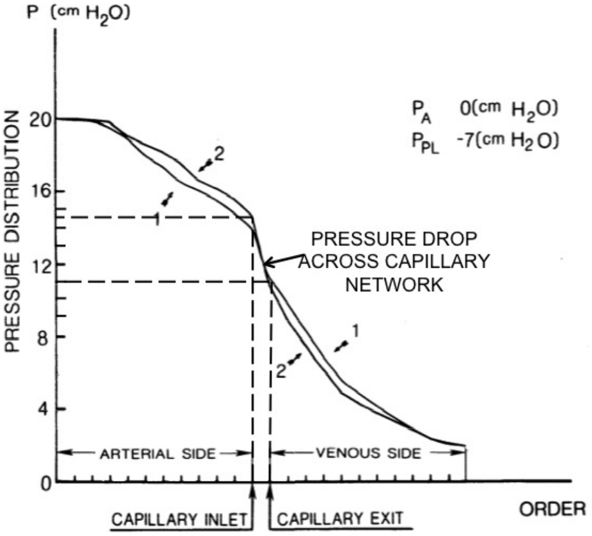

Figure 5.6: Longitudinal pressure distribution in pulmonary blood vessels of cat plotted against the order number of the vessel (Strahler order system in which smallest noncapillary vessels is of order one). Numerals 1 and 2 refer to branching models 1 (symmetric) and 2 (asymmetric) in this study from Zhuang *et al.* [190]. The figure has been annotated slightly to point-out the pressure drop across the capillary network, which has been excluded in our model.

circulation, as a consequence of rapid branching and increasing total cross–sectional area after each generation. However, like venules, pulmonary capillaries are also known to contribute towards the total periphery resistance [24], however small it is. Figure 5.3.1, from Zhuang [190], also shows a pressure drop of about 3.5 cmH_2O (2.6 mmHg or 21.9 %) across the asymmetric pulmonary capillary network.

The current formulation of our model does not provide any information about the magnitude or patterns of pressure drop within the capillary network as the two trees have been truncated and joined together neglecting the blood vessels of radius $< 50\,\mu$m. Since the topology of the network of pulmonary capillaries is more sheetlike than the treelike [55], extending the structure trees below the predetermined minimum radius of $50\,\mu$m, in order to include the capillary vessels, is not a trivial task. This is one of the limitations of our model and certainly merits consideration for improvements in any future work. Foe now, we augment our analysis to determine if the current structure tree representation is sufficient to provide a crude estimate of likely pressure drop across the vessels with radii $< 50\,\mu$m or what changes may improve the structured tree model in order to provide an accurate representation of the capillary beds. Firstly, we may extrapolate equation (5.10) linearly by choosing $r = 0.005\,\text{cm}$ ($50\,\mu$m) and $r = 0.0005\,\text{cm}$ ($5\,\mu$m, typical capillary radius) and then compute the pressure difference. For these values a further 3.06 and 3.8 mmHg of pressure drop may be predicted on arterial and venous sides, providing an overall estimate of 7.14 mmHg between $5 < r < 50\,\mu$m. This is about 47.6% of the pressure drop between large terminal arteries and veins, computed with $r_{\text{min}} = 50\,\mu$m from the full-scale model, and much higher than the capillary pressure drop predicted by Zhuang [190]. Moreover, extrapolation of arterial and venous fits in equation (5.10) provides a terminal venous pressure of 11.21 mmHg, overlapping the terminal arterial pressure of 8.19 mmHg at $r_{\text{min}} = 5\,\mu$m, which clearly violates the pressure continuity at the joining point of arterial and venous vascular beds. Thus extrapolating equation (5.10) outside its domain is not a good choice to illustrate the pressure drop across the capillary network.

Alternatively, assuming viscosity to be constant, the structure of the tree to be uniform at all levels, and neglecting the effects of phase separation at the junctions for vessels with radii smaller than $50\,\mu$m, the current model may be augmented to provide an estimate of pressure drop across the initially neglected capillary network. For example, for a given $r_{\text{root}} = 0.55\,\text{cm}$, (RIA-RIV) and fixed mean pressure $P^A_{\text{in}} = 17.1\,\text{mmHg}$ and $P^V_{\text{in}} = 2.2\,\text{mmHg}$ at the arterial and venous root vessels, respectively, of the connected structured tree (yielding $\Delta P = 14.9\,\text{mmHg}$ between the two locations), we get the following statistics.

r_{min} [μm]	$P^A_{\text{r}=50\mu m}$	ΔP^A	(%)	$P^V_{\text{r}=50\mu m}$	ΔP^V	(%)	$\Delta P^{\text{capp}}_{\text{est}}$	(%)
50	10.1	7.0	47	10.1	7.9	53	–	–
40	10.7	6.4	43	9.3	7.1	48	1.4	9
30	11.2	5.9	40	8.5	6.3	42	2.7	18
20	12.3	4.8	32	7.3	5.1	34	5.0	34
10	14.0	3.1	21	5.5	3.3	22	8.5	57

Table 5.1: Estimate of likely mean pressure–drop, $\Delta P^{\text{capp}}_{\text{est}}$, across vessels with radii $< 50\,\mu$m (capillary network) using the structured tree.

From Table 5.1, it is clear that, despite the flow distribution in a rapidly branching structured tree, adding more vessels of smaller radii would progressively increase the resistance in part of the system below the small terminal radius $r_{\text{min}} = 50\,\mu$m. It may easily be shown that this is an expected behaviour with the current structure of the tree. From the Hagen–Poiseuille law, the laminar flow resistance Ω across a circular tube of radius r

and length L is given by

$$\Omega = \frac{8\mu L}{\pi r^4}.$$

From equation (2.5), the length (in units of cm) of an arterial segment for $r < 50\,\mu$m (0.005 cm) is given by

$$L^A = 1.79\, r^{0.47},$$

then the resistance of a vessel segment at generation $(i, 0)$ in the α–branch, for example, is given by

$$\Omega^A_\alpha(i, 0) = \frac{8\mu}{\pi} \frac{1.79}{r^{3.53}(i, 0)},$$

and in a vessel at generation $(i + 1, 0)$ as

$$\Omega^A_\alpha(i + 1, 0) = \frac{8\mu}{\pi} \frac{1.79}{r^{3.53}(i + 1, 0)} = \frac{1}{\alpha^{3.53}} \Omega^A_\alpha(i, 0),$$

since $r(i+1, 0) = \alpha r(i, 0)$. Thus the resistance in the vessel in α–branch at n^{th} generation is given by

$$\Omega^A_\alpha(i + n, 0) = \frac{1}{\alpha^{3.53n}} \Omega^A_\alpha(i, 0).$$

Now the total resistance along the path between vessel at generation $(i, 0)$ to vessel at generation $(i + k, 0)$ is given by

$$\mathrm{R}^A_\alpha = \frac{\Omega^A_\alpha(i, 0)}{\alpha^{3.53}} \sum_{j=1}^{k} \frac{1}{\alpha^j}.$$

For $k \to \infty$, the geometric series in the above relation diverges for $\alpha < 1$. Thus adding more generations, and hence more vessels, in the structured tree (leading $r_{\text{min}} \to 0$) would progressively increase the resistance in the tree. This aspect once more highlights the shortcoming of the current structured tree model for a detailed analysis of micor–circulation. However, according to Poiseuille law, the pressure drop across the α–branch with n generations, beyond a critical radius ($50\,\mu$m) is given by

$$P(i + n, 0) = P(i, 0) - \frac{\Omega^A_\alpha(i, 0)}{\alpha^{3.53}} \sum_{j=1}^{n} \frac{\dot{Q}(j, 0)}{\alpha^j},$$

where $\dot{Q}(j, 0)$ is the mean flow–rate in the vessel at j^{th} generation. Thus the progressive resistance in the tree may be compensated by accounting for variable viscosity, different scaling ratios and phase separation effects below a certain critical radius within the tree, in order to develop a better representation of capillary beds via structured tree representation.

5.4 Discussion of results and conclusion

The aim of this chapter was to be able to simulate the pressure drop phenomenon across pulmonary vascular beds, by developing a recursive algorithm to compute the mean pressure as a function of radius in small vessels while reading the pressures at the terminals of large arteries and vein (roots of structured trees) as inflow and outflow boundary conditions.

As suggested by [56], mean-pressure predictions along pulmonary arteries and veins can be used to study the contribution of the small pulmonary veins toward the total peripheral resistance and haemodynamic regulation. It is observed that not only does the blood pressure continue to drop across the convergent tree of small veins (Figure 5.1), but the decrease is slightly greater across the venous tree compared to the arterial tree (8 vs. 7 mmHg). Since both trees are topologically equivalent and mirror images with same number of vessels in each tree, these are the different length-to-radius ratios, which are responsible for this difference as the venules are slightly longer than the arterioles in this study (see equation (2.5)). Moreover, there is close agreement with results reported by Zhuang *et al.* [190], who studied the haemodynamics of cat pulmonary vessels and reported that veins contribute approximately 49% toward the total pulmonary vascular resistance (see Figure 5.3.1). Besides arterioles and venules, Zhuang studied the pressure drop across the capillaries and reported a 15.4% and 21.9% pressure drop across capillary network using a symmetric and an asymmetric branching modulus, respectively. Moreover, corresponding pressure drop within arterioles was found to be 35.9% and 29.3% for the symmetric and asymmetric networks.

As for the linear–log relation (5.10), a similar scaling law is reported by Olufsen *et al.* [115] to describe the relation between the mean pressure and radius in the arterial side of pulmonary vascular beds, given by

$$p = 14\log_{10} r_{\text{pulm}} - 25. \tag{5.11}$$

Here r and p are the vessel radius (in units of μm) and mean pressure (in units of mmHg), respectively, in the pulmonary arterioles only. The reason why our relation for pulmonary arterioles in equation (5.10) is different than the Olufsen's relation is that Olufsen *et al.* used a one–sided structured tree that terminates after $r_{\text{min}} = 50\mu$m and does not link to a venous tree. At each terminal branch a zero terminal impedance, which implicitly assumes pressure to be zero at theses points, is imposed to recursively compute the total input impedance of the pulmonary arterial vascular beds. This assumption forces pressure to be zero when $r = 61\mu\text{m}$ (0.0061 cm) in (5.11), whereas the mean pressure in (5.10) remains positive for all r as no such assumption is imposed on pressure or flow at the joining point of the arterial and venous vascular beds. The results in equations (5.10) and (5.11) are not comparable due to the fact that Olufsen's model incorporates a smaller domain of downstream pulmonary vasculature (no venules) and impose a very restricting assumption on the terminal pressures, which limits the application of one–sided structured tree to analyse the microcirculatory haemodynamics. Since our model is free from any such assumption, we believe that our model and method provide a more realistic picture of the true physiological phenomenon.

We also conclude that the structured tree representation has great potential for further improvements; both, in terms of taking into account the effects of pulmonary capillaries on global haemodynamics and to analyse the pressure–drop phenomenon across the pulmonary capillary beds in more detail. Among the cases of hypertension, the maximum change in pressure is observed under HLD where pressure increases rapidly with increasing rarefaction of the vascular beds. HLD significantly raises the mean pressure in the vascular beds, especially in the arteries (see Figure 5.4). This suggests that microvascular rarefaction not only impacts the blood pressure in the large arteries but also in the smaller vessels enhancing the risk of further small vessel pathology. This effect illustrates that an initial elevation in the arterial blood pressure due to hypoxia would further damage the small blood vessel due to high blood pressure, which may consequently lead to worsen the hypoxia.

In summary, in this chapter we have successfully predicted the mean pressure across pulmonary vascular beds of different sizes and densities and extended our results to study the influence of PH on microcirculatory pressure drop. The results show good agreement with other reported studies and confirm the contribution of small pulmonary veins to overall vascular resistance.

Chapter 6

Reflections In The Pulmonary Arteries

In previous chapters we developed a multi–scale one–dimensional fluid dynamical model of the human pulmonary circulation to simulate the pressure and flow–rate waveforms in the largest pulmonary arteries and veins during health and disease. In this chapter we extend our analysis to interpret our results in a rather different and more insightful way by analysing the pulse waveforms in more detail. To do so, we apply the method of Wave Intensity Analysis (WIA) [118] on the data generated numerically in our model of pulmonary circulation with the aim of identifying the nature of wave reflections in the largest pulmonary arteries and their contribution in shaping the pulse waveforms. Where possible, we have made qualitative comparisons with the existing results in the literature, obtained from haemodynamic data measured in *in vivo* pulmonary arteries of animals or human. The chapter is divided into three main sections; the first section gives an introduction to wave reflections in the arteries, which is followed by the description of method of WIA in second section. Finally we apply the WIA on the simulated pulse waveforms shown in Chapter 4 to analyse the contribution of wave reflections in shaping the pulse waveforms under physiological and pathological conditions.

6.1 Introduction

Blood pressure is an important index in the assessment of disease condition such as hypertension, but the shape of the pulse wave at a given location in the arteries also carries valuable information about the health of blood vessels, workload on heart ventricles, and the nature of complex dynamic interaction between heart and arteries. Therefore from a clinical point of view, the shape of the pressure pulse is as important as its magnitude. Throughout our simulations, we also observed significant variations in particular in the shape and magnitude of propagating pressure wave both in physiology and pathology. Understanding the underlying mechanisms involved in shaping the normal and abnormal pressure pulse is vital to an early detection and treatment of diseases like hypertension.

It has long been recognized that the pulse wave, originated by cardiac contraction, gets partially reflected and partially transmitted whenever it meets a discontinuity in the material properties of vessels such as an abrupt change in compliance or the cross–sectional area (e.g. at junctions) [13,111]. Since the arterial pulse wave velocity (PWV) is high (1.8–4.8 ms^{-1} in the MPA [48, 106] and 3.5–14 ms^{-1} in the systemic arteries [188] in human), the initial wave generated during systole has sufficient time to travel to and back from distal reflection sites in the circulation within the same cardiac cycle and meet the incident wave in the systole. These reflections make significant contributions to ventricular afterload and overall haemodynamics, as the pulse wave observed at any given location is the composition of forward running (originating from heart) incident and backward running reflected waves (originating in the circulation) [172]. Understanding the contributions of these reflected waves to overall haemodynamics requires the decomposition of the observed pulse waveform into its incident and reflected components along with the quantification of reflected waves and their arrival times. In this thesis, we use the term forward or incident, denoted by a '+' in the subscripts, to describe the properties associated with the waves propagating from heart toward periphery and the terms backward or reflected, represented by a '−' sign in subscripts, to describe the attributes of waves traveling in the direction opposite to the forward wave i.e. from periphery towards heart.

About quarter of century ago, based on the method of characteristics solution of one–dimensional conservation laws in a compliant tube, Parker & Jones [118] developed the new time domain technique of Wave Intensity Analysis (WIA). The objective of WIA was to provide an alternative to traditionally used Fourier based impedance analysis [181] to identify and analyse the origin, type, magnitude and direction of local waves in the space–time domain without being the hostage of any periodicity or linearity assumption. The WIA requires simultaneously measured pressure and velocity and the knowledge of pulse wave velocity (PWV) at a fixed position in an artery to separate the pulse wave into forward and backward running components.

Since Parker & Jones [118], several studies used WIA to study the role of wave reflections in shaping the apparent pressure and flow–rate/velocity waveforms in the systemic [79, 80, 84, 112, 157] and coronary [44, 158] arteries using simultaneously measured *in vivo* pressure and velocity data. Some investigators [6, 7, 109, 110] also utilized the numerically generated pressure and flow data from one dimensional models of circulation to test the technique of WIA. Most of these studies, however, explicitly relate to the systemic or coronary arteries and to the best of our knowledge, to date only a few studies can be found which specifically discuss the wave reflections in pulmonary circulation [47, 70, 71, 150, 151]. Non of these studies use numerically obtained pressure and flow data from pulmonary circulation models to investigate the contribution of wave reflections in the pulmonary arteries.

The pulmonary system differs from the systemic circulation in more than one way including the differences in compliance and geometry, which influence the PWV and pressures in the system. Moreover, there is no dominant arterial pathway such as the aorta in the systemic circulation, which makes it difficult to interpret the results in terms of reflection sites in the pulmonary circulation [126]. As for the disease conditions, under clinical situations, it has been observed that due to the high compliance and an exceptional ability of the pulmonary circulation to recruit blood vessels in the microcirculation during the periods of high flow, about 50–60% of the pulmonary microcirculation is diseased before a pressure rise is manifest in the large arteries [42] and that the pulmonary hypertension is a late manifestation of pulmonary vascular disease [48]. This suggests that comparing *in vivo* results of pulmonary WIA with the numerically generated results from a model that does not truly represent the the pulmonary circulation, would not be the best approach.

In Chapter 4 we showed that the diseases like PAH and PH associated with HLD, which have their pathophysiology located in the microcirculation, can be simulated by changing the structured tree parameters in our model. This allows us to carry out an in-depth analysis of observed pressure and flow waveforms under functional and structural changes in the periphery circulation by investigating the influence of microcirculatory parameters on wave reflections, which is not possible to do in *in vivo* studies. This may help in explaining the contribution of wave reflections on the progression of diseases like PAH and PH in HLD. Where possible, we have tried to test the reliability and validity of our model through qualitative comparison of our WIA results with the existing results from *in vivo* studies [47, 48, 69, 70].

6.2 Method of wave intensity analysis (WIA)

In this section we describe the details of wave intensity analysis (WIA) by first giving the definition of wave intensity ($\mathrm{d}I'$) followed by the separation of the nonlinear pulse wave into forward and backward components. The method of WIA is well established but still developing [117]. The analysis presented in this section is the "traditional WIA" [5], which is used by many investigators [44, 47, 70, 71, 79, 80, 84, 112, 150, 151, 157, 158] to study the patterns of wave reflections. The analysis below is based on the original work of Parker & Jones [118], Mynard *et al.* [109] and Sherwin *et al.* [145].

6.2.1 The wave intensity ($\mathrm{d}I$)

Parker and Jones [118] suggested that instead of treating pulse wave as summation of sinusoidal wavetrains, it can be studied by fragmenting the simultaneously measured pressure and velocity waves into infinitesimal elements, usually referred as 'wavefronts' in the context of WIA [117–119], which run forwards and backwards in (x,t) space. In the WIA these wavefronts are the fundamental elements, defined as the temporal changes in p and u at a fixed position $x = X$ along the arteries

$$\mathrm{d}p(x,t) = p(x,t+\delta t) - p(x,t), \tag{6.1}$$

$$\mathrm{d}u(x,t) = u(x,t+\delta t) - u(x,t), \tag{6.2}$$

which sum up to provide the original wave [175]. The net wave intensity, $\mathrm{d}I'$, at a given location in an artery is simply defined as the product of simultaneously occurring pressure and velocity wavefronts i.e.

$$\mathrm{d}I'(x,t) = \mathrm{d}p(x,t)\,\mathrm{d}u(x,t). \tag{6.3}$$

In the above definition, $\mathrm{d}I'$ has the dimensions of energy flux per unit area and the units of $\mathrm{W/m^2}$, which corresponds to acoustic intensity [93]. However, it refers to energy flux associated with the wave motion only and is much smaller quantity than the flow power per unit area, PU [118]. The dimensional interpretation of $\mathrm{d}I'$ in analogy with acoustic intensity does contribute to its physical meaning, however, the actual utility of this definition relies on its ability to identify the contribution of forward and backward running waves at all times during the cardiac cycle [117]. The problem with this definition though is that it requires the segmentation of p and u, which implies that the value of $\mathrm{d}I'$ necessarily depends on the time discretisation and e.g. doubling the time interval would double the magnitude of $\mathrm{d}I'$. To tackle this issue many investigators [47,48,81,112,139,157] have used an alternative definition where the wave intensity is defined as the product of rate of change of p and u instead of simple wavefronts i.e.

$$\mathrm{d}I = \frac{\mathrm{d}p}{\mathrm{d}t}\frac{\mathrm{d}u}{\mathrm{d}t}, \tag{6.4}$$

which has the uints of $\mathrm{W/m^2s^2}$. However, $\mathrm{d}I$ now loses its analogy with the acoustic intensity as there does not seem to have any physical quantity with the same dimensions as $\mathrm{d}I$. Nevertheless $\mathrm{d}I$ retains the utility to identify the contribution of forward or backward running waves [81, 157].

The sign of $\mathrm{d}I$ (and $\mathrm{d}I'$) indicates the presence of four predominant waves at any given location. If the net wave intensity, $\mathrm{d}I$, is positive then the forward running waves are dominant and if $\mathrm{d}I$ is negative that would indicate the dominance of backward running waves. The forward and backward waves are further classified into forward and backward compression or decompression waves. The successive wavefronts add up to a compression wave, if there is a positive change in pressure ($\mathrm{d}p > 0$); a decompression or expansion wave, if the changes in pressure are negative ($\mathrm{d}p < 0$); accelerating waves, with positive changes in the velocity ($\mathrm{d}u > 0$) and the decelerating waves with negative changes in the velocity ($\mathrm{d}u < 0$). This interpretation of $\mathrm{d}I$ is summarised in Table 6.1.

$\mathrm{d}p$	Wavefront	$\mathrm{d}u$	Wave Nature	$\mathrm{d}I$	Wave Type	Wave Origin
> 0	Compression	> 0	Accelerating	> 0	Forward Compression	heart
< 0	Decompression	< 0	Decelerating	> 0	Forward Decompression	heart
> 0	Compression	< 0	Decelerating	< 0	Backward Compression	circulation
< 0	Decompression	> 0	Accelerating	< 0	Backward Decompression	circulation

Table 6.1: Identification of compression and decompression waves, their nature and location of origin, through wave intensity.

Although the calculation of $\mathrm{d}I$ does not require the knowledge of the local PWV or a linearising assumption that approximate the PWV [117], the wave intensity in this case only reflects the net effect of forward and backward waves so that, e.g. a backward wave may not be detected if a large forward wave exists around the same time. Also, $\mathrm{d}I$ may be zero if there are no wavefronts at all or a forward and backward wavefronts of same magnitudes exist at the same time. Thus to further clarify the contribution of forward and backward waves it is necessary to decompose $\mathrm{d}I$ by separating the wave intensity

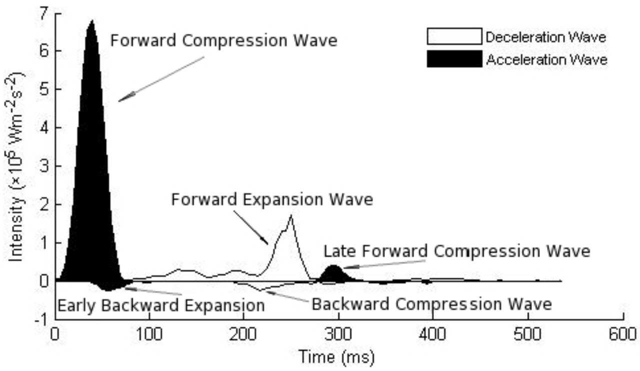

Figure 6.1: Figure 3.1 (p. 68) from Dwyer (2010) [48] shows typical pattern of wave intensity profile in the resting proximal pulmonary artery of a healthy sheep over one cardiac cycle. Different types and nature of the local waves, explained in Table 6.1, are identified and indicated in the figure. The expansion waves, indicated in the figure, are defined as decompression waves in this thesis. (Figure reproduced with permission from the rights holder.)

profiles into forward and backward components. This requires the knowledge of PWV which is a challenge, especially when the simultaneous pressure and velocity measurements are obtained using invasive means of data acquisition. Since we have the advantage of prescribing the pressure–PWV relation through tube law, we can perform the non–linear wave separation without making any linearity assumption about the PWV [109].

Below we present the mathematical analysis which leads us to decompose the pressure and velocity waves and hence the wave intensity profiles. The theory is based on the time–domain analysis of conservation of mass and momentum by the method of characteristics, also known as the Riemann method of characteristics, after his work on the solution of hyperbolic PDEs in 1859 [143], which was exploited by Parker & Jones [118], for the first time in 1990, to study the wave reflections in the arteries. Although mathematically subtle, the analysis leads us to the results which are simple to implement.

6.2.2 Separation of pulse wave

Consider the conservation of volume and momentum in (A, q, p) variables, given by (2.15) and (2.24)

$$\frac{\partial A}{\partial t} + \frac{\partial q}{\partial x} = 0, \tag{6.5}$$

$$\frac{\partial q}{\partial t} + \frac{\partial}{\partial x}\left(\frac{q^2}{A}\right) + \frac{A}{\rho}\frac{\partial p}{\partial x} = -\frac{2\pi\mu R}{\rho\delta}\frac{q}{A}. \tag{6.6}$$

Conventionally the WIA is carried out by using the governing equations in (A, u, p) instead of (A, q, p) system [76]. If the viscous losses are small then the interconversion of flow-rate and velocity only requires the knowledge of area as $q = Au$. Substituting this into (6.5) and (6.6) and expanding, we obtain

$$\frac{\partial A}{\partial t} + u\frac{\partial A}{\partial x} + A\frac{\partial u}{\partial x} = 0, \tag{6.7}$$

$$\frac{\partial u}{\partial t} + u\frac{\partial u}{\partial x} + \frac{1}{\rho}\frac{\partial p}{\partial x} = \frac{\mathcal{F}}{\rho A}, \tag{6.8}$$

where

$$\mathcal{F} = -\frac{2\pi\mu R u}{\delta},$$

is the viscous dissipation or frictional loss term. The pressure–area relation for a purely elastic vessel is given by (2.28), which states that

$$p(x,t) = p_0 + f(r_0(x))\left(1 - \sqrt{\frac{A_0}{A}}\right), \tag{6.9}$$

where

$$f(r_0(x)) = \frac{4}{3}\frac{Eh}{r_0(x)}.$$

From (6.9) one can rewrite the pressure gradient term in (6.8) as

$$\frac{\partial p}{\partial x} = \frac{\partial p}{\partial A}\frac{\partial A}{\partial x} + \frac{\partial p}{\partial A_0}\frac{\partial A_0}{\partial x} + \frac{\partial p}{\partial f}\frac{\partial f}{\partial x}. \tag{6.10}$$

Inserting it back into (6.8) will yield

$$\frac{\partial u}{\partial t} + u\frac{\partial u}{\partial x} + \frac{1}{\rho}\frac{\partial p}{\partial A}\frac{\partial A}{\partial x} = \frac{1}{\rho}\left(\frac{\mathcal{F}}{A} - \frac{\partial p}{\partial A_0}\frac{\partial A_0}{\partial x} - \frac{\partial p}{\partial f}\frac{\partial f}{\partial x}\right). \tag{6.11}$$

Method of characteristics

Writing system of equations (6.7) and (6.11) in a non-conservative form, we get

$$\frac{\partial \mathbf{U}}{\partial t} + \mathbf{A}\frac{\partial \mathbf{U}}{\partial x} = \mathbf{B}, \tag{6.12}$$

where

$$\mathbf{U} = \begin{bmatrix} A \\ u \end{bmatrix}, \qquad \mathbf{A} = \begin{bmatrix} u & A \\ \frac{1}{\rho}\frac{\partial p}{\partial A} & u \end{bmatrix}, \quad \text{and} \quad \mathbf{B} = \begin{bmatrix} 0 \\ \frac{1}{\rho}\left(\frac{\mathcal{F}}{A} - \frac{\partial p}{\partial A_0}\frac{\partial A_0}{\partial x} - \frac{\partial p}{\partial f}\frac{\partial f}{\partial x}\right) \end{bmatrix}.$$

The system (6.12) is a fully non–linear system where the non–linearities arise from convective term, pressure–area relation, frictional loss term, non–uniform compliance and spatial variation of cross–sectional area A_0 due to taper. It is also apparent that, apart from frictional losses, the matrix $\mathbf{A}$ contains all the necessary information, such as distensibility, fluid density, local geometry and convective acceleration, which may influence the pulse wave propagation. Further more, since A and $\frac{1}{\rho}\frac{\partial p}{\partial A} > 0$, $\mathbf{A}$ has two real eigenvalues, given by

$$\Lambda_{\pm} \, = \, u \pm \sqrt{\frac{A}{\rho}\frac{\partial p}{\partial A}}. \tag{6.13}$$

Bramwell and Hill [23] noted that the square root term in (6.13) has the dimensions of velocity and therefore recognised it as the velocity of wave propagation (PWV), conventionally denoted by c. Thus the eigenvalues can be written as

$$\Lambda_{\pm} \, = \, u \pm c. \tag{6.14}$$

Since the eigenvalues of the $\mathbf{A}$ are real, (6.7) and (6.8) coupled with (6.9) form a nonlinear system of hyperbolic equations. Corresponding left eigenvectors $\mathbf{v}_{\pm}$ of $\mathbf{A}$ can easily be determined as

$$\mathbf{v}_{\pm}^{\dagger} \left[\mathbf{A} - \Lambda_{\pm}\right] \, = \, 0,$$

which gives us

$$\mathbf{v}_{+} \, = \, \zeta \begin{bmatrix} \frac{c}{A} \\ 1 \end{bmatrix} \quad \text{and} \quad \mathbf{v}_{-} \, = \, \zeta \begin{bmatrix} -\frac{c}{A} \\ 1 \end{bmatrix},$$

where ζ is the scaling constant. By introducing the matrix of left eigenvectors, $\mathbf{L}$ of $\mathbf{A}$, the matrix $\mathbf{A}$ can be decomposed in terms of diagonal vector $\mathbf{D}$ of $\Lambda_{\pm}$, as

$$\mathbf{A} \, = \, \mathbf{L}^{-1}\mathbf{D}\mathbf{L}, \tag{6.15}$$

where

$$\mathbf{L} \, = \, \zeta \begin{bmatrix} \frac{c}{A} & 1 \\ -\frac{c}{A} & 1 \end{bmatrix} \quad \text{and} \quad \mathbf{D} \, = \begin{bmatrix} \Lambda_f & 0 \\ 0 & \Lambda_b \end{bmatrix}.$$

Substituting (6.15) in (6.12) and premultiplying by $\mathbf{L}$ we get

$$\mathbf{L}\frac{\partial \mathbf{U}}{\partial t} + \mathbf{D}\,\mathbf{L}\frac{\partial \mathbf{U}}{\partial x} \, = \, \mathbf{L}\,\mathbf{B}. \tag{6.16}$$

In order to solve the above system we introduce the following change of variable

$$\mathbf{L} \, = \, \frac{\partial \mathbf{R}}{\partial \mathbf{U}}, \tag{6.17}$$

where $\mathbf{R} = [R_+ \;\; R_-]^\dagger$ is the vector of characteristic functions or Riemann variables. Substituting (6.17) into (6.16), we obtain

$$\frac{\partial \mathbf{R}}{\partial \mathbf{U}}\frac{\partial \mathbf{U}}{\partial t} + \mathbf{D}\frac{\partial \mathbf{R}}{\partial \mathbf{U}}\frac{\partial \mathbf{U}}{\partial x} = \mathbf{L}\,\mathbf{B}, \tag{6.18}$$

or

$$\frac{\partial \mathbf{R}}{\partial t} + \mathbf{D}\frac{\partial \mathbf{R}}{\partial x} = \mathbf{L}\,\mathbf{B}. \tag{6.19}$$

Let us define $\hat{x} = \hat{x}(t)$ as a parametric function in the (x,t) space, then the variation in $\mathbf{R}$ along $\hat{x}(t)$ may be written as

$$\frac{\mathrm{d}\mathbf{R}(\hat{x}(t),t)}{\mathrm{d}t} = \frac{\partial \mathbf{R}}{\partial t} + \frac{\mathrm{d}\hat{x}}{\mathrm{d}t}\mathbf{I}\frac{\partial \mathbf{R}}{\partial \hat{x}}. \tag{6.20}$$

Comparing (6.20) with (6.19), we observe that if

$$\frac{\mathrm{d}\hat{x}}{\mathrm{d}t}\mathbf{I} = \mathbf{D}, \tag{6.21}$$

then along the path $\hat{x}(t)$ we have

$$\frac{\mathrm{d}\mathbf{R}}{\mathrm{d}t} = \mathbf{L}\,\mathbf{B}, \tag{6.22}$$

where $\frac{\mathrm{d}}{\mathrm{d}t} = \frac{\partial}{\partial t} + \Lambda_\pm \frac{\partial}{\partial x}$ is the total time derivative. Equation (6.22) tells us that one can solve for $\mathbf{R}(\hat{x}(t),t)$ along the path $\hat{x}(t)$ merly by integrating (6.22) along $\hat{x}(t)$ and by using the initial value of $\mathbf{R}$. Thus $\hat{x}(t)$ defines the characteristic paths or directions, $\mathrm{C}_\pm$, in (x,t) space along which the information (about the wave) contained in $\mathbf{R}$ propagates with speed $\Lambda_\pm$. From (6.21), two characteristic paths C_+ and C_- are given as

$$\mathrm{C}_\pm \equiv \frac{\mathrm{d}\hat{x}_\pm}{\mathrm{d}t} = \Lambda_\pm = u \pm c\,. \tag{6.23}$$

According to (6.22) the values of Riemann variables $R_\pm$ change due to the frictional losses and elastic and geometric changes along $\mathrm{C}_\pm$ in the (x,t) space. Moreover, under normal physiological conditions $u \ll c$, so $\Lambda_f > 0$ and $\Lambda_b < 0$. Since $\Lambda_f > 0$, it follows that the information about pressure and velocity perturbations contained in R_+ propagates along C_+ in the forward direction in (x,t) space i.e. from proximal to distal locations in the arterial system, whereas along C_-, the path with negative slope, the information contained in R_- travels backward in (x,t) space i.e. in the opposite direction from distal to proximal locations in the arteries.

The system (6.12) is non–linear due to the convective term $u\frac{\partial u}{\partial x}$, the non–linear pressure–area relation (6.9) and the frictional loss term $\frac{\mathcal{F}}{\rho A}$, which makes it impossible to analytically solve the coupled system (6.22) for $\mathbf{R}$. However, the system can be decoupled under certain simplifying assumptions before solving for Rieman variables R_+ and R_-.

Since under physiological conditions the flow in the large arteries is inertia driven with a flat velocity profile [126] and the frictional losses can be neglected, which leads us to ignore the term in (6.8) by assuming $\frac{\mathcal{F}}{\rho A} \ll 1$. This assumption may be overly restrictive if applied to the arterial system as a whole but in the WIA we only require local validity of this assumption as p and u are measured at a fixed location in the arteries. Therefore as long as this and other assumptions are valid in the neighbourhood of the measurement site, the analysis is valid [118]. Moreover, if the equilibrium cross–sectional area A_0 and material properties $f(r_0(x))$ are constant along the length of an artery then $\mathbf{B} = 0$ in (6.22), which makes (6.22) a decoupled system of equations

$$\frac{\mathrm{d}\mathbf{R}}{\mathrm{d}t} = 0 \tag{6.24}$$

that provides us two equations in $R_\pm$ as

$$\left(\frac{\partial}{\partial t} + \Lambda_\pm \frac{\partial}{\partial x}\right) R_\pm = 0, \tag{6.25}$$

In conventional one-dimensional fluid dynamics, for any function g, if $\frac{Dg}{Dt} = 0$, where $\frac{D}{Dt} = \frac{\partial}{\partial t} + u\,\frac{\partial}{\partial x}$, then the rate of change of g moving with a fluid particle with speed u is zero implying that g is a constant function. Thus a comparison of $\frac{\mathrm{d}}{\mathrm{d}t}$ in equation (6.24) with $\frac{D}{Dt}$ illustrates that the Riemann variables $R_\pm$, propagating along the characteristic paths $\mathrm{C}_\pm$ with speed $\Lambda_\pm$, are constants. In this case $R_\pm$ are called “Riemann invariants” instead of “Riemann variables” of the system (6.7) and (6.8) [117]. This result, however, only remains valid subject to the assumptions of a uniform vessel and negligible viscous dissipation in the neighbourhood of measurement location. In order to integrate (6.17) for the Riemann invariants, the following equation has to be satisfied

$$\frac{\partial^2 R_\pm}{\partial A\,\partial u} = \frac{\partial^2 R_\pm}{\partial u\,\partial A},$$

which requires the scaling factor ζ of matrix $\mathbf{L}$ to be constant. Thus, for $\zeta = 1$, the Riemann invariants in terms of u and A can be determined by integrating (6.17) about the reference state (A_0, u_0) as

$$R_\pm = \int_{u_0}^{u} du^* \pm \int_{A_0}^{A} \frac{c\,(A^*)}{A^*} dA^* = u - u_0 \pm \int_{A_0}^{A} \frac{c\,(A^*)}{A^*} dA^*. \tag{6.26}$$

Using the pulse wave velocity relation

$$c^2 = \frac{A}{\rho}\frac{\partial p}{\partial A} \tag{6.27}$$

and the known pressure–area relation (6.9), we get

$$c(A) = \sqrt{\frac{f}{2\,\rho}} \left(\frac{A_0}{A}\right)^{\frac{1}{4}}. \tag{6.28}$$

Using (6.28) in (6.26) and assuming that during diastole, when $A = A_0$, there is no velocity in the arteries i.e. $u_0 = 0$, we get

$$R_{\pm} = u \pm 4\,(c_0 - c), \tag{6.29}$$

where c_0 is the constant PWV at $A = A_0$, given by

$$c_0 = \sqrt{\frac{f}{2\,\rho}}. \tag{6.30}$$

The expression (6.30) for c_0 above is the Moens–Korteweg PWV given by Moens and Korteweg in 1878, although first discovered by Young in 1809 [187]. A similar looking result for $R_{\pm}$ is also obtained by Sherwin *et al.* [145] by using a different equation of state, given by

$$p(x,t) = p_0 + \Psi(x)\left(\sqrt{\frac{A}{A_0}} - 1\right), \tag{6.31}$$

where $\Psi(x) = f(r_0(x))$ in equation (6.9). The tube law in (6.31) corresponds to slightly different expressions for Riemann invariants, given by

$$R_{\pm} = u \,\pm\, 4\,(c - c_0),$$

where

$$c = \sqrt{\frac{\Psi}{2\,\rho}} \left(\frac{A}{A_0}\right)^{1/4}$$

due to a different pressure area relation. Noting from (6.27) that

$$c = \frac{A}{c\rho}\frac{\partial p}{\partial A},$$

the integral in (6.26) can be written as

$$\int_{A_0}^{A} \frac{c\,(A^*)}{A^*} dA^* = \int_{p_0}^{p} \frac{dp^*}{\rho\, c\,(p^*)}.$$

Thus the Riemann invariants can also be expressed in terms of p instead of A as

$$R_{\pm} = u - u_0 \pm \int_{p_0}^{p} \frac{dp^*}{\rho\, c\,(p^*)}, \tag{6.32}$$

where the pressure dependent PWV in (6.32) is given by

$$c\,(p) = \sqrt{\frac{f - p(A)}{2\,\rho}}, \tag{6.33}$$

and $p(A) = p(x,t) - p_0$. The conversion from $c(A)$ to $c(p)$ leads to the same expression for R_+ and R_- given by (6.29).

Wave separation

By using the solution of $\mathbf{R}$ from the method of characteristics one can decompose the pulse wave into forward and backward running components by incorporating the non–linear effects arising due to convective acceleration and dependance of c on p or A. However this technique does not capture the non–linear effects due to frictional losses on wave separation.

From equation (6.32), the changes in Riemann invariants corresponding to changes in p and u can be written as

$$\mathrm{d}R_\pm = \mathrm{d}u \pm \frac{\mathrm{d}p}{\rho\, c(p)}, \tag{6.34}$$

Solving for dp and du, we obtain

$$\mathrm{d}p = \frac{\rho\, c(p)}{2}(\mathrm{d}R_+ - \mathrm{d}R_-), \tag{6.35}$$

$$\mathrm{d}u = \frac{1}{2}(\mathrm{d}R_+ + \mathrm{d}R_-). \tag{6.36}$$

Since the Riemann invariant along a backward characteristic, C$_-$, that intersects two forward characteristics, must be preserved for all times, the changes in pressure and velocity in the absence of changes in R_-, between the two points of intersection are defined as 'forward', and vice versa, so

$$\mathrm{d}p_+ = \mathrm{d}p\,|_{\mathrm{d}R_-=0} \quad \text{and} \quad \mathrm{d}p_- = \mathrm{d}p\,|_{\mathrm{d}R_+=0},$$

$$\mathrm{d}u_+ = \mathrm{d}u\,|_{\mathrm{d}R_-=0} \quad \text{and} \quad \mathrm{d}u_- = \mathrm{d}u\,|_{\mathrm{d}R_+=0}.$$

Thus the forward and backward wavefronts of pressure and velocity in terms of Riemann invariants can be deduced from (6.35) and (6.36) as

$$\mathrm{d}p_\pm = \pm\rho\, c_\pm \frac{\mathrm{d}R_\pm}{2}, \tag{6.37}$$

$$\mathrm{d}u_\pm = \frac{\mathrm{d}R_\pm}{2}, \tag{6.38}$$

where $c_\pm = c(p_\pm)$ indicating the pressure dependent PWV that would vary from net $c(p)$ if only forward or backward waves exist. Also writing (6.37) and (6.38) together yield an expression

$$\mathrm{d}p_\pm = \pm\,\rho\, c_\pm\, \mathrm{d}u_\pm, \tag{6.39}$$

which is the well known Water–Hammer (WH) equation, first derived by Johannes Von Kries in 1883, a German physiologist, during his work on pulse propagation in blood vessels [174]. The WH equation reveals the coupled nature of pressure and velocity in elastic tubes and provide an expression for PWV, given by

$$c_{\pm} = \pm \frac{1}{\rho} \frac{\mathrm{d}p_{\pm}}{\mathrm{d}u_{\pm}}. \tag{6.40}$$

Moreover, plugging (6.34) into (6.37) and (6.38) gives us

$$\mathrm{d}p_{\pm} = \frac{1}{2}(\mathrm{d}p \pm \rho\, c(p)\, \mathrm{d}u), \tag{6.41}$$

$$\mathrm{d}u_{\pm} = \frac{1}{2}\left(\mathrm{d}u \pm \frac{\mathrm{d}p}{\rho\, c(p)}\right). \tag{6.42}$$

Equation (6.41) tells us that a forward pressure wave is a compression wave if $\mathrm{d}p_{+} > 0$ and a decompression wave of $\mathrm{d}p_{+} < 0$. Similarly the backward pressure wave is compression or decompression wave if $\mathrm{d}p_{-} > 0$ or $\mathrm{d}p_{-} < 0$, respectively.

Finally, the separated forward and backward components of pressure and velocity waveforms can be obtained by integrating the corresponding wavefronts over a complete cardiac cycle, which provides us

$$p_{\pm} = p_0 + \int_{t_0}^{t} \mathrm{d}p_{\pm}, \tag{6.43}$$

$$u_{\pm} = u_0 + \int_{t_0}^{t} \mathrm{d}u_{\pm}, \tag{6.44}$$

or in discrete from as

$$p_{\pm} = p_0 + \sum_{t_0}^{t} \mathrm{d}p_{\pm}. \tag{6.45}$$

$$u_{\pm} = u_0 + \sum_{t_0}^{t} \mathrm{d}u_{\pm}. \tag{6.46}$$

Here p_0 and u_0 are the constants of integrations, normally chosen as the values of p and u at the end of diastole but may be taken differently such as the values of p and u at any $t = t_0$ or $p = u = 0$.

Separated wave intensity: Using the solution for Riemann invariants, the net wave intensity can also be expressed in terms of Riemann invariants as

$$\mathrm{d}I' = \mathrm{d}p\, \mathrm{d}u = \frac{\rho\, c(p)}{4}(\mathrm{d}R_{+}^{2} - \mathrm{d}R_{-}^{2}). \tag{6.47}$$

The separated wave intensities are given by

$$\mathrm{d}I'_{\pm} = \mathrm{d}p_{\pm}\, \mathrm{d}u_{\pm} = \pm \frac{\rho\, c_{\pm}}{4}\, \mathrm{d}R_{\pm}^{2}. \tag{6.48}$$

Or in the time derivative form as

$$\mathrm{d}I_{\pm} = \frac{\mathrm{d}p_{\pm}}{\mathrm{d}t}\frac{\mathrm{d}u_{\pm}}{\mathrm{d}t} = \pm\frac{\rho\, c_{\pm}}{4}\left(\frac{\mathrm{d}R_{\pm}}{\mathrm{d}t}\right)^2. \tag{6.49}$$

$\mathrm{d}I'_{\pm}$ and $\mathrm{d}I_{\pm}$ may also be calculated explicitly in terms of $\mathrm{d}p$ and $\mathrm{d}u$ by using (6.41) and (6.42). The results above show that the forward or backward running wave components make strictly positive or negative contribution to the net wave intensity i.e. the associated wave intensities of forward or backward waves are strictly positive or negative. Moreover, $\mathrm{d}p_{\pm}$, $\mathrm{d}u_{\pm}$ and $\mathrm{d}I_{\pm}$ are computed non–linearly by incorporating the pressure (or area) dependence of PWV, therefore the forward and backward components are not additive in general [136].

6.2.3 Quantification of reflections

The pulse waves are partially reflected and partially transmitted at the site of impedance ($\rho c_0/A_0$) mismatch, such as the arterial junctions, and the type of reflections depend on the local properties of reflection sites. Several authors [32, 55, 126] discuss the quantification of reflected waves by calculating a linear reflection coefficient $\mathcal{R}$, defined as the ratio of amplitude of reflected waves to that of incident wave, in terms of local impedances at the junction. However, it is possible to quantify the amount of reflected waves by relating the changes in the wave intensities to the properties of reflection sites in the circulation.

For a network of arteries with a single parent and two daughter vessels, it has been shown in [5, 145] that the changes in the reflected pressure and velocity $(\mathrm{d}p_-, \mathrm{d}u_-)$ in the parent and two daughter vessels can be related to the corresponding changes in the incident pressure and velocity $(\mathrm{d}p_+, \mathrm{d}u_-)$ by using the method of characteristic solution of linearized version of (6.5) and (6.6), coupled with (6.9), about the reference state $(A, p, q) = (A_0, p, 0)$ with small perturbations (a', p', q') in the quantities.

Considering the frictional effects to be negligible ($\mathcal{F} \approx 0$) in the parent and daughter vessels of an arterial bifurcation, initial small perturbations $(\triangle a^i, \triangle p^i, \triangle q^i)$ (for $i = p, d_1, d_2$) in the undisturbed state $(A^i, p^i, q^i) = (A^i_0, p^i_0, 0)$ will propagate toward the junction to produce a wave in each vessel with perturbations $(\hat{\delta} a^i, \hat{\delta} p^i, \hat{\delta} q^i)$ that propagates away from the junction. Consequently, using the method of characteristics solution of linearized system of equations along with pressure continuity and flow conservation at the junction, the reflected pressure and velocity wavefronts $(\mathrm{d}p_-, \mathrm{d}u_-)$ in each vessel are related to the corresponding changes in the incident pressure and velocity $(\mathrm{d}p_+, \mathrm{d}u_-)$ by [5]

$$\mathrm{d}p_-^i = \mathcal{R}^i\,\mathrm{d}p_+^i, \qquad \mathrm{d}u_-^i = -\mathcal{R}^i\,\mathrm{d}u_+^i, \qquad i = p, d_1, d_2, \tag{6.50}$$

where $\mathcal{R}^i$ is the linear reflection coefficient, given by

$$\mathcal{R}^p = \frac{Y^p - Y^{d_1} - Y^{d_2}}{Y^p + Y^{d_1} + Y^{d_2}}, \quad \mathcal{R}^{d_1} = \frac{Y^{d_1} - Y^{d_2} - Y^p}{Y^p + Y^{d_1} + Y^{d_2}}, \quad \mathcal{R}^{d_2} = \frac{Y^{d_2} - Y^{d_1} - Y^p}{Y^p + Y^{d_1} + Y^{d_2}}. \tag{6.51}$$

Here Y is local admittance of the vessels given by

$$Y = \frac{A_0}{\rho\,c_0},$$

the reciprocal of which is known as local impedance of vessel, normally denoted by Z [32] (see Appendix C of [5] for the derivations of (6.50) and (6.51)).

Clearly the reflection coefficient $\mathcal{R}^i$ depends on the local properties of vessel and defines the behaviour of reflection site, a junction in this case. Considering the case of the parent vessel as an instance, from (6.51) one may observe that if the sum of the admittances of daughter vessels is same as that of parent vessel, then $\mathcal{R}^p = 0$ and the junction is called a *well–matched* junction. In this case no waves are reflected into parent vessels and the incident wave is completely transmitted into the daughter vessels without getting reflected. However, if the sum of admittances of daughter vessels is greater than the parent vessels, then $\mathcal{R}^p$ is negative and there is a reflected wave back into parent vessel which is out of phase with the incident wave. Such reflections are called negative or open–end type wave reflections and have a cancelling effect on the incident wave so they serve to reduce the amplitude of observed pressure or velocity wave at a given location. These kind of junctions are known as *open–end* junctions and may only occur if the sum of the cross-sectional areas of daughter vessels or the compliances are much larger than the parent vessel. In this case $\mathcal{R}^p \to -1$ with increasing compliance and (or) the total cross–sectional area of daughter vessels. On the other hand, at a *closed–end* junction, the total cross–sectional area at the entrance (proximal end) of daughter vessels is smaller than the outlet (distal end) cross–sectional area of the parent vessel and (or) they are stiffer than the parent vessel, which means that the sum of their admittances would be less than the admittance of parent vessel yielding a positive $\mathcal{R}^p$. A positive $\mathcal{R}^p$ causes a positive or closed–end type wave reflection which is in phase with the incident wave and serve to augment the amplitude of incident wave. In this case $\mathcal{R}^p \to 1$ with narrowing of passage at the junction with stiffer daughter vessels. Thus for any situation $\mathcal{R}^p$ ranges between -1 and 1 to reflect the junction behaviour.

From (6.50) the wave intensities of reflected and incident waves can be related through local reflection coefficient $\mathcal{R}$ as

$$\mathrm{d}I_- = -\mathcal{R}^2 \mathrm{d}I_+. \tag{6.52}$$

Using the relation between local $\mathcal{R}$ and $\mathrm{d}I_\pm$, an apparent reflection coefficient may be computed for any arbitrary vessel as the ratio of area averaged values of forward to backward intensities [5], given by

$$\mathcal{R}_{\mathrm{app}} = \pm\sqrt{-\frac{I_-}{I_+}}, \tag{6.53}$$

where

$$I_\pm = \frac{1}{T}\int_0^T \mathrm{d}I'_\pm \mathrm{d}t,$$

or given in the discrete form

$$I_\pm = \frac{1}{t_{\mathrm{end}} - t_0}\sum_{i=0}^{N} \mathrm{d}I'_\pm(t_i)\delta t \tag{6.54}$$

is the averaged wave area or cumulative intensity and N is the number of equally spaced time points in the cardiac cycle T such that $\forall\, t \in [0,T]$, $t_i = i\delta t$, where $i = 0, 1, \ldots, N$. The sign of $\mathcal{R}_{app}$ is determined by the nature of reflected wave i.e. $\mathcal{R}_{app} < 0$ if the reflected wave is a decompression wave ($\mathrm{d}p_- < 0$) or positive of the reflected wave is a compression wave ($\mathrm{d}p_- < 0$). The $\mathcal{R}_{app}$ defined above is comparable with the traditionally used $\mathcal{R}_{\Delta p}$ [32,55,85], which is defined as the amplitude ratio of reflected to incident pressure wave [110] i.e.

$$\mathcal{R}_{\Delta p} = \frac{\Delta p_-}{\Delta p_+}, \tag{6.55}$$

where Δp_+ and Δp_- are the amplitudes of incident and reflected waves, which become known after separating the waves thus making it possible to compute the reflection coefficient.

By using a computer model, Mynard *et al.* [110] showed that $\mathcal{R}_{\mathrm{app}}$ does not reflect the true behaviour of $\mathcal{R}$ in the case of non–linear flow whereas $\mathcal{R}_{\Delta p}$ remains relatively insensitive to the non–linearities and therefore suggests $\mathcal{R}_{\Delta p}$ to be the method of choice to calculate the local reflection coefficient. In this study, we also stick with $\mathcal{R}_{\Delta p}$ as the reflection coefficient. Furthermore, the transit (t_{T}) time between the forward and backward wave is defined as the time difference between the arrival of peak or foot of the backward and forward running waves i.e.

$$t_{\mathrm{T}} = t_- - t_+, \tag{6.56}$$

where t_- and t_+ are the arrival times of backward and forward running waves, respectively. The t_T can also be calculated as the time difference between the area averaged intensities associated with forward and backward wave, given by

$$t_\pm = \frac{1}{TI_\pm}\int_0^T \mathrm{d}I'_\pm\, t\, \mathrm{d}t$$

or equivilantely

$$t_\pm = \frac{1}{(t_\mathrm{end} - t_0)I_\pm}\sum_{i=0}^{N} \mathrm{d}I'_\pm(t_i)\, t_i\, \delta t. \tag{6.57}$$

Finally, with a known PWV c, the distance ($\mathrm{L}_\mathcal{R}$) to reflection site can be calculated by

$$\mathrm{L}_\mathcal{R} = \frac{1}{2}\, t_\mathrm{T}\, c. \tag{6.58}$$

Junctions in our model

Given the dimensions of largest pulmonary arteries, one may easily calculate the area ratio of daughters to parent vessels, Ξ, as

$$\Xi = \frac{A_{1_{prox}} + A_{2_{prox}}}{A_{p_{dist}}},$$

where $A_{1,2_{prox}}$ are the cross–sectional areas of the proximal end of the daughter vessels whereas $A_{p_{dist}}$ denotes the cross–sectional area of the distal end of the parent vessel. Before terminating the tree of large arteries, there are only three junctions in our model, which are: the main pulmonary arterial junction, bifurcating into RPA and LPA; the right pulmonary arterial junction, bifurcating into RIA and RTA and the left pulmonary arterial junction bifurcating into LIA and LTA. The corresponding local area ratios and the linear reflection coefficient $\mathcal{R}$, given by (6.51), at these junctions are given in Table 6.2.

Junction name	Distance from root [cm]	Area ratio Ξ [cm^2]	Reflection coeff. $\mathcal{R}^i$
MPA	4.50	1.23	-0.103
RPA	10.25	1.48	-0.097
LPA	7.00	1.22	-0.193

Table 6.2: Calculated from the model geometry and material properties, given are the local area ratios, Ξ, and the linear reflection coefficients, $\mathcal{R}^i$ (computed from (6.51)), for three junctions of the large pulmonary arteries.

The value of Ξ for MPA junction is within the suggested range of 1.2–1.3 given by Caro & Saffman [31] and Collins & Maccario [37] for the isolated perfused lungs. Moreover, the value of $\Xi > 1$ and $\mathcal{R} < 0$ for all three junctions suggest that they should behave as open–end reflectors.

6.3 Results

In this section we present the results of separated pressure, velocity and wave intensity profiles in the MPA, RPA and LPA. The results are simulated at the midpoint of each artery both for the normal case and for pulmonary hypertension. Throughout our results we have chosen p_0 and u_0 to be zero in equations (6.43) and (6.44) to simulate the forward and backward waveforms and we refer the originally simulated pressure and velocity simply as the pressure and velocity or the pulse wave in a general manner. Moreover, all the wave intensity profiles are given for the time derivative definition of wave intensity, $\mathrm{d}I$, while the numerically computed PWV is averaged over the cardiac cycle to estimate the distance, $\mathrm{L}_{\mathcal{R}}$, to the reflection sites.

6.3.1 Patterns of reflected waves in the large pulmonary arteries in normal physiology

Figure 6.2 shows the simulations of forward and backward components of pressure, velocity, pressure wavefronts and the wave intensity at the midpoints of the MPA, RPA and LPA. From the panels in the first two rows, we observe that the shapes of p_+ and u_+ look similar, which suggests that it is p_- that defines the characteristic shape of the pressure waveform. For pressure wavefronts, the positive region in the panels in third row defines the compression waves (forward if $\mathrm{d}p_+ > 0$ and backward if $\mathrm{d}p_- > 0$) and the negative region illustrates the decompression waves (forward if $\mathrm{d}p_+ < 0$ and backward if $\mathrm{d}p_- < 0$). With the help of panels in the row three and the wave intensity profiles shown in row four, one may identify six distinct waves passing through the midpoints of all three arteries during the cardiac cycle. These are an early systolic forward compression wave (FCW), followed by two distinct forward decompression waves (FDCW) in the late systole which are immediately followed by another forward compression wave at the end of systole. As for the reflected waves, an early mid systole backward decompression wave (BDCW) may be spotted in the MPA, which is almost non-existent in the RPA. However a rather pronounced BDCW is observed in the LPA, which arrives almost in the early systole. In all three arteries, a significantly large backward decompression wave (BDCW) may also

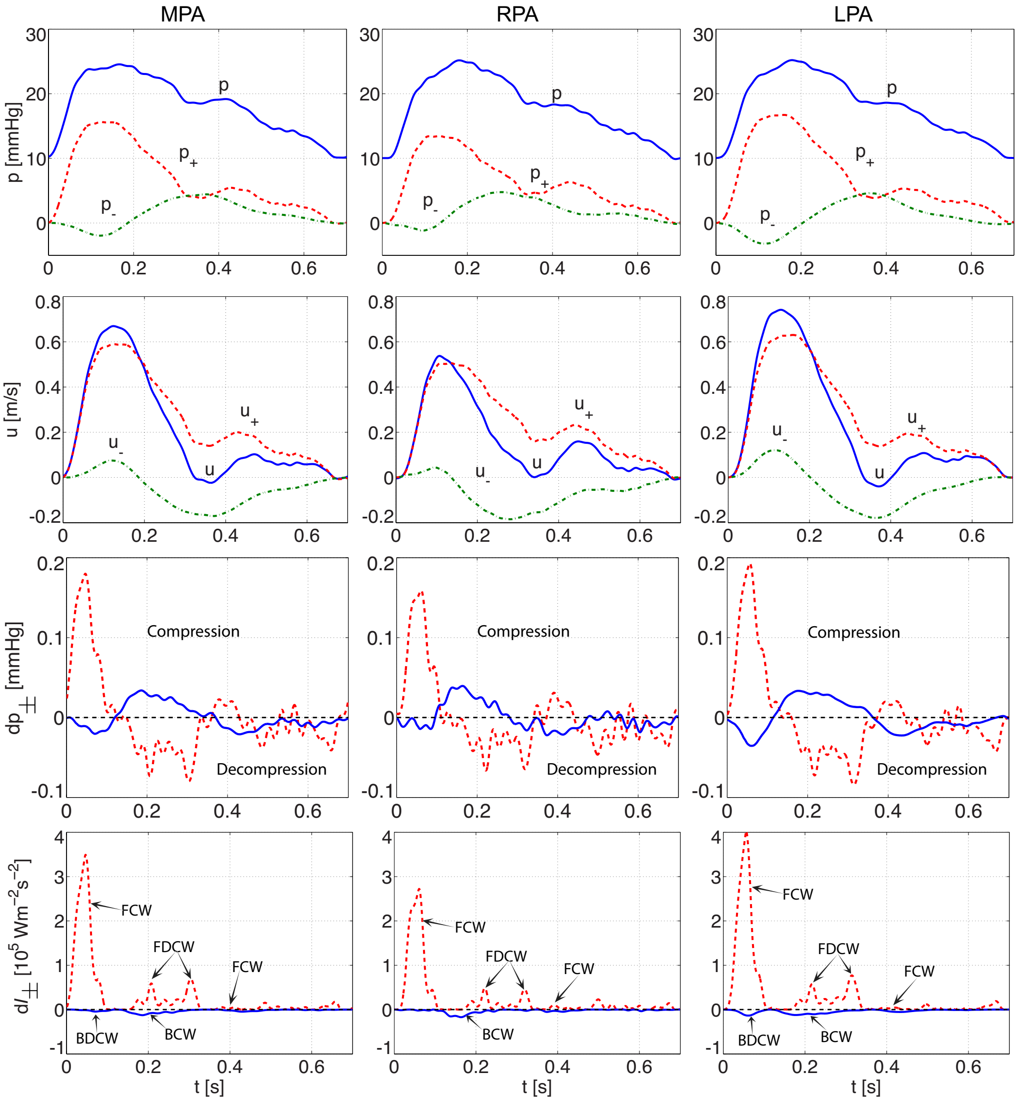

Figure 6.2: Simulation of pressure and velocity waveforms (solid blue) separated into forward (dashed red) and and backward (dashed-dot green) running components at the midpoint in the MPA, RPA and LPA (first two rows). The separated wave intensities and wave fronts, dI_+ and dp_+ (solid blue) and dI_- and dp_- (dashed red) in the MPA, RPA and LPA are shown in the last two rows.

be observed in the late systole. The effects of these waves on the observed blood pressure and flow may be interpreted from the panels in the first two rows, where the early FCW corresponds to forward flow acceleration in the velocity graphs whereas the late systole FDCW decelerates the blood flow. Moreover, the mid systole BDCW also contributes in accelerating the forward flow by reducing the systolic pressure pressure whereas the late systolic BCW serves to decelerate the forward flow by augmenting the blood pressure.

Artery	$\mathcal{R}_{\Delta p}^{\mathrm{BCW}}$	$\mathcal{R}_{\Delta p}^{\mathrm{BDCW}}$	$L_{\mathcal{R}}$ [cm]	t_{T} [s]
MPA	0.28	-0.13	23	0.14
RPA	0.36	-0.09	17	0.10
LPA	0.28	-0.19	16	0.10

Table 6.3: The table shows the calculated reflection coefficients, given by (6.55), and the distance to reflection site ($L_{\mathcal{R}}$), given in (6.58), at the midpoints of MPA, RPA and LPA. The transit time (t_{T}) that an initial wave takes to travel to and from a reflection site is estimated by using (6.56).

Table 6.3 shows that the reflection coefficient for the BCW ($\mathcal{R}_{\Delta p}^{\mathrm{BCW}}$) and BDCW ($\mathcal{R}_{\Delta p}^{\mathrm{BDCW}}$) increases in the RPA. Moreover, for BCW the distance to reflection site form the midpoint of the MPA is estimated to be 23 cm which reduces to 17 and 16 cm in the RPA and LPA respectively. However, it must be noted that $\mathrm{L}_{\mathcal{R}}$ computed here is approximated and not exact as it is calculated by averaging the numerically computed value of c over the cardiac cycle. Also clear from the table is that a nearer reflection site means a shorter t_{T} for the waves to and from the reflection sites which is evident in the case of RPA and LPA.

Figures 6.3 show a three–dimensional depiction of numerically simulated pressures and their forward and backward running components in (x, t, p) space. The panels in the figure illustrate the wave propagation effects on the forward and backward running pressure waves as we observe the peaking of p_+ toward the distal locations in all three vessels, with significantly higher degree of incident pressure peaking in the RPA. For the reflected pressure waves, the mid systole BDCW observed in Figure 6.2 at the midpoint of these arteries, shows a considerably broader and more amplified wave profile near the distal junctions in these arteries but becomes narrow and diminished as it propagates towards the heart. Again, this effect is exaggerated in the RPA where the BDCW almost vanishes at the proximal end.

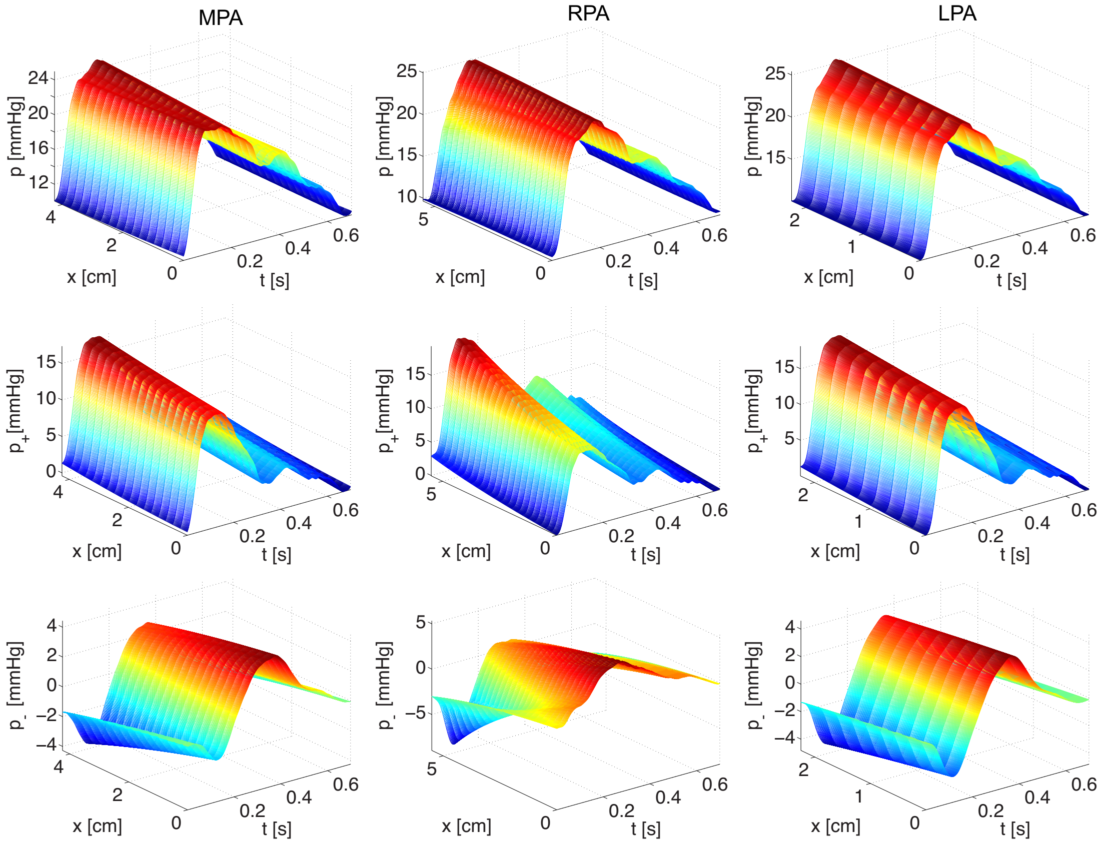

Figure 6.3: Three–dimensional depiction of originally simulated pressures (first row) and their forward (second row) and backward (third row) running components along the arterial lumen in the (x, t, p) space. The waveforms are simulated in the MPA, RPA and LPA.

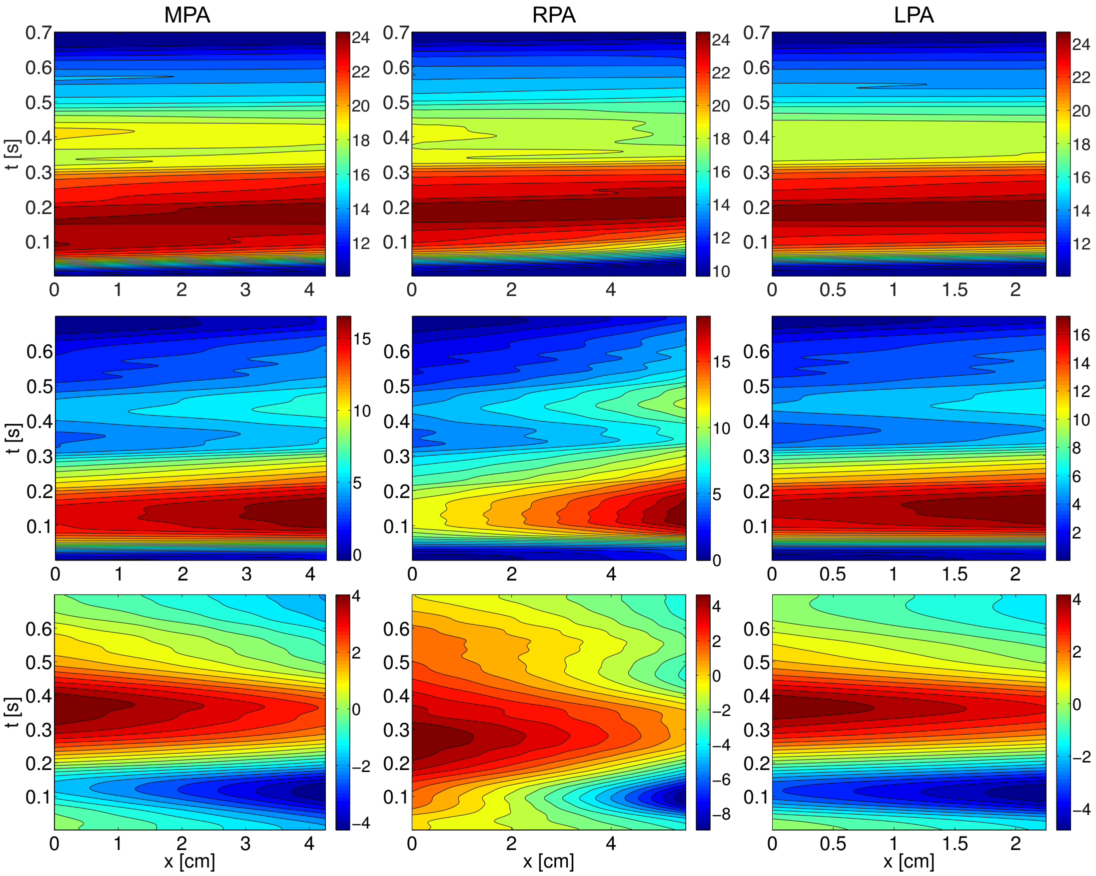

Figure 6.4: Contours of simulated pressure waveforms, shown in Figure (6.3), in (x, t) space. The results are presented in the MPA, RPA and LPA for the observed pressure waveforms (first row) and their incident (second row) and reflected (third row) components.

Figure 6.4 gives us a bird's-eye view of pressure profiles shown in Figure 6.3 in the form of two–dimensional pressure contours in the (x, t) space. From the figure, the different haemodynamics in the RPA becomes clearer as both forward and backward components show significantly more oscillatory behaviour than the MPA and the RPA. However, the general pattern of reflected waves remains similar in all three arteries i.e. a broader BDCW in mid systole tends to become weak towards the heart whereas the late systole BCW shows an opposite behaviour.

6.3.2 Influence of pulmonary hypertension on the patterns of wave reflections in the large pulmonary arteries

In this section we present the simulations of separated pressure, velocity and wave intensity profile during pulmonary hypertension. We investigate the effects of three categories of pulmonary hypertension, viz. pulmonary arterial hypertension (PAH, Group-I), pulmonary hypertension associated with hypoxic lung disease (HLD, Group-III) and the chronic thromboembolic pulmonary hypertension (CTEPH, Group IV), on the pattern of reflected waves. All theses groups are explained in Section 4.2. Since the pathologies of PAH and developed form of CTEPH are similar, we simulate the effects of PAH and initial effects of CTEPH only. The simulated pressure waveforms have already been shown in Section 4.2.1. The velocity profiles are also deduced from the corresponding flow–rate profiles in the Section 4.2.1 and used here to simulate their forward and backward components.

Effects of pulmonary arterial hypertension (Group-I)

Figures 6.5 and 6.6 depict the effects of PAH on forward and backward running pressure and velocity components in the MPA, RPA and the LPA. The results are produced by decomposing the pressure waveforms shown in Figure 4.6. It is observed that FC and FDC waves amplify with stiffened small vessels during PAH whereas earlier arrival and peaking of the late systole BC wave can also be observed with increasing PAH. However, the late systole BDCW shows a rather inconsistent behaviour in that the BDCW first amplifies with an initial increase in small arterial stiffness but its amplitude reduces with a further increase in stiffness. These changes corresponds to acceleration or deceleration of forward blood flow, which is evident from panels in the third and fourth rows exhibiting the u_+ and u_- in all three arteries.

Furthermore, it is clear from Figure 6.6 that the peak wave intensity associated with

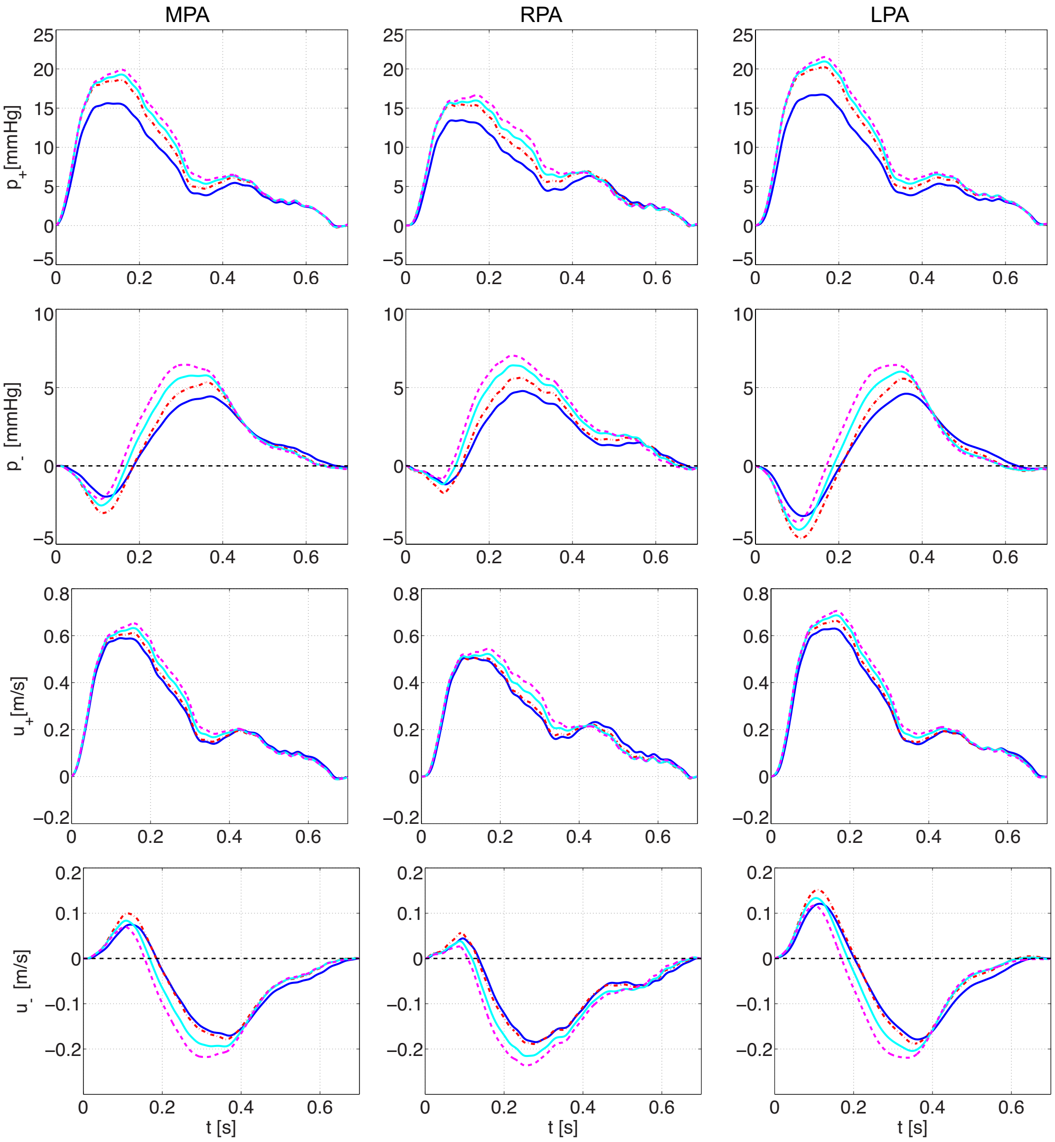

Figure 6.5: Influence of PAH (Group-I) on the patterns of wave reflections at midpoint of the MPA, RPA and LPA. The results are obtained by decomposing the arterial pressure profiles, shown in Figure 4.6, and arterial velocity waveforms, obtained from the flow waveforms in Figure 4.6, into incident and reflected components. The curves correspond to change in small vessel stiffness parameters as: normal stiffness (solid blue), 25% increase (dashed-dot red), 50% increase (solid cyan), 75% increase (dashed magenta).

forward waves increases with an increase in the small vessel stiffness, whereas the wave intensity associated with BCWs amplifies with the development of PAH, but shows a non–uniform behaviour for the BDCW.

Effects of pulmonary hypertension associated with hypoxic lung disease (Group-III)

Figures 6.7 and 6.8 illustrate how the pulmonary hypertension associated with hypoxic lung disease contributes in amplifying the pressure pulse in the MPA, RPA and the LPA by affecting the patterns of reflected waves. The incident and reflected pressure components are simulated by decomposing the pressure waveforms shown in Figure 4.10. The general observations from these figures suggest that the FCW amplifies, with an initial increase in microvascular rarefaction but this behaviour changes as amplitude of the FCW decreases with further loss in vascular density. Moreover, both figures show significant amplification and earlier arrival of the BCW with increasingly rarefied vascular beds whereas the BDCW reflects the effects of the initial FCW i.e it amplifies with an initial reduction in vascular density but starts to diminish as the vascular density is reduced by 30%.

Effects of chronic thromboembolic pulmonary hypertension (Group-IV)

Finally, the effects of CTEPH on separated pressure, velocity, and wave intensities are shown in Figures 6.9 and 6.10. The results are simulated for the initial development of CTEPH that involves the stiffening of large arteries only. From the figures one may observe the amplification of FCW, which returns as an amplified BDCW that arrives back earlier with increasingly stiffened arteries. However, the stiffened large arteries do not significantly affect the patterns of FDCW. The effects of the amplified FCW and BDCW on the forward flow cancel out and the net velocity of forward flow remains very much unaltered. This behaviour is consistent in all three arteries, although the degree of wave amplification is much greater in the LPA. These observations are also translated in the plots of wave intensity profiles shown in Figure 6.10 where the amplification of BDCW and BCW with stiffened large arteries is evident.

Figure 6.11 shows that in PAH the transit time to and from reflection site decreases with an initial increase of small vessel stiffness but does not alter with a further increase in pathology. However, in CTEPH when larger arteries are made stiffer the wave transit time, t_{T}, shortens gradually as the waves in forward and backward directions travel much

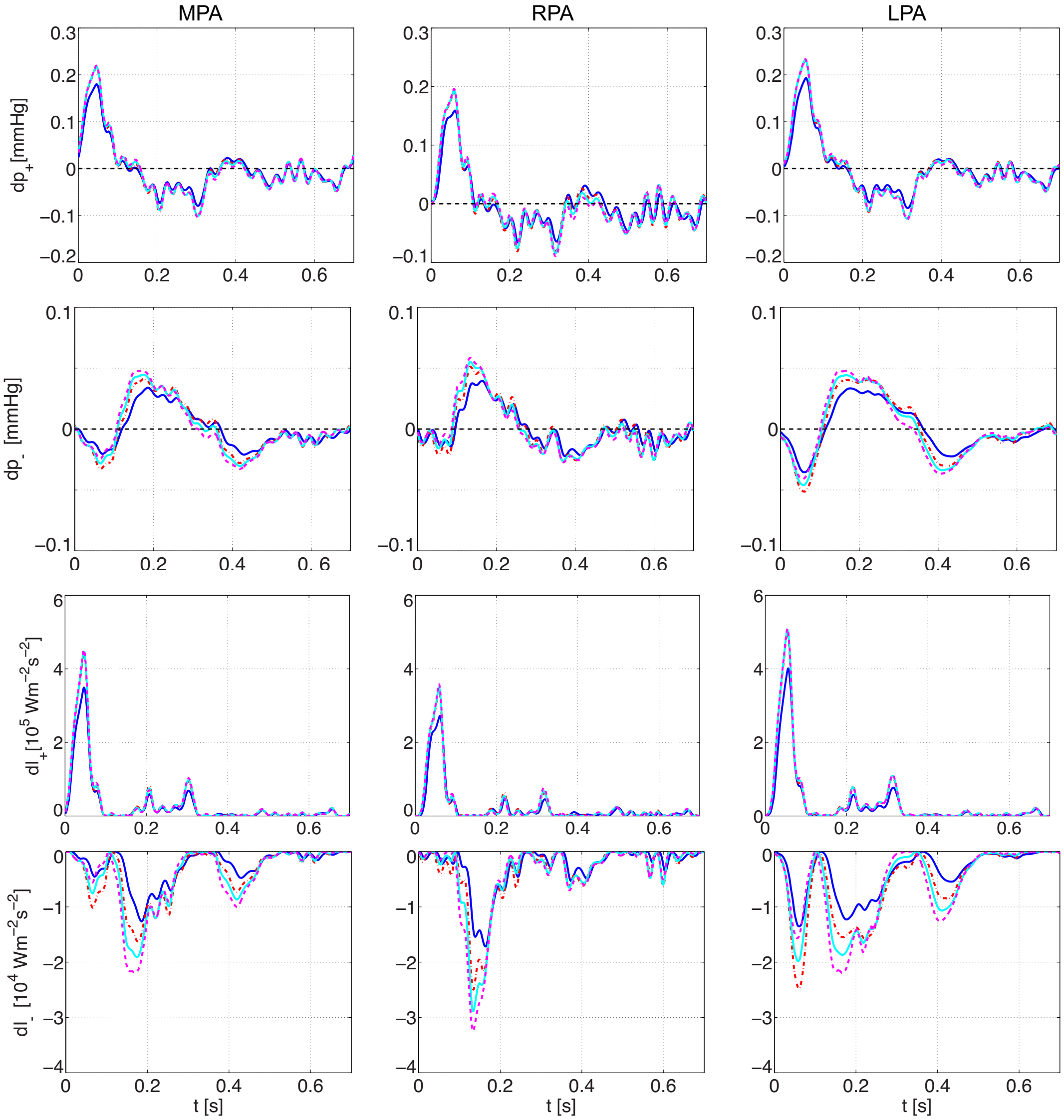

Figure 6.6: Behaviour of separated wavefronts d$p_\pm$ and d$I'_\pm$ under PAH (Group-I). The results are plotted at the midpoint of the MPA, RPA and LPA whereas the curves correspond to change in small vessel stiffness parameters as: normal stiffness (solid blue), 25% increase (dashed-dot red), 50% increase (solid cyan), 75% increase (dashed magenta).

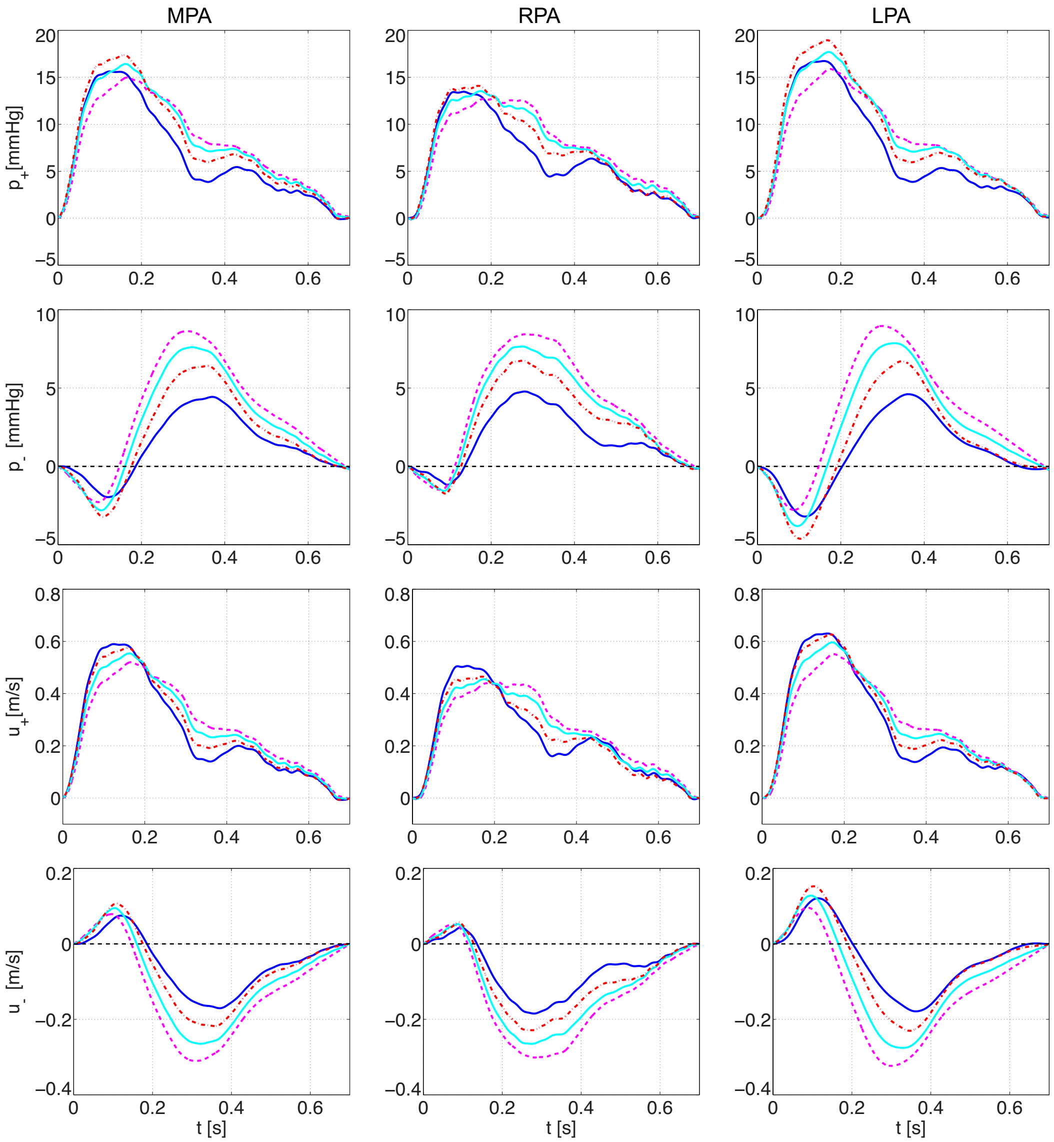

Figure 6.7: Effect of HLD associated PH (Group-III) on separated pressure and velocity at midpoints of the MPA, RPA and LPA. The p_+ and p_- are the incident and reflected components of the pressures given in Figure 4.10 while u_+ and u_- are also deduced from the flow wave forms given in the same figure. The curves correspond to the reduction in vascular bed densities: normal vascular bed density (solid blue), 10% decrease (dashed-dot red), 20% decrease (solid cyan) and 30% decrease (dashed magenta) in the density of small vessels in the vascular beds.

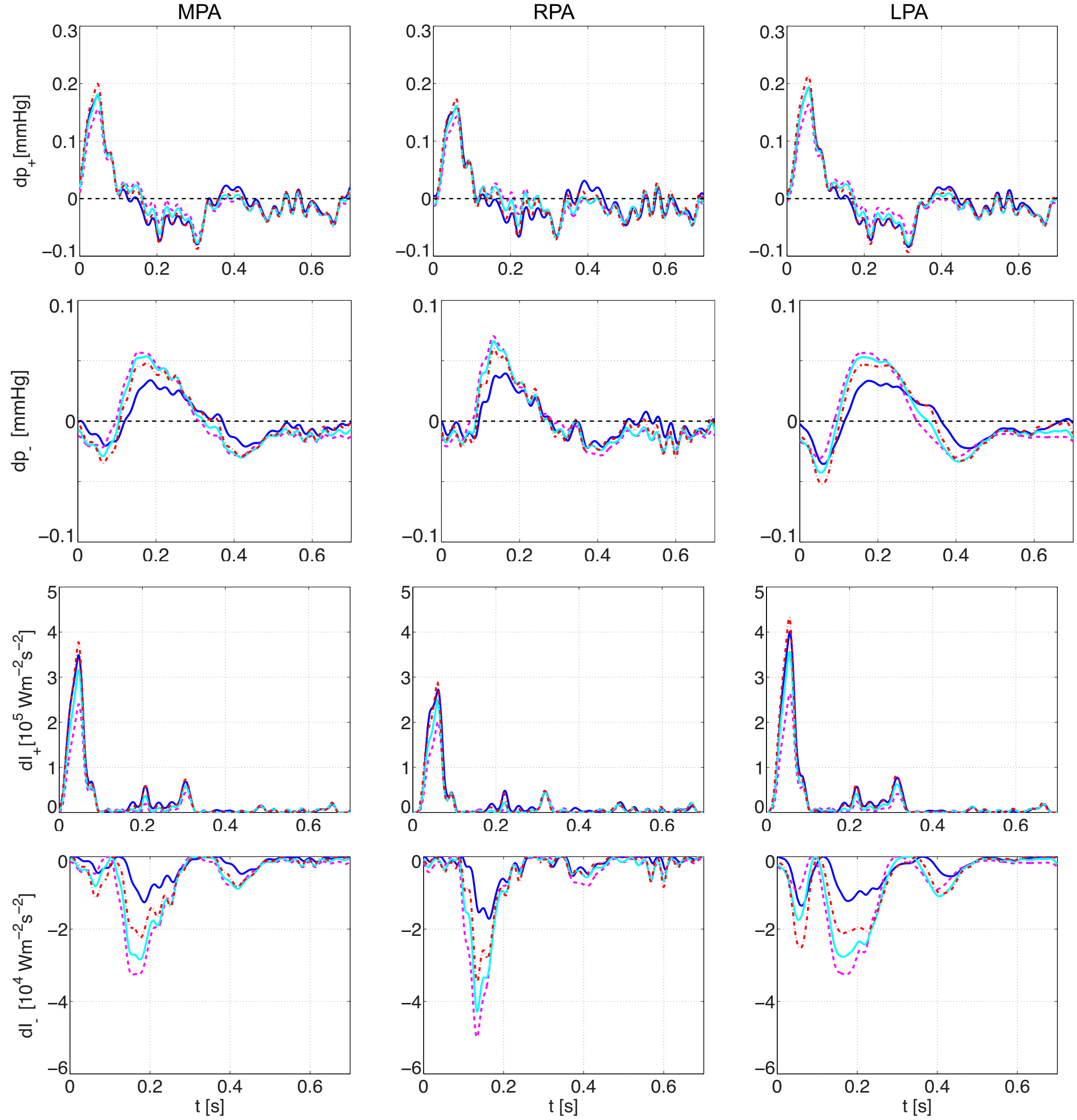

Figure 6.8: Variations in the separated wavefronts d$p_\pm$ and d$I_\pm$ due to HDL associated PH (Group-III). The results are plotted at the midpoint of the MPA, RPA and LPA where the curve correspond to: normal vascular bed density (solid blue), 10% decrease (dashed-dot red), 20% decrease (solid cyan) and 30% decrease (dashed magenta) in the density of small vessels in the vascular beds.

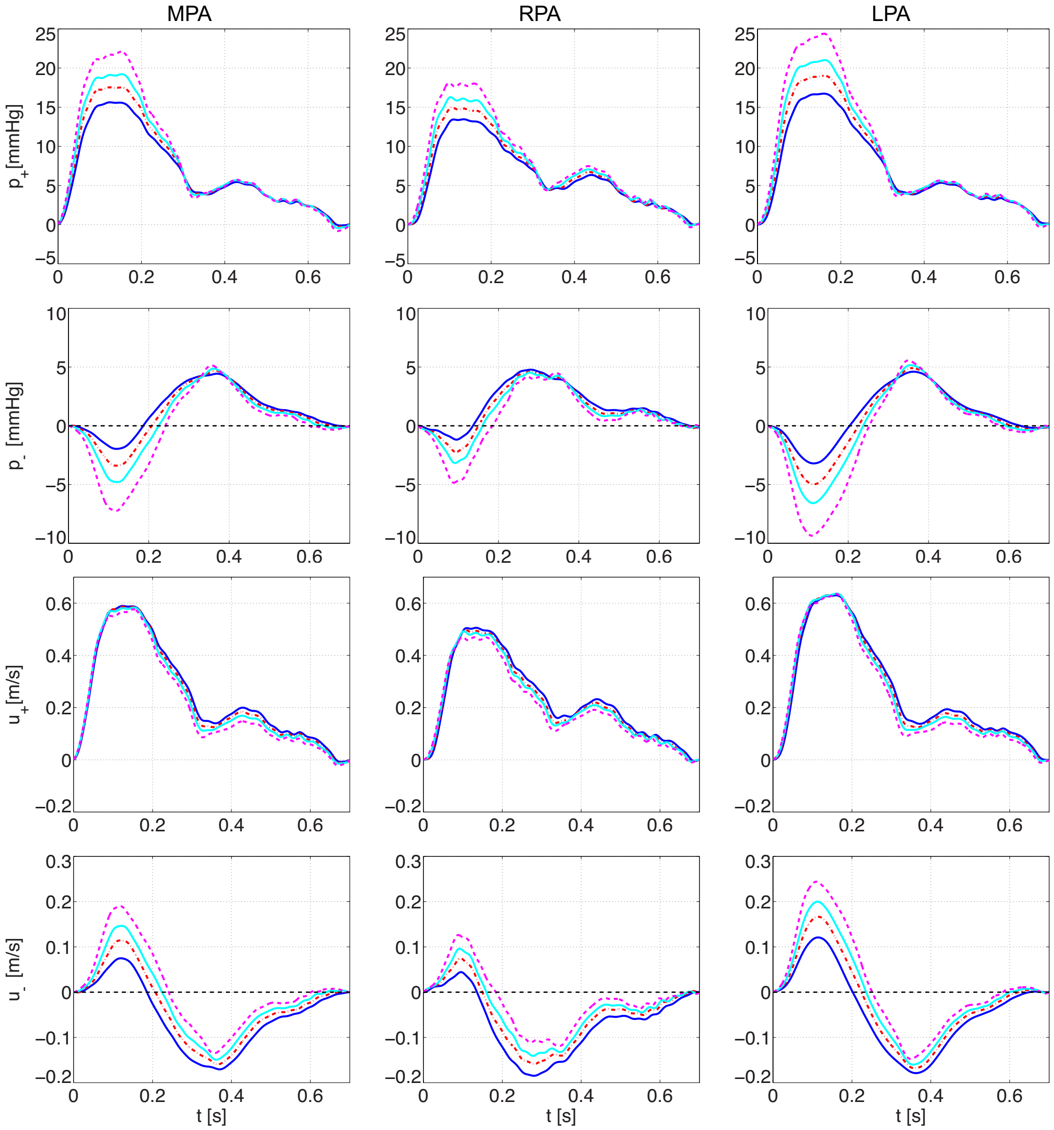

Figure 6.9: Effects of CTEPH (Group-IV) on $p_\pm$ and $u_\pm$ at midpoints of the MPA, RPA and LPA. Only the nitial effects of CTEPH (modulation of large arterial stiffness only) are shown in this figure where the separated waveforms are obtained by decomposing the pressure waveforms in Figure 4.12 (first row only) whereas the velocity waveforms are also deduced from the flow waveform shown in the third row of the same figure. The results are simulated for the normal stiffness (solid blue), 25% increase (dashed-dot red), 50% increase (solid cyan) and 100% increase (dashed magenta) in the large arterial stiffness.

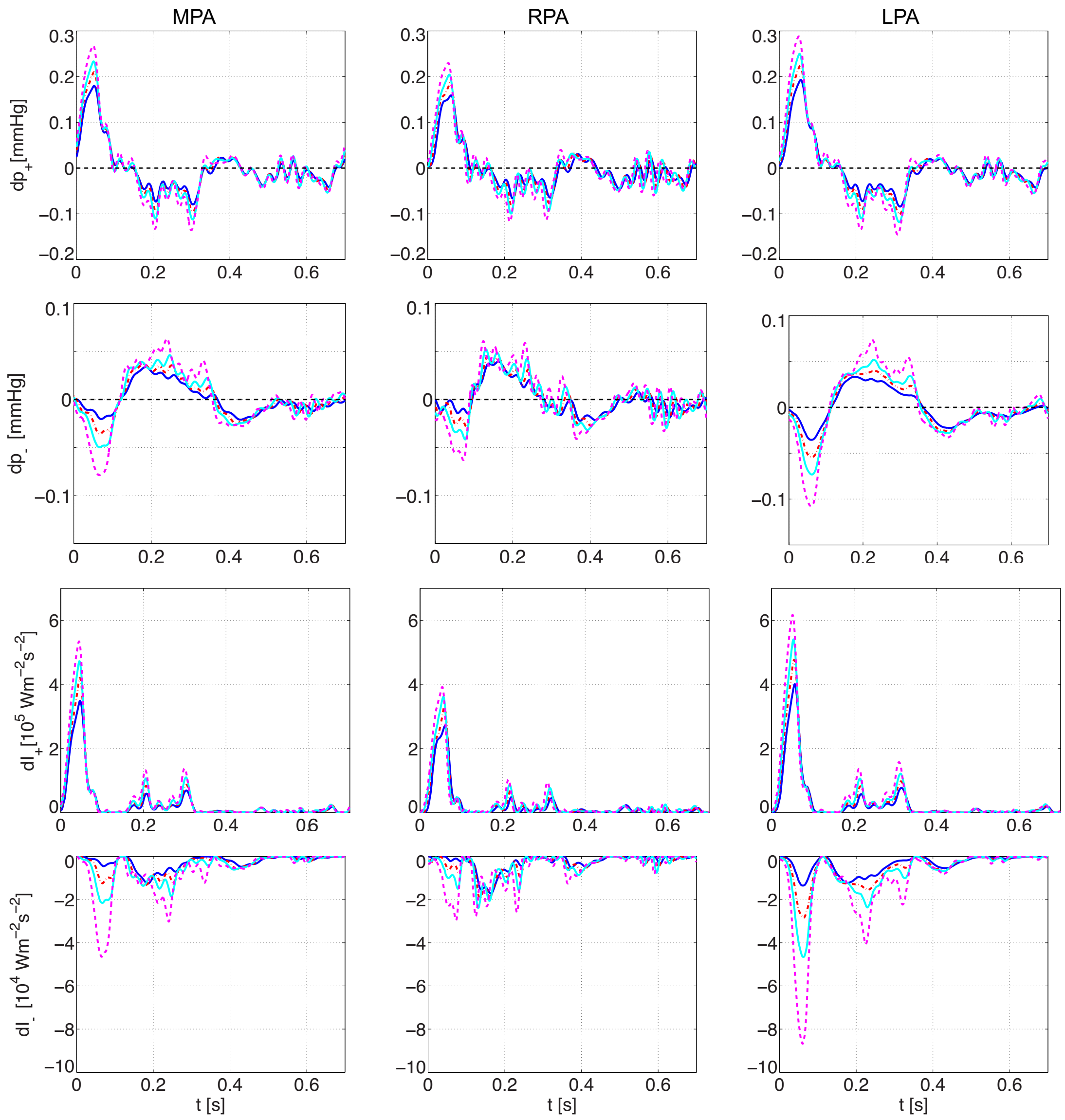

Figure 6.10: Variations in the separated wavefronts $\mathrm{d}p_{\pm}$ and $\mathrm{d}I'_{\pm}$ due to CTEPH (Group-IV). The results are plotted at the midpoint of the MPA, RPA and LPA where the results are simulated for the normal stiffness (solid blue), 25% increase (dashed-dot red), 50% increase (solid cyan) and 100% increase (dashed magenta) in the large arterial stiffness.

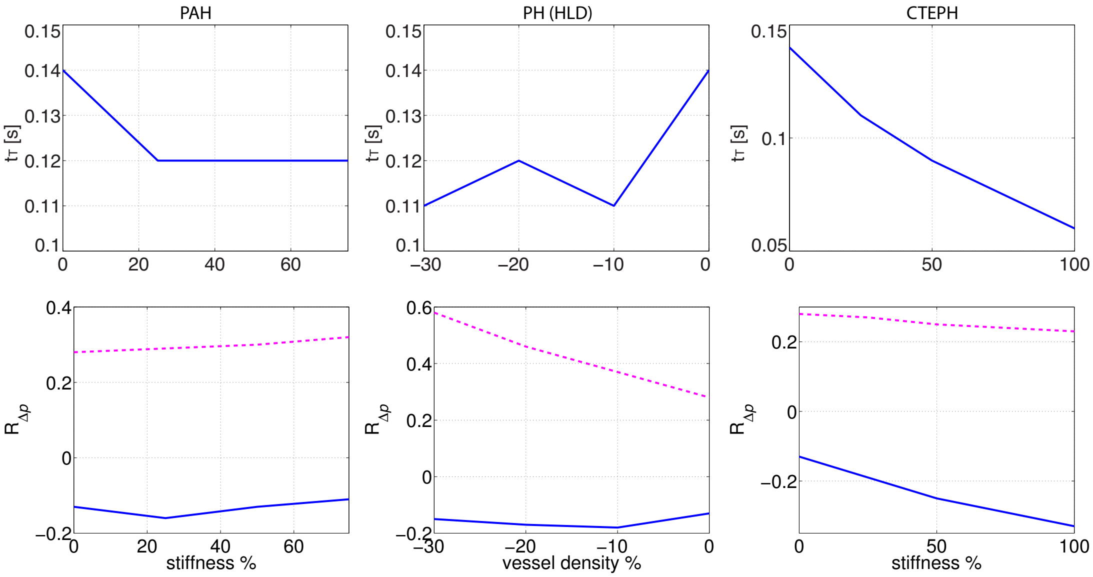

Figure 6.11: Variation in transit time (t_{T}) of of reflected waves (first row) and reflection coefficient $\mathcal{R}_{\Delta\, p}$ (second row) at the midpoint of the MPA during pulmonary hypertension. The positive $\mathcal{R}_{\Delta\, p}$ (dashed magenta) is for backward compression waves whereas the negative $\mathcal{R}_{\Delta\, p}$ (solid blue) is for backward decompression waves.

faster in the case of stiffer large arteries. As for the PH associated with HLD, the wave transit time show an unpredictable behaviour as t_{T} increase with a 20% reduction in the microvascular density but reduces with further reduction in the microvascular density. Moreover, the reflection coefficient associated with BCW increases with an increases in small vessel stiffness and the degree of microvascular rarefaction whereas it decreases with increasingly stiffened large arteries. Also the reflection coefficient associated with the BDCW decrease in CTEPH and increases in PAH but does not show significant variation in HLD after an earlier reduction due to rarefaction.

6.4 Discussion of results

Simulations of wave intensity profiles in this chapter reveals the direction, timing and nature of six different waves which suggest the behaviour of reflection sites in our model of pulmonary circulation. In all three arteries considered for this study, we identify an early FCW followed by two late systole FDCWs. These waves correspond to contraction and relaxation of the right ventricle and serve to accelerate or decelerate the forward blood flow, respectively. The FDCWs are also followed by a small FCW that corresponds to the dicrotic notch in the pressure waveform, which marks the closure of the pulmonary valve and the start of diastole. The highlight of this chapter is the simulation of a very early BDCW followed by a BCW in all three arteries (see Figure 6.2). The BDCW serves to accelerate the forward flow which enhances RV emptying by supplementing the FCW. In physiology, this early BDCW explains the remarkable ability of pulmonary circulation to draw an entire cardiac load under such a low pressure. Moreover, the early arrival of the BDCW and the comparison of $\mathcal{R}$ from Table 6.2 with $\mathcal{R}_{\Delta p}^{\mathrm{BCW}}$ form Table 6.3 suggest that it is reflected from proximal junctions in the circulation, and not the distal microcirculation, thus confirming these junctions of open–end type reflectors. This observation is mathematically supported as the geometric properties of all the junctions in our model also support this conclusion (see Table 6.2). Furthermore, the observed late systole BCW decelerates the forward flow and serves to augment the pressure wave to give pressure profile its characteristic shape. The t_{T} of BCW and the distance to reflection site (23 cm for MPA) suggest pulmonary microcirculation to be the site of its origin.

All the above observations are in close agreement with Hollander *et al.* [71] and Dwyer *et al.* [47,48], who observed the same type of wave presence approximately during the same cardiac phase, as identified in our simulations, from their *in vivo* studies in the pulmonary arteries of dog and sheep by using the method of WIA. Both authors also identified distal microcirculation as the site of positive wave reflections (BCW) and the proximal junctions as the sites of negative wave reflections (BDCW) to reach the conclusion that unlike the systemic circulation, pulmonary circulation is characterised by negative waves reflections in the systole. Dwyer [48] also reported the first ever results of WIA *in vivo* of a healthy human. For humans, unlike the two FDCW found in our model, Dwyer reported a single, broader late systole FDCW while observing the consistently present BDC and BC waves. However, Dwyer mentions the difficulties involved in accurate measurement of *in vivo* blood velocity in humans which, in his opinion, limit his analysis and he stresses the need of further work to understand the patterns of reflections in human pulmonary arteries.

The different behaviour of forward and backward pressure waves observed in the RPA goes back to the discussion in Chapter 4 where we pointed out the different dimensions of this particular vessel. In this chapter, we continue to observe standout haemodynamic features in the RPA (see figure 6.4). A close examination of second panel in the third row of Figure 6.4 may possibly explain the RPA haemodynamics further in terms of reflected and re–reflected waves (the wave trapping phenomenon [32,55]) in relation to vessel geometry.

However, this aspect requires a further in depth analysis before any conclusion can be drawn.

As for the effect of pulmonary hypertension, in the PAH and PH in HLD, the amplification of BCW explains the observed amplification of pressure wave in hypertension (see Section 4.2.1). Since the pathophysiology of these conditions is located in the microcirculation, their influence on the BDCW, which are reflected prior to microcirculation, is very little in comparison to that of BCW. This observation is also in agreement with the experimental study by Hollander *et al.* [71] who reported the creation and amplification of BCW under hypoxia without significantly affecting the open–end type BDCW. These observations also suggest that the loss of blood vessels during HLD trigger positive wave reflections, which elevate the blood pressure in the large pulmonary arteries that consequently lead to an increased RV afterload. In the CTEPH, the amplified BDCW and the shorter t_{T} is due to change in the properties of proximal reflection sites, which are the large arterial junctions. Since the wave travels faster in stiffer vessels, the amplified negative reflections from the proximal junctions arrive back much quicker.

6.5 Conclusion

For the first time, in this study, we have simulated the patterns of wave reflections in the human pulmonary arteries, both for healthy and diseased condition, by using a full scale mathematical model of pulmonary circulation and the traditional approach of WIA. Our results show agreement with those reported in the experimental studies by applying the WIA on invasively obtained pressure and velocity measurements *in vivo* animals [47, 71] and human [48]. We have also reported for the very first time the effects of pulmonary hypertension on the patterns of wave reflections by using a theoretical model, which helps us to understand the underlying mechanisms of hypertension and the behaviour of reflection sites in pathology.

However, it should be noted that despite being well established, the theory of WIA is relatively new and still developing with the recent introduction of reservoir wave approach that accounts for the pressure effects during diastole and claims to explain some of the unexplained effects, like the self-cancellation of velocity components in the diastole [165]. Since our study misses a detailed comparison with *in vivo* data, a strict clinical interpretation of these results may be a step too far. Also missing from our study is the detailed analysis that investigates any effects of downstream boundary condition, the structured tree matching conditions in this case, in producing artificial reflections. Nevertheless, this study provides us useful insight of clinically observed features of pulmonary pulse wave.

Chapter 7

Effects Of Linear PWV On The Wave Separation

In this chapter we study the effects of linear pulse wave velocity (PWV) estimates on the wave separation in the pulmonary arteries. We compare two common techniques, P-U loop and Sum of Squares, to estimate the local PWV at different locations in the large pulmonary arteries by applying them to numerically simulated pressure and velocity, and comparing the results with averaged theoretical PWV. Finally we analyse the effectiveness of these estimates in linear pulse wave separation by comparing results obtained in Chapter 6.

7.1 Introduction

Knowledge of the PWV is necessary for the wave separation in the WIA. However, in the absence of a prescribed pressure–area relation for the *in vivo* studies, it becomes almost impossible to compute the non–linear PWV. This limitation makes it far from trivial to evaluate the integrals in (6.26) or (6.32) in the WIA. However, one may adopt a linear approach by ignoring the pressure dependance of local PWV and assuming it to be constant over the cardiac cycle (i.e. $\bar{c} = c(x)$ only), which makes it straightforward to evaluate these integrals and obtain the separated waveforms [117].

Since the PWV is known to vary with pressure under physiological conditions with intra-beat variation of 20–30 % [68] or even higher in the patients with hypertension [66], any estimates of pressure independent PWV would be subject to some errors, which may be compounded in the WIA due to other assumptions about the vessel geometry and frictional losses. Many investigators have studied the effects of weak non–linearities, including the non–linear PWV, on the pressure, velocity and the wave intensity decomposition by using simple one–dimensional models with the prescribed pressure–PWV relation and reported an error of 5–10 % for pressure [135–137, 155], 2–5% for velocity and 10–12% for the wave intensity [109] under normal physiological conditions. These errors are comparable to measurement uncertainty under experimental conditions and therefore are considered small, leading most researchers to believe that the linear wave separation makes only small differences compared to non-linear separation [117]. Nevertheless, it has also been observed [109] that the linear separation error may become significant under conditions when the PWV varies substantially over the cardiac cycle and the local constant PWV ($\bar{c}$) used for linear separation is closer to the minimum or maximum pressure–dependent PWV rather than the averaged value.

Depending on the type of measurements, various techniques are used to determine the local PWV in the arteries [4]. Among these are the commonly used P-U loop [84] and the Sum of Squares techniques [45]. Both these techniques require pressure and velocity measurements only at a single location, to estimate the constant local PWV ($\bar{c}$) and therefore often referred as the single point techniques. The resulting PWV only represents the local wave–velocity at a prescribed location and not the average speed over a distance. These techniques are consistently used for the *in vivo* studies of WIA and also in the clinical situations where these estimates are used as a predictor of arterial stiffness, through the Bramwell–Hill equation (6.27) [20, 22, 171]. Thus an incorrect estimate of PWV may not only effect the patterns of local waves in the arteries but may also potentially lead to a wrong prognosis in clinical situations.

Since the high compliance of pulmonary circulation yields a much lower PWV (1.8–4.8 ms^{-1} in the MPA [48, 106] and 3.5–14 ms^{-1} in the systemic arteries [188] in human), non–linear effects are important when investigating the wave reflections in the pulmonary arteries. Moreover, due to the difference in geometric structures of pulmonary and systemic arteries, it is possible that the techniques which are suitable for the systemic or coronary arteries may not be ideal for the use in the pulmonary arterial WIA. Since the waveforms generated from computational models are free from experimental errors and provide theoretical estimates of various haemodynamic properties including the PWV, they make a useful resource to test the effectiveness of commonly used techniques to determine the PWV and their influence on the WIA, by comparing the results from linear and non–linear approaches. To the best of our knowledge, this is the first study that investigates the influence of these techniques on the wave separation in the pulmonary arteries.

7.2 Reported pulse wave velocity in the pulmonary arteries

Table 7.1 shows the reported pulse wave velocities determined using *in vivo* pressure and velocity measurements in the MPA of human, dog and sheep. We observe that for humans the estimated pulmonary PWV is about 1.8–2.0 ms^{-1} in normal conditions and it is more than double during hypertension. Moreover, in comparison to humans, the normal pulmonary arterial PWV is higher in sheep and dogs.

Source	Specious	Wave Speed	Condition
[30, 58, 106]	Human	$1.8\,\mathrm{ms}^{-1}$	Normal
[106, 141]	Human	$4.8\,\mathrm{ms}^{-1}$	Hypertension
[48]	Human	$1.9 \pm 0.7\,\mathrm{ms}^{-1}$	Normal
[48]	Human	$4.8 \pm 2.4\,\mathrm{ms}^{-1}$	Hypertension
[14]	Dogs	$2.75 \pm 0.16\,\mathrm{ms}^{-1}$	Normal
[126]	Dogs	$2.5\,\mathrm{ms}^{-1}$	Normal
[126]	Dogs	$3.5\,\mathrm{ms}^{-1}$	Calculated
[71]	Dogs	$2.5\,\mathrm{ms}^{-1}$	Normal
[47]	Sheep	$2.1 \pm 0.3\,\mathrm{ms}^{-1}$	Normal

Table 7.1: Reported wave speeds in the main pulmonary artery of various species.

7.3 Methods

In this section we describe the linear approach (using constant PWV) to separate the pressure, velocity and wave intensity profiles along with P-U loop and Sum of Squares techniques, which provide the estimates of constant, local, PWV for use in the linear approach.

7.3.1 Linear wave separation

The assumption of constant PWV makes it much simpler to solve the integral equation (6.32) by writing the constant factor $\rho\,\bar{c}$ outside the integral, which yields

$$R_{\pm} = u \pm \frac{p}{\rho\,\bar{c}}. \tag{7.1}$$

Solving (7.1) for p and u in terms of R_+ and R_-, we obtain

$$p = \frac{\rho\,\bar{c}}{2}\,(R_+ - R_-), \tag{7.2}$$

$$u = \frac{1}{2}\,(R_+ + R_-). \tag{7.3}$$

The wavefronts or infinitesimal changes in p and u are given by

$$\mathrm{d}p = \frac{\rho\,\bar{c}}{2}\,(\mathrm{d}R_+ - \mathrm{d}R_-), \tag{7.4}$$

$$\mathrm{d}u = \frac{1}{2}\,(\mathrm{d}R_+ + \mathrm{d}R_-). \tag{7.5}$$

Taking the product of $\mathrm{d}p$ and $\mathrm{d}u$ from (7.4) and (7.5) yields the expression for the net wave intensity and gives

$$\mathrm{d}I' = \mathrm{d}p\,\mathrm{d}u = \frac{\rho\,\bar{c}}{4}(\mathrm{d}R_+^2 - \mathrm{d}R_-^2), \tag{7.6}$$

which is similar to that given by (6.47). Recalling the Water–Hammer equation (6.39) with constant pulse wave velocity $\bar{c}$

$$\mathrm{d}p_{\pm} = \pm\,\rho\,\bar{c}\,\mathrm{d}u_{\pm}, \tag{7.7}$$

and assuming that the forward and backward components of pressure and velocity are additive, such that

$$\mathrm{d}p = \mathrm{d}p_+ + \mathrm{d}p_-, \tag{7.8}$$

$$\mathrm{d}u = \mathrm{d}u_+ + \mathrm{d}u_-, \tag{7.9}$$

then one may separate the pressure and velocity wavefronts in terms of $\mathrm{d}p$ and $\mathrm{d}u$ using (7.7) in (7.8) and (7.9) and solving for $\mathrm{d}p_{\pm}$ and $\mathrm{d}u_{\pm}$, to get

$$\mathrm{d}p_{\pm} = \frac{1}{2}(\mathrm{d}p \pm \rho\,\bar{c}\,\mathrm{d}u), \tag{7.10}$$

$$\mathrm{d}u_{\pm} = \frac{1}{2}\left(\mathrm{d}u \pm \frac{1}{\rho\,\bar{c}}\mathrm{d}p\right). \tag{7.11}$$

The corresponding components of wave intensity are given by

$$\mathrm{d}I'_{\pm} = \mathrm{d}p_{\pm}\,\mathrm{d}u_{\pm} = \pm\frac{\rho\,\bar{c}}{4}\left(\mathrm{d}u \pm \frac{\mathrm{d}p}{\rho\,\bar{c}}\right)^2, \tag{7.12}$$

or

$$\mathrm{d}I_{\pm} = \frac{\mathrm{d}p_{\pm}}{\mathrm{d}t}\,\frac{\mathrm{d}u_{\pm}}{\mathrm{d}t} = \pm\frac{\rho\,\bar{c}}{4}\left(\frac{\mathrm{d}u}{\mathrm{d}t} \pm \frac{1}{\rho\,\bar{c}}\frac{\mathrm{d}p}{\mathrm{d}t}\right)^2. \tag{7.13}$$

Finally the forward and backward components of pressure and velocity can be obtained by integrating $\mathrm{d}p_{\pm}$ and $\mathrm{d}u_{\pm}$ over the cardiac cycle using (6.43) and (6.44).

Equations (7.6) and (7.12) are apparently similar to those of (6.47) and (6.48), but using the linear approach, $\mathrm{d}p_{\pm}$, $\mathrm{d}u_{\pm}$ and $\mathrm{d}I_{\pm}$ are additive, which is not generally true in the non–linear approach [136].

7.3.2 Theoretical pulmonary PWV in our model

The numerically determined PWV in our model implicitly depends on time through area or pressure (see eq. (6.27)). From (6.33), we may write

$$c^2 = \frac{A}{\rho}\frac{dp}{dA} = c_0^2 - \frac{p(A)}{2\rho}, \tag{7.14}$$

which illustrates that due to the constant values of ρ and c_0^2 $(=\Psi/\rho)$, c^2 decreases with increasing pressure. This observation is qualitatively opposite to that observed in physiology, i.e. an increasing PWV with an increase in pressure [14], and it can be tackled by using Lighthill's expression of tube law [94] (also used by Sherwin *et al.* [145], see equation (6.31)). However, as far as the relative expansion of cross–sectional area remains small, which is the case for the longitudinally tethered arteries *in vivo*, both models predict identical and physiologically correct behaviour as

$$\frac{r - r_0}{r_0} \approx \frac{r - r_0}{r},$$

in the arteries and the error between these models is negligible.

7.3.3 PWV by using the P-U loop

In the absence of a prescribed pressure–area relation the local PWV can be determined by careful analyses of pressure–velocity loop of simultaneously measured pressure and velocity at a fixed position [64, 84]. This technique is based on the Water–Hammer equation (7.7) that gives

$$\bar{c} = \pm\frac{1}{\rho}\frac{\mathrm{d}p_{\pm}}{\mathrm{d}u_{\pm}}.$$

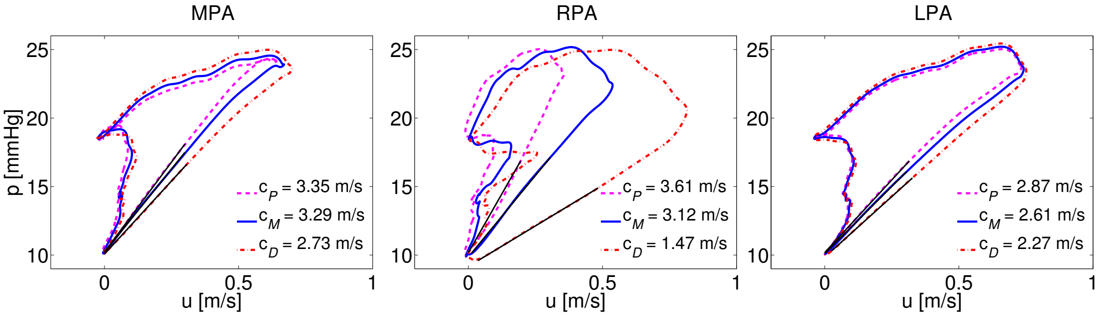

Figure 7.1: Estimation of pulse wave velocity in the MPA, RPA and LPA by using the pressure–velocity loop of the numerically generated pressure and velocity in our model. The wave speeds are estimated at proximal, midpoint and distal locations in the arteries, which are denoted by P, M and D, respectively, in the subscript of c in legends.

Assuming that there are no reflected waves present in the early systolic upstroke i.e. $\mathrm{d}p = \mathrm{d}p_+$ and $\mathrm{d}u = \mathrm{d}u_+$, then the constant local PWV ($\bar{c}$) can be calculated by determining the slope of linear portion of the P-U loop at the start of systole i.e.

$$\bar{c} = \frac{1}{\rho}\frac{\mathrm{d}p}{\mathrm{d}u}. \tag{7.15}$$

It has been shown, *in vitro* [85] and *in vivo* [86], that $\bar{c}$ from P-U loop method agrees well with the $\bar{c}$ determined form traditional, two point foot–to–foot method, which gives an average PWV over a distance i.e. $\bar{c} = \Delta l/\Delta t$, where Δt is the time taken by the foot of the pulse wave to travel between two locations separated by a known distance Δl [111]. However, it has also been noted that the P-U loop method works well in the long vessels like the aorta, but the assumption of only forward waves during the early systole makes it unsuitable for the shorter arteries, such as the coronary arteries, where the early systole waves are subject to influence from the peripheral wave reflections [48, 158], which makes it difficult to determine a linear, reflection free, portion in the P-U loop.

7.3.4 PWV by using the Sum of Squares

Keeping in view the influence of early reflections and multiple haemodynamic interactions on the linearity of PWV in the early systole, Davies *at el.* [45] introduced a new single–point technique that does not depend on the assumption of linear relation between pressure and velocity in the early systole. From equation (7.11) the difference of separated velocity wavefronts gives

$$\mathrm{d}u_+ - \mathrm{d}u_- = \frac{\mathrm{d}p}{\rho\bar{c}}\,. \tag{7.16}$$

Squaring and summing over an integer number of cardiac cycle provides us a pulse wave velocity definition

$$(\rho\bar{c})^2 = \frac{\sum(\mathrm{d}p)^2}{\sum(\mathrm{d}u_+ - \mathrm{d}u_-)^2}. \tag{7.17}$$

The denominator in (7.17) cannot be determined directly from the haemodynamic measurements but it can be approximated by using the readily determined $\sum(\mathrm{d}u)^2$, which is equal to $\sum(\mathrm{d}u_+ + \mathrm{d}u_-)^2$. So

$$\sum\left[(\mathrm{d}u_+)^2 + 2\mathrm{d}u_+\mathrm{d}u_- + (\mathrm{d}u_-)^2\right] \approx \sum\left[(\mathrm{d}u_+)^2 - 2\mathrm{d}u_+\mathrm{d}u_- + (\mathrm{d}u_-)^2\right]$$

if and only if $2\sum \mathrm{d}u_+\mathrm{d}u_-$ is much smaller than $\sum\left[(\mathrm{d}u_+)^2 + (\mathrm{d}u_-)^2\right]$. Under this assumption we get

$$(\rho\bar{c})^2 = \frac{\sum(\mathrm{d}p)^2}{\sum(\mathrm{d}u_+ - \mathrm{d}u_-)^2} \approx \frac{\sum(\mathrm{d}p)^2}{\sum(\mathrm{d}u_+ + \mathrm{d}u_-)^2} = \frac{\sum \mathrm{d}p^2}{\sum \mathrm{d}u^2}, \tag{7.18}$$

which implies that

$$\bar{c} = \frac{1}{\rho}\sqrt{\frac{\sum \mathrm{d}p^2}{\sum \mathrm{d}u^2}}. \tag{7.19}$$

An alternate derivation of the expression (7.19) can also be found in the Appendix in [45], which is obtained by minimizing the sum of absolute value of the separated wave intensities with respect to $\bar{c}$. The advantage of this technique is that it does not require the vessel to be long enough for two measurements or nor does it rely on a period during which only forward waves are present.

7.4 Results

7.4.1 Pulse wave velocity

Table 7.2 shows numerical PWV (c), computed through equation (7.14), $\bar{c}_{\text{loop}}$ estimated from the P-U loops in Figure 7.1 using equation (7.15)[1] and estimates of $\bar{c}_{\text{sqrs}}$ from the Sum of Squares technique using equation (7.19). The values are given at proximal, midpoint and distal locations in the MPA, RPA and LPA.

It can be observed that c fluctuates significantly, $0.07\,\mathrm{ms}^{-1}$ ($7\,\mathrm{cm\,s}^{-1}$) about $\bar{c}_{\text{avg}}$ over the cardiac cycle but $\bar{c}_{\text{avg}}$ remains almost constant along various locations in the arteries except for a small increase of $0.01\,\mathrm{ms}^{-1}$ in the RPA. This observation is due to the use of constant compliance in our model and qualitatively it agrees with Attinger [12]

---

[1] By multipleying the slope of p [mmHg] u [ms^{-1}] loop by a conversion factor of 0.1333 and dividing by constant blood density [$\rho = 1.055\,\mathrm{g/cm}^3$].

Artery	Location	c_{max}	c_{min}	$\bar{c}_{\text{avg}}$	$\bar{c}_{\text{loop}}$	$\%_{\text{error}}$	$\bar{c}_{\text{sqrs}}$	$\%_{\text{error}}$
MPA	Proximal	3.42	3.28	3.34	3.35	0.30	2.76	17.37
	Mid-point	3.42	3.28	3.34	3.29	1.50	2.57	23.05
	Distal	3.42	3.28	3.34	2.73	18.26	2.34	29.94
RPA	Proximal	3.42	3.28	3.34	3.61	8.08	4.25	27.25
	Mid-point	3.42	3.28	3.35	3.12	6.59	2.90	13.43
	Distal	3.42	3.28	3.35	1.47	56.12	1.73	48.36
LPA	Proximal	3.42	3.28	3.34	2.87	14.07	2.25	32.63
	Mid-point	3.42	3.28	3.34	2.61	21.86	2.17	35.03
	Distal	3.42	3.27	3.34	2.27	32.03	2.10	37.13

Table 7.2: Fluctuation in the numerically computed pulse wave velocity [$\text{m}\,\text{s}^{-1}$] during the cardiac cycle and its comparison with the wave speed determined by using P-U loop and Sum of Squares techniques is shown in the table. The % error is computed about $\bar{c}_{\text{avg}}$, the average of numerically computed non–linear PWV. All values are given to 2 d.p, measured at the proximal, midpoint and distal positions in the MPA, RPA and LPA.

who reported a constant spatial PWV in the pulmonary arteries. Furthermore, in most cases the PWV estimates from the Sum of Squares technique are significantly smaller than $\bar{c}_{\text{min}}$ (minimum of theoretical c) and when compared with $\bar{c}_{\text{avg}}$, the estimates of $\bar{c}_{\text{loop}}$ yield much smaller errors than $\bar{c}_{\text{sqrs}}$. Also both techniques provide their best estimates at the proximal and midpoint locations in the arteries while the errors amplify dramatically at distal location i.e. near bifurcating junctions, suggesting these locations to be unsuitable for estimation of local PWV using these techniques. To the best of our knowledge no *in vivo* or *in vitro* study suggest a precise location to obtain the best estimates of linear PWV, although in most cases the PU-loop analysis is performed in the proximal arteries at locations away from the junctions. Nevertheless, this observation requires further investigations and validation, e.g. in a simpler tube model with a single bifurcation. Moreover, the haemodynamics differences in the RPA are also translated in the PWV estimates as, unlike the MPA and LPA, the best estimates are obtained at the midpoint instead of the proximal location.

A more general observation suggest that the best estimates of the local PWV are obtained close to the heart, and farther the pressure and velocity measurements are obtained, more erroneous the estimates are. As for the estimates using the Sum of Squares techniques, the only possible explanation may be in terms of the assumption of smaller

$\sum \mathrm{d}u_+\mathrm{d}u_-$ than the $\sum[(\mathrm{d}u_+)^2 + (\mathrm{d}u_-)^2]$. This might be a valid assumption in the arteries where there is no linear portion in the P-U loop in early systole but in cases where there is, the relative contribution of the term $\sum \mathrm{d}u_+\mathrm{d}u_-$ can not be neglected. Clearly this is not the case in our simulations and a quick calculation at the proximal MPA shows that $\sum(\mathrm{d}u_+ + \mathrm{d}u_-)^2 \not\approx \sum(\mathrm{d}u_+ - \mathrm{d}u_-)^2$ as

$$\frac{\sum(\mathrm{d}u_+^2 + \mathrm{d}u_-^2)}{2\sum \mathrm{d}u_+\mathrm{d}u_-} \approx 3 \times 10^{-3}.$$

Observations from Table 7.2 suggest that the PWV estimates using different methods are bound to produce errors in the wave separation. However, at this point, the potential impact of these errors on the type and nature of reflections is not clear to us. This is studied further in the next section by using these estimates in the WIA.

7.4.2 Wave separation using WIA

In this section we present the results depicting the effects of local estimates of PWV, using the P-U loop and the Sum of Squares methods, coupled with linear pulse wave separation. The wave separation is performed by using WIA at proximal, midpoint and distal locations in the MPA, RPA and LPA. The linearly separated forward and backward wave components are compared with those obtained in Chapter 6 using the non–linear approach.

Figure 7.2 shows the effects of different wave velocities on separation of pressure, flow velocity and wave intensity profiles at proximal, midpoint and distal locations in the MPA. It is observed that results using the P-U loop method are in complete agreement with the non–linear PWV at the proximal and midpoint positions in the MPA but as the wave propagates towards distal MPA near the junction, a significant deviation of linearly separated wave components from the non–linearly separated components can be observed as the amplitudes of both forward and backward pressure waves decrease towards the junction. On the other hand, the estimates of PWV using the Sum of Squares technique yield a significantly prominent backward compression wave (BCW) while underestimating the forward compression wave (FCW) at all locations in the MPA. However, to our surprise, the amplitude of BCW reduces progressively towards the junction despite the fact that the estimated $\bar{c}_{\mathrm{sqrs}}$ yields greatest error at this location. The appearance of an artificial BCW in the early systole leads to wrong interpretation of flow nature i.e. a flow deceleration would take place due to an increased right ventricular afterload in the early systole.

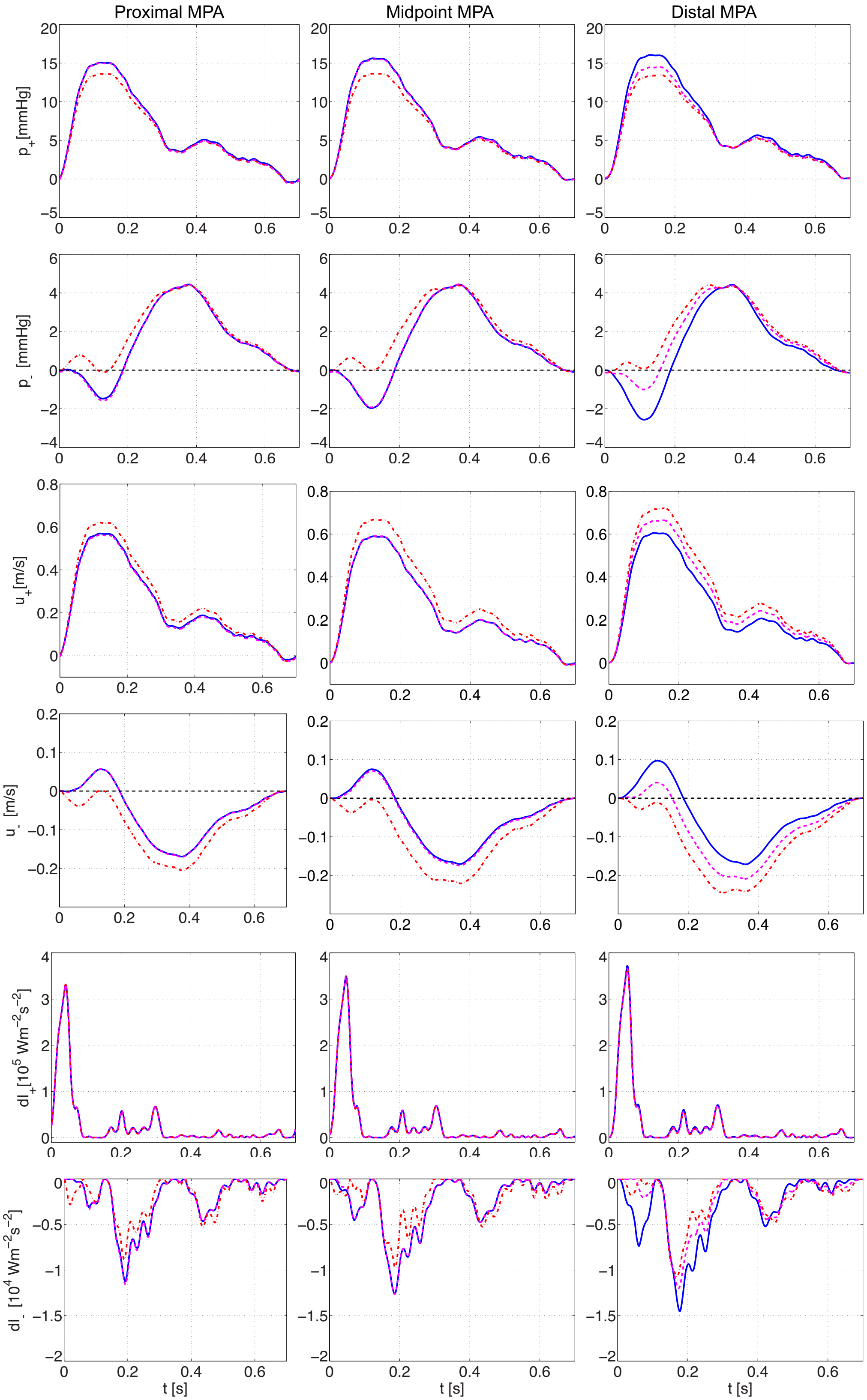

Figure 7.2: Influence of estimated PWV on the pulse wave separation in the MPA. The results are plotted for: proximal (first column), midpoint (second column) and the distal end (third column) for the numerically evaluated non-linear PWV (solid blue), PWV from P-U loop (dashed magenta) and the PWV from Sum of Squares technique (dashed-dot red).

Figure 7.3 illustrates the influence of different wave velocities on the patterns of reflected waves along three positions in the RPA. In the RPA too, the separated waveforms using the estimates of P-U loop are observed to closely follow the patterns of non–linearly separated pressure, velocity and wave intensity profiles at the proximal and midpoint locations. Although $\bar{c}_{\mathrm{sqrs}}$ yields a greater error in the wave separation in the RPA too but unlike the MPA, $\bar{c}_{\mathrm{sqrs}}$ does not alter the type of reflected wave in the RPA. As observed in the previous chapters, the haemodynamic along the RPA changes most radically from an initial state of early systole BCW at the proximal RPA to an amplified backward decompression wave (BDCW) at the distal RPA. It is observed that the estimates of constant PWV consistently fail to translate the haemodynamic changes near the junctions and, as seen in this case, the linear wave separation completely fails to capture the highly non–linear behaviour of reflected pressure wave as an amplified BDCW close to the junction goes almost unnoticed in the wave intensity profiles.

Finally, we observe the effects of $\bar{c}_{\mathrm{loop}}$ and $\bar{c}_{\mathrm{sqrs}}$ coupled with linear wave separation, in the LPA. The P-U loops in Figure 7.1 and the normal waveforms in Chapter 4 illustrate a similar haemodynamic pattern in the MPA and LPA. Consequently, the estimates from the P-U loop and Sum of Squares techniques lead to similar patterns of reflected waves as observed in the MPA. Here too, the use of $\bar{c}_{\mathrm{sqrs}}$ leads to BCW in the early systole, instead of BDCW, which diminishes at the distal RPA. Moreover, although $\bar{c}_{\mathrm{loop}}$ successfully captures the arrival of BDCW in the systole at all locations, due to a bigger error about $\bar{c}_{\mathrm{avg}}$, the use of $\bar{c}_{\mathrm{loop}}$ significantly underestimate the BDCW in the LPA.

7.5 Discussion

As expected, the estimates of local PWV using P-U loop perform much better than the Sum of Squares technique in the analysis of linear pulse wave separation and despite accumulating a progressive error farther from the heart, at no point the $\bar{c}_{\mathrm{loop}}$ fails to identify actual type of reflected waves. Moreover, the simultaneous existence of FCW and the BCW in the MPA and LPA in the early systole using the $\bar{c}_{\mathrm{sqrs}}$ indicates that the BCW is nothing but an artifact of the PWV under consideration. The appearance of artificial BCW raises doubts on the effectiveness of Sum of Squares technique in the pulmonary arteries (in particular for this geometry and the model). This is the first time that we have come across misleading results using the $\bar{c}_{\mathrm{sqrs}}$ in separating the pulse wave in the

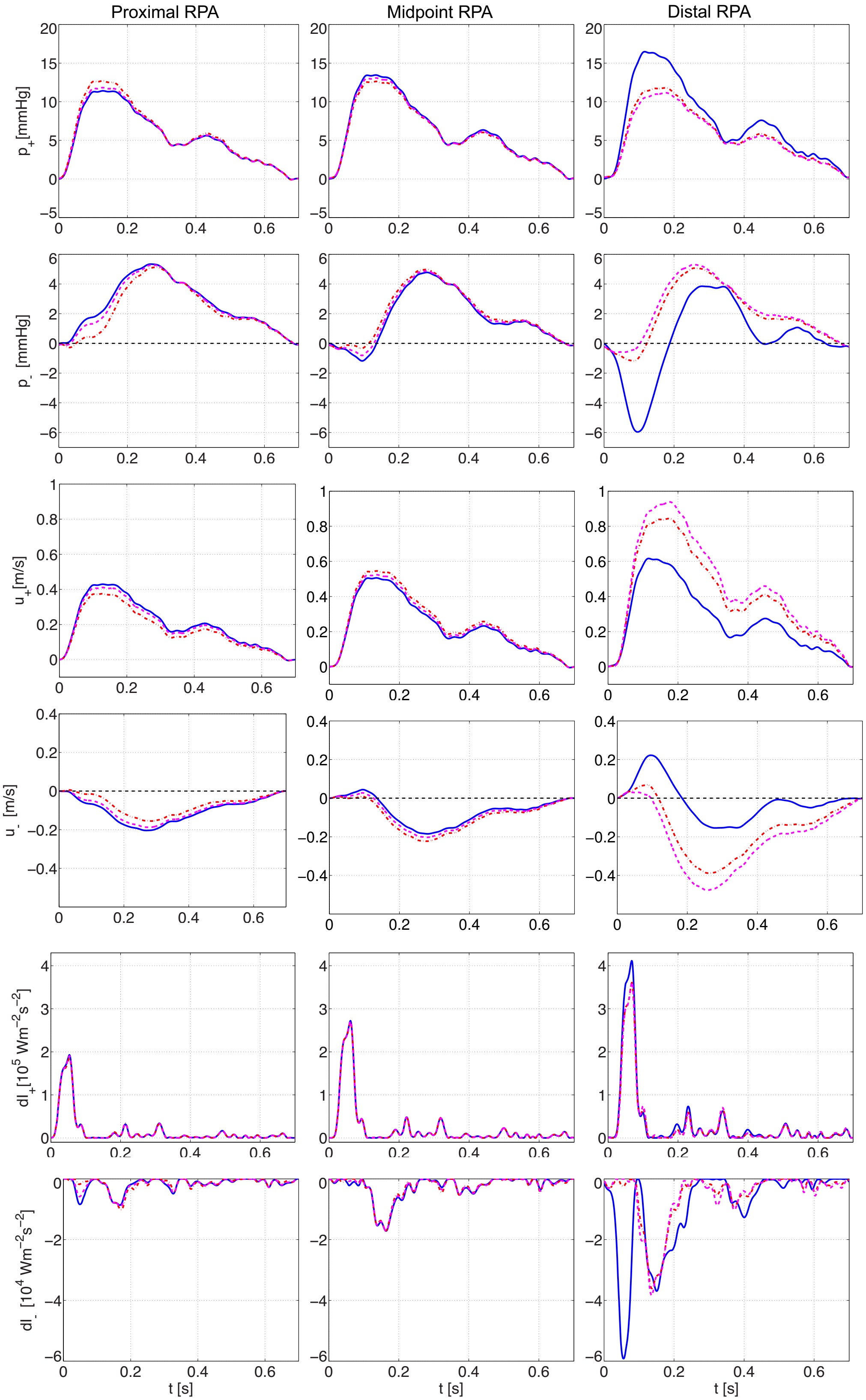

Figure 7.3: Influence of estimated PWV on the pulse wave separation in the RPA. The results are plotted for: proximal (first column), midpoint (second column) and the distal end (third column) for the numerically evaluated non-linear PWV (solid blue), PWV from P-U loop (dashed magenta) and the PWV from Sum of Squares technique (dashed-dot red).

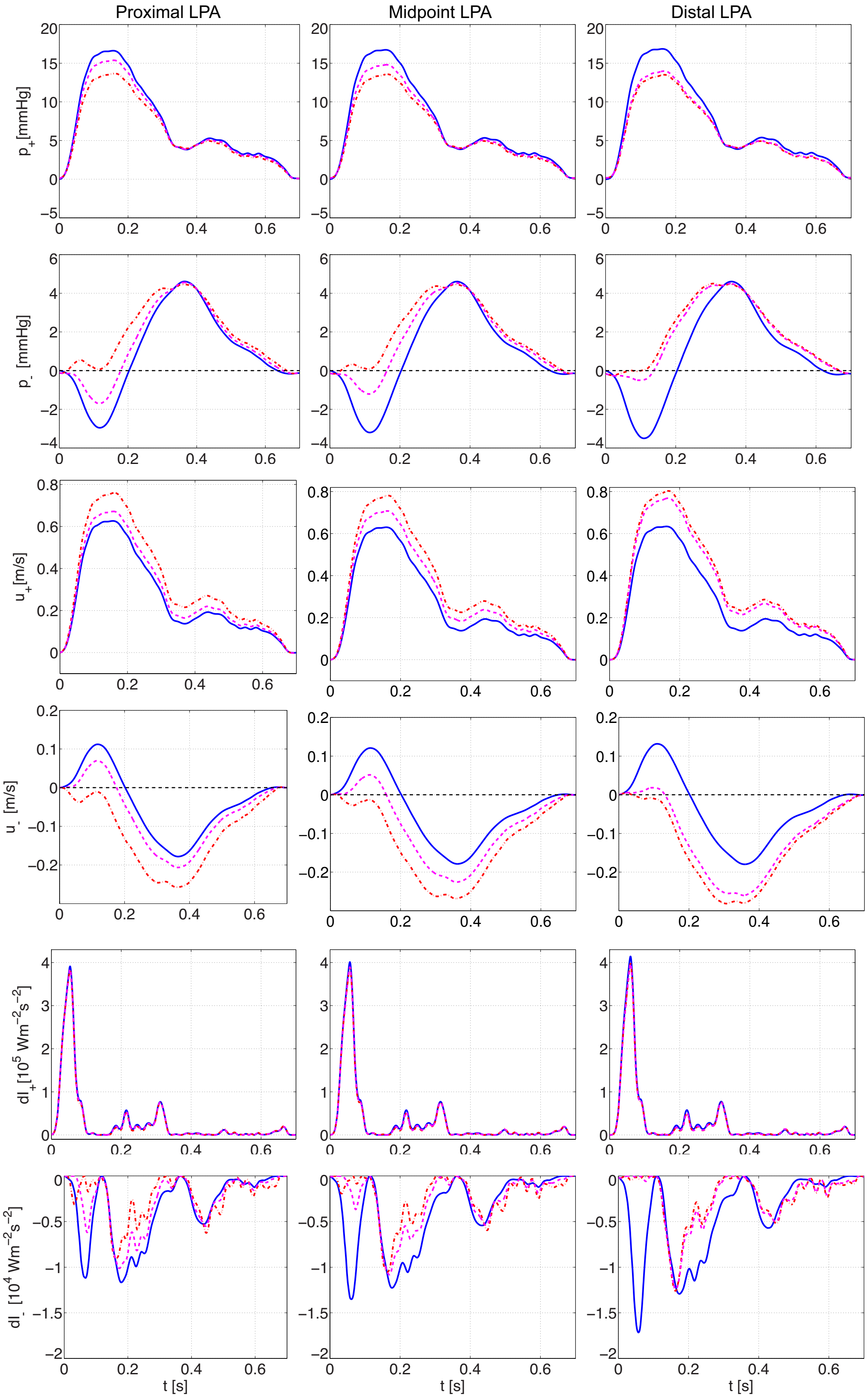

Figure 7.4: Influence of estimated PWV on the pulse wave separation in the LPA. The results are plotted for: proximal (first column), midpoint (second column) and the distal end (third column) for the numerically evaluated non-linear PWV (solid blue), PWV from P-U loop (dashed magenta) and the PWV from Sum of Squares technique (dashed-dot red).

pulmonary arteries, but this is certainly not the first time that erroneous behaviour of Sum of Square technique has been reported. In [1], it was reported that this technique can produce erroneous results when measurements are performed very close to a reflection site. However, in a study using a detailed one–dimensional model of systemic arteries, Alastruey [4] concluded that the Sum of Squares technique performs better at the proximal positions away from the junction, which is opposite to the observation in our model. This suggests that the behaviour of Sum of Squares techniques may strongly depend on the geometry and the physiological conditions, which are significantly different in the two circulatory systems. Nevertheless, we recommend that any further use of this technique in the pulmonary arteries should be subject to careful assessment of this technique using various geometries and models of pulmonary circulation.

The accurate behaviour of $\bar{c}_{\text{loop}}$ in the linear pulse wave separation at the proximal and midpoint MPA highlights many aspects of this technique and the linear pulse wave separation, few of which are: (i) the closer the estimates of local PWV to the average of actual PWV ($\bar{c}_{\text{avg}}$) and within the range of maximum and minimum of actual PWV (i.e. if $\bar{c} \in [c_{\text{min}}, c_{\text{max}}]$), the more accurate the predicted patterns of reflected waves are; (ii) the technique produces large errors if $\bar{c}_{\text{loop}}$ is estimated close to a mismatched junction or in the arteries after the first generation away from the heart, so the locations away from reflection sites and proximal to the heart provide best estimates of linear PWV using the P-U loop; (iii) the linear wave separation does not make significant difference if the constant value of PWV, used for the analysis, is close to the averaged value of original PWV ($\bar{c}_{\text{avg}}$), however, this observation is specific to the conditions when variations of c about $\bar{c}_{\text{avg}}$ are similar to those in this study and it may not be trivial to extrapolate this conclusion if c_{max} and c_{min} fluctuate over a bigger interval about $\bar{c}_{\text{avg}}$. Observation (ii) is also in partial agreement with Alastruey [4] who reported a decreased error for the P-U loop method at locations close to well matched junctions in a full scale numerical model of systemic circulation.

7.6 Conclusion

In this chapter we studied the effectiveness of two commonly used techniques of P-U loop and the Sum of Squares methods to estimate the PWV in the pulmonary arteries and to investigate their influence on the patterns of reflected waves obtained by linear wave separation technique. Based on our results and discussion, we may conclude that the estimates of local PWV in the pulmonary arteries, simulated in this model, using Sum of Squares method do not provide good approximations of actual PWV, which consequently lead to misleading results, such as producing an artificial BCW at the beginning of systole, and hence erroneous conclusions about the pattern of reflected waves. In contrast, the performance of the P-U loop method is very satisfactory particularly when the PWV is estimated close to the heart and away from mismatched junctions and therefore the P-U loop technique proves to be a better choice for determining the local PWV in the pulmonary arteries. However, one of the limitations of the P-U loop is the careful choice of the linear portion in the loop and even the small change in the value of linear PWV may become significant in the WIA. Finally, this is the first study that investigates the effectiveness of these techniques in the pulmonary circulation model. Moreover, this study also highlights that a detailed validation of the model presented in this thesis with *in vivo* data present a good prospect of clinical applications of this model such as assessing and developing tools for clinical investigations.

Chapter 8

Conclusion

The primary objective of this thesis is to simulate the physiologically relevant, one–dimensional, pulse waveforms in the human pulmonary arteries and veins. This and other specific aims, described in Section 1.4, are successfully achieved by improving and extending an existing model by G. D. Vaughan [169]. Below we give the summary of achievements and the observations made throughout this thesis and state some of the limitations of this work, which also set the course of our future work in this area.

8.1 Summary of achievements

The pressure and flow waveforms are simulated in the large pulmonary arteries and veins by setting up a network including both small and large arteries and veins enabling simulations of blood flow and pressure along the complete path emanating at the right ventricle and ending at the left atrium. The waveforms are simulated in the large blood vessels by numerically solving the non–linear, cross–sectionally averaged, Navier–Stokes equations combined with a state equation, subject to one inflow and four outflow conditions, whereas the linearised Navier–Stokes equations with the same state equation are solved analytically in each small vessel. The linearised model is first used to incorporate the effects of downstream haemodynamics, through a structured tree based matching condition, on the pressure and flow simulations in the large vessels, and then to predict the mean pressure drop within the pulmonary vascular beds by treating the structured trees as an active fluid dynamical part in the model. The model is exploited to simulate a pathological condition viz. the pulmonary hypertension and all results, both for physiological and pathological conditions, are interpreted in a more useful and insightful manner by separating the pulse waveforms into their forward and backward running components by using the tool of WIA.

We observed that by incorporating the more prevalent venous anatomy with four outflow veins, compared to a single outflow vein in the previous model, and by modifying the compliance parameter (a constant compliance), pressure predictions are improved and the simulated pressure waveforms give physiologically accurate predictions with values agreeing with pressures reported in [55] and [63]. The waveforms also share features observed for *in vivo* MPA waveform, as given by Greenfield & Griggs [59] (see Figures 3.11 and 3.12). We also observed that our simulations are extremely sensitive to the value of compliance parameter and how different compliance values may lead to chaotic waveforms. The observations in Section 4.1 show that, for the given set of parameters and boundary conditions, the model shows the expected behaviour throughout the tree, e.g. wave propagation and peaking of pressure away from the heart due to vessel tapering and the high flow–rate through vessels with bigger cross–sectional areas is visible in all the results. Moreover, although the variations in the venous pressure about the imposed outflow pressure are small, the model predicts a visible pulse pressure in the veins. We also observed in this section that the basic geometrical data for the large blood vessels imparts significantly on the results, and the haemodynamics in individual blood vessels vary a lot with local geometric properties such as the vessel length and the amount of taper.

The simulations of pulmonary hypertension in Sections 4.2 and 4.3 show how the pressure and flow vary under different types of pulmonary hypertension for two extreme cases, (i) when a healthy heart is able to maintain an adequate flow of blood through the system, and (ii) when right ventricular dysfunction may only produce a certain pressure to pass the blood in the face of growing downstream pathology. In either case, we have simulated the qualitative effects (pressure rise and flow reversal) of these conditions on pressure and flow, however, the quantitive effects (the amount of pressure rise and flow reversal) is not in good agreement with related studies in the literature. Moreover, the simultaneous effects on pressure and flow under progressing hypertension are also missing form our results. The reason for this is that the two cases considered here are two extreme ends of the same condition which are simulated by prescribing two different inflow conditions (time varying flow–rate and pressure profile), which can not react to correspond the distal geometrical and material changes in the model. Furthermore, venous hypertension only leads to an upward shift in the pressure and flow by changing the LA pressure in our model and does not show any effects on wave propagation or pulse pressure. This observation also highlights the limitation of our model, which is associated with outflow boundary conditions. These aspect are further discussed in future work section.

In Section 5.2, we further extended our model to predict the mean pressure drop across the pulmonary vascular beds and provided a new algorithm to compute the mean pressure within the smallest arterioles and venules included in our model. We provided a power–law relation between mean pressure and vessel radius ($\geq 50\mu$m) (see equation (5.10)), separately for arterial and venous sides and observed how pressure drop continues across the venous side of vascular beds. We concluded that the vascular beds are the site of maximum resistance where most, and an almost equal amount, of the pressure drops on the arterial and venous sides of vascular beds while the steepest pressure drop occurs through the vessels of smallest radius. We also extended this analysis to understand the two way effects of pulmonary hypertension, in particular when the pathophysiology is located in the microcirculation, i.e. PAH and PH associated with HLD, and observed that in the case of HLD increase in rarefaction further risks increase in pathology. The microcirculatory characteristic of pulmonary circulation has previously not been studied in great detail and our work highlights this new aspect of pulmonary haemodynamics. The limitation of this study, however, is that our model does not include the effects of pulmonary capillaries and the arterial and venous structured trees are connected bypassing the complexity of the capillary network and flow around alveoli.

In Chapter 6, we interpret our results by analysing the patterns of reflected waves in the pulmonary arteries and use the traditional WIA to simulate the incident and reflected components of pressure, blood flow velocity and the wave intensity profiles. We observed that the proximal large arterial junctions in our model behave as open–end type reflectors and serve to reduce the RV afterload whereas we recognised the micro–circulations as the site of closed–end type reflections which augment the blood pressure and increase the RV afterload. Moreover, the WIA of hypertension simulations suggest that the BCW amplifies during hypertension that causes an elevation in the arterial pressure. These observations are in agreement with related *in vivo* studies of pulmonary circulation which characterise normal pulmonary circulation with negative or open–end type reflections. This observation also highlights the physiological relevance and promising prospect of this model. However, it should be noted that the traditional theory of WIA does not incorporate the non–linear effects due to the frictional losses on the wave separation. Moreover the traditional theory does not explain the role of reflected waves from previous cycles, which can be studied by using the most recent developments in the theory [5].

In Chapter 7, we analyse how the linear PWV influences the pulse wave separation and observe that in the pulmonary arteries the PU–loop method provides more realistic estimates of PWV than the Sum of the Squares technique and therefore the former technique also provides more reliable results when used in the WIA. However, the current analysis does not provide sufficient details to mathematically justify this difference, which certainly merits further investigation in order to better understand the pitfalls of such, clinically relevant, techniques.

8.2 Future directions

Although the current simulations, set up to predict pressure and flow dynamics under physiological and pathological conditions, display good qualitative agreement with physiologically observed features and observations about pulmonary haemodynamics during hypertension, there is significant room to further improve this model both from modelling and application point of view.

Validation: First of all, the model developed here is only partially patient specific; we included geometric and flow measurements for the pulmonary arteries, whilst data from the venous networks were estimated from literature. Since the vessel dimensions have been observed to influence the local haemodynamics, the first step toward improving this model should be to make it completely subject–specific. Moreover, throughout the thesis we have used published studies from physiological literature to validate our model but a detailed comparison of simulated pressure and flow waveforms with measured data is missing. This is very important from the application point of view and in the long run a practical validation would increase the confidence in the clinical applicability of this model. To do this we recommend a new MRI experiment that can provide new measurements of arterial and venous vessels and the blood flow–rate, from a single subject. The experiment should be focused on collecting the dimensions (lengths and diameters) of the largest pulmonary arteries and veins to as many generations as possible. Moreover, during the experiment, besides the inflow at the entry of MPA, it may be possible to collate the blood flow at different locations in the first three arteries and veins. These non–invasively measured waveforms may then be used to compare the simulated waveforms at the same locations in those arteries.

Structured trees: Other than the length to radius ratios, structured trees for arterial and venous sides in our model are constructed by using the same values for the parameters like radius exponent (ξ) and asymmetry ratio (γ), throughout the trees. However, it has recently been shown (R.B. Clipp [34]; W. B. Cousins [40]) that altering these parameters within the structured tree better reflects the total resistance at different levels within the vascular beds and gives improved predictions. The approaches in these studies can easily be followed in our model too, with a further investigation into similarities and differences within and between the arterial and venous side of circulation. Furthermore, in this model we do not model the capillary level, and the vessels of diameter $\leq 100\mu$m are left out. Two issues appear if we look to include these vessels: firstly the blood at capillary level behaves as a non-Newtonian fluid [126] and therefore the constant viscosity assumption becomes invalid and does not give good predictions. Secondly, it has been shown that choosing $\mathrm{r}_{\mathrm{min}} \leq 50\,\mu$m makes r_{min} incompatible with other well defined structured tree parameters, such as ξ, and may cause convergence issues (Cousins & Gremaud [38]). Following the approach in [38], a preliminary study from one of our colleagues[1] in the group shows that the same condition is also true for a two–sided connected structured trees with finite number of generations, i.e. the resulting admittance matrix $\mathbf{Y}$ is non–singular and converges as $r_{\mathrm{min}} \to 0$ if and only if $\xi > 3$ in equation (2.2) (personal communication). Since the physiological value of $\xi \in [2.33, 3]$, the total admittance of the connected trees become very sensitive to the choice of r_{min}. In addition, G. D. Vaughan [169] also showed that the structured tree is not a suitable model to simulate the blood flow at the capillary level as the blood pressure increases well above the physiological range for $\mathrm{r}_{\mathrm{min}} \leq 100\mu$m. There may be two possible ways to find a way round this problem: (i) modelling the capillary level with different structured tree parameters and using a radius dependent viscosity modulus [39], or (ii) using the existing theory of sheet flow in lung alveoli given by Y. C. Fung [55]. For the first approach, physiological measurements of pressure and flow and use of optimization techniques would be required to obtain the zone–specific structured–tree parameters.

---

[1] Ellen den Ouden worked with Prof. Niholas A Hill as a summer project student in the mathematical biology group at school of mathematics and statistics, university of Glasgow.

Boundary conditions: Other significant improvements which can increase the sophistication of this model are improvements in the boundary conditions, as the current model misses an active mechanical response at the system inlet and outlets. The contraction of the left atrium causes a biphasic flow profile in the large pulmonary veins, which may propagate upstream while the remodelling of the right heart in disease is clearly linked to disease within the pulmonary circulation. However, due to the prescribed pressure or flow inflow as boundary condition the right heart can not react to any changes occurring in the circulation. Moreover, due to the fixed pressure outflow at the opening of four veins, any perturbation due to the left heart activity is prevent from propagation through the circulation, thus leaving pulmonary haemodynamics insensitive to heart response. Therefore coupling of this system with a dynamic heart model would invoke a feed back mechanism in the face of downstream changes in the circulation and would significantly improve our ability to simulate the conditions of pulmonary hypertension including the pulmonary venous hypertension, which is associated with the left heart condition.

In conclusion, this thesis is a step forward in understanding the performance of the pulmonary circulation and its behaviour in response to various anatomical and physiological changes in health and disease. The thesis presents a promising model of the pulmonary circulation, which gives significantly improved predictions of normal pulmonary pressure and flow at a reasonable computational cost. The model can be developed further to study the effects of respiration, gravity, and branching patterns on pressure and flow distribution within the lung. Doing so may further enhance our ability to study a wide range of pulmonary diseases that would further improve our understanding of the underlying mechanisms of more complex disease processes. Finally, the current model is a base for a more sophisticated model and with further extensions, improvements and validation, the model has a great potential for clinical applications in the long run .

Appendix A

One–dimensional system

It is convenient to first make the equations (2.7) and (2.8) dimensionless to derive one–dimensional system of non–linear equations. In order to perform dimensional analysis let us define V_r and V_x as the characteristic velocities in axial and radial directions. V_r and V_x also define the characteristic length, λ, in the x direction, over which deviation from the axis is R_0, characteristic vessel radius. We also define the characteristic pressure p_0 by $p_0 = \rho V_x^2$ and the time scale T in terms of V_r and V_x as

$$T = \frac{R_0}{V_r} = \frac{\lambda}{V_x}.$$

Here we notice that $R_0/V_r = \lambda/V_x$, which stems from the fact that we want to use only one time scale. From these quantities we define our dimension less variables as

$$u_r = V_r \tilde{u_r}, \quad u_x = V_x \tilde{u_x}, \quad r = R_0 \tilde{r}, \quad x = \lambda \tilde{x} \text{ and } \quad p = p_0 \tilde{p} = \rho V_x^2 \tilde{p}.$$

Due to the natural structure of the blood vessels, i.e. vessels are much longer in the axial direction than in the radial direction, we assume that $R_0 \ll \lambda$, which also leads to that fact that for a laminar flow in compliant tube the maximum value of radial velocity u_r is the radial velocity of the vessel wall. In the case of arteries the vessel walls undergo small transverse motion which leads to the fact that $u_r \ll u_x$, which ultimately means that $V_r \ll V_x$. Thus we define

$$\frac{V_r}{V_x} = \frac{R_0}{\lambda} = \varepsilon.$$

The analysis below is only valid for $\varepsilon \ll 1$.

We begin by rewriting and non–dimensionalizing (2.7) to determine the pressure dependence on radial coordinate.

$$\frac{\partial p}{\partial r} = \mu\left(\frac{\partial^2 u_r}{\partial r^2} + \frac{1}{r}\frac{\partial u_r}{\partial r} + \frac{\partial^2 u_r}{\partial x^2} - \frac{u_r}{r^2}\right) - \rho\left(\frac{\partial u_r}{\partial t} + u_r\frac{\partial u_r}{\partial r} + u_x\frac{\partial u_r}{\partial x}\right), \tag{A.1}$$

after using the dimensionless quantities, we get

$$\frac{\rho V_x^2}{R_0}\frac{\partial \tilde{p}}{\partial \tilde{r}} = \mu\left(\frac{V_r}{R_0^2}\frac{\partial^2 \tilde{u_r}}{\partial \tilde{r}^2} + \frac{V_r}{R_0^2\tilde{r}}\frac{\partial \tilde{u_r}}{\partial \tilde{r}} + \frac{V_r}{\lambda^2}\frac{\partial^2 \tilde{u_r}}{\partial \tilde{x}^2} - \frac{V_r}{R_2}\frac{\tilde{u_r}}{\tilde{r}^2}\right) - \rho\left(\frac{V_r}{T}\frac{\partial \tilde{u_r}}{\partial \tilde{t}} + \frac{V_r^2}{R}\tilde{u_r}\frac{\partial \tilde{u_r}}{\partial \tilde{r}} + \frac{V_r V_x}{\lambda}\tilde{u_x}\frac{\partial \tilde{u_r}}{\partial \tilde{x}}\right),$$

$$\frac{\partial \tilde{p}}{\partial \tilde{r}} = \frac{\nu}{R_0}\frac{V_r}{V_x}\left(\frac{\partial^2 \tilde{u_r}}{\partial \tilde{r}^2} + \frac{1}{\tilde{r}}\frac{\partial \tilde{u_r}}{\partial \tilde{r}} - \frac{\tilde{u_r}}{\tilde{r}^2}\right) + \frac{R_0\nu}{\lambda^2}\frac{V_r}{V_x^2}\frac{\partial^2 \tilde{u_r}}{\partial \tilde{x}^2} - \frac{V_r^2}{V_x^2}\left(\frac{\partial \tilde{u_r}}{\partial \tilde{t}} + \tilde{u_r}\frac{\partial \tilde{u_r}}{\partial \tilde{r}} + \frac{\partial \tilde{u_r}}{\partial \tilde{x}}\right),$$

$$\frac{\partial \tilde{p}}{\partial \tilde{r}} = \varepsilon\frac{\nu}{R_0}\left(\frac{\partial^2 \tilde{u_r}}{\partial \tilde{r}^2} + \frac{1}{\tilde{r}}\frac{\partial \tilde{u_r}}{\partial \tilde{r}} - \frac{\tilde{u_r}}{\tilde{r}^2}\right) + \varepsilon\frac{R_0}{\lambda^2}\frac{\nu}{V_x}\frac{\partial^2 \tilde{u_r}}{\partial \tilde{x}^2} - \varepsilon^2\left(\frac{\partial \tilde{u_r}}{\partial \tilde{t}} + \tilde{u_r}\frac{\partial \tilde{u_r}}{\partial \tilde{r}} + \frac{\partial \tilde{u_r}}{\partial \tilde{x}}\right).$$

Since each term in the above equation contains ε and by our assumption $\varepsilon \to 0$, so we are left with

$$\frac{\partial \tilde{p}}{\partial \tilde{r}} \approx 0, \tag{A.2}$$

which implies that dependency of pressure on radial coordinate is negligible i.e. $p \neq p(r)$.

We now non–dimensionalise (2.10) by using the dimension less quantities.

$$\rho\left(\frac{V_x}{T}\frac{\partial \tilde{u_x}}{\partial \tilde{t}} + \frac{V_r V_x}{R_0}\tilde{u_r}\frac{\partial \tilde{u_x}}{\partial \tilde{r}} + \frac{V_x^2}{\lambda}\tilde{u_x}\frac{\partial \tilde{u_x}}{\partial \tilde{x}}\right) = -\frac{\rho V_x^2}{\lambda}\frac{\partial \tilde{p}}{\partial \tilde{x}} + \mu\left(\frac{V_x}{R_0^2}\frac{\partial^2 \tilde{u_x}}{\partial \tilde{r}^2} + \frac{V_x}{R_0^2\tilde{r}}\frac{\partial \tilde{u_x}}{\partial \tilde{r}} + \frac{V_x}{\lambda^2}\frac{\partial^2 \tilde{u_x}}{\partial \tilde{x}^2}\right),$$

$$\left(\frac{\partial \tilde{u_x}}{\partial \tilde{t}} + \tilde{u_r}\frac{\partial \tilde{u_x}}{\partial \tilde{r}} + \tilde{u_x}\frac{\partial \tilde{u_x}}{\partial \tilde{x}}\right) = -\frac{\partial \tilde{p}}{\partial \tilde{x}} + \frac{\lambda\nu}{R_0^2 V_x}\left(\frac{\partial^2 \tilde{u_x}}{\partial \tilde{r}^2} + \frac{1}{\tilde{r}}\frac{\partial \tilde{u_x}}{\partial \tilde{r}}\right) + \frac{\nu}{\lambda V_x}\frac{\partial^2 \tilde{u_x}}{\partial \tilde{x}^2},$$

$$\left(\frac{\partial \tilde{u_x}}{\partial \tilde{t}} + \tilde{u_r}\frac{\partial \tilde{u_x}}{\partial \tilde{r}} + \tilde{u_x}\frac{\partial \tilde{u_x}}{\partial \tilde{x}}\right) = -\frac{\partial \tilde{p}}{\partial \tilde{x}} + \frac{\nu}{R_0 V_x}\left(\frac{\lambda}{R_0}\frac{\partial^2 \tilde{u_x}}{\partial \tilde{r}^2} + \frac{\lambda}{R_0\tilde{r}}\frac{\partial \tilde{u_x}}{\partial \tilde{r}} + \frac{R_0}{\lambda}\frac{\partial^2 \tilde{u_x}}{\partial \tilde{x}^2}\right)$$

$$\left(\frac{\partial \tilde{u_x}}{\partial \tilde{t}} + \tilde{u_r}\frac{\partial \tilde{u_x}}{\partial \tilde{r}} + \tilde{u_x}\frac{\partial \tilde{u_x}}{\partial \tilde{x}}\right) = -\frac{\partial \tilde{p}}{\partial \tilde{x}} + \frac{\nu}{R_0 V_x}\left(\frac{1}{\varepsilon}\frac{\partial^2 \tilde{u_x}}{\partial \tilde{r}^2} + \frac{1}{\varepsilon\tilde{r}}\frac{\partial \tilde{u_x}}{\partial \tilde{r}} + \varepsilon\frac{\partial^2 \tilde{u_x}}{\partial \tilde{x}^2}\right)$$

$$\left(\frac{\partial \tilde{u_x}}{\partial \tilde{t}} + \tilde{u_r}\frac{\partial \tilde{u_x}}{\partial \tilde{r}} + \tilde{u_x}\frac{\partial \tilde{u_x}}{\partial \tilde{x}}\right) = -\frac{\partial \tilde{p}}{\partial \tilde{x}} + \frac{\nu}{R_0 V_x}\frac{1}{\varepsilon}\left(\frac{\partial^2 \tilde{u_x}}{\partial \tilde{r}^2} + \frac{1}{\tilde{r}}\frac{\partial \tilde{u_x}}{\partial \tilde{r}}\right)$$

$$\left(\frac{\partial \tilde{u_x}}{\partial \tilde{t}} + \tilde{u_r}\frac{\partial \tilde{u_x}}{\partial \tilde{r}} + \tilde{u_x}\frac{\partial \tilde{u_x}}{\partial \tilde{x}}\right) = -\frac{\partial \tilde{p}}{\partial \tilde{x}} + \frac{\nu\lambda}{R_0^2 V_x}\left(\frac{\partial^2 \tilde{u_x}}{\partial \tilde{r}^2} + \frac{1}{\tilde{r}}\frac{\partial \tilde{u_x}}{\partial \tilde{r}}\right)$$

Since the Reynolds number is defined by only one length scale, we choose to keep our length scale R_0 and set $\lambda = R_0$, thus

$$\mathcal{R}e = \frac{R_0^2 V_x}{\nu\lambda} = \frac{R_0 V_x}{\nu}$$

So that the x–momentum equation reduces to

$$\left(\frac{\partial \tilde{u_x}}{\partial \tilde{t}} + \tilde{u_r}\frac{\partial \tilde{u_x}}{\partial \tilde{r}} + \tilde{u_x}\frac{\partial \tilde{u_x}}{\partial \tilde{x}}\right) = -\frac{\partial \tilde{p}}{\partial \tilde{x}} + \frac{1}{\mathcal{R}e}\left(\frac{\partial^2 \tilde{u_x}}{\partial \tilde{r}^2} + \frac{1}{\tilde{r}}\frac{\partial \tilde{u_x}}{\partial \tilde{r}}\right) \tag{A.3}$$

Appendix B

Numerical Implementation of Bifurcation and Matching Conditions

The numerical equations derived in this Appendix are same as those derived in [113] and [169]. However, in our model, $f(r_0) = \textit{constant}$, throughout our analysis, which leads all derivatives of $f(r_0)$ to be vanished from the equations below. Thus the resulting equations would be a special case of a more general case considered in [113] and [169]. However, here we also present the equations for more general case when $f(r_0) = f(r_0(x))$ and the derivation for special case become trivial.

B.1 Bifurcation conditions

Equations (2.51) and (2.51) give the bifurcation conditions prescribed on the pressure and flow i.e.

$$\begin{aligned} p_p(L,t) &= p_{d_1}(0,t) = p_{d_2}(0,t), && \text{(B.1)} \\ q_p(L,t) &= q_{d_1}(0,t) + q_{d_2}(0,t). && \text{(B.2)} \end{aligned}$$

So each bifurcation there is an outflow boundary condition at the outlet of parent vessel and inflow boundary conditions at the inlet of two daughter vessels. Thus the quantities $\mathbf{\Omega}_M$, for the parent vessels and $\mathbf{\Omega}_0$ for the daughter vessels ($\mathbf{\Omega}$=$\mathbf{W}, \mathbf{S}$) are unknown and are to be determined. Moreover, for the solution at both interior and boundary points, the quantities $\mathbf{\Omega}^{n+1/2}_{\mathcal{M}+1/2}$ and $\mathbf{\Omega}^{n+1/2}_{\mathcal{M}-1/2}$, with $\mathcal{M} = M$ for $\mathbf{\Omega}$ originating from the parent vessels and $\mathcal{M} = 0$ for $\mathbf{\Omega}$ originating from daughter vessels, in this case cannot be estimated explicitly at each time-level by using the ghost points

$$\begin{aligned} q_{\mathcal{M}}^{n+1/2} &= \frac{1}{2}\left(q_{\mathcal{M}-1/2}^{n+1/2} + q_{\mathcal{M}+1/2}^{n+1/2}\right), & \text{(B.3)}\\ A_{\mathcal{M}}^{n+1/2} &= \frac{1}{2}\left(A_{\mathcal{M}-1/2}^{n+1/2} + A_{\mathcal{M}+1/2}^{n+1/2}\right), & \text{(B.4)} \end{aligned}$$

as they also require values at unknown boundary points, $x = M$ and $x = 0$ at the half time-step, (see Figures 2.11 and 2.12). Thus creating the ghost point at the junction for parent and daughter vessels would increase the number of unknowns variables in the system.

The bifurcation conditions at time level $n + 1/2$ and $n + 1$ can be written as

$$\begin{aligned} (p^{(p)})_M^j = (p^{(d_1)})_0^j &= (p^{(d_2)})_0^j, & \text{(B.5)}\\ (q^{(p)})_M^j - (q^{(d_1)})_0^j &= (q^{(d_2)})_0^j, & \text{(B.6)} \end{aligned}$$

where $j = n+1/2, n+1$. Equations (B.5) can be written in terms of A using the equation of state (2.28) as

$$(f^{(p)})_M\left(1 - \sqrt{\frac{(A_0^{(p)})_M}{(A^{(p)})_M^{n+1/2}}}\right) = (f^{(d_i)})_0\left(1 - \sqrt{\frac{(A_0^{(d_i)})_0}{(A^{(d_i)})_M^{n+1/2}}}\right) \qquad \text{(B.7)}$$

and

$$(f^{(p)})_M\left(1 - \sqrt{\frac{(A_0^{(p)})_M}{(A^{(p)})_M^{n+1}}}\right) = (f^{(d_i)})_0\left(1 - \sqrt{\frac{(A_0^{(d_i)})_0}{(A^{(d_i)})_M^{n+1}}}\right), \qquad \text{(B.8)}$$

where $i = d_1, d_2$ and $f(r_0) = 4Eh/3r_0$. Since $f(r_0)$ is a constant function in the present model, we may eliminate it from the above equations and throughout the system but for the sake of generality, the numerical equations are derived with f as a function of r_0. With S_1 being zero, from the numerical equations (2.104), q and A for the parent vessel at the junction can be written as

$$\begin{aligned} (q^{(p)})_M^{n+1} = (q^{(p)})_M^n &- \frac{\Delta t}{\Delta x}\left((W_2^{(p)})_{M+1/2}^{n+1/2} - (W_2^{(p)})_{M-1/2}^{n+1/2}\right)\\ &+ \frac{\Delta t}{2}\left((S_2^{(p)})_{M+1/2}^{n+1/2} + (S_2^{(p)})_{M-1/2}^{n+1/2}\right), \qquad \text{(B.9)}\\ (A^{(p)})_M^{n+1} = (A^{(p)})_M^n &- \frac{\Delta t}{\Delta x}\left((W_1^{(p)})_{M+1/2}^{n+1/2} - (W_1^{(p)})_{M-1/2}^{n+1/2}\right). \qquad \text{(B.10)} \end{aligned}$$

Similarly for the inflow to daughter vessel at the junction, we get

$$\begin{aligned} (q^{(i)})_0^{n+1} = (q^{(i)})_0^n &- \frac{\Delta t}{\Delta x}\left((W_2^{(i)})_{1/2}^{n+1/2} - (W_2^{(i)})_{-1/2}^{n+1/2}\right)\\ &+ \frac{\Delta t}{2}\left((S_2^{(i)})_{1/2}^{n+1/2} + (S_2^{(i)})_{-1/2}^{n+1/2}\right), \qquad \text{(B.11)} \end{aligned}$$

$$(A^{(i)})_0^{n+1} = (A^{(i)})_0^n - \frac{\Delta t}{\Delta x}\left((W_1^{(i)})_{1/2}^{n+1/2} - (W_1^{(i)})_{-1/2}^{n+1/2}\right), \tag{B.12}$$

where $i = d_1, d_2$. The system of equations (B.5)–(B.10) involves the following unknowns

$$\begin{array}{lll}
x_1 = (q^{(p)})_M^{n+1} & x_2 = (q^{(p)})_M^{n+1/2} & x_3 = (q^{(p)})_{M+1/2}^{n+1/2} \\
x_4 = (q^{(d_1)})_0^{n+1} & x_5 = (q^{(d_1)})_0^{n+1/2} & x_6 = (q^{(d_1)})_{-1/2}^{n+1/2} \\
x_7 = (q^{(d_2)})_0^{n+1} & x_8 = (q^{(d_2)})_0^{n+1/2} & x_9 = (q^{(d_2)})_{-1/2}^{n+1/2} \\
x_{10} = (A^{(p)})_M^{n+1} & x_{11} = (A^{(p)})_M^{n+1/2} & x_{12} = (A^{(p)})_{M+1/2}^{n+1/2} \\
x_{13} = (A^{(d_1)})_0^{n+1} & x_{14} = (A^{(d_1)})_0^{n+1/2} & x_{15} = (A^{(d_1)})_{-1/2}^{n+1/2} \\
x_{16} = (A^{(d_2)})_0^{n+1} & x_{17} = (A^{(d_2)})_0^{n+1/2} & x_{18} = (A^{(d_2)})_{-1/2}^{n+1/2}
\end{array}$$

Newtonian's method

Each of equations (B.5)–(B.10) can be expressed as residual equations $f_r(x_1, x_2, \ldots, x_{18}) = 0$. Thus the resulting system comprises eighteen non–linear equations in the variables listed above. At each time step, n, the system can be solved to estimate $\mathbf{x} = (x_1, x_2, \ldots, x_{18})$ by using the Newton's method which solves $\mathbf{f_r}(\mathbf{x}_i) = 0$ by extending the tangent line at some current guess for the root $\mathbf{x}_i$ until it crosses zero. Then it sets the next guess for $\mathbf{x}_{i+1}$ the abscissa of that zero-crossing i.e. $|\mathbf{x}_i|$.

Algebraically, based on the first order expansion of Taylor's series in the neighborhood of a point x, the method gives

$$x_i = x_{i-1} - \left(\frac{df(x_{i-1})}{dx_{i-1}}\right)^{-1} f(x_{i-1}),$$

where the index $i = 1, 2, 3, \ldots$ represent the number of iterations which continue until the error $|f(x_i) - f(x_{i-1})| < \epsilon$. The method only works if $df/dx_i \neq 0$ and there is an appropriate initial guess x_0 is available.

Thus using the Newton's method, we have

$$\mathbf{x}_i = \mathbf{x}_{i-1} - (D\mathbf{f_r}(\mathbf{x}_{i-1}))^{-1}\mathbf{f_r}(\mathbf{x}_{i-1}), \tag{B.13}$$

where $i = 1, 2, 3, \ldots$ refer to number of iterations and for method to converge subject to a suitable initial guess $\mathbf{x}_0$ the Jacobian $D\mathbf{f_r}(\mathbf{x})$ has to be non–singular in all iterations.

Residual equations for the Newton's scheme

Eighteen residual equations $((f_r)_1, (f_r)_2, (f_r)_3, \ldots (f_r)_{18})$ are required to be extracted from (B.5)–(B.10) to apply Newtonian's method to approximate eighteen unknowns $(x_1, x_2, x_3, \ldots x_{18})$. Derivation of these equations is given below.

$(f_r)_1$ from equation (B.9)

$$\begin{aligned}(f_r)_1 = -x_1 + (q^{(p)})^n_M - \theta\left(\frac{x_3^2}{x_{12}} + B(M+1/2, x_{12}) - \left(W_2^{(p)}\right)^{n+1/2}_{M-1/2}\right) + \\ \gamma\left(F(M+1/2, x_3, x_{12}) + \frac{dB(M+1/2, x_{12})}{dx} + \left(S_2^{(p)}\right)^{n+1/2}_{M-1/2}\right).\end{aligned}$$

Here

$$\theta = \frac{\Delta t}{\Delta x} \qquad \text{and} \qquad \gamma = \frac{\Delta t}{2},$$

and

$$\begin{aligned}B(M+1/2, x_{12}) &= f(r_0)_{M+1/2}\sqrt{x_{12}\,(A_0)_{M+1/2}} \\ F(M+1/2, x_3, x_{12} &= \frac{2\pi(r_0)_{M+1/2}}{\delta\mathcal{R}}\frac{x_3}{x_{12}} \\ \frac{dB(M+1/2, x_{12})}{dx} &= \left(\frac{\partial B}{\partial r_0}\frac{dr_0}{d_x}\right)^{n+1/2}_{M+1/2}, \\ &= \left(2\sqrt{x_{12}}\left(\sqrt{\pi}f(r_0) + \sqrt{A_0}\frac{df}{dr_0}\right) - A\frac{df}{dr_0}\right)_{M+1/2}\left(\frac{dr_0}{dx}\right)_{M+1/2}\end{aligned}$$

Let

$$k_1 = (q^{(p)})^n_M + \theta\left(W_2^{(p)}\right)^{n+1/2}_{M-1/2} + \gamma\left(S_2^{(p)}\right)^{n+1/2}_{M-1/2}$$

then $(f_r)_1$ can be written as

$$\begin{aligned}(f_r)_1 = k_1 - x_1 - \theta\left(\frac{x_3^2}{x_{12}} + B(M+1/2, x_{12})\right) + \\ \gamma\left(F(M+1/2, x_3, x_{12}) + \frac{dB(M+1/2, x_{12})}{dx}\right)\end{aligned} \qquad \text{(B.14)}$$

$(f_r)_{2,3}$ from equation (B.11)

Similarly, we may find two the residual equations originating from daughter vessels i.e.

$$\begin{aligned}(f_r)_{2,3} = -x_{4,7} + (q^{(d_1,d_2)})^n_0 - \theta\left(\left(W_2^{(d_1,d_2)}\right)^{n+1/2}_{1/2} - B(-1/2, x_{15,18})\right) + \\ \gamma\left(F(-1/2, x_{6,9}, x_{15,18}) + \frac{dB(-1/2, x_{15,18})}{dx} + \left(S_2^{(d_1,d_2)}\right)^{n+1/2}_{1/2}\right)\end{aligned}$$

where corresponding B, F and dB/dx are defined in a similar ways as above. Now let

$$k_{2d_1,2d_2} = (q^{(d_1,d_2)})_0^n - \theta \left(W_2^{(d_1,d_2)}\right)_{1/2}^{n+1/2} + \gamma \left(S_2^{(d_1,d_2)}\right)_{1/2}^{n+1/2}$$

then

$$(f_r)_{2,3} = k_{2d_1,2d_2} - x_{4,7} - \theta \left(\frac{x_{6,9}^2}{x_{15,18}} + B(-1/2, x_{15,18}) \right) + \gamma \left(F(-1/2, x_{6,9}, x_{15,18}) + \frac{dB(-1/2, x_{15,18})}{dx} \right) \tag{B.15}$$

$(f_r)_4$ **from equation (B.10):**

$$(fr)_4 = -x_{10} - \theta x_3 + k_3 \tag{B.16}$$

where

$$k_3 = (A^{(p)})_M^n + \theta \left(W_1^{(p)}\right)_{M-1/2}^{n+1/2}$$

$(f_r)_{5,6}$ **from equation (B.12)**

Similarly for two daughter vessels, the residual equations are

$$(fr)_{5,6} = -x_{13,16} + \theta x_{6,9} + k_{4d_1,4d_2} \tag{B.17}$$

where

$$k_{4d_1,4d_2} = (A^{(d_1,d_2)})_0^n - \theta \left(W_1^{(d_1,d_2)}\right)_{1/2}^{n+1/2}$$

$(f_r)_7$ **from equation (B.3):**

$$(f_r)_7 = -x_2 + \frac{x_3}{2} + k_5 \tag{B.18}$$

where k_5 is given by

$$k_5 = \frac{(q^{(p)})_{M-1/2}^{n+1/2}}{2}$$

$(f_r)_{8,9}$ **from equation (B.3)**

Similarly for two daughter vessels, we have

$$(f_r)_{8,9} = -x_{5,8} + \frac{x_{6,9}}{2} + k_{6d_1,6d_2} \tag{B.19}$$

where

$$k_{6d_1,6_d2} = \frac{(q^{(d_1,d_2)})_{1/2}^{n+1/2}}{2}$$

$(f_r)_{10}$ **from equation (B.4)**

$$(f_r)_{10} = -x_{11} + \frac{x_{12}}{2} + k_7 \tag{B.20}$$

where

$$k_7 = \frac{(A^{(p)})^{n+1/2}_{M-1/2}}{2}$$

$(f_r)_{11,12}$ **from equation (B.4)**

For daughter vessels, we have

$$(f_r)_{11,12} = -x_{14,17} + \frac{x_{15,18}}{2} + k_{8d_1,8d_2} \tag{B.21}$$

where

$$k_{8d_1,8d_2} = \frac{(A^{(d_1,d_2)})^{n+1/2}_{1/2}}{2}$$

$(f_r)_{13,14}$ **from equation (B.6)**

$$(f_r)_{13,14} = -x_{2,1} + x_{5,4} + x_{8,7} \tag{B.22}$$

$(f_r)_{15,16}$ **from equation (B.7)**

$$\begin{aligned}(f_r)_{15,16} &= -p(M, x_{11}) + p(0, x_{14,17}) \\ &= -(f^{(p)})_M \left(1 - \sqrt{\frac{(A_0^{(p)})_M}{x_{11}}}\right) + (f^{(d_1,d_2)})_0 \left(1 - \sqrt{\frac{(A_0^{(d_1,d_2)})_0}{x_{14,17}}}\right),\end{aligned}$$

where $f = Eh/r_0$. Let

$$\begin{aligned}k_{9d_1,9d_2} &= -(f^{(p)})_M + (f^{(d_1,d_2)})_0 \\ k_{10} &= \left(f^{(p)}\sqrt{A_0^{(p)}}\right)_M \\ k_{11d_1,11d_2} &= \left(f^{(d_1,d_2)}\sqrt{A_0^{(d_1,d_2)}}\right)_0\end{aligned}$$

then $(f_r)_{15,16}$ can be written as

$$(f_r)_{15,16} = \frac{k_{10}}{\sqrt{x_{11}}} - \frac{k_{11d_1,11d_2}}{\sqrt{x_{14,17}}} + k_{9d_1,9d_2} \tag{B.23}$$

$(f_r)_{17,18}$ **from equation (B.8)**

$$\begin{aligned}(f_r)_{17,18} &= -p(M, x_{10}) + p(0, x_{13,16}) \\ &= -(f^{(p)})_M \left(1 - \sqrt{\frac{(A_0^{(p)})_M}{x_{10}}}\right) + (f^{(d_1,d_2)})_0 \left(1 - \sqrt{\frac{(A_0^{(d_1,d_2)})_0}{x_{13,16}}}\right).\end{aligned}$$

Since neither f or A_0 depend on t, we may use the constants k_9, k_{10} and $k_{11d_1,11d_2}$ once more to express $(f_r)_{17,18}$ as

$$(f_r)_{17,18} = \frac{k_{10}}{\sqrt{x_{10}}} - \frac{k_{11d_1,11d_2}}{\sqrt{x_{13,16}}} + k_{9d_1,9d_2}. \tag{B.24}$$

Jacobian for the Newton's scheme

The Jacobian for Newton's scheme (B.13), is given by

$$D\mathbf{f_r}(\mathbf{x}) = \begin{pmatrix}
-1 & 0 & \chi_1 & 0 & 0 & 0 & 0 & 0 & 0 & 0 & 0 & \chi_2 & 0 & 0 & 0 & 0 & 0 & 0 \\
0 & 0 & 0 & -1 & 0 & \chi_3 & 0 & 0 & 0 & 0 & 0 & 0 & 0 & 0 & \chi_4 & 0 & 0 & 0 \\
0 & 0 & 0 & 0 & 0 & 0 & -1 & 0 & \chi_5 & 0 & 0 & 0 & 0 & 0 & 0 & 0 & 0 & \chi_6 \\
0 & 0 & -\theta & 0 & 0 & 0 & 0 & 0 & 0 & -1 & 0 & 0 & 0 & 0 & 0 & 0 & 0 & 0 \\
0 & 0 & 0 & 0 & 0 & \theta & 0 & 0 & 0 & 0 & 0 & 0 & -1 & 0 & 0 & 0 & 0 & 0 \\
0 & 0 & 0 & 0 & 0 & 0 & 0 & 0 & \theta & 0 & 0 & 0 & 0 & 0 & 0 & -1 & 0 & 0 \\
0 & -1 & \frac{1}{2} & 0 & 0 & 0 & 0 & 0 & 0 & 0 & 0 & 0 & 0 & 0 & 0 & 0 & 0 & 0 \\
0 & 0 & 0 & 0 & -1 & \frac{1}{2} & 0 & 0 & 0 & 0 & 0 & 0 & 0 & 0 & 0 & 0 & 0 & 0 \\
0 & 0 & 0 & 0 & 0 & 0 & 0 & -1 & \frac{1}{2} & 0 & 0 & 0 & 0 & 0 & 0 & 0 & 0 & 0 \\
0 & 0 & 0 & 0 & 0 & 0 & 0 & 0 & 0 & 0 & -1 & \frac{1}{2} & 0 & 0 & 0 & 0 & 0 & 0 \\
0 & 0 & 0 & 0 & 0 & 0 & 0 & 0 & 0 & 0 & 0 & 0 & 0 & -1 & \frac{1}{2} & 0 & 0 & 0 \\
0 & 0 & 0 & 0 & 0 & 0 & 0 & 0 & 0 & 0 & 0 & 0 & 0 & 0 & 0 & 0 & -1 & \frac{1}{2} \\
0 & -1 & 0 & 0 & 1 & 0 & 0 & 1 & 0 & 0 & 0 & 0 & 0 & 0 & 0 & 0 & 0 & 0 \\
-1 & 0 & 0 & 1 & 0 & 0 & 1 & 0 & 0 & 0 & 0 & 0 & 0 & 0 & 0 & 0 & 0 & 0 \\
0 & 0 & 0 & 0 & 0 & 0 & 0 & 0 & 0 & 0 & \chi_7 & 0 & 0 & \chi_8 & 0 & 0 & 0 & 0 \\
0 & 0 & 0 & 0 & 0 & 0 & 0 & 0 & 0 & 0 & \chi_7 & 0 & 0 & 0 & 0 & 0 & \chi_9 & 0 \\
0 & 0 & 0 & 0 & 0 & 0 & 0 & 0 & 0 & \chi_{10} & 0 & 0 & \chi_{11} & 0 & 0 & 0 & 0 & 0 \\
0 & 0 & 0 & 0 & 0 & 0 & 0 & 0 & 0 & \chi_{10} & 0 & 0 & 0 & 0 & 0 & \chi_{12} & 0 & 0
\end{pmatrix}$$

where

$$\begin{aligned}
\chi_1 &= -2\theta\frac{x_3}{x_{12}} + \gamma\frac{dF(M+1/2, x_3, x_{12})}{dx_3}\\
\chi_2 &= \theta\left(\frac{x_3^2}{x_{12}^2} - \frac{dB(M+1/2, x_{12})}{dx_{12}}\right) + \gamma\left(\frac{dF(M+1/2, x_3, x_{12})}{dx_{12}} + \frac{d^2B(M+1/2, x_{12})}{dxdx_{12}}\right)\\
\chi_3 &= 2\theta\frac{x_6}{x_{15}} + \gamma\frac{dF(-1/2, x_6, x_{15})}{dx_6}\\
\chi_4 &= \theta\left(-\frac{x_6^2}{x_{15}^2} + \frac{dB(-1/2, x_{15})}{dx_{15}}\right) + \gamma\left(\frac{dF(-1/2, x_6, x_{15})}{dx_{15}} + \frac{d^2B(-1/2, x_{15})}{dxdx_{15}}\right)\\
\chi_5 &= 2\theta\frac{x_9}{x_{18}} + \gamma\frac{dF(-1/2, x_9, x_{18})}{dx_9}\\
\chi_6 &= \theta\left(-\frac{x_9^2}{x_{18}^2} + \frac{dB(-1/2, x_{18})}{dx_{18}}\right) + \gamma\left(\frac{dF(-1/2, x_9, x_{18})}{dx_{18}} + \frac{d^2B(-1/2, x_{18})}{dxdx_{18}}\right)\\
\chi_7 &= -\frac{dp(M, x_{11})}{dA}\\
\chi_8 &= \frac{dp(0, x_{14})}{dA}\\
\chi_9 &= \frac{dp(0, x_{17})}{dA}\\
\chi_{10} &= -\frac{dp(M, x_{10})}{dA}\\
\chi_{11} &= \frac{dp(0, x_{13})}{dA}\\
\chi_{12} &= \frac{dp(0, x_{16})}{dA}
\end{aligned}$$

where the derivatives of B, F and p involved in $\chi_1 - \chi_{12}$ are given by

$$\begin{aligned}
\frac{dB(l, x_i)}{dx_i} &= \frac{f(r_0)_l}{2}\sqrt{\frac{(A)_l}{x_i}}\\
\frac{d^2B(l, x_i)}{dxdx_i} &= \left[\frac{1}{2\sqrt{x_i}}\left(f(r_0)_l\sqrt{\pi} + \left(\frac{df}{dr_0}\right)_l\sqrt{(A_0)_l}\right) - \left(\frac{df}{dr_0}\right)_l\right]\left(\frac{dr_0}{dx}\right)_l\\
\frac{dF(l, x_{i_1}, x_{i_2})}{dx_{i_2}} &= \frac{2\pi(r_0)_l}{\delta\mathcal{R}}\frac{x_{i_1}}{x_{i_2}^2}\\
\frac{dF(l, x_{i_1}, x_{i_2})}{dx_{i_1}} &= \frac{2\pi(r_0)_l}{\delta\mathcal{R}}\frac{1}{x_{i_2}}\\
\frac{dp(l, x_i)}{dx_i} &= -\frac{f(r_0)_l}{2}\sqrt{\frac{d(A)_l}{x_i^3}}
\end{aligned}$$

B.2 Matching conditions

The matching conditions linking the flows at the terminals of large arteries and veins are given by two convolution integrals defined in equations (2.90) and (2.91) and given in a compact form by

$$q_k(t) = \sum_{l=1}^{2} \int_0^T y_{kl}(\tau)\, p_l(t-\tau)\, d\tau, \quad k = 1, 2, \tag{B.25}$$

with q_1 representing the flow at arterial terminal and q_2 at the corresponding venous terminal. The incorporation of these integrals in the numerical scheme is described below for the arterial and venous sides.

Arterial Side

On the arterial side of the matching boundary, the convolution integral can be written as

$$q_A(M\Delta x, t) = \int_0^T \left(p_A(M\Delta x, t-\tau)y_{11}(M\Delta x, \tau) + p_V(0, t-\tau)y_{12}(M\Delta x, \tau)\right) d\tau \tag{B.26}$$

where the subscripts A and V denote the arterial and venous sides of the matching boundary, respectively, and the matrix $\mathbf{Y}$ relates the flow and pressure on either side of the matching boundary by

$$\begin{pmatrix} q_A \\ q_V \end{pmatrix} = \begin{pmatrix} y_{11} & y_{12} \\ y_{21} & y_{22} \end{pmatrix} \begin{pmatrix} p_A \\ p_V \end{pmatrix}$$

Equation (B.26) can be discretised by

$$q_M^n = \left(p_A(M, A_M^n)(y_{11})^0 + p_V(0, A_0^n)(y_{12})^0\right) \Delta t + (q_{tms}^A)_M^n \tag{B.27}$$

where the current time is $t = n\Delta t$ and

$$(q_{tms}^A)_M^n = \sum_{k=1}^{N-1} \left((p_A)_M^{<n-k>_N} y_{11}^k + (p_V)_M^{<n-k>_N} y_{12}^k\right) \Delta t. \tag{B.28}$$

Here, N is the number of time-steps per period, and $< \cdot >_N$ denotes the modulo operator, the range of which is the set $\{0, 1, \ldots, N-1\}$. Since $S_1 = 0$, from the numerical scheme (2.104), the q and A at the terminal of larger arteries are given by

$$\begin{aligned} q_M^{n+1} = q_M^n &- \frac{\Delta t}{\Delta x}\left((W_2)_{M+1/2}^{n+1/2} - (W_2)_{M-1/2}^{n+1/2}\right) \\ &+ \frac{\Delta t}{2}\left((S_2)_{M+1/2}^{n+1/2} + (S_2)_{M-1/2}^{n+1/2}\right) \end{aligned} \tag{B.29}$$

$$A_M^{n+1} = A_M^n - \frac{\Delta t}{\Delta x}\left((W_1)_{M+1/2}^{n+1/2} - (W_1)_{M-1/2}^{n+1/2}\right) \tag{B.30}$$

The unknowns in these equations are

$$q_M^{n+1}, \quad A_M^{n+1}, \quad (W_1)_{M+1/2}^{n+1/2}, \quad (W_2)_{M+1/2}^{n+1/2} \quad \text{and} \quad (S_2)_{M+1/2}^{n+1/2}.$$

Similar to inflow, outflow and bifurcation conditions, these can be determined by establishing a ghost point (see Figure 2.12), such that

$$A_M^{n+1/2} = \frac{1}{2}\left(A_{M-1/2}^{n+1/2} + A_{M+1/2}^{n+1/2}\right), \tag{B.31}$$

$$q_M^{n+1/2} = \frac{1}{2}\left(q_{M-1/2}^{n+1/2} + q_{M+1/2}^{n+1/2}\right). \tag{B.32}$$

Creating a ghost point add two more unknowns, $q_M^{n+1/2}$ and $A_M^{n+1/2}$, to the system. These can be found using the boundary condition at the time levels $n+1/2$ and $n+1$,

$$q_M^{n+1/2} = \left(p_A(M, A_M^{n+1/2})(y_{11})^0 + p_V(L, A_L^{n+1/2})(y_{12})^0\right)\Delta t + (q_{tms}^A)_M^{n+1/2} \tag{B.33}$$

$$q_M^{n+1} = \left(p_A(M, A_M^{n+1})(y_{11})^0 + p_V(L, A_L^{n+1})(y_{12})^0\right)\Delta t + (q_{tms}^A)_M^{n+1} \tag{B.34}$$

Venous Side

By following an identical argument as for the arterial side of the matching boundary, we find the following six equations for the venous side of the matching boundary for a vessel of length $L\Delta x$,

$$A_L^{n+1} = A_L^n - \frac{\Delta t}{\Delta x}\left((W_1)_{L+1/2}^{n+1/2} - (W_1)_{L-1/2}^{n+1/2}\right) \tag{B.35}$$

$$q_L^{n+1} = q_L^n - \frac{\Delta t}{\Delta x}\left((W_2)_{L+1/2}^{n+1/2} - (W_2)_{L-1/2}^{n+1/2}\right) + \frac{\Delta t}{2}\left((S_2)_{L+1/2}^{n+1/2} + (S_2)_{L-1/2}^{n+1/2}\right) \tag{B.36}$$

$$A_L^{n+1/2} = \frac{1}{2}\left(A_{L-1/2}^{n+1/2} + A_{L+1/2}^{n+1/2}\right) \tag{B.37}$$

$$q_L^{n+1/2} = \frac{1}{2}\left(q_{L-1/2}^{n+1/2} + q_{L+1/2}^{n+1/2}\right) \tag{B.38}$$

$$q_L^{n+1/2} = \left(p_A(M, A_M^{n+1/2})(y_{21})^0 + p_V(L, A_L^{n+1/2})(y_{22})^0\right)\Delta t + (q_{tms}^V)_L^{n+1/2} \tag{B.39}$$

$$q_L^{n+1} = \left(p_A(M, A_M^{n+1})(y_{21})^0 + p_V(L, A_L^{n+1})(y_{22})^0\right)\Delta t + (q_{tms}^V)_L^{n+1} \tag{B.40}$$

Solving the equations

The twelve equations (B.30)–(B.34) and (B.35)–(B.40) have twelve unknowns listed below

$$\begin{array}{cccccc} A_M^{n+1} & q_M^{n+1} & A_M^{n+1/2} & q_M^{n+1/2} & A_{M+1/2}^{n+1/2} & q_{M+1/2}^{n+1/2} \\ A_L^{n+1} & q_L^{n+1} & A_L^{n+1/2} & q_L^{n+1/2} & A_{L+1/2}^{n+1/2} & q_{L+1/2}^{n+1/2} \end{array}$$

The number of equations can be reduced by substituting (B.31), (B.32) and (B.37) into (B.33), and by substituting (B.31), (B.37) and (B.38) into (B.39). Hence (B.33) and (B.39) can be written as

$$\begin{aligned}\frac{q_{M-1/2}^{n+1/2}+q_{M+1/2}^{n+1/2}}{2} &= \left(p_A(M,\frac{A_{M-1/2}^{n+1/2}+A_{M+1/2}^{n+1/2}}{2})(y_{11})^0\right)\Delta t\\ &+\left(p_V(L,\frac{A_{L-1/2}^{n+1/2}+A_{L+1/2}^{n+1/2}}{2})(y_{12})^0\right)\Delta t+(q_{tms}^A)_M^{n+1/2}\end{aligned} \tag{B.41}$$

and

$$\begin{aligned}\frac{q_{L-1/2}^{n+1/2}+q_{L+1/2}^{n+1/2}}{2} &= \left(p_A(M,\frac{A_{M-1/2}^{n+1/2}+A_{M+1/2}^{n+1/2}}{2})(y_{21})^0\right)\Delta t\\ &+\left(p_V(L,\frac{A_{L-1/2}^{n+1/2}+A_{L+1/2}^{n+1/2}}{2})(y_{22})^0\right)\Delta t+(q_{tms}^V)_L^{n+1/2}\end{aligned} \tag{B.42}$$

Thus a system of eight non–linear equations (B.30), (B.29), (B.34), (B.35), (B.36), (B.40), (B.41) and (B.42) comprising eight unknowns

$$\begin{array}{llll} x_1=A_M^{n+1} & x_2=q_M^{n+1} & x_3=A_{M+1/2}^{n+1/2} & x_4=q_{M+1/2}^{n+1/2}\\ x_5=A_L^{n+1} & x_6=q_L^{n+1} & x_7=A_{L+1/2}^{n+1/2} & x_8=q_{L+1/2}^{n+1/2}\end{array}$$

is to solved. As for the bifurcation conditions, we can solve this system by Newton's scheme subject to the initial guesses

$$\begin{array}{llll} (x_1)_0=A_{M-1/2}^{n+1/2} & (x_2)_0=q_{M-1/2}^{n+1/2} & (x_3)_0=A_M^n & (x_4)_0=q_M^n\\ (x_5)_0=A_{L-1/2}^{n+1/2} & (x_6)_0=q_{L-1/2}^{n+1/2} & (x_7)_0=A_L^n & (x_8)_0=q_L^n\end{array}$$

Residual equations for the Newton's scheme

From these equations we can write eight residual equation $\mathbf{f_r}(\mathbf{x})=((fr)_1,(fr)_2,\ldots,(fr)_8)$ to solve for eight unknowns $\mathbf{x}=(x_1,x_2,\ldots,x_8)$.

$(fr)_1$ from equation (B.30)

$$(fr)_1=k_1-x_1-\theta x_4 \tag{B.43}$$

where

$$k_1=A_M^n+\theta(R_1)_{M-1/2}^{n+1/2}$$

$(fr)_2$ **from equation (B.29)**

$$(fr)_2 = k_2 - x_2 - \theta\left(\frac{x_4^2}{x_3} + B(M+1/2, x_3)\right) + \gamma\left(F(M+1/2, x_4, x_3) + \frac{dB(M+1/2, x_3)}{dx}\right) \tag{B.44}$$

where

$$k_2 = q_M^n + \theta(R_2)_{M-1/2}^{n+1/2} + \gamma(S_2)_{M-1/2}^{n+1/2}$$

$$B(M+1/2, x_3) = f(r_0)_{M+1/2}\sqrt{x_3(A_0)_{M+1/2}}$$

$$F(M+1/2, x_4, x_3) = \frac{-2\pi(r_0)_{M+1/2}}{\delta R}\frac{x_4}{x_3}$$

$$\begin{aligned}\frac{dB(M+1/2, x_3)}{dx} &= \left(\frac{dB}{dr_0}\frac{dr_0}{dx}\right)_{M+1/2}^{n+1/2} \\ &= \left(2\sqrt{x_3}\left(\sqrt{\pi}f(r_0) + \sqrt{A_0}\frac{df}{dr_0}\right) - A\frac{df}{dr_0}\right)_{M+1/2}\left(\frac{dr_0}{dx}\right)_{M+1/2}\end{aligned}$$

$(fr)_3$ **from equation (B.34)**

$$(fr)_3 = k_3 - x_2 + k_4 p_A(M, x_1) + k_5 p_V(L, x_5) \tag{B.45}$$

where

$$k_3 = (q_{tms}^A)_M^{n+1}, \qquad k_4 = (y_{11})^0\Delta t, \quad \text{and} \quad k_5 = (y_{12})^0\Delta t.$$

$(fr)_4$ **from equation (B.35)**

$$(fr)_4 = k_6 - x_5 - \theta x_8 \tag{B.46}$$

where

$$k_6 = A_L^n + \theta(R_1)_{L-1/2}^{n+1/2}$$

$(fr)_5$ **from equation (B.36)**

$$(fr)_5 = k_7 - x_6 - \theta\left(\frac{x_8^2}{x_7} + B(L+1/2, x_7)\right) + \gamma\left(F(L+1/2, x_8, x_7) + \frac{dB(L+1/2, x_7)}{dx}\right) \tag{B.47}$$

where

$$k_7 = q_L^n + \theta(R_2)_{L-1/2}^{n+1/2} + \gamma(S_2)_{L-1/2}^{n+1/2}$$

$$B(L+1/2, x_7) = f(r_0)_{L+1/2}\sqrt{x_7(A_0)_{L+1/2}}$$

$$F(L+1/2, x_8, x_7) = \frac{-2\pi (r_0)_{L+1/2}}{\delta R}\frac{x_8}{x_7}$$

$$\begin{aligned}\frac{dB(L+1/2, x_7)}{dx} &= \left(\frac{dB}{dr_0}\frac{dr_0}{dx}\right)^{n+1/2}_{L+1/2} \\ &= \left(2\sqrt{x_7}\left(\sqrt{\pi}f(r_0) + \sqrt{A_0}\frac{df}{dr_0}\right) - A\frac{df}{dr_0}\right)_{L+1/2}\left(\frac{dr_0}{dx}\right)_{L+1/2}\end{aligned}$$

$(fr)_6$ from equation (B.40)

$$(fr)_6 = k_8 - x_6 + k_9 p_A(M, x_1) + k_{10} p_V(L, x_5) \tag{B.48}$$

where

$$k_8 = (q^V_{tms})^{n+1}_L, \qquad k_9 = (y_{12})^0 \Delta t, \quad \text{and} \quad k_{10} = (y_{22})^0 \Delta t$$

$(fr)_7$ from equation (B.41)

$$(fr)_7 = k_{11} - \frac{x_4}{2} + k_4 p_A(M, (k_{12} + x_3)/2) + k_5 p_V(L, (k_{13} + x_7)/2) \tag{B.49}$$

where

$$k_{11} = (q^A_{tms})^{n+1/2}_M - \frac{1}{2}(q^{n+1/2}_{M-1/2})$$
$$k_{12} = A^{n+1/2}_{M-1/2} \quad \text{and} \quad k_{13} = A^{n+1/2}_{L-1/2}$$

$(fr)_8$ from equation (B.42)

$$(fr)_8 = k_{14} - \frac{x_8}{2} + k_9 p_A(M, (k_{12} + x_3)/2) + k_{10} p_V(L, (k_{13} + x_7)/2) \tag{B.50}$$

where

$$k_{14} = (q^V_{tms})^{n+1/2}_L - \frac{1}{2}(q^{n+1/2}_{L-1/2})$$

Jacobian for the Newton's Scheme

The Jacobian for Newton's scheme (B.13), is given by

$$D\mathbf{f_r}(\mathbf{x}) = \begin{pmatrix} -1 & 0 & 0 & -\theta & 0 & 0 & 0 & 0 \\ 0 & -1 & \chi_1 & \chi_2 & 0 & 0 & 0 & 0 \\ \chi_3 & -1 & 0 & 0 & \chi_4 & 0 & 0 & 0 \\ 0 & 0 & 0 & 0 & -1 & 0 & 0 & -\theta \\ 0 & 0 & 0 & 0 & 0 & -1 & \chi_5 & \chi_6 \\ \chi_7 & 0 & 0 & 0 & \chi_8 & -1 & 0 & 0 \\ 0 & 0 & \chi_9 & -\frac{1}{2} & 0 & 0 & \chi_{10} & 0 \\ 0 & 0 & \chi_{11} & 0 & 0 & 0 & \chi_{12} & -\frac{1}{2} \end{pmatrix}$$

where,

$$
\begin{aligned}
\chi_1 &= \theta\left(\left(\frac{x_4}{x_3}\right)^2 - \frac{dB(M+1/2,x_3)}{dx_3}\right) + \gamma\left(\frac{dF(M+1/2,x_4,x_3)}{dx_3} + \frac{d^2B(M+1/2,x_3)}{dxdx_3}\right)\\
\chi_2 &= -\theta\frac{2x_4}{x_3} + \gamma\frac{dF(M+1/2,x_4,x_3)}{dx_4}\\
\chi_3 &= k_4\frac{dP_A(M,x_1)}{dx_1}\\
\chi_4 &= k_5\frac{dP_V(L,x_5)}{dx_5}\\
\chi_5 &= \theta\left(\left(\frac{x_8}{x_7}\right)^2 - \frac{dB(L+1/2,x_7)}{dx_7}\right) + \gamma\left(\frac{dF(L+1/2,x_8,x_7)}{dx_7} + \frac{d^2B(L+1/2,x_7)}{dxdx_7}\right)\\
\chi_6 &= -\theta\frac{2x_8}{x_7} + \gamma\frac{dF(L+1/2,x_8,x_7)}{dx_8}\\
\chi_7 &= k_9\frac{dP_A(M,x_1)}{dx_1}\\
\chi_8 &= k_{10}\frac{dP_V(L,x_5)}{dx_5}\\
\chi_9 &= k_4\frac{dP_A(M,(k_{12}+x_3)/2)}{dx_3}\\
\chi_{10} &= k_5\frac{dP_V(L,(k_{13}+x_7)/2)}{dx_7}\\
\chi_{11} &= k_9\frac{dP_A(M,(k_{12}+x_3)/2)}{dx_3}\\
\chi_{12} &= k_{10}\frac{dP_V(L,(k_{13}+x_7)/2)}{dx_7}
\end{aligned}
$$

where the derivatives of B, F and p involved in $\chi_1 - \chi_{12}$ are same as defined previously for bifurcation conditions.

References

[1] Aguado-Sierre, K.H. Parker, J. E. Davies, D. Francis, A.D. Hughes, and J. Mayet. Arterial pulse wave velocity in coronary arteries. *Annual International Conference of IEEE Engineering in Medicine and Biology, Proceedings, New York City*, pages 867–870, 2006.

[2] A. Al-Tinawi, A. V. Clough, D. R. Harder, J. H. Linehan, D.A. Rickaby, and C. A. Dawson. Distensibility of small veins of the dog lung. *J. Appl Physiol.*, 73:2158–2165, 1992.

[3] A. Al-Tinawi, J. A. Madden, C. A. Dawson, J. H. Linehan, D. R. Harder, and D. A. Rickaby. Distensibility of small arteries of the dog lung. *J. Appl Physiol.*, 71:1714–1722, 1991.

[4] J. Alastruey. Numerical assessment of time-domain methods for the estimation of local arterial pulse wave speed. *Journal of Biomechanics*, 44:885–891, 2011.

[5] J. Alastruey, Anthony A. E. Hunt, and Peter D. Weinberg. Novel wave intensity analysis of arterial pulse wave propagation accounting for peripheral reflections. *Int. J. Numer. Meth. Biomed. Engng*, page DOI: 10.1002/cnm.2602, 2013.

[6] J. Alastruey, A. W. Khir, K. S. Matthys, P. Segers, S.J. Sherwin, P.R. Verdonck, K.H. Parker, and J. Peiro. Pulse wave propagation in a model human arterial network: Assessment of 1–d visco–elastic simulations against in vitro measurements. *Journal of Biomechanics*, 44:2250–2258, 2011.

[7] J. Alastruey, K.H. Parker, and J. Peiro. Analysing the pattern of pulse waves in the arterial networks: a time–domain study. *J Eng Math*, 64:331–351, 2009.

[8] M. Anliker, L. Rockwell, and E. Ogden E. Nonlinear analysis of flow pulses and shock waves in arteries. *ZAMP*, 22:217–246, 1971.

[9] Jordi Alastruey Arimon. *Numerical modelling of pulse wave propagation in the cardiovascular system: development, validation and clinical applications*. PhD thesis, Department of Aeronautics and Bioengineering, Imperial College, London, Uk, 2006.

[10] H. B. Atabek. Wave propagation through a viscous fluid contained in a tethered, initially stressed, orthotropic elastic tube. *Biophys J*, 8:626–649, 1968.

[11] H. B. Atabek and H. S. Lews. Wave propagation through a viscous incompressible fluid contained in an initially stressed elastic tube. *Biophys J*, 6(4):481–503, 1966.

[12] E. O. Attinger. Pressure transmission in pulmonary arteries related to frequency and geometry. *Circ Res*, 12(6):623–641, 1963.

[13] E. O. Attinger, editor. *Pulsatile Blood Flow*. McGraw–Hill, Proceedings of the first international Symposium on pulsatile blood flow. New York, 1963.

[14] J. D. Bargainer. Pulse wave velocity in the main pulmonary artery of the dog. *Circ Res.*, 20:630–637, 1967.

[15] A. Barnard, W. Hunt, W. Timlake, and E. Varley. A theory of fluid flow in compliant tubes. *J. Biophys*, 6:717–724, 1966.

[16] P. J. Barnes and S. F. Liu. Regulation of pulmonary vascular tone. *Pharmacol Rev*, 47:87–131, 1995.

[17] R. J. Barst, M. McGoon, A. Torbicki, O. Sitbon, M. J. Krowka, H. Olschewski, and S. Gaine. Diagnosis and differential assessment of pulmonary arterial hypertension. *J Am Coll Cardiol*, 43:40S–47S, 2004.

[18] D. H. Bergel and W. R. Milnor. Pulmonary vascular impedance in the dog. *Circulation Research*, 16(401–15), 1965.

[19] S. Berger. Flow in large blood vessels. *Contemp Math*, 141:479–518, 1993.

[20] J. Blacher, R. Asmar, S. Djane, G. M. London, and M. E. Safar. Aortic pulse wave velocity as a marker of cardiovascular risk in hypertensive patients. *Hypertension*, 33:1111–1117, 1999.

[21] Hugo G. Bogren, Richard H. Klipstein, Raad H. Mohiaddinand David N. Firmin, S. Richard Underwood, R. Simon O. Rees, and Donald B. Longmore. Pulmonary

artery distensibility and blood flow patterns: A magnetic resonance study of normal subject and patients with pulmonary arterial hypertension. *Am Heart J*, 118:990–999, 1989.

[22] P. Boutouyrie, M. Briet, C. Collin, S. Vermeersch, and B. Pannier. Assessment of pulse wave velocity. *Artery Research*, 3:3–8, 2009.

[23] J. C. Bramwell and A. V. Hill. The velocity of pulse wave in man. *Proc. Soc Lond B*, 93:298–306, 1922.

[24] J. S. Brody, E. J. Stemmler, and A. B. Dubois. Longitudinal distribution of vascular resistance in the pulmonary arteries, capillaries, and veins. *J. Clin. Invest.*, 47:783–798, 1968.

[25] R. Burattini, S. Natalucci, and K. B. Campbell. Viscoelasticity modulates resonance in the terminal aortic circulation. *Med Eng Phys*, 21:175–185, 1999.

[26] Kelly S Burrowes. *A mathematical model of the human pulmonary circulation.* PhD thesis, Bioengineering Institute, The University of Auckland, 2005.

[27] Kelly S. Burrowes, Peter J. Hunter, and Merryn H. Tawhai. Anatomically based finite element models of the human pulmonary arterial and venous trees including supernumerary vessels. *J Appl Physiol*, 99:731–738, 2005.

[28] Kelly S Burrowes, Merryn H Tawhai, and Peter J Hunter. Evaluation of arterial blood flow heterogeneity via an image-based computational model. *In Medical Imaging 2005: Physiology, Function, and Structure from Medical Images, 257 edited by Amir A Amini, Armando Manduca, Proceedings of SPIE, Bellingham, WA.*, 5746:1605–7422, 2005.

[29] A. C. Burton. Physiology and biophysics of the circulation. *Chicago, IL, Year Book Medical Publishers, p*, pages 86–94, 1972.

[30] C. G. Caro and G. K. Harrison. Observations on pulse wave velocity and pulsatile blood pressure in the human pulmonary circulation. *Clinical Science*, 23:317–329, 1965.

[31] C. G. Caro and P. G. Saffman. Extensibility of blood vessels in isolated rabbit lungs. *The journal of physiology*, 178(2):193–193, 1965.

[32] C.G. Caro, T.J. Pedley, R.C. Schroter, and W.A. Seed. *The Mechanics of the Circulation.* Cambridge University Press, Cambridge, UK, Cambridge, 2nd edition, 2012.

[33] V. Castelain, P. Herve, Y. Lecarpentier, P. Duroux, G. Simonneau, and D. Chemla. Pulmonary artery pulse pressure and wave reflection in chronic pulmonary thromboembolism and primary pulmonary hypertension. *J Am Coll Cardiol*, 7(4):1085–1092, 2001.

[34] R. B. Clipp. *Determination of Impedance Boundary Conditions For the Pulmonary Vasculature.* PhD thesis, North Carolina State University, Raleigh, USA, 2007.

[35] R. B. Clipp and B. N. Steele. Impedance boundary conditions for the pulmonary vasculature including the effects of geometry, compliance, and respiration. *IEEE Trans Biomed Eng*, 56:862–870, 2009.

[36] R. B. Clipp and B. N. Steele. An evaluation of dynamic outlet boundary conditions in a 1d fluid dynamics model. *Math Biosci and Eng.*, 9:61–74, 2012.

[37] R. Collins and J. A. Maccario. Blood flow in the lungs. *Journal of Biomechanics*, 12(5):373–395.

[38] W. Cousins and P. A. Germaud. Boundary conditions for hemodynamics: The structured tree revisited. *J Comp Phys*, 231:6086–6096, 2012.

[39] W. Cousins and P. A. Gremaud. Impedance boundary conditions for general transient hemodynamics. *Int. J. Numer. Meth. Biomed. Engn.*, submitted, 2013.

[40] W. B. Cousins. *Boundary Conditions and Uncertainty Quantification for Hemodynamics.* PhD thesis, North Carolina State University, Raleigh, USA, 2013.

[41] R. H. Cox. Comparison of mechanical and chemical properties of extra- and intralobar canine pulmonary arteries. *Am. J Physiol. Heart Circ. Physiol.*, 242:H245–H253, 1982.

[42] J. E. Dalen, F. W. Haynes, F. G. Hoppin Jr., G. L. Evans, P. Bhardwaj, and L. Dexter. Cardiovascular responses to experimental pulmonary embolism. *The Am J*, 20(1):3–9, 1967.

[43] P. Dartevelle, E. Fadell, S. Mussot, A. Chapelier, P. Hervel, M. de Perrot, J. Cerrinal, F. L. Laduriel, D. Lehouerou, M. Humbert, O. Sitbon, and G. Simonneau. Chronic thromboembolic pulmonary hypertension. *Eur Respir J*, 23:637–648, 2004.

[44] J. E. Davies, Z. I. Whinnett, D. P. Francis, C. Manisty, Aguado-Sierra, K. Willson, R. A. Foale, I. S. Malik, A. D. Huges, and K. H. Parker *et al.* Evidence of dominant backward propagating "suction" wave responsible for diastolic coronary filling in humans, attenuated in left ventricular hypertrophy. *Circulation*, 113:1768–1778, 2006.

[45] J.E. Davies, Z. I. Whinnett, D. P. Francis, K. Willson, R. A. Foale, I. S. Malik, A. D. Huges, K. H. Parker, and J. Mayet. Use of simultaneous pressure and velocity measurements to estimate arterial wave speed at a single site in humans. *Am J Physiol Heart Circ Physiol*, 290:H878–H885, 2005.

[46] C. A. Dias, R. S. Assad, L. F. Caneo, M. C. Abduch, V. D. Aiello, A. R. Dias, M. B. Marcial, and S. A. Oliveira. Reversible pulmonary trunk banding, ii: an experimental model for rapid pulmonary ventricular hypertrophy. *J. Thorac Cardiovasc. Surg.*, 124:999–1006, 2002.

[47] N. Dwyer. Yong ah chot and kilpatrick david *Variable open-end wave reflection in the pulmonary arteries of anesthetized sheep. J Physiol Sci*, 62:21–28, 2012.

[48] Nathan Dwyer. *Pulmonary arterial wave intensity analysis in health and disease.* PhD thesis, Faculty of Health Science, University of Tasmania, 2010.

[49] R. L. Evans, J. W. Pelley, and L. Quenemoen. Some simple geometric and mechanical characteristics of mammalian blood vessels. *Am J Physio*, 199:1150–1152, 1960.

[50] C. A. Figueroa, I. E. Vignon-Clementel, K. E. Jansen, T. Hughes, and C. A. Taylor a coupled momentum method for modeling blood flow in three-dimensional deformable arteries. *Comput Meth Appl Mech Eng*, 195(5685–5706), 2006.

[51] G. H. Fonseca, R. Souza, V. M. Salemi, Jardim C. V, and S. F. Gualandro. Pulmonary hypertension diagnosed by right heart catheterization in sickle cell disease. *Eur Respir J*, 39(1):112–118, 2012.

[52] L. Formaggia, D. Lamponi, and A. Quarteroni. One-dimensional models for blood flow in arteries. *J Eng Math*, 47:251–276, 2003.

[53] O. Frank. Die grundform des arteriellen pulses. *Z Bio*, 37:483–526, 1899.

[54] MD Frank H. Netter. *Atlas of Human Anatomy*. Saunders, Elsevier, Philadelphia, 5th edition, 2011.

[55] Y. C. Fung. *Biomechanics: Circulation*. Springer, New York, 2nd edition, 1996.

[56] Y. Gao and U. J. Raj. Role of veins in regulation of pulmonary circulation. *Am J Physiol Lung Cell Mol Physiol*, 288:L213–L226, 2005.

[57] K. Gear and F. Marcus. Arrhythmogenic right ventricular dysplasia/cardiomyopathy. *Circulation*, 107:e31–e33, 2003.

[58] E. R. Gozna, A. E. Marble, A. Shaw, and J. G. Holland. Age–related changes in the mechanics of the aorta and pulmonary artery of man. *Journal of Applied Physiology*, 36(4):407–411, 1974.

[59] J. C. Greenfield and M. G. Douglas. Relation between pressure and diameter in main pulmonary artery of man. *J Appl Physiol*, 18(3):557–559, 1963.

[60] B. E. Griffith, X. Luo, D. M. McQueen, and C. S. Peskin. Simulating the fluid dynamics of natural and prosthetic heart valves using the immersed boundary method. *Int. J. Appl. Mech.*, 1:137–177, 2009.

[61] L. Grinberg, T. Anor, E. Cheever, J. R. Madsen, and G.E. Karniadakis. Simulation of the human intracranial arterial tree. *Phil. Trans. R. Soc.*, 367:2371–2386, 2009.

[62] E. Hachulla, V. Gressin, and *et al.* L. Guillevin. Early detection of pulmonary arterial hypertension in systemic sclerosis: a french nationwide prospective multicenter study. *Arthritis Rheum*, 52:3792–3800, 2005.

[63] J. E. Hall. *Guyton and Hall textbook of medical physiology*. Saunders Elsevier, Philadelphia, PA, 12th edition, 2011.

[64] A. Harada, T. Okada, K. Niki, D. Chang, and M. Sugawara. On-line noninvasive one-point measurements of pulse wave velocity. *Heart Vessels*, 17:61–68, 2002.

[65] Junichiro Hashimoto and Sadayoshi Ito. Aortic stiffness determines diastolic blood flow reversal in the descending thoracic aorta; potential implication for retrograde embolic stroke in hypertension. *Hypertension*, 62:DOI: 10.1161/HYPERTENSIONAHA.113.01318, 2013.

[66] E. Hermeling, A. P. G. Hoeks, M. H. M. Winkens, J. L. Waltenberger, R. S. Reneman, A. A. Kroon, and K. D. Reesink. Noninvasive assessment of arterial stiffness should discriminate between systolic and diastolic pressure ranges. *Hypertension*, 55:124–130, 2010.

[67] P. Herve, D. Musset, G. Simonneau, Jr. W. Wagner, and P. Duroux. Almitrine decreases the distensibility of the large pulmonary arteries in man. *Chest*, 96:572–577, 1989.

[68] M. B. Histand and M. Anilker. Influence of flow and pressure on wave propagation the canine aorta. *Circ Res*, 32:524–529, 1973.

[69] E. H. Hollander. *Wave-Intensity Analysis of Pulmonary Arterial Blood Flow In Anesthetized Dogs.* PhD thesis, Department of Cardiovascular Sciences. Calgary, Alberta, Canada, University of Calgary, 1998.

[70] E. H. Hollander, G. M. Dobson, J. J. Wang, K. H. Parker, and J. V. Tyberg. Direct and series transmission of left arterial pressure perturbations to the pulmonary artery: A study using wave–intensity analysis. *Am J. Physiol Herat Circ Physiol*, 286(55-1):H267–H275, 2004.

[71] E. H. Hollander, J. J. Wang, G. M. Dobson, K. H. Parker, and J. V. Tyberg. Negative wave reflections in pulmonary arteries. *Am J Physiol Heart Circ Physiol*, 281(2):895–902, 2001.

[72] William Hopkins and Lewis J. Rubin. Treatment of pulmonary hypertension in adults. *Official reprint from UpToDate, Wolters Kluwer Health (www.uptodate.com)*, pages 1–20, 2013.

[73] K. Horsfield. Morphometry of the small pulmonary arteries in man. *Circulation Research.*, 42(5):593–597, 1978.

[74] K. Horsfield and W. Gordon. Morphometry of pulmonary veins in man. *Lung.*, 159(1):211–218, 1981.

[75] W. Huang, R. T. Yen, M. McLaurine, and G. Bledsoe. Morphometry of the human pulmonary vasculature. *J Appl Physiol*, 81:2123–2133, 1996.

[76] A. D. Huges and K. H. Parker. Forward and backward waves in the arterial system: impedance or wave intensity analysis? *Med Biol Eng Comput*, 47:207–210, 2009.

[77] T. J. R. Hughes. *A Study of the One-Dimensional Theory of Arterial Pulse Propagation*. PhD thesis, University of California Berkeley, Berkeley, USA, 1974.

[78] T. J. R. Hughes and J. Lubliner. On the one–dimensional theory of blood flow in the larger vessels. *Mathematical Biosciences*, 18(1-2):161–170, 1973.

[79] C. Jones, K. Parker, R. Hughes, and D. Sheridan. Nonlinearity of human arterial pulse wave transmission. *Transactions of ASME Journal of Biomechanical Engineering*, 114:10–14, 1992.

[80] C. Jones, M. Sugawara, Y. Kondoh, K. Uchida, and K. Parker. Compression and expansion wavefront travel in canine ascending aortic flow: wave intensity analysis. *Heart Vessels*, 16:91–98, 2002.

[81] K. Niki K., M. Sugawara, K. Uchida, R. Tanaka, K. Tanimoto, and H. Imamura. A noninvasive method of measuring wave intensity, a new hemodynamics index: application to the carotid artery in patients with mitral regurgitation before and after surgery. *Heart Vessels*, 14:263–271, 1999.

[82] R. Kato, L. Lickfett, G. Meininger, T. Dickfeld, R. Wu, G. Juang, P. Angkeow, J. LaCorte, D. Bluemke, R. Berger, H. R. Halperin, and H. Calkins. Pulmonary vein anatomy in patients undergoing catheter ablation of atrial fibrillation. lessons learned by use of magnetic resonance imaging. *Circulation*, 107:2004–2010, 2003.

[83] Y. Kawahira, H. Kishimoto, H. Kawata, S. Ikawa, H. Ueda, T. Nakajima, F. Kayatani, N. Inamura, and T. Nakada. Diameters of the pulmonary arteries and veins as an indicator of bilateral and unilateral pulmonary blood flow in patients with congenital heart disease. *J Card Surg*, 12:253–260, 1997.

[84] A. Khir, M. Henein, T. Koh, S. Das, K. Parker, and D. Gibson. Arterial waves in humans during peripheral vascular surgery. *Clinical Science*, 101:749–757, 2001.

[85] A. W. Khir and Kim H. Parker. Measurements of wave speed and reflected waves in elastic tube and bifurcations. *J Biomech*, 35:775–783, 2002.

[86] A. W. Khir, A. Zambanini, and Kim H. Parker. Local and regional wave speed in the aorta: effects of arterial occlusion. *Med Eng Phys*, 26:23–29, 2004.

[87] Y. H. Kim, E. M. Marom, J. E. Herndon, and H. P. McAdams. Pulmonary vein diameter, cross-sectional area, and shape: Ct analysis. *Radiology*, 235:43–50, 2005.

[88] G. S. Krenz and C. A. Dawson. Vessel distensibility and flow distribution in vascular tree. *J. Math Biol.*, 44:360–374, 2002.

[89] G. S. Krenz and C. A. Dawson. Flow and pressure distributions in vascular networks consisting of distensible vessels. *Am J Physiol*, 284:H2192–H2203, 2003.

[90] J-W. Lankhaar, N. Westerhof, T. J. C. Faes, K. M. J. Marques, J. T. Marcus, P. E. Post-mus, and A. Vonk-Noordegraaf. Quantification of right ventricular afterload in patients with and without pulmonary hypertension. *Am J Physiol Heart Circ Physiol*, 291:H1731–H1737, 2006.

[91] B. I. Levy, G. Ambrosio, A. R. Pries, and H. A. Struijker-Boudier. Microcirculation in hypertension: a new target for treatment? *Circulation*, 2001.

[92] C. W. Li and H. D. Cheng. A nonlinear fluid model for pulmonary blood circulation. *J Biomech*, 26(6):653–664, 1993.

[93] J. Lighthill. *Waves in Fluid.* Cambridge University Press, Cambridge, Chapter 2, 1978.

[94] J. Lighthill. *Mathematical Biofluiddynamics, third printing edn.* Society For Industrial and Applied Mathematics, Philadelphia, USA, Philadelphia, 3rd edition, 1987.

[95] Peter C. Luchsinger, Murray Sachs, and Dali J. Patel. Pressure–radius relationship in large blood vessels in man. *Circ Res.*, 11:885–888, 1962.

[96] X. Y. Luo and T. J. Pedley. A numerical simulation of steady flow in a 2–d collapsible channel. *Journal of Fluid and Structure*, 9:149–174, 1995.

[97] X. Y. Luo and T. J. Pedley. A numerical simulation of unsteady flow in a two–dimensional collapsible channel. *J. Fluid. Mech.*, 314:191–225, 1996.

[98] X. Y. Luo and T. J. Pedley. The effects of wall inertia on flow in a two–dimensional collapsible channel. *J. Fluid. Mech.*, 363:253–280, 1998.

[99] D. G. Lynch, S. L. Waters, and T. J. Pedley. Flow in a tube with non–uniform, time–dependent curvature: governing equations and simple examples. *J. Fluid Mech.*, 323:237–265, 1996.

[100] R. F. Machado and M. T. Gladwin. Pulmonary hypertension in hemolytic disorders: pulmonary vascular disease: the global perspective. *Chest*, 137(30S–38S), 2010.

[101] J. E. Maloney, D. H. Bergel, J. B. Glazier, J. M. Hughes, and J. B. West. Transmission of pulsatile blood pressure and flow through the isolated lung. *Circulation Research*, 23(1):11–24, 1968.

[102] A. L. Marsden, I. E. Vignon-Clementel, F. P. Chan, J. A. Feinstein, and C. A. Taylor. Effects of exercise and respiration on hemodynamic efficiency in cfd simulations of the total cavopulmonary connection. *Annals of Biomedical Engineering*, 35(2):250–263, 2007.

[103] K. S. Matthys, J. Alastruey, J. Peiro, A. W. Khir, P. Segers, P. R. Verdonck, K. H. Parker, and S. J. Sherwin. Pulse wave propagation in a model human arterial network: Assessment of 1-d numerical simulations against in vitro measurements. *J of Biomech*, 40:3476–3486, 2007.

[104] W. W. Meyer and P. Schollmeyer. Die volumendehnbarkeit und die druck-umfang-beziehungen des lungenschlagader-windkessels in abhngigkeit vom alter und pulmonalen hochdruck (in german). *Klinische Wochenschrift*, 35(21):1070–1076, 1957.

[105] W. R. Milnor. *Hemodynamics.* Williams and Wilkins, Baltimore, 2nd edition, 1989.

[106] W. R. Milnor, C. R. Conti, K. B. Lewis, and M. F. O' Rourke. Pulmonary arterial pulse wave velocity and impedance in man. *Circulation Research*, 25(6):637–649, 1969.

[107] S. M. Moore, K.T. Moorhead, J. G. Chase, T. David, and J. Fink. One-dimensional and three-dimensional models of cerebrovascular flow. *Journal of Biomechanical Engineering*, 127(3):440–449, 2005.

[108] D. Mukerjee, D. St George, and *et al.* B. Coleiro. Prevalence and outcome in systemic sclerosis associated pulmonary arterial hypertension: application of a registry approach. *Ann Rheum Dis.*, 62:1088–1093, 2003.

[109] J. P. Mynard, M. R. Davidson, D. J. Penny, and J. J. Smolich. Non–linear separation of pressure, velocity and wave intensity into forward and backward components. *Med Biol Eng Comput*, 50:641–648, 2012.

[110] J. P. Mynard, D. J. Penny, and J. J. Smolich. Wave intensity amplification and attenuation in non–linear flow: Implication for the calculation of local reflection coefficients. *Journal of Biomechanics*, 41:3314–3321, 2008.

[111] W. W. Nichols and M. F. O'Rourke. *MacDonald's blood flow in arteries: Theoretical experimental and clinical principles.* Edward Arnold, Philadelphia, PA, 4th edition, 1998.

[112] N. Ohte, H. Narita, M. Sugawara, K. Niki, T. Okada, A. Harada, J. Hayano, and G. Kimura. Clinical usefulness of carotid arterial wave intensity in assessing left ventricular systolic and early diastolic performance. *Heart and Vessels*, 18:107–111, 2003.

[113] M. S. Olufsen. *Modeling the arterial system with reference to an anesthesia simulator.* PhD thesis, Department of Mathematics, Roskilde University, Denmark, 1998.

[114] M. S. Olufsen. Structured tree outflow condition for blood flow in larger systemic arteries. *Am J Physiol Heart Circ Physiol*, 276:H257–H268, 1999.

[115] M. S. Olufsen, N. A. Hill, G. D. A. Vaughan, C. Sainsbury, and M. Johnson. Rarefaction and blood pressure in systemic and pulmonary arteries. *J Fluid Mech*, 705:280–305, 2012.

[116] M. S. Olufsen, C. S. Peskin, W. Y. Kim, E. M. Pedersen, and A. Nadim. Numerical simulation and experimental validation of blood flow in arteries with structured-tree outflow conditions. *Ann Biomed Eng*, 28:1281–1299, 2000.

[117] Kim H. Parker. An introduction to wave intensity analysis. *Med Biol Eng Comput*, 47:175–188, 2009.

[118] Kim H. Parker and C. J. Jones. Forward and backward running waves in the arteries: Analysis using the method of characteristics. *Journal of Biomechanical Engineering*, 112:322–326, 1990.

[119] Kim H. Parker, C. J. Jones, J. R. Dawson, and D. G. Gibson. What stops the flow of blood from the heart? *Heart and Vessels*, 4:241–245, 1988.

[120] D. J. Patel, F. M. De Freitas, and A. J. Mallos. Mechanical function of the main pulmonary artery. *J Appl Physiol*, 17:205–208, 1962.

[121] D. J. Patel, D. P. Schilder, and A. J. Mallos. Mechanical properties and dimensions of major pulmonary arteries. *J Appl Physiol*, 15:92–106, 1960.

[122] A. J. Peacock, N. F. Murphy, and J. J. V. McMurray *et al.* An epidemiological study of pulmonary arterial hypertension. *Eur Respir J*, 30:104–109, 2007.

[123] A. J. Peacock and L. J. Rubin. *Pulmonary circulation: diseases and their treatment.* Hodder Arnold Publication, London, UK, 2nd edition, 2004.

[124] E. M. Pedersen. Technical report: In vitro and in vivo studies of blood flow in the normal abdominal aorta and aorta bifurcation (in danish), 1993.

[125] E. M. Pedersen, H. W. Sung, A. C. Burlson, and A. P. Yoganathan. Two–dimensional velocity measurements in a pulsatile flow model of abdominal aorta simulating different hemodynamic conditions. *J. Biomech.*, 26:237–1247, 1993.

[126] T. J. Pedley. *The fluid mechanics of large blood vessels.* Cambridge University Press, Cambridge, UK, 1980.

[127] T. J. Pedley. Mathematical modelling of arterial fluid dynamics. *J. Eng. Math.*, 44:419–444, 2003.

[128] T. J. Pedley and X. Y. Luo. Modelling flow and oscillations in collapsible tubes. *Theoret. Comput. Fluid Dynamics*, 10:277–294, 1998.

[129] F. Perren, P. Reymond, F. Lazeyras, and N. Stergiopolus. Patient–specfic mean pressure drop in the systemic arterial tree, a comparison between 1-d and 3-d models. *Journal of Biomechanics*, 45:2499–2505, 2012.

[130] C. S. Peskin. *Partial differential equations in biology.* Courant Institute of Mathematical Sciences, New York University, New York, 1st edition, 1976.

[131] E. Peskin. *Transient and steady-state analysis of electric networks, Chapter 7, pp. 304–378.* Van Nostrand Company, Princeton, NJ, USA, 1961.

[132] M. S. Pollanen. Dimensional optimization at different levels at the arterial hierarchy. *J Theor Biol*, 159:267–270, 1992.

[133] G. P. Porenta, D. F. Young, and T. R. Rogge. A finite-element model of blood flow in arteries including taper, branches, and obstructions. *J. Biomech.*, 108:161–167, 1986.

[134] A. R. Pries, T. W. Secomb, and P. Gaehtgens. Design principles of vascular beds. *Circ Res*, 77:1017–1023, 1995.

[135] F. Pythoud, N. Stergiopulos, C. D. Bertram, and J. J. Meister. Effects of friction and nonlinearities on the separation of arterial waves into their forward and backward components. *J. Biomech*, 29:1419–1423, 1996.

[136] F. Pythoud, N. Stergiopulos, and J. J. Meister. Forward and backward waves in the arterial system: nonlinear separation using riemann invariants. *Technol Health Care*, 3:201–207, 1995.

[137] F. Pythoud, N. Stergiopulos, and J. J. Meister. Separation of arterial pressure waves into their forward and backward running components. *J. Bio Eng.*, 118:295–301, 1996.

[138] M. U. Qureshi, G. D. A. Vaughan, C. Sainsbury, M. Johnson, C. S. Peskin, M. S. Olufsen, and N. A. Hill. Numerical simulation of blood flow and pressure drop in the pulmonary arterial and venous circulation. *Biomechanics and Modeling in Mechanobiology*, doi:10.1007/s10237-014-0563-y.

[139] M. W. Ramsey and M. Sugawara. Arterial wave intensity and ventriculoarterial interaction. *Heart Vessel Suppl.*, pages 128–134, 1997.

[140] J. T. Reeves, J. H. Linehan, and K. R. Stenmark. Distensibility of the normal human lung circulation during exercise. *Am J Physiol Lung Cell Mol Physiol*, 288:L419–L425, 2005.

[141] S. R. Reuben. Wave transmission in the pulmonary arterial system in disease in man. *Circulation Research*, 27(4):523–529, 1970.

[142] Stuart Rich and Marlene Rabinovitch. Diagnosis and treatment of secondary (non–category 1) pulmonary hypertension. *Circulation*, 118:2190–2199, 2008.

[143] G. F. B. Riemann. U eber die fortzflanzung ebener luftwellen von endlicher schwingungsweite. pages 145–176. originally published in Bande VIII,, Abhandlungen der Koniglechen Geselschaft der Wissenschaften zu Gottingen, pp 43–65, 1859.

[144] N. Saouti, N. Westerhof, P. E. Postmus, and A. Vonk-Nordegraaf. The arterial load in pulmonary hypertension. *Eur. Respir Rev*, 19(117):197–2023, 2010.

[145] S. J. Sherwin, V. Franke, J. Perio, and K. Parker. One-dimensional modelling of a vascular network in space-time variables. *J Eng Math*, 47:217–250, 2003.

[146] G. Simonneau, N. Galie, L. J. Rubin, D. Langleben, W. Seeger, G. Domenighetti, S. Gibbs, D. Lebrec, R. Speich, M. Beghetti, S. Rich, and A. Fishman. Clinical classification of pulmonary hypertension. *J Am Coll Cardiol*, 43:5–12, 2004.

[147] G. Simonneau, I. M. Robbins, M. Beghetti, R. N. Channick, M. Delcroix, C. P. Denton, C. G. Elliott, S. P. Gaine, M. T. Gladwin, Z. Jing, M. J. Krowka, D. Langleben, N. Nakanishi, and R. Souza. Updated clinical classification of pulmonary hypertension. *J Am Coll Cardiol*, 54:S43–S54, 2009.

[148] S. Singhal, R. Henderson, K. Horsfield, K. Harding, and G. Cumming. Morphometry of the human pulmonary arterial tree. *Circ Res*, 33:190–197, 1973.

[149] O. Sitbon, C. Lascoux-Combe, and J. F. Delfraissy. et al. *Prevalence of HIV-related pulmonary arterial hypertension in the current antiretroviral therapy era, Am J Respir Crit Care Med*, 177:108–111, 2008.

[150] J. J. Smolich, J. P. Mynard, and D. J. Penny. Simultaneous pulmonary trunk and pulmonary arterial wave intensity analysis in fetal lamb: evidence for cyclic, midsystolic pulmonary vasoconstriction. *Am J Physiol Regul Comp Physiol*, 294:R1554–R1562, 2008.

[151] J. J. Smolich, J. P. Mynard, and D. J. Penny. Wave intensity analysis of right ventricular and pulmonary vascular contribution to higher pulmonary than aortic blood pressure in fetal lambs. *Am J Physiol Herat Circ Physiol.*, 299:H890–H897, 2010.

[152] J. J. Smolich, J. P. Mynard, and D. J. Penny. Pulmonary trunk, ductus arteriosus, and pulmonary arterial phasic blood flow interactions during systole and diastole in fetus. *J. Appl Physiol*, 110:1362–1373, 2011.

[153] B. N. Steele, M. S. Olufsen, and C. A. Taylor. Fractal network model for simulating abdominal and lower extremity blood flow during resting and exercise conditions. *Comp Meth Biomech Biomed Eng*, 10:39–51, 2007.

[154] N. Stergiopulos, D. F. Young, and T. R. Rogge. Computer simulation of arterial flow with applications to arterial and aortic stenosis. *J. Biomech.*, 25:1477–1488, 1992.

[155] N. Stergiopulous, Y. Tardy, and J. J. Meidter. Nonlinear separation of forward and backward waves in elastic conduits. *J. Biomech*, 26:201–209, 1993.

[156] J. C. Stettler, P. Niederer, and M. Anliker. Theoretical analysis of arterial hemodynamics including the influence of bifurcations. part i: Mathematical model and prediction of normal pulse patterns. *Ann. Biomed. Eng.*, 9:145–164, 1981.

[157] M. Sugawara, Niki, N. Ohte, T. Okada, and A. Harada. Clinical usefulness of wave intensity analysis. *Med Biol Eng Comput*, 47:197–206, 2009.

[158] Yi-Hui Sun, T. J. Anderson, Kim H. Parker, and J. V. Tyberg. Wave–intensity analysis: a new approach to coronary hemodynamics. *J Appl Physiol*, 89:1636–1644, 2000.

[159] N. Suwa, T. Niwa, H. Fukasawa, and Y. Sasaki. Estimation of intravascular blood pressure gradients by mathematical analysis of arterial casts. *Tohoku J. Exp. Med*, 79:168–198, 1963.

[160] Y. Tardy, J. J. Meiseter, F. Perret, H. R. Burnner, and M. Arditi. Non–invasive estimate of the mechanical properties of peripheral arteries from ultrasonic and photoplethysmographic measurements. *Clin. Phys. Physiol. Meas.*, 12:39–54, 1991.

[161] M. H. Tawhai and K. S. Burrowes. Modelling pulmonary blood flow. *Respiratory Physiology and Neurobiology*, 163:150–157, 2008.

[162] Merryn H. Tawhai and Kelly S. Burrowes. Developing integrative computational models of pulmonary structure. *The anatomycal record*, 275B:207–218, 2003.

[163] W. M. Thurlbeck and A. M. Churg. *Pathology of the lungs.* Thieme Med Pub, New York, 2nd edition, 1995.

[164] R. M. Tuder, J. H. Yun, A. Bhunia, and I. Fijalkowska. Hypoxia and chronic lung disease. *J Mol Med*, 85:1317–1324, 2007.

[165] J. V. Tyberg, J. E. Davis, Z. Wang, W. A. Whitelaw, J. A. Flewitt, N. G. Shrive, D. P. Francis, A. D. Huges, K. H. Parker, and J. Wang Jr. Wave intensity analysis and the development of the reservoir–wave approach. *Med Biol Eng Comput*, 47:221–232, 2009.

[166] H. B. M Uylings. Optimization of diameters and bifurcation angles in lung and vascular tree structures. *Bull Math Biol.*, 39:509–520, 1977.

[167] D. Valdez-Jasso, M. A. Haider, S. L. Campbell, D. Bia, Y. Zocalo, R. L. Armentano, and M. S. Olufsen. Modeling viscoelastic wall properties of ovine arteries. In *Proc ASME 2009*, pages 2009–20564, SBC0Summer Bioeng Conf, SBC0, 2009. Summer Bioeng Conf.

[168] F. N. van de Vosse and N. Stergiopulos. Pulse wave propagation in the arterial tree. *Annu. Rev. Fluid Mech.*, 43:467–499, 2011.

[169] Gareth D. A. Vaughan. *Pulse propagation in the pulmonary and systemic arteries.* PhD thesis, Department of Mathematics, University of Glasgow, Glasgow, UK, 2010.

[170] I. E. Vignon-Clementel, C. A. Figueroa, K. E. Jansen, and C. A. Taylor. Outflow boundary conditions for three-dimensional finite element modeling of blood flow and pressure in arteries. *Comp. Meth. Appl. Mech. Eng.*, 195:29–32, 2006.

[171] C. Vlachopoulos, K. Aznaouridis, and C. Stefanadis. Prediction of cardiovascular events and all-causes mortality with arterial stiffness: a systematic review and meta-analysis. *Journal of American College of Cardiology*, 55:1318–1327, 2010.

[172] C. Vlachopoulos and M. O'rouke. Genesis of the normal and abnormal pulse. *Curr Prob Cardiol*, 25(5):303–367, 2000.

[173] N. F. Voelkel, R. A. Quaife, L. A. Leinwand, R. J. Barst, M. D. Mcgoon, D. R. Meldrum, J. Dupuis, C. S. Long, L. J. Rubin, F. W. Smart, Y. J. Suzuki, M. Gladwin, E. M. Denholm, and D. B. Gail. Right ventricular function and failure: Report of a national heart, lung, and blood institute working group on cellular and molecular mechanisms of right heart failure. *Circulation*, 114:1883–1891, 2006.

[174] J. von Kries. Ueber die beziehungen zwischen druck und geschwindigkeit, welche bei der wellenbewegung in elastischen schl?uchen bestehen. (on the relationship between pressure and velocity, which exist in connection with wave motion in elastic tubing). *Festschrift der 56. Versammlung Deutscher Naturforscher und rzte (Festschrift of the 56th Convention of German Scientists and Physicians), (Tbingen, Germany: Akademische Verlagsbuchhandlung, 1883)*, pages pages 67–88, 1883.

[175] J. Wang, N. G. Shrive, K. H. Parker, and J. V. Tyberg. "waves" as defined by wave intensity analysis. *Med Biol Eng Comput*, 47(2):189–95, 2009.

[176] S. L. Waters and T. J. Pedley. Oscillatory flow in a tube of time–dependent curvature. part 1. perturbation to flow in a stationary curved tube. *J. Fluid Mech.*, 383:327–352, 1999.

[177] E. R. Weibel. Weibel what makes a good lung? *The morphometric basis of lung function, Swiss Med Wkly*, 139:375–386, 2009.

[178] E. R. Weibel and J. Gil. *Structure-function relationships at the alveolar level.* M. Dekker, New York, 1977.

[179] J. B. West, A. M. Schneider, and M. M. Mitchell. Recruitment in networks of pulmonary capillaries. *Journal of Applied Physiology*, 39(6):976–984, 1975.

[180] N. Westerhof, J. W. Lankhaar, and B. E. Westerhof. The arterial windkessel. *Med Biol Eng Comput*, DOI: 10.1007/s11517-008-0359-2, 2008.

[181] N. Westerhof, P. Sipkema, D. Van, G.C. Bos, and G. Elzinga. Forward and backward waves in arterial system. *Cardiovascular Research*, 6:648–656, 1972.

[182] J. R. Womersley. An elastic tube theory of pulse transmission and oscillatory flow in mammalian arteries, 1957.

[183] P Wood. Pulmonary hypertension with special reference to the vasoconstrictive factor. *Br Heart J.*, 20:557–568, 1958.

[184] N. Xiao, J. D. Humphrey, and C. A. Figueroa. Multi–scale computational model of three–dimensional hemodynamics within a deformable full–body arterial network. *Journal of Computational Physics*, 244:22–40, 2013.

[185] R. T. Yen, Z. Rong, and B. Zhang. Elasticity of pulmonary blood vessels in human lungs. *In: Respiratory Biomechanics: Engineering analysis of structure and function, New York: Springer–Verlag*, pages 109–116, 1990.

[186] R. T. Yen and S. S. Sobin. Elasticity of arterioles and venules in postmortem human lungs. *J. Appl Physiol*, 64(2):611–619, 1988.

[187] T. Young. on the function of the heart and arteries. the croonian lecture. *Phil. Trans. Roy. Sco.*, 99:1–31, 1809.

[188] A. Zambanini, S. L. Cunningham, K. H. Parker, A. W. Khir, S. A. McG Thom, and A. D. Hughes. Wave-energy patterns in carotid, brachial, and radial arteries: a non-invasive approach using wave–intensity analysis. *Heart and Circulatory Physiology*, 289(1):H270–H276, 2005.

[189] C. K. Zarins and C. A. Taylor. *Structure-function relationships at the alveolar level.* W. S. Moore and W. B. S. Company, Editors., 2002.

[190] F. Y. Zhuang, Y. C. Fung, and R. T. Yen. Analysis of blood flow in cats lung with detailed anatomical and elasticity data. *J Appl Physiol*, 55(4):1341–1348, 1983.